**Precise and Efficient Ultrashort Pulse Laser Materials Processing Using Phase-Only Beam Shaping**

**Präzise und effiziente Materialbearbeitung mit Ultrakurzpulslasern mittels Wellenfrontformung**

Der Technischen Fakultät
der Friedrich-Alexander-Universität
Erlangen-Nürnberg

zur
Erlangung des Doktorgrades Dr.-Ing.

vorgelegt von

Lisa Ackermann, M.Sc.

aus Bamberg

Als Dissertation genehmigt
von der Technischen Fakultät
der Friedrich-Alexander-Universität Erlangen-Nürnberg

| | |
|---|---|
| Tag der mündlichen Prüfung: | 18.12.2023 |
| Gutachter: | Prof. Dr.-Ing. Michael Schmidt |
| | Prof. Dr.-Ing. habil. Andreas Ostendorf |

# Preface

It was the winter of the year 2020. I had just finished my first experimental setup for performing beam shaping experiments when it began to snow. Tiny snowflakes fell on the windowsill and I stopped for a while to admire this little gift of nature. Suddenly, I realized that I had found the right motif to test the beam shaping capabilities of my experimental setup.
Now, three years later, I'm glad for having this wink of fate, because the snowflakes have become faithful companions in my scientific work. They reappeared in various publications as demonstrators of beam shaping, and I could not have chosen a better motif, since studying their formation is related to the physical theory of shaping light.

This work is based on the research during my time at the Institute of Photonic Technologies and I am very grateful to numerous people for accompanying me throughout this time. First, I want to thank my advisor Prof. Dr.-Ing. Michael Schmidt for guiding me through this journey by providing the freedom to explore my research field and giving me constructive advise when needed. Furthermore, I want to thank Prof. Dr.-Ing. habil. Andreas Ostendorf for reviewing this dissertation and Prof. Dr.-Ing. Silvia Budday and Prof. Dr. rer. nat. Norbert Lindlein for being part in my doctoral examination committee.
I want to thank all my former colleagues at the institute, in particular all research associates and advisors, the technicians, the administration staff, members of the SAOT, my master's students, and student assistants, for their support. Special thanks go to Clemens who was always there to help and I am especially grateful for his creative solutions and the interest in various research fields that he awakened in me during our joint discussions. Likewise, I want to thank Kristian for his constant support, his exciting research ideas, and the entertaining and culinary enriching evenings. Above all, I would like to thank Benedikt and my family, because their unconditional encouragement has given me the necessary support and confidence to sit here now and complete this work.

Erlangen, October 2023

# Contents

# List of Symbols and Abbreviations

| *Symbol* | *Unit* | *Description* |
|---|---|---|
| $c$ | $3 \cdot 10^8$ m/s² | speed of light in a vacuum |
| $d_{\text{abl}}$ | m | ablated depth |
| $d_{\text{eff}}$ | pm/V | effective nonlinear coefficient |
| $e$ | 2.72 | Euler number |
| $E$ | V/m | electric field |
| $\tilde{E}$ | V/m | angular spectrum representation of electric field |
| $\mathcal{E} = E^{i\omega t}$ | V/m | electric field strength |
| $E$ | V/m | electric field amplitude |
| $E^*$ | V/m | complex conjugate of electric field amplitude |
| $f$ | m | focal length |
| $f_x, f_y$ | Hz | scanning frequency |
| $F$ | J/cm² | fluence (energy per area) |
| $F_{\text{th}}$ | J/cm² | threshold fluence |
| $i$ | - | imaginary unit |
| $I^{(\omega)}, I^{(2\omega)}$ | W/m² | field intensity at fundamental and second harmonic |
| $\mathbf{k}$ | 1/m | reciprocal wave vector |
| $\Delta k$ | 1/m | wave vector mismatch |
| $k_x, k_y, k_z$ | 1/m | wave vector components |
| $L$ | m | length of the nonlinear crystal |
| $n$ | - | refractive index |
| $n_x, n_y, n_z$ | - | refractive index components |
| $n_{o/e}^{(\omega)}$ | - | ordinary/extraordinary refractive index corresponding to the angular frequency $\omega$ |
| $N$ | - | number of laser pulses |
| $P$ | C/m² | polarization density |
| $P^{(1)}$ | C/m² | linear polarization density |
| $P^{\text{NL}}$ | C/m² | nonlinear polarization density |

| *Symbol* | *Unit* | *Description* |
|---|---|---|
| $P^{(2)}, P^{(3)}$ | $C/m^2$ | second and third order nonlinear polarization density |
| $S_a$ | µm | surface roughness |
| $t$ | s | time |
| $u$ | - | variable |
| $U$ | % | uniformity |
| $x, y, z$ | m | coordinates in space |
| $\Delta z$ | m | relative distance along optical axis |
| $\delta$ | m | optical penetration depth |
| $\epsilon_0$ | 8.85 $F/m$ | vacuum permittivity |
| $\epsilon^{(1)}$ | $F/m$ | linear material-specific permittivity |
| $\eta$ | % | efficiency |
| $\theta_m$ | deg | phase matching angle |
| $\delta\theta$ | deg | deviation of phase matching angle |
| $\kappa$ | $W/mK$ | thermal conductivity |
| $\lambda$ | nm | wavelength |
| $\mu$ | - | mean value |
| $\sigma$ | - | standard deviation |
| $\tau$ | s | pulse length |
| $\Phi$ | - | wave front (if applicable phase mask) |
| $\Delta\Phi$ | - | relative phase difference |
| $\phi_m$ | deg | phase matching angle |
| $\delta\phi$ | deg | deviation of phase matching angle |
| $\chi$ | - | electric susceptibility |
| $\chi^{(1)}$ | - | linear electric susceptibility |
| $\chi^{(2)}, \chi^{(3)}$ | - | second/third order nonlinear electric susceptibility |
| $\omega$ | $1/s$ | angular frequency |

| ***Mathematical Operator*** | ***Description*** |
|---|---|
| $\mathcal{F}$ | Fourier transform |
| $\mathcal{F}^{-1}$ | inverse Fourier transform |
| $\int$ | integral |
| $\partial/\partial x$ | partial derivative (for variable $x$) |
| $\nabla^2$ | Laplace operator |

| ***Abbreviation*** | ***Description*** |
|---|---|
| c.c. | complex conjugate |
| cw | continuous wave |
| DOE | diffractive optical element |
| LCoS | liquid crystal on silicon |
| SLM | spatial light modulator |
| UV | ultraviolet |

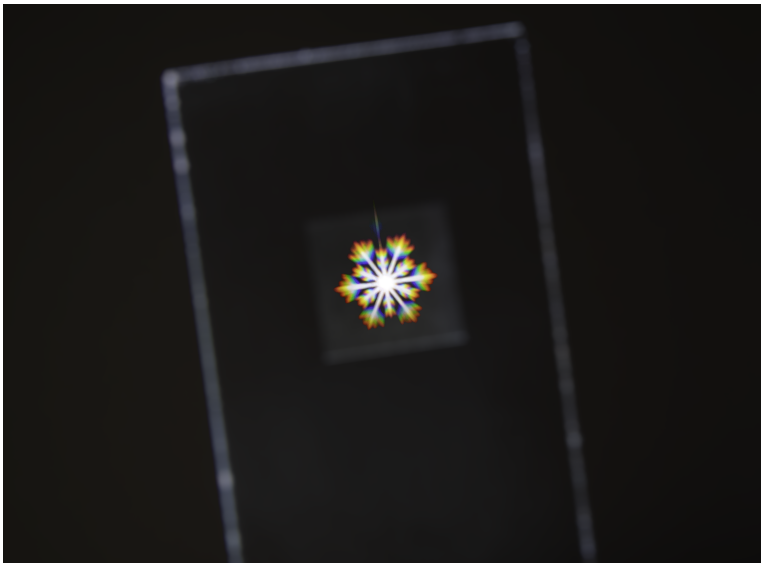

Figure 1: Beam shaping with a structured element.

# 1 Introduction

Manipulating light can allow for fascinating effects and a wide range of possibilities. A small piece of plastic film may manipulate light to form colourful snowflakes as shown in Figure 1. The printed version of this thesis contains this little element as a viewing window on the left page and the reader is invited to conduct a little experiment: bring the piece of plastic close to the eyes and look through it towards a point-like light source, e.g. a smartphone's flash light or any other light source which is ideally far away. A colourful snowflake will appear as shown in Figure 1. To shape the snowflake, the element is manufactured with light diffracting structures. This little experiment shall make the reader familiar with the concept of beam shaping and provide some hands-on experience.

Controlling the spatial distribution of light is a powerful tool and it is thus present in everyday life. Mixed reality devices expand the visually perceived environment by superimposing additional information; think of head up displays in auto mobility or virtual reality glasses. Or consider how a light projector may generate the colourful images on the projection screen. An ancient legend reports that Aristotle ignited the Roman fleet by bundling reflected light with spherically shaped bronze mirrors [1]. Even though the last ancient example is far away from current technology and not fully proven, it demonstrates the power of controlling light.
Applications for beam shaping are diverse but they usually have the same intention: enhanced precision in light guidance and optimized process efficiency. Given those conditions, beam shaping enables localized, highly-accurate light-matter interaction. Thus, controlling light not only improves experimental conditions but also provides further opportunities. This is why the Greek had to focus the sunlight by reflecting it with curved mirrors to a common point until it could ignite the Roman fleet. Moving from ancient and daily life examples to research and industry, there are many fields that employ beam shaping because of the presented benefits: medical surgery [2] and diagnostics [3], production techniques [4], like laser materials processing [5], optical communication [6], microscopic [7] or computational imaging [8], and fundamental research on quantum optics [9] are just a few examples.
The focus of this thesis is on laser materials processing. From a production perspective, beam shaping increases manufacturing precision, processing speed, throughput and thus improves the overall quality and efficiency. The scope of this thesis is to enable precise and efficient laser materials processing by means of beam shaping. Methods and technical solutions are developed to enable high-quality beam shaping, all of which can be realized in practical

applications. Moreover, these methods are validated and evaluated by performing laser ablation experiments. This analysis allows for conclusions on the influence of the processed material — a factor that affects the final result and should thus be included when designing methods for beam shaping and choosing processing parameters. Another influencing factor is the wavelength of the chosen light source as it determines the mechanisms and strength of energy coupling. This thesis thus also investigates nonlinear beam shaping as this may be used to expand the spectral range for phase-only beam shaping devices. Throughout this thesis, the motif of a snowflake will accompany the reader. It serves as a demonstrator to experimentally validate the conceived methods.

# 2 Technical Background

Beam shaping is a general term for controlling the spatial, temporal, and spectral appearance of light. Spatial beam shaping refers to all methods manipulating the spatial intensity profile. Temporal beam shaping forms the intensity profile over time and spectral beam shaping modulates the frequencies. A strict differentiation between spatial, temporal, and spectral beam shaping is not possible as they affect each other. In a practical implementation, several devices and methods are combined which are mutually dependent. Instead of differentiating between physical phenomena which affect each other, it makes sense to focus on the application and the desired outcome, e.g. shaping a targeted intensity profile, and choosing an appropriate method based on the requirements. This highlights the intention of beam shaping which is utilized to adapt a light field for an envisaged application, benefiting from improved precision and efficiency.

This thesis focuses on shaping the spatial intensity distribution for an application in laser materials processing. To this end, light is redistributed to form a targeted beam profile. Sometimes the term tailoring the light field is used to stress the intervention into the process and its optimization. For laser materials processing it is often beneficial to work with uniform intensity distributions as this provides a homogeneous energy deposition. More sophisticated beam shapes may be required to optimize specific applications and to control and refine laser material interaction. All these requirements can be met with spatial beam shaping. This chapter provides an overview on the theoretical background and is structured in three major topics: Beam shaping methodology, ultrashort pulse laser material interaction, and nonlinear optics.

## 2.1 Beam Shaping Methodology

In the introduction, the intuitive term »*redistributing light*« was utilized to envision the concept of »*spatial beam shaping*«, without giving any insights in the underlying physical principles. This section presents the mathematical formalism of light propagation to derive an analytical toolkit for light manipulation. The methodology is inspired by preceding research in holography and this section will place current developments in that context. For the practical implementation, there exist various devices, all of which have their advantages and disadvantages. Those aspects will be evaluated with respect to an application in ultrashort pulse laser materials processing. Achieving uniformity without inducing significant losses turns out to be challenging.

This section will thus conclude with a review on methods for beam shaping, aiming for high quality, uniformity, and high efficiency.

### 2.1.1 Mathematical Formalism of Light and Beam Propagation

The physical framework for the description of light is given by Maxwell's equations and the resulting wave equation [10]. For simplicity, the wave equation is here presented in scalar representation:

$$\nabla^2 E = \frac{1}{c^2}\frac{\partial^2 E}{\partial t^2} \tag{1}$$

$E$ is the electric field, $\nabla^2$ is the second order partial derivation along the spatial $x$-, $y$-, and $z$-coordinates, and $\partial^2/\partial t^2$ is the second order partial derivation with respect to time $t$. This differential equation requires solutions to be periodic in space and time and it is thus called wave equation. The periodicity is defined by the wavelength $\lambda$. Furthermore, the equation defines the speed of wave propagation to be $c$ which is well-known as the speed of light in a vacuum. Solutions for this equation are called electromagnetic waves and a specific wavelength range between 390 nm and 780 nm is called visible light [11].
The perceived brightness of light is proportional to the modulus squared of the electric field $|E|^2$ and does not contain the full information. Both amplitude and phase are required to mathematically describe a wave. The scalar electric field $E$ can be represented as complex number to incorporate both parameters in a single value[1]:

$$E = \mathcal{E} \cdot e^{i\Phi} + \text{c.c.} \tag{2}$$

While the amplitude $\mathcal{E} = \left(Ee^{i\omega t} + \text{c.c.}\right)$ describes the field strength with an oscillating wave term $e^{i\omega t}$ at angular frequency $\omega$ and the field amplitude $E$, the phase $\Phi$ encodes the wave front of the light field. The term wave front refers to points which have the same relative phase.
This definition not only mathematically describes the light field, but also unambiguously determines the field at any position in space and time if it is fully characterized in one plane. Thereby, the wave front has a major influence on the propagation properties. Think of a prism as a simple example. Light that propagates through this element exhibits a shift of the wave front as the optical path length within the prism differs from propagation through

[1] The term c.c. denotes the complex conjugate as the electromagnetic wave is a real quantity. When evaluating the complex exponential and its complex conjugate, a sinusoidal wave is derived.

air. The triangular geometry of the prism will induce a continuous shift of $\Phi$, resulting in a tilted wave front. Effectively, the beam is deflected by that angle when leaving the prism.

**Angular Spectrum Representation**

Angular spectrum representation is a powerful tool to analytically calculate the propagation of the electromagnetic field, a detailed description of which can be found in [12] and [13]. The principle is based on the linearity of the wave equation: any linear combination of individual solutions will also fulfill the wave equation and is thus also a solution. Further, this principle allows for the decomposition of a complicated input signal into a set of simple signals. Thus, any complicated light field can be decomposed in a spectrum of plane waves, the intuitive solution of the wave equation. The propagation for each plane wave can be calculated individually and the results are superimposed to deduce the final solution of the complete system [12].
The mathematical tools are provided by the Fourier analysis, which decomposes a signal at the position $z = 0$ into a linear combination of elementary functions

$$E(x, y; z = 0) = \iint_{-\infty}^{+\infty} \tilde{E}(k_x, k_y; z = 0) e^{i(k_x x + k_y y)} \, dk_x \, dk_y + \text{c.c.}, \qquad (3)$$

where $\tilde{E}(k_x, k_y; z = 0)$ represents the angular spectrum with the reciprocal wave vector $\mathbf{k}$. The decomposed spectrum represents the spatial frequencies of the analyzed signal. The complex exponentials within the integral representation can be considered as plane waves with individual propagation direction. This direction is given by the wave vector $\mathbf{k}$ along the spatial frequencies $k_x$ and $k_y$. The strength of the corresponding plane waves contributions is weighted by the complex amplitude $\tilde{E}(k_x, k_y; z = 0)$. By definition, this complex amplitude is the Fourier transform of the light field $\tilde{E}(k_x, k_y; z = 0) = \mathcal{F}\{E(x, y; z = 0)\}$. This resulting field $\tilde{E}(k_x, k_y; z = 0)$ is called angular spectrum, as every point in space corresponds to a plane wave with the corresponding spatial frequency $k_x$ and $k_y$. This spatial frequency is directly linked to the propagation angle of the plane wave. Thus, this representation is a powerful tool as it decomposes a complicated input signal into a spectrum of plane waves with different propagation angles which can be treated mathematically in a simple way. Propagation through space causes the plane waves to gain an additional phase term. This phase term depends on the propagation distance $\Delta z$ and the propagation angle. The latter accounts for the differing travel distance, depending on the propagation angle of the plane wave and is thus given by the corresponding z-component of the wave

vector $k_z$ in propagation direction. The relative phase due to propagation reads:

$$\Delta\Phi = \Delta z \cdot k_z = \Delta z \cdot \sqrt{k^2 - k_x^2 - k_y^2} \tag{4}$$

This provides a mathematical toolkit for calculating the propagated light field in an arbitrary plane. First, the angular spectrum of the light field is calculated by performing a Fourier transform $\mathcal{F}$. Propagation in Fourier space is simply a multiplication with the propagation phase term $e^{i\Delta\Phi}$. Finally, the inverse Fourier transform $\mathcal{F}^{-1}$ provides the propagated field at $z = \Delta z$.

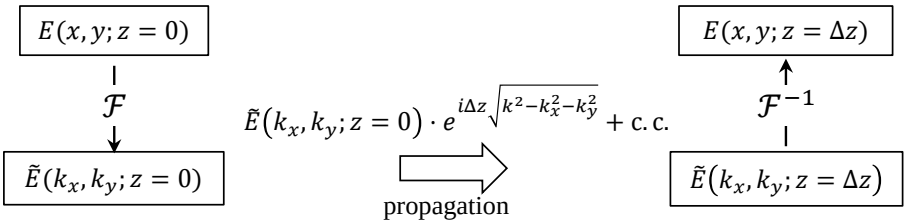


The angular spectrum of the light field is associated with the far field when the light propagates to infinity. This propagation spatially separates the individual angular frequencies. Likewise, a lens assigns those spatial frequencies to a specific position in the focal plane. Focusing with a lens thus effectively brings the far field into the focal plane. The lens corresponds to a wave front $\Phi_{\text{lens}}$ which assigns the individual spatial frequency components to a position in space in the focal plane at the focal distance $f$:

$$\Phi_{\text{lens}} = \frac{k}{2f}(x^2 + y^2) \tag{5}$$

Focusing by a lens can thus be mathematically treated as a Fourier transform. This propagation can also be calculated with the method of angular spectrum. The incoming light field is propagated to the lens, where the lens introduces a spherical wave front. The complex exponential with this phase term $e^{i\Phi_{\text{lens}}}$ is multiplied to the field in front of the lens. Next, the field is propagated to the focal plane which is given by the distance of the focal length $f$. Likewise, any other wave front can be multiplied as complex exponential to the electromagnetic field at the corresponding position, e.g. a more complex phase distribution of a beam shaping element.
The method of angular spectrum is a powerful toolkit to propagate the light field in space and it accounts for wave front modifications as e.g. introduced by a lens. Similarly, the wave front modification of the beam shaping element from the introduction could be added to the calculation to shape the beam into a snowflake. This analysis shows the importance and impact of the wave front. It strongly affects light propagation. Effectively, a lens is

performing wave front shaping by inducing a spherical phase term on the input field which results in a focused intensity profile. Having control over the the beam's wave front enables, to some extent, shaping the intensity distribution in another plane. Equipped with mathematical methods for beam propagation, it is possible to calculate the required phase configurations for shaping specific intensity distributions. While the method of angular spectrum enables forward and backward beam propagation to arbitrary positions in space, the Fourier transform directly relates the field with its far field by a single mathematical operation.

### 2.1.2 From Holography to Phase-Only Beam Shaping

Photography can only acquire 2-dimensional image information as the camera sensor evaluates the absolute square of the light field $|E|^2$, i.e. the intensity pattern. The third dimension of spatiality cannot be captured. Holography goes one step beyond photography. It incorporates wave front and amplitude information by recording an interference pattern. This pattern is generated by interfering an object wave which carries the 3-dimensional object information and a plane reference wave. Consequently, the interference pattern carries information about the object wave. Thereby, the hologram typically incorporates either the corresponding phase shift of the wave front or the attenuation of the amplitude which is introduced by the interference pattern. When evaluated with the reference wave, the hologram reproduces the 3-dimensional object information [14].
While this concept inspired science fiction authors and is still a key element in various future visions [15], it was initially developed as technical solution to improve the image quality in the newly emerging field of electron microscopy in the 1940s [16]. It took until the development of the laser that the concept of holography became popular and it finally emerged to an independent research field with Dennis Gábor winning the nobel prize in physics in 1971 [17]. Holography can be considered as a holistic method that incorporates the full information of the light field. Angular and wavelength-specific characteristics of the recorded object wave can be captured within a thick hologram. Those parameters are degrees of freedom which can not only be utilized for 3-dimensional object reconstruction, but in return also as an analyzing tool [18] to discriminate wavelength- and angular-specific characteristics [19]. Moreover, a hologram acts as an enormous data storage [20] with the potential to be a lot more efficient than current methods [21]. Big tech companies such as IBM [22] and Microsoft [23] are conducting research on that topic. In this way, a hologram can be considered as the physical realization of a complex neural network [24] working at the speed of light [25]. For this reason, there is a lot of current research on this topic [26].

The concept of spatial beam shaping emerged from holography. Instead of interfering an object wave with a reference wave, there are several methods for calculating the required holographic information. This inverse problem can be solved by (back-)propagating the targeted light field to the plane of beam shaping to evaluate the corresponding amplitude and phase information. Based on that, there exist several algorithms to calculate the holographic information which are referred as computer-generated holograms.
Similar to a physically recorded hologram, a beam shaping device shapes the light field by imprinting a specific wave front or modulating the amplitude. As typically only one of those two modalities is shaped [27], many computer-generated holograms are conceived to only manipulate the wave front or the amplitude. While this provides no full control of the light field, there are some benefits for the practical implementation. Wave front shaping, which is referred as phase-only beam shaping, does not induce significant losses. In contrast to attenuating the amplitude, the full light field can be used and this provides high efficiency which is especially relevant when requiring high laser powers. The term *»efficiency«* refers to the portion of shaped light with respect to the unshaped input beam.
Both static and dynamic devices are available to apply the calculated beam shaping pattern to the light field. The computer-generated hologram shapes the wave front to tailor the light field in the target plane. This is illustrated in Figure 2. The resulting shape is referred as target distribution. In contrast to a physically recorded static hologram, the option to adapt and change the applied beam shaping information dynamically makes computer-generated holography a convenient method for a broad group of users. The next section will give an overview on phase-only beam shaping devices with focus on the liquid crystal on silicon spatial light modulator which is the tool of choice within the scope of this thesis.

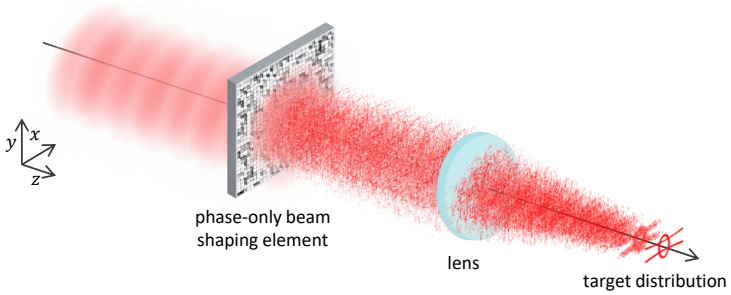


Figure 2: A phase-only beam shaping device introduces a spatially varying phase delay to the incoming light field. The shaped wave front affects beam propagation and the desired image emerges in the target plane.

### 2.1.3 Devices for Phase-Only Beam Shaping

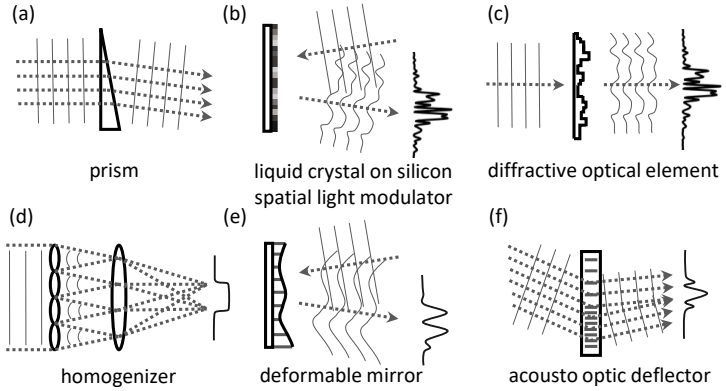


Figure 3: Devices and concepts for phase-only beam shaping with the resulting intensity distribution indicated (apart from (a) which only shows the basic concept of refractive beam deflection).

While the concept of beam shaping allows for the tailoring of complex light distributions, many of these are realized in practice by shaping the wave front. During light propagation, the beam with shaped wave front emerges into the target distribution. The process can be described by fundamental optical principles like diffraction and interference, and, depending on the dimensions, sometimes geometrical optics are sufficient. Two basic examples were already mentioned: a prism and a lens and Figure 3 a shows light deflection by a prism.
Besides the basic examples, there exists a broad range of commercially available phase-only beam shaping devices, all of which have their advantages and disadvantages. The tool of choice for this thesis is the liquid crystal on silicon spatial light modulator, abbreviated with *»LCoS SLM«*. It enables dynamic beam shaping and is applicable to high-energy lasers. The handling is convenient and makes the LCoS SLM operable for a broad group of users [28]. It consists of birefringent liquid crystals which are accommodated in pixelated cells. When applying a certain voltage to the individual liquid crystal cells, the crystals change their orientation. Due to their birefringence, the effective refractive index changes. Light that interacts with those crystals perceives a different refractive index depending on the locally applied voltage and this introduces an adjustable phase delay [29]. Shining light on this display enables shaping the wave front by modulating the phase pixel by pixel as shown in Figure 3 b. This diffracts the light field which interferes to a specific pattern in the target plane. The generated wave front can be adapted dynamically by changing the locally applied voltage. As the display is connected to a computer similar to an additional screen, the corresponding

phase shift is applied by displaying an image of varying brightness. With correct calibration [30], this enables dynamically shaping the wave front typically between 0 and $2\pi$.
LCoS SLMs for laser processing are typically designed to work in reflection and consist of a mirror backplane with a liquid crystal layer on top. With appropriate coating of the backplane mirror, e.g. dielectric coating, devices achieve beam shaping efficiencies $> 95\,\%$. This term refers to the technical capabilities of the device itself. The reflected light contains a tiny portion of non-diffracted light (typically $\ll 5\,\%$) which is often referred as $0^{\text{th}}$ order. Due to the optical properties of the liquid crystals, devices are limited to the visible, near-infrared, and mid-infrared spectral ranges and they are polarization-sensitive as wave front shaping is based on birefringence. Liquid crystal displays are typically available with switching frequencies around $30\,\text{Hz} - 60\,\text{Hz}$ and a modulation depth around 8-bit.
While this concept enables dynamic beam shaping, there exist many static beam shaping solutions. Similar to a pixelated display, a diffractive optical element (DOE) shapes the wave front statically. DOEs are transparent devices, typically made out of glass or polymer, which exhibit a locally varying thickness as Figure 3 c shows. This induces a phase variation. Both the illustration in Figure 2, and the snowflake showed in the introduction are based on that technique. Light shining through such an element gets diffracted and interferes to form the targeted distribution similar to dynamic beam shaping with an LCoS SLM. The technical advantage of a DOE usually lies in the higher damage threshold, finer pixel resolution, and broader spectral range of transparency. Besides a DOE, microlens arrays [31] can be used to transfer the input beam into a homogeneous structure [32], e.g. a top hat or flat top profile [33] as shown in Figure 3 d. Thereby, the shape of the microlenses determines the resulting target geometry and each individual microlens distributes its portion of the incoming beam over the whole area of the target pattern [34]. These elements are thus called homogenizers and they are well-established in laser manufacturing [35], e.g. in photolithography [36], surface ablation [37] and they are even used for applications in the ultraviolet spectral (UV) range [38] and in laser diagnostics [39]. Similarly, a lens-like element with adapted curvature may shape the light beam [40].In contrast to the examples for static beam shaping, dynamic devices provide higher flexibility. This flexibility is especially relevant in research where new methods are developed which require constant adaption and optimization. Moreover, this opportunity enables dynamic process control. Besides an LCoS SLM, the so-called deformable mirror enables dynamic beam shaping [41].It consists of a thin mirror membrane with underlying actuators to deform the mirror surface and shape the reflected wave front as Figure 3 e shows. Deformable mirrors are most typically used for wave front corrections [42]

in adaptive optics [43]. However, there are also some demonstrations of beam shaping for laser materials processing, as e.g. by Sanner et al. [44, 45], Henderson and Mansell [46], and Salter and Booth [47]. Moreover, acousto optical crystals enable beam shaping by generating a diffraction grating in an acousto optical crystal [48]. This is realized with an applied sound wave which causes a periodic variation of the refractive index to induce a grating where light gets diffracted [49]. The method is shown in Figure 3 f. There are publications using acousto optic beam shaping for laser material ablation [50] and laser-based powder bed fusion [51].
The examples show the versatility of phase-only beam shaping devices. The optimum device should be chosen according to the practical requirements. Besides capabilities and technical limitations, this includes arguments such as usability and costs. LCoS SLMs are a widely used tool for ultrashort pulse laser beam shaping as they exhibit relatively high damage thresholds on the order of several hundreds of $GW/cm^2$ for pulsed beams and around 200 W for a continuous wave (cw) beam [52]. Moreover, they are cost-effective and easy to operate. With pixel sizes around several microns, high phase strokes can be realized. Liquid crystal displays thus generate a broad spectrum of deflection angles and achieve beam shaping results with high resolution. This is due to the fact that the pixel size defines the maximum diffraction angle.
The term »*spatial light modulator*« (SLM) refers to almost all of the above introduced devices. However, due to their widespread use, LCoS SLMs are often abbreviated simply as SLM. Overall, their usability and the high beam shaping efficiency make LCoS SLMs favourable. They became an essential tool in optics and laser technology.

### 2.1.4 Algorithms for Phase-Only Beam Shaping and Speckle

Algorithms for calculating the required phase distribution are based on beam propagation because they relate the target distribution with the plane of the SLM. The frequently-used Gerchberg-Saxton algorithm [53] is one example which is based on phase-retrieval [54]. Similar to holography, it also originates from the field of electron microscopy. The initial intention was to reconstruct the wave front from well-known intensity recordings because the phase of the electron beam could not be measured. It is possible to reconstruct the wave front from several intensity recordings as beam propagation can be analytically described and this enables deducing the corresponding wave front which leads to the intensity distributions in the recorded observation planes.
Similarly, the Gerchberg-Saxton algorithm can be used to retrieve the phase for a desired beam shape when shaping a laser beam. Based on iterative propagation, the solution for the proper phase distribution is narrowed down

and the resulting wave front is referred as phase mask. In contrast to reconstructing the wave front, the focus lies on finding a proper wave front to shape the light. The target image is defined by the desired amplitude with an ideally flat wave front as this avoids undesired interference. Back-propagation to the plane of the beam shaping device provides an analytical solution of the light field. However, this solution accounts for wave front and amplitude shaping and the beam shaping device typically only modulates the wave front. Based on these conditions, a solution is required that works by only modulating the wave front of the incoming light beam while the amplitude in the beam shaping plane is fixed. This is only possible if the algorithm does not fully constrain the light field in the target plane, e.g. disregarding the wave front in the target plane while only optimizing the targeted amplitude.
This converse approach allows for shaping arbitrary amplitude distributions by phase-only beam shaping at the cost of an uncontrolled wave front in the target plane as only one modality is controlled in each plane. Thus, the resulting wave front in the target plane is not flat and may exhibit discontinuities causing undesired interference. In the basic configuration, the target plane and the beam on the SLM can be mathematically connected via a Fourier relation. The phase mask can be imagined as a superposition of various prisms with different directions and slopes. As phase-only beam shaping devices typically only modulate the wave front between 0 and $2\pi$, the corresponding phase pattern is wrapped which results in different phase gratings. Every point in the target plane can thus be related to a specific grating which is applied on the SLM to deflect the light beam under that specific angle. The sum of all the corresponding gratings results in the final phase mask. However, the overlap of the different spatial frequencies induces phase vortices on the phase mask. These vortices cause discontinuities in the wave front and remain existent in the target plane. The centre of such a vortex, which is effectively an interwined helical wave front, exhibits a singularity of undefined phase and this causes destructive interference [55]. As a result, areas of destructive and constructive interference overlay the intensity pattern in the target plane which is called speckle. The undesired interference effect of speckle is shown in Figure 4. The number and location of the resulting


Figure 4: Phase-only beam shaping cannot control wave front and amplitude in the beam shaping plane and a speckle pattern overlays the target structure.

speckle peaks are determined by the applied phase mask as they are directly related to the involved gratings and the resulting singularities. The freedom of shaping arbitrary geometries with high efficiency comes at the cost of an overlaying pattern of speckle noise. To avoid speckle, the wave front in the target plane needs to be continuous and ideally flat. This prevents the intensity pattern from undesired interference.
Besides this algorithm, there are several other methods, such as Fienup [56], Glückstad and Mogensen [57], and di Leonardo et al. [58]. Several current approaches include deep learning, such as those by Sinha et al. [59], Mikhaylov et al. [60], and Buske et al. [61]. A neural network may handle more complex scenarios, e.g. including setup-specific influences [62] and cross talk [S1], or realizing complicated multi-plane solutions [61]. However, the physical conditions remain the same. Shaping only the wave front in a single plane does not provide enough degrees of freedom to control the full light field.

### 2.1.5 Methods for Uniform Beam Shaping

Speckle during phase-only beam shaping is a serious issue. While light completely extinguishes at some positions due to destructive interference, other areas exhibit excessive intensities due to constructive interference.This severely impairs the beam shaping quality and the overall processing result. On the one hand, the entire beam should be converted into the desired shape without loss, which is possible with phase-only beam shaping. However, full control of the light field is required in the target plane to guarantee a flat wave front and this is only possible if the amplitude of the input beam is considered as well. Consequently, shaping speckle-free beam profiles while keeping high efficiency is challenging.
For specific geometries, there exist solutions [63]. However, this approach is limited to simple structures, e.g. a rectangle or circle, or only works for specific dimensions [64]. Thus, these approaches cannot be transferred to arbitrary beam shapes and arbitrary application scenarios.
Several methods were developed to avoid speckle noise to achieve a uniform beam profile. Usually they have in common that a continuous wave front is achieved in the target plane. This can be realized by simultaneous wave front and amplitude shaping within a single phase mask while accepting losses, averaging of different phase masks until discontinuities are equally distributed and cancel out, or working with further beam shaping planes to gain control over the wave front and the amplitude.

**Solutions with a Single Phase Mask**
In the first scenario, a single phase mask is used to control wave front and amplitude. Even though wave front shaping cannot modulate the amplitude

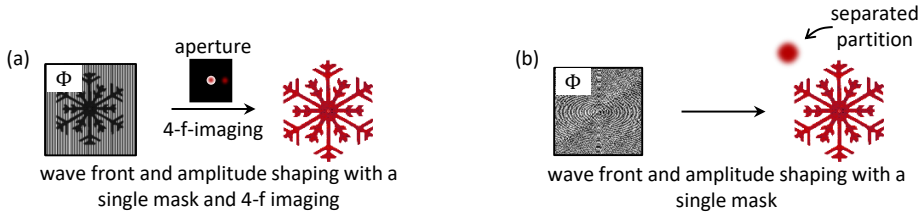


Figure 5: Illustration of two methods for uniform beam shaping based on a single phase mask, where Φ denotes the corresponding phase mask. The arrow indicates the beam propagation between the planes involved.

directly, e.g. by attenuation, it permits indirect amplitude shaping. This can be realized by incorporating an additional diffraction grating of variable strength into the phase mask. This diffraction grating is capable of locally separating an adjustable portion of light by sending it to a position in space far away from the target structure. This allows realizing perfect analytical solutions with simultaneous wave front and amplitude shaping.
In a basic configuration, the target image is directly displayed on the beam shaping device with a constant phase while the surrounding SLM region forms a diffraction grating. 4-f-imaging images this configuration to the target plane. The partition of the beam which is diffracted by the phase grating (not part of target image) locally separates in the Fourier plane. Here it is cut with an aperture. Thus, only the undiffracted target distribution is imaged into the target plane as Figure 5 a shows. This method is demonstrated, e.g., by Bagnoud and Zuegel [65], Hendriks et al. [66], Liu et al [67], and Nakata et al. [68].
In the case of 4-f imaging, distinctive areas on the phase mask were assigned to a grating and completely separated from the final target distribution. However, it is possible to generalize the concept and locally adjust the diffraction strength of a grating. This gives the opportunity to not diffract the full portion of the light field but select partitions with adjustable strength. The local adaption of the diffraction strength effectively enables additional amplitude shaping. This option provides the required degrees of freedom to gain full control of the light field in the target plane at the cost of efficiency. Effectively, not the full light field is converted into the target structure but only a partition of it. The remaining portion can e.g. be sent to an area far away from the target image as shown in Figure 5 b. By doing so, it is possible to achieve a plane wave front in the region of the target image. Besides the mentioned diffraction grating, any phase mask which works as a separator may be combined with the analytical solution. It should be mentioned that there exist various iterative approaches which were reported over the last

decades [69–79]. However, as this scenario can be described analytically, as shown e.g. by Bolduc et al. [80] and Clark et al. [81], there is little justification for using these estimates in recent years.
The superimposed amplitude modulation decreases the light efficiency by the partition of the separated light field. If the beam shaping plane and the target plane are mathematically related via a Fourier transformation, the light efficiency strongly depends on the dimensions of the target image because the size of the target image is inversely proportional to the size of its Fourier transform. Thus, the light efficiency is typically low, as the major contribution of the final signal is given by a tiny portion of spatial frequencies which are closely centred around the optical axis while the remaining partition of the input beam is diffracted away from the target image. Moreover, precise knowledge of the input beam shape and position on the SLM are required as this otherwise distorts amplitude modulation.

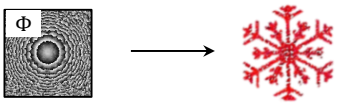


Figure 6: Illustration of a method for uniform beam shaping, called quadratic phase, because it involves a lens term within the phase mask. Φ denotes the corresponding phase mask and the arrow indicates the beam propagation between the planes involved.

To increase the light efficiency and make it fairly independent from the final dimensions of the target structure, a small target structure can be assumed whose final size is adjusted with an additionally applied lens term. This lens term is part of the final phase mask as shown in Figure 6 and the method is therefore referred to as quadratic phase, see e.g. Shimobaba and Ito [82], Shimobaba et al. [83], Pang et al. [84], Nagahama et al. [85], and Fischer and Sinzinger [86]. As the initially assumed target structure is tiny, its Fourier transform increases in size and losses due to diffraction-based amplitude modulation can be strongly reduced. However, the increase in efficiency comes at the cost of resolution. The target structure is scaled to size and does not provide more spatial resolution than the originally assumed small image. Similar to the aforementioned method, this concept also requires precise knowledge of the beam's shape and position on the SLM. As the light efficiency can be increased with the additionally applied lens term, many applications based on that method skip diffraction-based amplitude modulation and work with the full light field. This causes some vortices and speckle while the light efficiency is maximized. Nonetheless, this solution only offers a compromise of achievable resolution, quality, usability, and efficiency.

### Averaging of Phase Masks

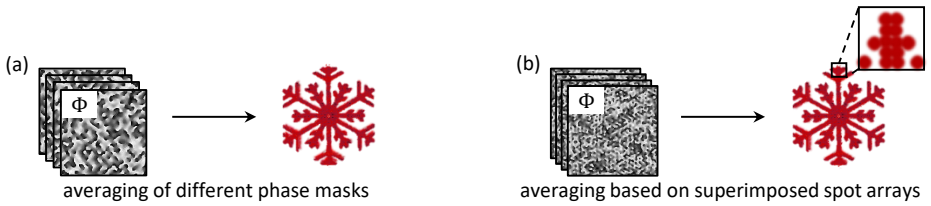


Figure 7: Illustration of two averaging-based methods for uniform beam shaping, where $\Phi$ denotes the corresponding phase masks. The arrow indicates the beam propagation between the planes involved.

Methods, which aim for both optimum efficiency and quality, need to incorporate another degree of freedom. One option is to temporally superimpose shaped beam profiles originating from different phase masks. Depending on the initial starting conditions, the Gerchberg-Saxton algorithm will provide varying speckle patterns. While the shaped target profile remains the same, the speckle pattern changes and the final image can be averaged over time as Figure 7 a shows. Therefore, the individual solutions have to be separated temporally, as the fields would otherwise interfere. While Caulfield [87], Goodman [88], and Amako et al. [89] use the method to average intensity profiles, Häfner et al. demonstrate the method for uniform material ablation with a pico second laser in [90] and [91]. According to the statistical properties of speckle, the amount of speckle scales with $1/\sqrt{N}$ [92], where $N$ is the number of independent phase masks.
Golan and Shoham show that a single phase mask may remove speckle completely if all possible spatial shifts are performed [93]. Alternatively, independent patterns of spot arrays can be superimposed to achieve a uniform surface, compare Figure 7 b. Wlodarczyk et al. [94] and Liu et al. [95] use the method to achieve uniform intensity images, and by Wang et al. [96] perform micorpattern printing. While those approaches are reliable and unsusceptible to deviations in the experimental implementation, the low frame rate of the SLM limits the speed of exchanging phase masks. This causes laser dead times and reduces the achievable processing efficiency. Consequently, a solution is required which overcomes this technical limitation.

#### Working with Several Phase-Only Beam Shaping Planes

Another option is working with several phase shaping planes. Each additional plane provides more control of light propagation. While a single beam

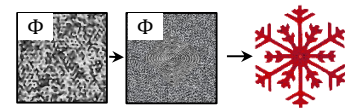


Figure 8: Illustration of uniform beam shaping involving two phase-only beam shaping planes, where Φ denotes the corresponding phase masks. The arrow indicates the beam propagation between the planes involved.

shaping plane only controls either the wave front or the amplitude without introducing losses, a second plane may be used to control the other modality. This concept finds various implementations.
Inspired by phase contrast microscopy, the method of generalized phase contrast [57] employs two phase shaping planes to create high-quality images which are free of speckle [97]. This method transforms phase modulation to intensity contrast and induces no losses [98]. Likewise, two shaped beam profiles from two SLM planes with crossed polarization can be superimposed [99]. A second SLM plane can also be used to realize amplitude and wave front shaping without inducing additional losses, as realized by Bartelt with two phase filters [100, 101] and by Jesacher et al. with two SLM planes [102, 103]. Figure 8 shows the principle. Including even more beam shaping planes provides further degrees of freedom. This can be used to shape several intensity patterns in different planes [61] or to design wavelength- and angular-specific solutions as is possible with volume holograms. This can be realized with cascaded beam shaping devices [104], or 3-dimensional photonic crystals [105]. Although this approach provides a variety of opportunities, excessive fluences in intermediate planes need to be avoided when working with ultrashort pulse lasers. This requires broad illumination of the involved beam shaping planes. Moreover, the involved phase masks are calculated for a specific amplitude and phase distribution which needs to be met in the experimental implementation by precise alignment and a good characterization of the setup.
Overall, the methods presented show that there are different ways to achieve a uniform beam profile. However, these methods are not generally applicable, as they typically allow only a compromise between efficiency and achievable quality, or induce excessive fluences on the involved beam shaping planes.

## 2.2 Materials Processing Using Ultrashort Pulse Lasers

Instead of continuously emitting light, pulsed lasers sources concentrate the available laser power in short pulses. Within that time frame, unprece-

dentedly high peak powers and pulse energies are reached, while the overall average power remains moderate. The term »*ultrashort pulse*« refers to the regime, where the laser pulse is shorter than the electron phonon coupling time in the bulk material and exceptional physical mechanisms appear. As those mechanisms depend on the involved material, no exact numbers can be given but for metals the pulse duration is typically within the range of femto seconds up to pico seconds [4]. In this regime, laser ablation is no longer based on evaporation and the processing results exhibit outstanding characteristics. Ablated edges are exceptionally clean and the heat affected zones in the surrounding area are negligibly small [106]. As an additional benefit, the ablation process is more efficient with respect to the applied energy than when working with longer pulses [4] and choosing optimal parameters enables functionalizing the surface by inducing periodic formations [107]. After giving an overview on the mechanisms of ultrashort pulse laser materials processing, this section will discuss the benefits of beam shaping when working with ultrashort pulse lasers.

### 2.2.1 Ultrashort Pulse Laser Interaction with Metals

The mechanisms of energy absorption depend on the material type and this section focuses on the interaction with metals. When light enters the bulk material, it first interacts with the electron system. In case of metals, the photon energy is higher than the band gap of the material and the free carriers of the electron gas directly absorb the emitted energy. The Drude model describes this process with absorption being characterized by Beer-Lambert's law [108].

#### Time Scales

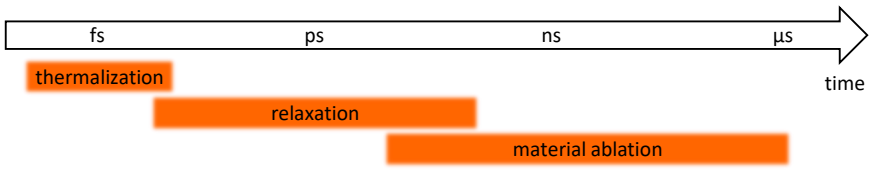


Figure 9: Typical time scales during ultrashort pulse laser material interaction with metals.

The energetic electrons produce heat via electron-electron collisions. This leads to the thermalization of the electron system within approximately 100 fs [109]. Figure 9 gives an overview of the corresponding time scales. While electron thermalization happens relatively fast, the energy transfer to the lattice requires longer time scales. Due to a significant mass mismatch

between electrons and lattice, it requires many collisions to transfer the energy. While the lattice is at its initial temperature, the thermalized electrons are a lot hotter. The temperature mismatch between these two systems leads to a non-equilibrium state. The two temperature model [110] can be used to describe this scenario and the corresponding energy transfer to the lattice [111]. The time frame to restore the thermal equilibrium is called electron phonon relaxation time. Within this context, ultrashort means that the laser pulse duration is shorter than this relaxation time.
This condition implies that the absorbed laser energy remains within the small volume that is determined by the electron diffusion length. When material is ablated, the generated heat is directly evacuated with the removed matter and does not remain in the bulk material. For this reason, this process is also called *»cold ablation«*. In contrast to the laser material interaction, the time scale for ablation lies in the range of nano seconds [112].

**Ablation Regimes**
The mechanisms of material ablation depend on the laser fluence $F$, which is defined as the pulse energy per area. To enable material ablation, the laser fluence has to reach a certain threshold value $F_{\mathrm{th}}$ which can be assumed as required energy for heating, melting, and evaporation. As the enthalpy of vaporization has the highest impact, this value can be taken to estimate the threshold fluence theoretically [113]. In practice, there are several methods for determining the ablation threshold $F_{\mathrm{th}}$, such as those by Liu [114], and Samad and Vieira [115]. Those measurements may also account for experimental-specific conditions and multi pulse effects like incubation [116] and heat accumulation [117]. Depending on the fluence with respect to its threshold fluence, different ablation regimes apply:
For fluences just above the threshold fluence, compressive stresses dominate the ablation regime [118]. Energy is rapidly deposited into a small volume without enabling volumetric changes as heating happens faster than the material could expand. This rapidly melts the material while mechanical stress is induced. This generates tensile waves and sub-surface voids [119]. Consequently, thin layers of material are ejected and with them most of the residual heat is taken away from the bulk material [120]. This regime is called *»photo-mechanical spallation«* and it is also referred to as stress confinement regime. Ablation in that regime features excellent smoothness and a minimum heat affected zone.
For fluences further above the threshold fluence, the ablation process exceeds the limits of stability within the liquid phase [121]. The high fluence values induce a metastable superheated liquid and material ablation is characterized by explosive boiling [122] and disintegration [123]. Liquid droplets and vapour are thrown up within the ejection plume. This ablation regime is called

»*phase explosion*« and processing results exhibit lower quality with more heat remaining in the material.

### 2.2.2 Beam Shaping for Ultrashort Pulse Laser Materials Processing

The applied laser fluence has a major impact on the processing results. Excessive fluences affect the resulting quality when changing from spallation to phase explosion. Moreover, ultrashort pulse laser material ablation is a nonlinear process and the amount of ablated material does not increase linearly with an increase in fluence.

**Tailoring the Energy Input**

In a basic model, the ablated depth and the relative laser fluence $F/F_{\mathrm{th}}$ are related logarithmically [106]:

$$d_{\mathrm{abl}} = \delta \cdot \log\left(\frac{F}{F_{\mathrm{th}}}\right) \tag{6}$$

Here $d_{\mathrm{abl}}$ is the ablated depth, $\delta$ is the optical penetration depth, and $F$ is the chosen laser fluence. This implicates that for fluences far above the threshold fluence only little more material is ablated. Assuming a homogeneous top hat profile, simple calculation shows that the maximum volume ablation rate (ablated volume over time per applied laser power) is achieved for $F_{\mathrm{opt}} = e \cdot F_{\mathrm{th}}$ [124] and this value is called optimum fluence. In practical implementation, many laser profiles follow a Gaussian geometry. Even with knowledge of the optimum fluence, a Gaussian distribution cannot meet these requirements as the fluence varies spatially. Depending on the position within the beam, different ablation regimes may appear as the fluence varies significantly. Wu and Zhigilei simulated various fluence regions of a laser beam by splitting it into independent areas and showed the simultaneous coexistence of phase explosion and spallation, depending on the particular fluence [125]. This behaviour was also measured in pump probe experiments [126]. While the prevalence of different ablation regimes affects the experimental results, it also strongly affects the achievable efficiency.
Neuenschwander et al. show that the optimum fluence for a Gaussian beam is $F_{\mathrm{opt}}^{\mathrm{Gauss}} = e^2/2 \cdot F_{\mathrm{th}}$ [124]. While the peak fluence on the optical axis is $e^2/2$ higher than the threshold fluence, the outer edges are still below the ablation threshold and induce heat which impairs the result. However, if all contributions are accumulated, this condition provides the best result for a Gaussian beam. An analysis in [127] and [128] shows that the maximum ablation efficiency for a Gaussian beam is only around 70 % of the possible

ablation efficiency of a top hat profile. The advantage of a top hat profile is thus twofold: it enables working at the optimum fluence to maximize the ablation efficiency while heat input from fluences below the ablation threshold is avoided as it is sketched in Figure 10.

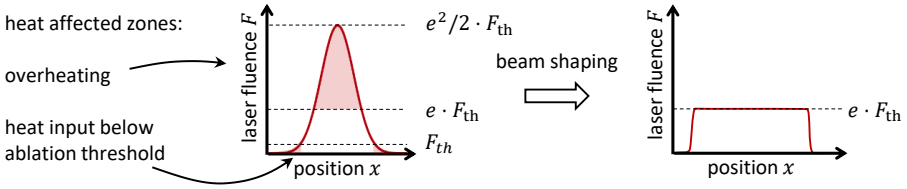


Figure 10: Phase-only beam shaping enables tailoring the intensity profile and optimizing the amount of locally deposited energy.

Commercially available laser systems provide pulse energies which are magnitudes above the optimum fluence when the beam is focused on the work piece. However, limiting the maximum pulse energy does not maximize the potential of state of state-of-the-art laser sources. Within a typical setup for ultrashort pulse micro machining, the laser beam is focused to a size of 10 µm − 50 µm and a galvanometer scanner guides the beam to the corresponding positions on the workpiece. Typically, several pulses are emitted and the target structure is composed of adjacent spots. However, excessive fluences cause heat accumulation and the scanning motion of the galvanometer mirror cannot balance those effects as the deflection speed is too slow with respect to typical pulse repetition frequencies. The scanner movement is in the range of a few hundred Hz to a maximum of kHz versus several kHz up to MHz pulse repetition frequencies [129]. To this end, beam shaping not only enables tailoring the energy input, but it may also directly shape the target geometry.
The overall advantage is thus fourfold: (1) Working at the optimum fluence provides the highest volume ablation rate with (2) excellent ablation quality and minimum heat affected zone. (3) Processing large areas at once further speeds up ablation, and (4) the target geometry is directly set by the beam shaping device with in the ideal case not even requiring additional scanning gear.

**Current Approaches in Research and Industry**
In the early 1990s, ultrashort pulse lasers were in their infancy, as shown by publications on femtosecond pulse generation by Spence et al. [130] and Squier et al. [131]. However, the first papers about beam shaping for laser materials processing were published a few years later. While Momma et

al. [132] and Kuroiwa et al. [133] utilized a DOE, Sanner et al. performed dynamic beam shaping with a combination of a deformable mirror and liquid crystals in [44] and [45].
Since then, the topic has been widely researched. Phase-only beam shaping can be applied to a broad range of ultrashort pulse laser applications. Chromatic dispersion due to an increased spectral bandwidth usually only becomes relevant when working below a few hundred femto seconds. However, typical pulse durations for laser material processing are above that value.
One major field of application is process parallelization by ablating several regions concurrently. A (typically simple) pattern, e.g. a focused spot, is duplicated several times to spread the available laser energy over a large area and to parallelize and speed up production [134–141]. There are also several reports of uniform beam shaping for material ablation [142–145]. Current publications indicate a trend towards beam shaping for laser additive manufacturing [146–151]. Additionally, commercial beam shaping systems were developed. Pulsar Photonics designed a dynamic beam shaping module which combines an SLM with a galvanometer scanner. The simultaneous option for beam shaping and scanning should ease the practical implementation for the end user and it finds application in the work of Gafner et al. [152] and Lutz et al. [153]. Nokia Bell Labs conducted research on multi-plane beam shaping for optical communication technology [154] and Cailabs offer beam shaping solutions for a broad range of applications, spanning from laser processing and additive manufacturing to telecommunications [155]. Moreover, there exist various companies that produce customer-specific DOE solutions. LCoS SLMs are constantly improved to achieve higher damage thresholds with better pixel resolution.
Even though phase-only beam shaping for ultrashort pulse laser materials processing is a highly researched topic, it is not yet fully established in industrial applications. One potential reason might be that diminishing speckle noise is still challenging and practical implementation is thus intricate. Many methods have been developed but they usually give a compromise between the achievable quality and efficiency. Both parameters are crucial and moreover, the methods must be practically realizable for industrial applications.

**Influence of the Material**

To this point, the focus has been on optimizing the beam profile with respect to the fluence [124] and target shape precision. However, the influence of the material has not yet been considered. If the beam profile is tailored for material ablation, the material's characteristics should be equally considered. This topic has not been widely researched thus far.
Speckle patterns have been shown to strongly reduce the quality of ablation

profiles and temporal averaging of speckle patterns provides homogeneous ablation results [5]. However, as methods for uniform beam shaping are based on different concepts, also their influence on material ablation needs to be investigated as well as the material's influence on the ablation process.

## 2.3 Application of Nonlinear Optics to Phase-Only Beam Shaping

Nonlinear optical phenomena appear as a material's response to an intense light field. New frequencies are generated which originate from the underlying light-matter interaction. This effect can be used to convert the laser wavelength, e.g. it can be reduced by half which is called second harmonic generation.
The wavelength is inversely proportional to the photon energy and determines the physical mechanisms of light absorption with respect to the chosen material. Although the desired energy coupling mechanisms may vary depending on the application, the laser wavelength is an important parameter that should be selected accordingly. This enables inducing certain interactions, such as two-photon polymerization [156]. In turn, direct linear absorption of the laser light may be required. However, some materials only absorb in the UV spectral range. Working at that range is particularly important when handling delicate and temperature-sensitive materials as this enables precise energy deposition without affecting the surrounding area. This includes in particular semiconductors [157], thin films [158], and corneal tissue [159] with applications in surface functionalization [160], photovoltaics [161], and ophthalmology [162]. It is thus beneficial to adapt the laser wavelength to the experimental requirements. Therefore, many ultrashort pulse laser systems are directly equipped with nonlinear conversion elements. Those devices make use of nonlinear effects to convert the laser light to another wavelength, e.g. from the near-infrared to the visible or UV spectral range.
While nonlinear optics broaden the spectral range of ultrashort pulse laser systems, liquid crystal displays are technically limited to the visible, near-infrared, and mid-infrared spectral ranges. Dynamic phase-only beam shaping is thus only possible within that range. Beam shaping in the UV spectral range is typically realized with digital micro mirror devices (amplitude modulation) [163] or phase modulation with static elements or dedicated mirrors [164]. However, this involves losses and limitations in flexibility.
There is research on new liquid crystals for the deep-UV spectral ranges [165]. However, by means of nonlinear optics, it should also be possible to use state-of-the-art liquid crystal displays for beam shaping while converting the

wavelength thereafter. The concept is based on the coherence of nonlinear light conversion. The phase information of the light field is conserved during frequency conversion. It is thus also possible to perform phase-only beam shaping before the light field is frequency-converted. This provides all the benefits of dynamic phase-only beam shaping while the spectral range is expanded. In practice, this requires taking into account the mechanisms of frequency conversion when designing phase masks and conceiving the optical setup. This section will therefore give a brief introduction to relevant topics in nonlinear optics based on [166], ending with review on nonlinear beam shaping.

**Origin of Nonlinear Optical Phenomena**

Within the Drude model, electrons are treated as a cloud of free carriers which exhibit no binding force to the atomic core. This model covers conductors as they exhibit a low-energy band gap which allows the free electrons to directly absorb the incoming field. However, this is not generally the case. For dielectrics the Lorentz extension of the Drude model treats the electrons as bound elements to the massive atomic core. An incoming field acts as a force which displaces the electrons but due to their binding, the restoring force works against the incoming field. The electron cloud gets deformed and the combination of excitation and restoration induces an oscillation which can be described by an anharmonic oscillator for a nonlinear medium. From the perspective of a single electron, its oscillation induces a dipole and the accumulation of all individual dipole moments forms the so-called polarization density $P$, which can be considered as the material's response to an incoming field. Even though the direction of oscillation of the electric field is also referred as polarization vector, it denotes a different effect and should not be mixed up.

As the polarization density depends on the field strength, it makes sense to treat it as power series in terms of the excitation field [167]. For simplicity, the polarization density $P$ and the electric field $E$ are treated as scalar quantities in a lossless and dispersionless medium:

$$P = \epsilon_0[\chi^{(1)}E + \chi^{(2)}E^2 + \chi^{(3)}E^3 + ...] = \underbrace{P^{(1)}}_{\text{linear}} + \underbrace{P^{(2)} + P^{(3)} + ...}_{\text{nonlinear: } P^{\text{NL}}} \qquad (7)$$

Here, $\epsilon_0$ is the vacuum permittivity. The susceptibility $\chi$ connects both fields and is thus responsible for material-specific effects: $\chi^{(1)}$ is the linear susceptibility and can be related with refraction and birefringence. Higher order nonlinear susceptibilities appear along the power series and they are responsible for nonlinear optical effects, as e.g. second harmonic generation. However, as higher order susceptibility contributions are orders of magnitude

smaller, nonlinearity only becomes significant for high electric field strengths. This is the case when working with ultrashort pulse lasers.
The connection between the electron displacement and the restoring force determines the mathematical character of the relation between the exciting, incoming field and the material's response. This relation can only be treated linearly for small electron displacements which can be assumed as harmonic oscillation, resulting in the linear polarization density. Intense fields promote the actual nonlinear behaviour which is covered by the nonlinear polarization density. While the polarization density can be comprised into a linear and nonlinear contribution, it will be seen that its nonlinear part acts as source term for new frequencies.

**Nonlinear Wave Equation**
When considering the Maxwell equations in presence of a medium, the nonlinear wave equation can be derived [166]:

$$\nabla^2 E - \frac{\epsilon^{(1)}}{c^2}\frac{\partial^2}{\partial t^2}E = \frac{1}{\epsilon_0 c^2}\frac{\partial^2}{\partial t^2}P^{\mathrm{NL}} \tag{8}$$

Here, $\epsilon_0$ is the vacuum permittivity, and $\epsilon^{(1)}$ is the linear, material-specific dielectric permittivity. This equation resembles the linear wave equation but in addition to the periodicity in space and time, it includes the nonlinear polarization density as the material's response. This field acts as driving force. Based on this differential equation, the nonlinear polarization density can be considered as a source term whose time-varying field generates new frequencies.

**Second Harmonic Generation**
The relationship within the power series in Equation 7 suggests that besides the initial excitation frequency also higher order frequencies are generated when an intense light field interacts with a medium. This is shown for a sinusoidal wave at angular frequency $\omega$ whose electric field can be written as:

$$E = Ee^{-i\omega t} + \text{c.c.} \tag{9}$$

For simplicity, a plane wave front is assumed and Equation 9 does thus not contain a phase term $e^{i\Phi}$ as it vanishes (compare Equation 2). The second order nonlinearity of $P^{(2)}$ is given by inserting the electric field of Equation 9 into Equation 7:

$$P^{(2)} = \epsilon_0\chi^{(2)}E^2 = 2\epsilon_0\chi^{(2)}EE^* + \underbrace{\epsilon_0\chi^{(2)}(E^2e^{-i2\omega t} + \text{c.c.})}_{\text{second harmonic generation at } 2\omega} \tag{10}$$

Here, $E^*$ denotes the complex conjugate of the field amplitude $E$. Besides a contribution at zero frequency, $P^{(2)}$ also exhibits a term which is two times the initial frequency $\omega$. According to Equation 8, this time-varying field leads to the generation of light at twice the initial frequency. This effect is called second harmonic generation and Figure 11 shows the decomposition of the polarization density into the corresponding frequency components.

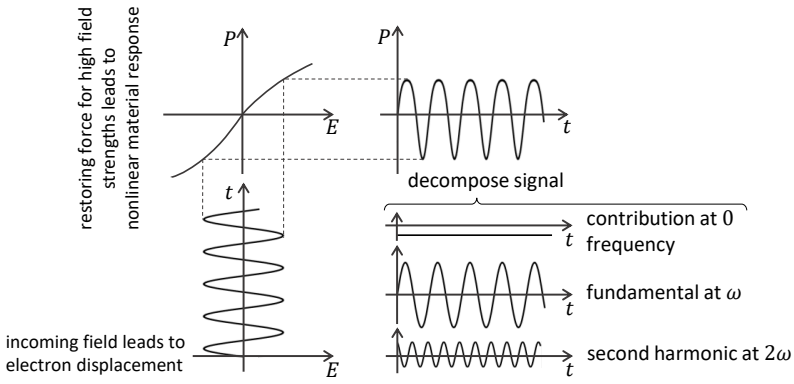


Figure 11: Decomposition of the polarization density for second harmonic generation: An intense field causes non-harmonic oscillations of the electrons in the bulk material which leads to the generation of new frequencies.

The nonlinear wave equation describes the interaction and propagation of the involved fields. However, as it represents a coupled system of mutually dependent fields, a solution for second harmonic generation is deduced by applying some approximations. A detailed derivation can be found in [166]. The incoming field interacts with the nonlinear medium and induces the second order nonlinear polarization density as it is shown in Equation 10. The nonlinear polarization density at frequency $2\omega$ acts as source term on the right side of Equation 8. After solving Equation 8 with the assumption of low depletion, i.e. the fundamental field remains constant at low conversion, the intensity of the second harmonic $I^{(2\omega)}$ can be related with the initial intensity at the fundamental $I^{(\omega)}$:

$$I^{(2\omega)} = \frac{2\omega^2 d_{\text{eff}}^2}{n^{(2\omega)}(n^{(\omega)})^2 c^3 \epsilon_0} L^2 \left(I^{(\omega)}\right)^2 \operatorname{sinc}^2\left(\frac{\Delta k L}{2}\right) \tag{11}$$

Here, $d_{\text{eff}}$ is the effective nonlinear coefficient of the medium, $L$ is the crystal length, and $n^{(\omega)/(2\omega)}$ is the corresponding refractive index at the fundamental frequency $\omega$ and second harmonic frequency $2\omega$. The mathematical function sinc is defined as $\operatorname{sinc}(u) = \sin(u)/u$ for $u \neq 0$ and becomes unity for $u = 0$. $\Delta k = k_1^{(\omega)} + k_2^{(\omega)} - k^{(2\omega)}$ accounts for the wave vector mismatch between

the two fields at the fundamental $k_1^{(\omega)}$ and $k_2^{(\omega)}$ and the second harmonic $k^{(2\omega)}$. As the sinc function declines for arguments that are further from 0, an increasing wave vector mismatch reduces the maximum possible conversion.

**Phase Matching**

Equation 11 represents an analytical solution of the second harmonic signal in a regime of low conversion. The field intensities at the fundamental and second harmonic exhibit a quadratic relation and also the crystal length $L$ increases the signal strength. The elements within the fraction can be considered as constants if the experimental parameters are fixed. The phase mismatch $\Delta k$ weights the whole output of the second harmonic signal as argument of the sinc function and it thus may extinguish almost the whole result. The wave vector mismatch indicates that different frequencies propagate with different phase velocities. In a normal dispersive medium, this causes the fundamental and second harmonic to diverge. Along the path of propagation, the second harmonic signal is continuously generated by the fundamental but the individual frequency-converted fields interfere destructively as long as there is no common phase relationship. Reducing the phase mismatch $\Delta k$ to zero defines the phase matching condition [168]:

$$\Delta k = k_1^{(\omega)} + k_2^{(\omega)} - k^{(2\omega)} \stackrel{!}{=} 0, \tag{12}$$

with $k_1^{(\omega)}$ and $k_2^{(\omega)}$ accounting for the two fields at the fundamental and $k^{(2\omega)}$ is the wave vector of the field at the second harmonic. This interaction of three fields is called three wave mixing. Equation 7 and Equation 10 show that there is a quadratic relationship between the fundamental and second harmonic. Thus, two fields at the fundamental need to combine to generate the signal at the second harmonic.

Based on the definition of the wave vector $k(\omega) = \omega n(\omega)/c$ and the condition that the frequency at the second harmonic is twice the initial frequency, Equation 12 requires the refractive index to fulfill

$$0.5 \cdot (n_1^{(\omega)} + n_2^{(\omega)}) = n^{(2\omega)} \tag{13}$$

for perfect phase matching [169]. The refractive index determines the speed of propagation within a medium and Equation 13 can be interpreted as constraint for the involved fields to maintain their common phase relationship by propagating at the same speed. For a normal dispersive medium ($n^{(\omega)} < n^{(2\omega)}$), this condition is not fulfilled [11]. However, birefringent crystals can be used to achieve phase matching [170]. The material exhibits a polarization-dependent refractive index and an incoming light field perceives a different refractive index depending on its polarization direction. The

concept resembles the working principle of liquid crystal displays. This time, the crystal direction is not dynamically changed, but a solid crystal is physically rotated and polished according to the phase matching angle at which fundamental and frequency-converted light propagate at the same speed.
Fulfilling the phase matching criterion in a birefringent medium requires the involved fields to exhibit different polarization states. For second harmonic generation, two options are possible: either the polarization of the fields at the fundamental and second harmonic are orthogonal to each other or the two incident fields at the fundamental exhibit orthogonal polarization states. To find possible phase matching angles, the direction-dependent refractive index of the nonlinear crystal can be modelled [171]. The effectively perceived refractive index depends on the polarization vector and propagation direction of the incoming light field. Therefore, a biaxial crystal can be modelled by three major refractive indices along its major axes in $x-$, $y-$, and $z-$direction. Light, that propagates along one of these axes, e.g. in $x-$direction, oscillates in the $y-z-$plane as the polarization vector of the electric field is orthogonal to the direction of propagation. The incoming light field perceives the refractive index which is given by the direction of its polarization vector. If the field e.g. oscillates along $z-$direction, it perceives the refractive index $n_z$. The refractive index for any arbitrary polarization direction within the $y-z-$plane can be calculated by the projection of the refractive indices $n_y$ and $n_z$ which span an ellipse. In three dimensions the crystal can be characterized by a refractive index ellipsoid. A segment of this refractive index ellipsoid is shown in Figure 12. The individual colours denote the refractive index at the corresponding wavelength. $\theta_m$ and $\phi_m$ indicate the phase matching angles.

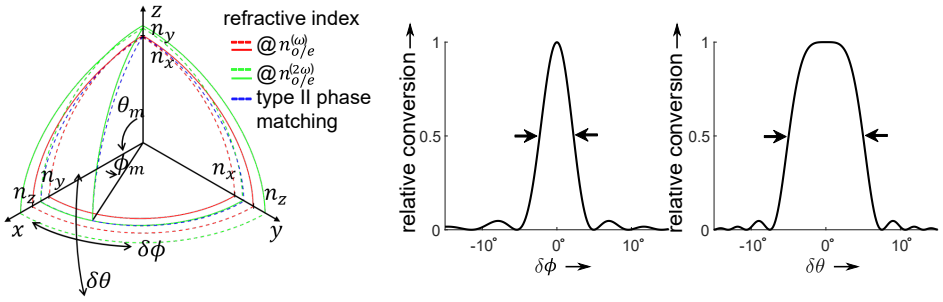


Figure 12: Refractive index ellipsoid and angular acceptance for the biaxial KTP crystal of length $L = 2$ mm. The refractive index mismatch for a deflection along $\delta\theta$ and $\delta\phi$ from the phase matching angles $\theta_m$ and $\phi_m$ results in a reduced relative conversion.

Instead of denoting the two mixing fields at the fundamental with numeric indices, they are typically called ordinary (o) or extraordinary (e) beam [172]. This convention comes from a perspective of symmetry within the birefringent crystal [170]. To explain this notation, it makes sense to assume an incoming field, e.g. a field that propagates along the phase matching angles and whose propagation vector thus lies in the $x-y-$plane. If the field is polarized along $z-$direction, it perceives the refractive index $n_z$ and if the field is orthogonally polarized in the $x-y-$plane, it perceives the projection of the refractive indices $n_x$ and $n_y$. Now assume that the propagation direction of the field vector changes slightly within the $x-y-$plane, i.e. a slight angular deviation $\delta\phi$ from the initial phase matching angle $\phi_m$. If the electric field vector is polarized within the $z-$direction, the perceived refractive index does not change as the polarization vector still points in $z-$ direction. Thus, this polarization state is called ordinary beam and it is marked as dashed line in Figure 12. However, if the polarization vector lies within the $x-y-$plane, the perceived refractive index changes accordingly. This beam is called extraordinary beam and it is marked as solid line in Figure 12. Consequently, $n_o$ and $n_e$ denote the refractive index of the ordinary and extraordinary beam which refers to the corresponding orthogonal polarization states. The same convention accounts for the generated field at the second harmonic.
In case the two incoming fields at the fundamental are orthogonally polarized, the phase matching condition is called type II phase matching [166]. The average value of the two refractive indices at the fundamental is equal to the refractive index at the second harmonic. The phase matching condition for type II phase matching thus reads:

$$0.5 \cdot (n_{o/e}^{(\omega)} + n_{e/o}^{(\omega)}) = n_{e/o}^{(\omega)} \tag{14}$$

Type II phase matching is of specific relevance within this thesis as the crossed polarization states make the two interacting fields for second harmonic generation distinguishable. In general, second harmonic generation is a degenerate process, i.e. the two mixing fields at the same frequency are not distinguishable. This changes if the input fields exhibit different polarization states. Within the three wave mixing process, two fields combine and the desired wave front can be conserved under specific conditions [173].

**Angular Acceptance**
Slight deviations from the optimum phase matching angle cause $\Delta k$ to be non-zero and the relative conversion efficiency decreases. While some crystals exhibit a high sensitivity on the exact angular position, others are more tolerant. This depends on how fast the corresponding refractive indices of the involved fields change in the area around the phase matching

angle. According to Equation 13, the refractive index mismatch determines the phase mismatch and spatially modelling the refractive index based on its Sellmeier coefficients allows for calculating the angular-dependent conversion efficiency [174]. The local phase mismatch can be calculated from the corresponding values within the index ellipsoid [175]. This mismatch results in a relative reduction of the maximum conversion when inserting it into Equation 11. The so-called *»angular acceptance«* or tolerance is the angular deviation from the optimum phase matching angle until the relative conversion decreases to half of its maximum value [169]. Figure 12 shows the angular acceptance for a KTP crystal. As KTP is a biaxial crystal, it exhibits three different refractive indices along the spatial axes and it is thus necessary to characterize the crystal for a deviation along the two phase matching angles $\delta\theta$ and $\delta\phi$, as shown in Figure 12.
Wave front shaping generates a spectrum of vectors which are centred around the optical axis. Effectively, the phase information is encoded in the orientation of the wave vectors. However, this impairs phase matching. To achieve high and homogeneous conversion efficiencies, the generated spectrum has to be within the range of angular acceptance. Otherwise, some wave vectors are not supported during nonlinear conversion. Modelling the refractive index ellipsoid and calculating the resulting phase mismatch thus helps to find an estimate for maximum acceptable deflection angles during beam shaping.

**Nonlinear Beam Shaping**
Nonlinear computer-generated holography is gaining increasing attention in the recent years [176]. Shaping and frequency-converting light provides a broad spectrum of opportunities with applications ranging from quantum computing to materials processing. Over the last decades there has been a lot of research on the nonlinear conversion of beams carrying spin or orbital angular momentum [177–186]. Likewise, nonlinear photonic crystals are a highly researched topic [187–192]. Those elements control the nonlinear beam generation and propagation by manipulating the nonlinear susceptibility within a crystal [193]. In theory, those three-dimensional elements provide more degrees of freedom than a thin hologram. However, the elements are static and their practical implementation is challenging.
In contrast, dynamic beam shaping with an SLM enables higher flexibility and fidelity. Phase-only beam shaping can be combined with nonlinear optics as the phase information is conserved during frequency conversion. Nonetheless, this research field is still in its infancy. Current publications in that field are rare and suffer from poor efficiency and low quality [194–197]. One potential reason might be that many nonlinear conversion processes are degenerate, i.e. mixing fields at the same frequency. By employing

polarization as a control mechanism [198], it should be possible to perform nonlinear beam shaping with the same spatial distribution as for linear beam shaping [S2]. Based on this understanding, the combination of nonlinear optics and phase-only beam shaping may be a potential starting point to overcome the current spectral limitations of liquid crystal displays.

# 3 Aim of the Thesis

The aim of this thesis is to realize precise and efficient ultrashort pulse laser materials processing by means of phase-only beam shaping. Figure 13 gives an overview of the research topics within the scope of this thesis and their internal connection. Methods and technical solutions for uniform beam shaping with high-energy lasers need to be developed and investigated. These methods should provide high precision and accuracy without introducing significant losses. Having developed appropriate methods, their effect on material ablation needs to be analyzed. In turn, the well-characterized methods can be used to deduce the influence of the processed material. Liquid crystal displays are limited to the visible, near-infrared, and mid-infrared spectral ranges but some typical applications require working at the UV spectral range. This thesis concludes with a method for nonlinear beam shaping which may be used to expand the spectral range of liquid crystal displays.

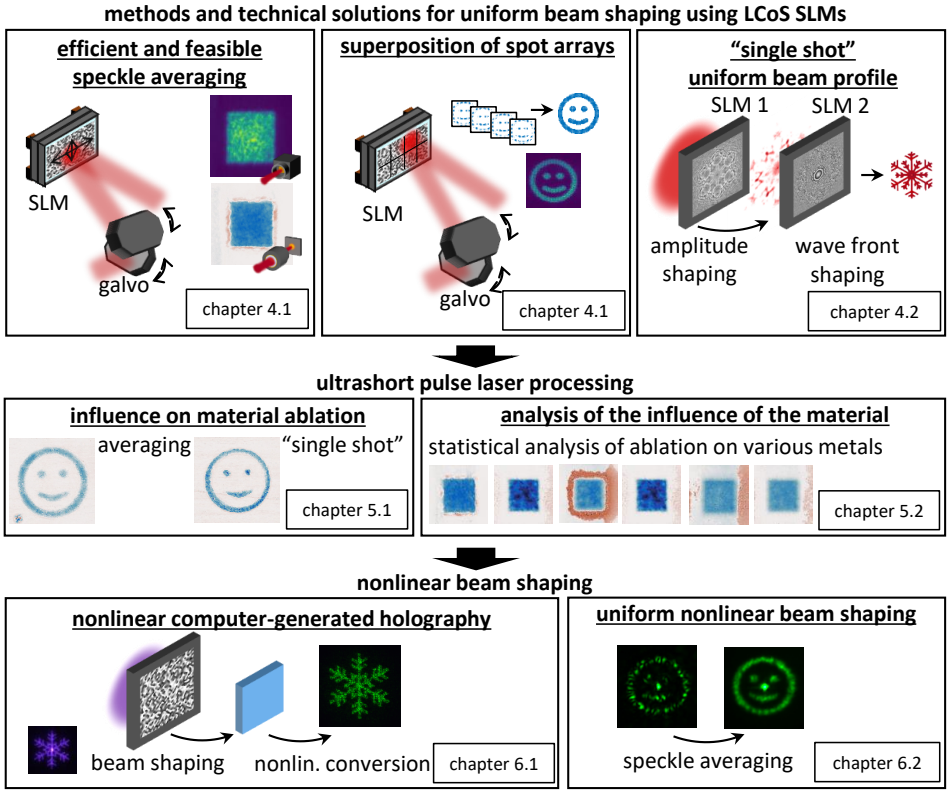


Figure 13: Structure and internal connection of research topics within this thesis.

**Methods for Uniform Beam Shaping**
As a first step, methods for uniform beam shaping are required which provide excellent uniformity and precision. In particular, speckle needs to be minimized. Furthermore, the methods should be capable of shaping structures with arbitrary geometry. While those requirements can be met, this typically goes along with low efficiency or poor resolution. Phase-only beam shaping cannot control the full light field and this intrinsically limits the achievable results. For this reason, further control is required which may be realized by including either an additional temporal or spatial level of intervention. Two methods will be introduced which are based on temporal averaging. A galvanometer scanner within the optical setup decouples the change of the speckle pattern from the slow frame rate of the liquid crystal display. Likewise, it enables high-speed changes between individual phase masks.
Moreover, the use of two beam shaping planes provides full control of wave front and amplitude. Therefore a solution is developed which avoids excessive fluences. This directly generates uniform beam profiles of excellent quality. All three methods are easy to implement, exhibit high-quality outcomes, and induce almost no losses.

**Ultrashort Pulse Laser Processing**
Having developed adequate methods for beam shaping, the shaped intensity profiles need to be evaluated by ultrashort pulse material ablation. While all methods result in similar intensity profiles, their methodology differs significantly and this influences the ablated profile. Results which were either achieved by averaging or direct uniform beam shaping are thus compared. Furthermore, a statistical analysis of ablation results for different metals enables conclusions of the material's influence - a factor that is of the same importance as tailoring the optimum intensity profile. If the beam profile is optimized for material ablation, it should also be known how the material responds to the shaped beam profile. This not only helps to assess the developed beam shaping methods but also to refine process parameters.

**Nonlinear Beam Shaping**
Returning to the big picture of beam shaping for laser materials processing, there are still many open challenges. One of them is the limited spectral range of liquid crystal displays as they absorb UV light. However, some applications require laser processing in the UV spectral range [160]. To this end, it is possible to extend this spectral range by means of nonlinear optics. This concept will be demonstrated by performing beam shaping at the second harmonic (532 nm) while modulating light at the fundamental (1064 nm). The method is further combined with efficient speckle averaging.

It is thus possible to directly diminish speckle noise during beam shaping at the second harmonic. While experimental demonstrations within the scope of this thesis cover the conversion of infrared light into the visible spectrum, the results and the corresponding analysis pave the way towards beam shaping in the UV spectral range.

# 4 Methods and Technical Solutions for Uniform Beam Shaping

The following chapter presents three methods for uniform beam shaping. All have in common, that they make no compromise between the achievable quality and efficiency. Furthermore, they are flexible and adaptable to changing requirements. This covers full freedom in the design of the target geometry and size (depending on the used optics). While the first section covers two methods which are based on temporal averaging, the subsequent section presents a solution for direct uniform beam shaping without averaging, i.e. the method provides instantly a constant and uniform intensity distribution, e.g. for single pulse applications.

## 4.1 Temporal Averaging

Temporal averaging is a convenient approach. Neither a specific algorithm, nor an elaborate setup are required. In particular, this approach features high simplicity and excellent reliability with respect to the experimental results. However, the speed of averaging is limited by the frame rate of the LCoS SLM and these typically lie within a range of 30 Hz – 60 Hz. This is several orders of magnitude below typical pulse repetition frequencies which are around several kHz up to MHz. Under those conditions, averaging can only be realized by committing high laser dead times which drastically reduces the process speed. Consequently, the elegant concept of temporal speckle averaging requires a solution to speed up the exchange of phase masks.

### 4.1.1 High-Speed Speckle Averaging for Phase-Only Beam Shaping in Laser Materials Processing

[P1] Published at *Optics and Lasers in Engineering*, 10.1016/j.optlaseng.2023.107537.

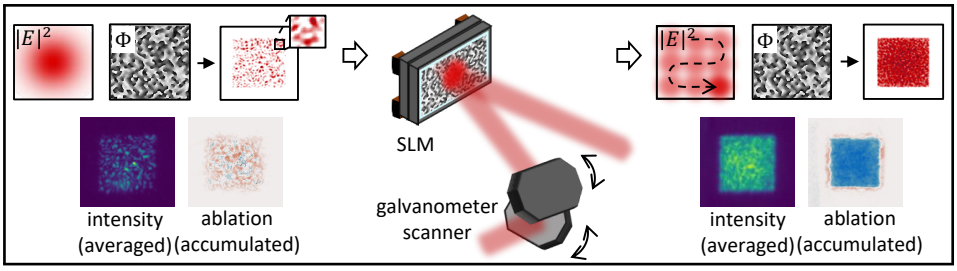


Graphical abstract: High-Speed Speckle Averaging for Phase-Only Beam Shaping

In a typical beam shaping scenario, the phase mask is calculated using the Gerchberg-Saxton algorithm [53] and there is a Fourier relation between the plane of the SLM and the shaped target image. This mask can be considered as a superposition of various gratings which form the target image. Those gratings are not sensitive to the exact shape and position of the beam on the SLM; the deflection angle remains the same. However, the superposition of the phase gratings causes singularities in form of phase vortices leading to destructive interference. While the generated intensity distribution is not sensitive to the exact position and size of the beam on the phase mask, the phase vortices have a position-dependent mapping. A cyclic shift within the phase mask thus changes the speckle pattern, while the target image remains the same. If the phase mask is shifted, the vortices and with them the corresponding singularities move within the image plane. If every possible shift is carried out, i.e. every cyclic shift is realized, speckle average out completely. This analysis motivates that a single phase mask carries the full information to shape a uniform beam profile [93].
While this fact enables working with a single phase mask, this does not solve the issue of the SLM's low frame rate. Every cyclic shift corresponds to a newly applied image on the SLM. However, the concept is invariant whether the phase mask is moved or the beam is shifted at a static phase mask. Instead of a beam that illuminates the whole SLM, a smaller beam can be used which evaluates only a partition of the phase mask while a galvanometer scanner sends the beam to different positions. By this method, the low frame rate of the SLM is overcome. A dedicated optical setup can be used to directly compensate for the introduced beam movement. The basic idea is to image the beam back on the galvanometer scanner to directly compensate for the initially introduced deflection angle by the second incidence. Similar setups for a one-dimensional displacement were previously reported by Radwell et al. [199], Bawart et al. [200], and Braverman et al. [201].
To realize perfect speckle averaging, a constant scanning movement of the laser beam is required to illuminate each area on the phase mask equally. However, in a practical implementation setup-specific aberrations and pixel cross-talk prevent speckle from being averaged out completely. Effectively, a random scanning path provides equal averaging results. It is thus sufficient to operate the galvanometer scanner with a sinusoidal movement. This provides near-perfect speckle averaging without causing laser dead times.

**Highlights**
- Near-perfect speckle averaging with a single phase mask
- Galvanometer scanner decouples averaging from the SLM's low frame rate
- Feasibility for an industrial implementation
- Analysis of ultrashort pulse laser material interaction

Optics and Lasers in Engineering 165 (2023) 107537

Contents lists available at ScienceDirect

Optics and Lasers in Engineering

journal homepage: www.elsevier.com/locate/optlaseng

# High-speed speckle averaging for phase-only beam shaping in laser materials processing

Lisa Ackermann [a,b,*], Clemens Roider [a], Matthias Gehring [a,b], Kristian Cvecek [a,b], Michael Schmidt [a,b]

[a] Institute of Photonic Technologies, Friedrich-Alexander-Universität Erlangen-Nürnberg, Konrad-Zuse-Straße 3/5, Erlangen, 91052, Bavaria, Garmany
[b] School of Advanced Optical Technologies, Friedrich-Alexander-Universität Erlangen-Nürnberg, Paul-Gordan-Straße 6, Erlangen, 91052, Bavaria, Germany

ARTICLE INFO

*Keywords:*
LCoS SLM
Phase-only beam shaping
Speckle averaging
Ultrashort pulsed laser materials processing

ABSTRACT

A phase-only spatial light modulator (SLM) is a powerful tool to shape arbitrary intensity distributions and finds application in various research fields and industry. However, since phase-only beam shaping cannot control the full complex light field, a speckle pattern overlays the shaped target intensity and strongly impairs the result. Several methods have been developed to diminish speckle noise, all of which have their advantages and disadvantages. Usually they offer a compromise between quality and efficiency. We present a method for phase-only beam shaping which achieves near-perfect and highly efficient speckle averaging with a liquid crystal on silicon SLM based on a single phase mask. A galvanometer scanner scans the laser beam over the active area of the SLM to achieve high-speed averaging. The applied angle resulting from the scanning movement is compensated by a proper optical setup to maintain a static target image with speckle averaging out. As an additional benefit of the scanning movement, artifacts from light not diffracted by the SLM disappear in the target plane. The setup is designed for high-energy laser beams as intermediate foci are avoided at all optical components. Besides optical averaging on camera images, we validate our method with ablation experiments where we make a profound analysis of the involved system parameters and the achieved quality. Thereby, it becomes apparent that the proposed method not only stands out by the high-quality results but also by its simplicity in implementation.

## 1. Introduction

Ultrashort-pulsed laser sources provide pulse energies up to several mJ and have many applications in laser materials processing [1–3]. However, the full potential of the high pulse energies often remains unused. They result in fluences far above the material's ablation threshold where heat accumulation impairs the process. Apart from reducing the quality, too high fluence values also decrease the processing efficiency [4]. To maintain high processing quality and prevent heat accumulation, the fluence needs to be reduced. Increasing the repetition frequency of the laser system effectively decreases the pulse energy while the average power remains the same. This does however not solve the problem since the deflection speed of current scanning systems is too slow to compete with the repetition frequencies of the laser system.

To make full use of the provided energy, beam shaping enables tailoring the amount of the deposited energy, inter alia, by distributing it over a large area, and furthermore adapting the ablation profile to the target geometry. A widely used tool in laser materials processing is the Liquid Crystal on Silicon (LCoS) Spatial Light Modulator (SLM) [5–8]. It works by shaping the wave front of an incoming light field which makes it possible to achieve a certain intensity distribution in the target plane. The required phase mask to shape the desired amplitude distribution is typically calculated with an iterative error reduction algorithm [9] like the Gerchberg-Saxton algorithm [10]. A major advantage of this method is the high efficiency since wave front shaping does not introduce significant losses. However, the complex light field is defined by its amplitude and the wave front. Shaping only the wave front gives not enough degrees of freedom to control the full complex light field. Without introducing significant losses, a single SLM can only be used to either tailor the wave front or to design it in such a way that it results in a specific intensity pattern. It is thus possible to exploit wave front shaping to achieve a certain amplitude distribution with the limitation that the wave front in the target plane remains uncontrolled and this leads to phase vortices. These vortices lead to destructive interference which manifests itself as a speckle pattern [11]. This is shown in Fig. 1 (a).

To overcome this problem without energy losses, two consecutive phase-only SLMs can be used to shape both wave front and amplitude

* Corresponding author.
*E-mail address:* lisa.ackermann@lpt.uni-erlangen.de (L. Ackermann).
*URL:* http://lpt.tf.fau.de (L. Ackermann)

https://doi.org/10.1016/j.optlaseng.2023.107537
Received 25 July 2022; Received in revised form 19 January 2023; Accepted 17 February 2023

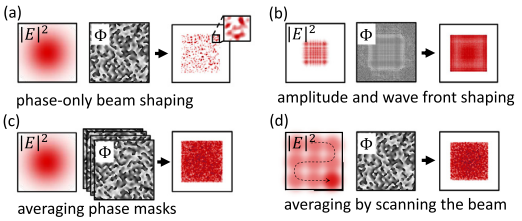


**Fig. 1.** Methods of phase-only beam shaping: (a) phase-only beam shaping induces speckle, (b) amplitude and wave front shaping, (c) averaging of phase masks, (d) averaging by scanning the beam over a single phase mask.

[12–16], compare Fig. 1 (b). While this method physically solves the problem of speckle, it involves higher alignment effort.

Another approach to reducing speckle is to average over different phase masks [17–19]. The calculation of the required phase mask based on an error reduction algorithm like the Gerchberg-Saxton algorithm tries to find a solution that comes as close as possible to the target distribution. The physical solution however requires wave front and amplitude shaping. Thus, this attempt can only approach the target profile to some extent and consequently the solution is not unique but depends on the starting conditions. Different phase masks can be generated which result in the same target structure with different overlaid speckle patterns, compare Fig. 1 (c). Smooth ablation profiles have been achieved with such averaging attempts where a pulsed laser source was shaped with an SLM [20]. Ideally, a new phase mask needs to be applied after a few laser pulses. However, this is practically impossible since the frame rate of the SLM (tens of Hz) is far from typical laser repetition frequencies (several kHz up to MHz). It is either possible to transfer the same phase information to many pulses, which effectively prevents averaging, or to reduce the laser repetition frequency, which, for such a strong reduction, means that pulses have to be suppressed and only a fraction of the available laser power can be used.

Instead of averaging phase masks, it is thus advisable to consider the role of the amplitude of the incoming beam on the SLM. Typical phase masks generated by the Gerchberg-Saxton algorithm act as phase gratings that generate the same target intensity distribution, independently of the irradiation properties, i.e. irradiated area or location of the incoming laser beam. However, while a shift of the illuminated area does not affect the formation of the target image, the vortices within this phase mask have a location-dependent mapping. A small shift can be approximated with a shift of the speckle pattern within the target image. While the speckle pattern gradually smears when the beam is shifted over the mask, new speckle arise with the additionally evaluated areas while others disappear. This means that every additional shift contributes in averaging speckle even if the speckle pattern is only slightly changing.

Golan and Shoham propose that cyclic shifting of a single phase mask provides perfect speckle averaging [21]. They shift the phase mask on the SLM by applying a new image on the SLM for each single shift and average speckle out with a single phase mask. This effect is intuitive when observing two interfering beams. While one beam may carry a complex phase information (e.g. it may carry orbital angular momentum which causes a vortex due to the singularity of a helical wave front), the other can act as reference with a plane wave front. The phase singularity maps as a fork within the interference fringes. If now the center of the helical wave front is shifted within the beam, the fringes and the singularity are shifted within the interference pattern. For all possible shifts which can be achieved by cyclic shifting, the singularity and the interference pattern average out completely. While this concept promises excellent results, it is limited by the low frame rate of the SLM similar to averaging of individual phase masks.

We present a method for fast and efficient speckle averaging by scanning the beam over an SLM instead of shifting the phase mask (Fig. 1 (d)). The scanning movement of the beam can be implemented with a galvanometer scanner, which enables scanning frequencies in the kHz-range. The resulting spatial shift of the beam needs to be compensated by an optical setup to only get a moving speckle pattern while maintaining a fixed target structure. This configuration is decoupled from the slow frame rate of the SLM and enables fast speckle averaging. As an additional benefit, the setup can be designed to defocus the $0^{th}$ order of non-diffracted light and keep it moving with the initial scanning motion contrary to the still target structure. Using this, we achieve smooth intensity profiles and ablation results with effectively no artifacts from the initially speckled beam shape.

This technical solution makes the concept of speckle averaging feasible due to the high efficiency and quality of the results. Likewise, we see the option of analyzing ultrashort pulsed laser material interaction on a timescale where spatial intensity distribution can be adapted from pulse to pulse. This involves the influence of the laser fluence and the scanning frequency on the ablation rate and quality.

The paper is structured in the following way: In Section 2, we introduce our method with a description of the experimental setup and thoughts on the design of the involved components. Averaged intensity profiles on a camera and the according ablation experiments follow thereafter in Section 3. The ablation results are characterized by their uniformity and the achieved ablation rate as a function of the threshold fluence $F_{th}$. Furthermore, we address the influence of the scanning frequency and show that there is usually no necessity to synchronize the laser emission with the scanning movement. Apart from that, we analyze the ablation quality as a function of the number of laser pulses. Section 4 follows with an investigation of the optimum phase mask and beam size. Moreover, we discuss the influence of the galvanometer's trajectory until Section 5 concludes our work.

## 2. Materials and methods

### 2.1. Experimental setup

Fig. 2 (a) shows our optical setup. A galvanometer scanner (6210H Cambridge Technology) scans the beam over the SLM (Holoeye LETO 1/2, $1920 \times 1080$ px) to evaluate different parts of the phase mask. To compensate for the introduced angle, the beam is sent back to its initial position on the galvanometer scanner. This is done via 4f imaging and a proper mirror configuration. A similar folded setup was proposed by Bawart et al. [22] to perform high-speed focusing with a modified Alvarez lens. By mapping on exactly the same position, the galvanometer scanner directly compensates for the previously applied angle of the laser beam and the beam exiting the galvanometer is not moving.

The setup in [22] scans the SLM along one line and thereby performs a 1D scan by rotating a single galvanometer mirror. This provides one pivot point and the rotational motion can be exactly compensated. However, a 1D scan with low scanning speed (i.e. a single line scan) requires synchronization between the start of the laser emission and the according scanning motion. At high scanning frequencies or for a 2D scan, this is not required. We aim for the option of a 2D scan to add more diversity in the phase information which provides rapid averaging.

A 2D scan is realized with two mirrors within the galvanometer scanner, now not providing a single pivot point anymore. The remaining residual movement is almost negligible since the two pivot points of the 2-mirror-system are close to each other with respect to the dimensions of the optical setup. For requirements with perfect angle compensation, two individual 1D scanning setups can be build (one in each direction) with 4f imaging in-between.

While the setup in [22] is designed to position the galvanometer scanner in the Fourier plane of the SLM, i.e. the laser has to be focused onto the galvanometer scanner, we conceive the setup for high-energy lasers and image the phase mask onto the galvanometer scanner. The

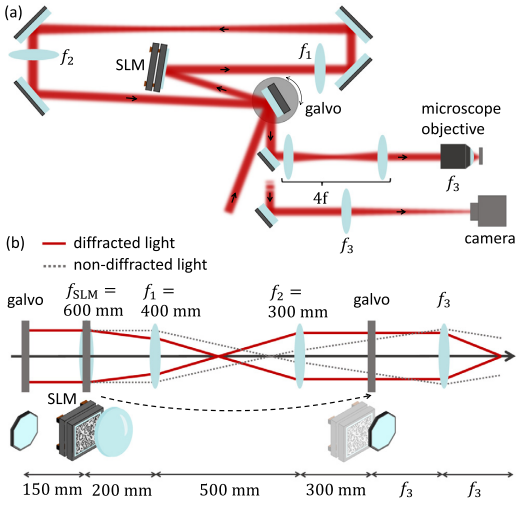


**Fig. 2.** (a) Experimental setup: The galvanometer scanner, abbreviated as galvo in the figure, scans the beam over the SLM. A set of four mirrors guides the beam back to the galvanometer scanner where it is imaged on itself with a 4f lens configuration. The target image is in the Fourier plane of the galvanometer scanner. It can either be imaged directly with a lens or with additional 4f imaging in case that more space is required in-between. (b) Experimental setup drawn in transmission with the according distances. Non-diffracted light remains defocussed on the optical elements and in the target plane. The focal length $f_3$ is not further specified since it can be chosen individually, depending on the application. For imaging on the camera, we worked with a focal length of $f_3 = 300$ mm. Ablation experiments were performed with a microscope objective ($f_3 = 18$ mm and $M = 1.7$ for the telescope with a $f = 300$ mm and $f = 500$ mm lens). Dimensions are not to scale.

SLM is placed within the 4f setup: In the simplest configuration only the SLM and one lens would be necessary as the SLM can replace the first lens of the 4f setup by adding a corresponding lens term to the phase mask, similar to a Fresnel hologram. The physical (second) lens of the 4f setup would image the corresponding phase hologram onto the galvanometer scanner. However, in this configuration non-diffracted, still collimated light light would be directly focused onto the galvanometer scanner since it would only interact with this single lens in the setup.

It thus makes sense to split the first required lens of the telescope into a lens term on the SLM and an additional physical lens which can be combined to one effective lens as Fig. 2 (b) shows. This defocuses non-diffracted light on the galvanometer scanner and in the target plane. Such a step is necessary for high-energy beams to avoid damage on the components. Another purpose of this design is to disrupt the 4f-setup-inherent angle preservation specifically for non-diffracted light which keeps moving in the target plane and gets thus averaged over time as it is illustrated in Fig. 3. Furthermore, this gives more freedom to choose the focal length of the lens term on the SLM, i.e. increasing it to avoid undersampling at the rapid phase jumps of the concentric rings of the lens term. Based on this, it is possible to keep relatively small distances between the physical lenses to have a compact setup while the lens term on the SLM keeps a high focal length.

Only a lens positioned in the focal distance after the galvanometer scanner is required to form the target distribution which remains static while the speckle pattern shifts with the motion of the galvanometer scanner. Depending on the application, if for example a microscope objective with a short focal length should be used, it is practical to add an additional 4f setup to image the Fourier plane to the back focal plane of the lens (compare the two options in Fig. 2 (a)). We use this option for

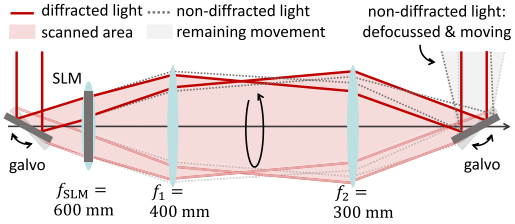


**Fig. 3.** Scheme of the folded setup in transmission: While the beam is imaged on the galvanometer scanner and the applied movement is compensated, non-diffracted light remains defocussed on all optical elements. Since it is not a part of the 4f imaging system, it exhibits a position and angle displacement, depending on the angle of the galvanometer scanner. Therefore, non-diffracted light keeps moving after leaving the folded setup and gets averaged which effectively results in a negligible contribution in the target distribution.

ablation experiments with a microscope objective ($f_3 = 18$ mm, Thorlabs LSM02-BB) while camera images (UI-3080SE-M-GL) and alignment were done with a long focal length ($f_3 = 300$ mm, Thorlabs).

Ablation experiments (compare Section 3) are performed with the ultrashort pulsed laser system Cepheus (Photon Energy) which emits 12 ps pulses at a wavelength of $\lambda = 1064$ nm at a repetition frequency of 20 kHz. The maximum laser power of our system is around 3.3 W and this results in 0.4 GW cm−2 peak power on the SLM for a 3 mm beam. Therefore, we utilize the LETO 2 SLM from Holoeye which is coated for the near infrared spectral range. For those purposes, SLM and galvanometer scanner are mounted on a water-cooled holder. SLMs with a dielectric reflective coating on the backplane and water-cooling can usually deal with significantly higher powers than we use in our experiments. In our case we were restricted by the maximum laser power of our system which also limits the size of the shaped structures. The full potential of water-cooled SLMs can probably be used at several 100 W average power and this enables significantly larger structures. For a further analysis of the method in Section 4, we are working with a HeNe laser (Melles Griot, 10 mW, $\lambda = 633$ nm) and the LETO 1 SLM from Holoeye with a coating for the visible spectral range.

### 2.2. Design of components

The LETO 1/2 SLM has a 16:9 display (1920 × 1080 px) and a pixel pitch of 6.2 µm. For the proposed method, we consider it as beneficial that lots of SLMs are designed as widescreen displays whereas laser beams normally do not follow this aspect ratio. It is usually a decision between illuminating the whole SLM and thereby cutting the beam or using only a portion, typically around the half of the display. Our setup is designed for a beam diameter of 3 mm. A 1D scan over the SLM along its long axis (x-direction) effectively provides four areas of independent phase masks. Moreover, approximately half of the SLM's active area is illuminated along a 1D scan while the 3 mm beam itself illuminates a sufficiently high number of pixels to shape the target pattern. We work with the natural movement of the galvanometer scanner, a sinusoidal trajectory. This does not provide equal weighting of the individual speckled patterns since the beam is non-equally sampled over the SLM but Section 4.3 shows that the results for a scan with constant velocity are equal. This is mainly due to the choice of our phase mask which we discuss in Section 4.1. Similar to applications without a scanning movement, the phase mask is calculated with the Gerchberg-Saxton algorithm for the whole area of the SLM. Thereby, the aspect ratio of the SLM needs to be considered in the calculation, for example by rescaling the target structure appropriately. This is necessary as the maximum diffraction angle does not depend on the number of pixels but on the pixel size itself. This means likewise that the reduced illumination size of the SLM

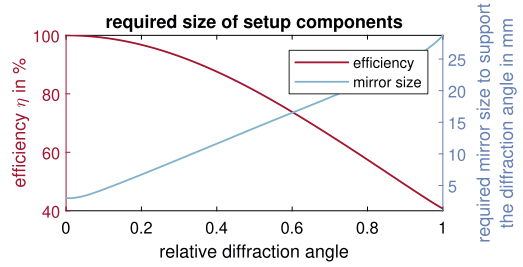


**Fig. 4.** To estimate the diffraction efficiency of the SLM, the phase mask is treated as a blazed grating. Since the absolute diffraction angle depends on the pixel size of the SLM, only relative values are shown. The diffraction efficiency $\eta$ for a blazed grating approximated with M pixels is given by $\eta = \left[\frac{\sin(\pi/M)}{\pi/M}\right]^2$ [23]. The blue line shows the relation between the relative diffraction angle, respectively the maximum size of the target structure, and the required mirror size to support the applied diffraction angle for our setup parameters. The relation depends on the distances and optical elements in the setup. (For interpretation of the references to colour in this figure legend, the reader is referred to the web version of this article.)

primarily affects the numerical aperture (NA) but not the maximum size of resolvable structures.

Independently from the fact that the maximum diffraction angle is not reduced due to the decreased beam size, it makes sense to consider up to which degree the full diffraction potential of the SLM is relevant: The diffraction angles and the applied angles from the scanner determine the size of the involved lenses and mirrors. We use 2" mirrors and lenses within the scanning path. The phase mask on the SLM affects the beam propagation and the galvanometer scanner needs to capture the diffracted beam on the second incidence. This size is determined by the applied diffraction angles of the phase mask. Thus, the size of the galvanometer scanner gives an upper limit for the diffraction angles that can be collected in our case and the final size of the target structure. The simulated blue curve in Fig. 4 shows the required mirror size as a function of the relative diffraction angle. Therefore, we assume a blazed grating in an arbitrary direction and calculate the required mirror size to capture 85% of the resulting intensity. Even though our galvanometer scanner's mirror aperture is designed for a 3 mm beam, it provides some tolerances since it is supposed to capture the light for scanning angles up to ± 20°, while we work in a range between ± 2°.

While limitations in size can be addressed with the appropriate mirror size, it should be mentioned that typical applications are far away from using the full diffraction potential of the SLM since there is often no need for large structures. Furthermore, the high diffraction angles are less efficient which manifests in a weaker illumination in the outer areas. To estimate the diffraction efficiency of the SLM, we use a blazed grating. The pixel structure of the SLM only enables a stepwise approximation of the blazed grating where the largest diffraction angle can only be realized with a binary grating applied to the SLM. This reduces the diffraction efficiency to 40.5%. Besides the fact that a galvanometer scanner with larger mirrors can be employed, the calculated efficiency in Fig. 4 suggests to also consider the general requirements on the target structure before designing the setup for all possible but probably unlikely phase masks.

Besides the diffraction efficiency of the applied phase mask, the efficiency of the whole system is determined by the losses of the involved optical elements (i.e. reflectivity and transmission of the optical components). If the experimental conditions are not designed such that the beam is obstructed by the galvanometer scanner, our proposed method causes no additional losses.

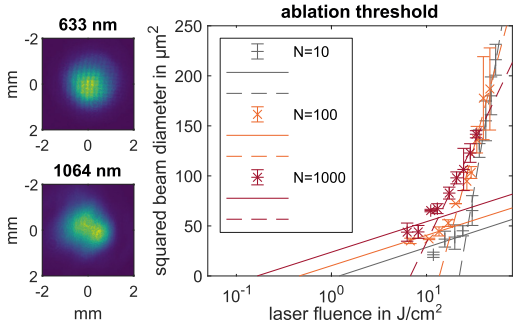


**Fig. 5.** Images of the laser modes at 633 nm and 1064 nm and the measurement of the ablation threshold for 10, 100 and 1000 pulses with $n = 3$ samples for each point. Two different lines are fitted to separate the two regimes of spallation (solid line) and phase explosion (dashed line).

### 2.3. Measurement of the ablation threshold

We use a polished silicon wafer for ablation experiments. It has a monocrystalline structure and thus provides a direct mapping of the beam profile in the ablation process. The perfectly polished surface prevents the ablation process from being affected by previously prevalent surface roughness or locally different ablation conditions. The ablation threshold is determined according to Liu [24]. 1000 pulses result in an ablation threshold of $0.17\ \frac{J}{cm^2}$ for spallation. Besides this measurement, Fig. 5 shows the two beam profiles of the HeNe laser and the ultrashort pulsed laser. Both beam profiles have a diameter around 3 mm but do not follow an exact Gaussian distribution. It should be mentioned that our proposed method is invariant to the exact beam profile so this does not impair the quality of the results at all.

After ablation experiments with the ultrashort pulsed laser, the silicon wafer is cleaned in an ultrasound bath and the depth profiles are measured with a laser scanning microscope from Olympus (LEXT OLS 4000).

## 3. Results and discussion

Besides the general presentation of the results, this section discusses some experimental parameters in more detail: The quality of the achieved results and the ablation depth, respectively the efficiency, depend on the applied laser fluence. Therefore, its influence will be evaluated in Section 3.1. Furthermore, a proper choice of the scanner frequency is discussed in Section 3.2. We also address that there is usually no necessity of synchronization between the emission of the laser system and the scanner movement in Section 3.3 and comment on the amount of pulses necessary to achieve a uniform outcome in Section 3.4.

Fig. 6 shows camera recordings and ablation profiles for a 1D and a 2D scan over the SLM. The square is 75 µm x 75 µm in size and fills 4.4% of the SLM's linear field of view, corresponding to 0.2% of the total area. This size is mainly chosen to have a proper range of the laser fluence due to an upper limit of available laser power of our laser system. As reference, a single position on the SLM is evaluated which corresponds to phase-only beam shaping with a single phase mask. For the ablation profiles, 1000 pulses with a repetition frequency of 20 kHz are used. To have a direct comparison of optical averaging with the resulting ablation profile, the intensity images in Fig. 6 are the corresponding camera recordings of the ultrashort pulsed laser at 1064 nm.

The intensity image for a single position on the SLM exhibits a clear speckle pattern. Strong intensity peaks alternate with areas of no signal. The $0^{th}$ order of non-diffracted light is defocussed but without a scanning movement on the SLM it remains still and overlays the center

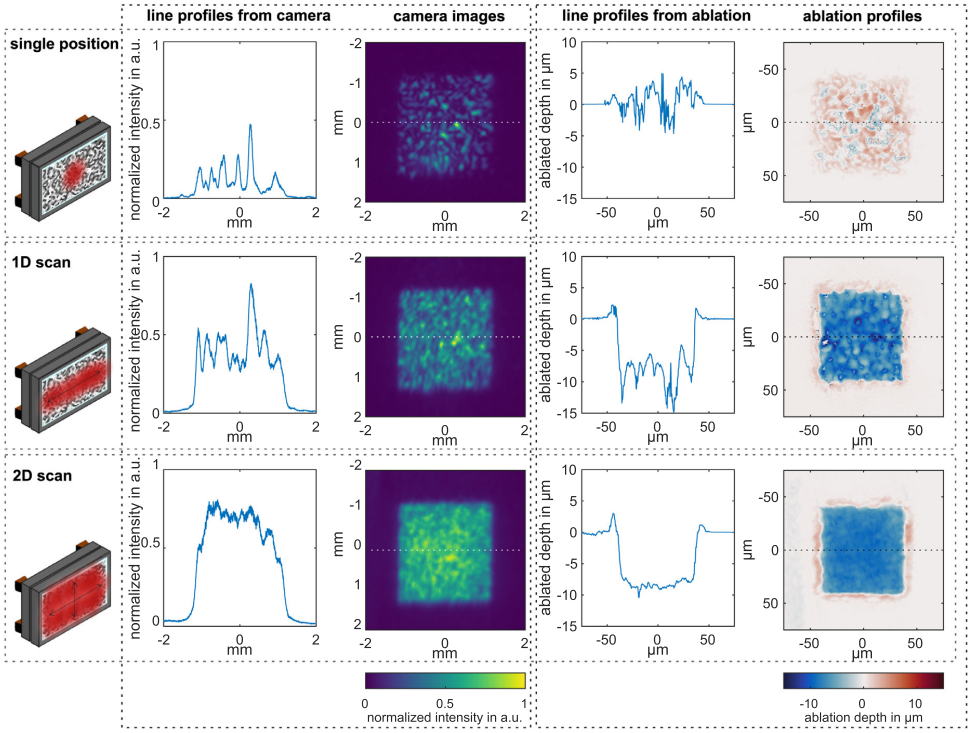


**Fig. 6.** Camera images and ablation profiles for different configurations: a single phase mask, a 1D scan, and a 2D scan over the SLM: The quality of the targeted square significantly improves with increasing scanning movement over the phase mask. The scanning frequency is $f_x = 2\,\text{kHz}$ for a 1D scan and $f_x = 813\,\text{Hz}$ and $f_y = 987\,\text{Hz}$ for a 2D scan. 1000 pulses were applied with a fluence of $5.5 \cdot F_{\text{th}}$ for the single phase mask, $6.8 \cdot F_{\text{th}}$ for the 1D scan and $4.5 \cdot F_{\text{th}}$ for the 2D scan. The position (0,0) corresponds to the center of the optical axis. The camera images are individually normalized to their maximum value while the ablation images show the amount of ablated material with the same color bar for all images. (For interpretation of the references to colour in this figure legend, the reader is referred to the web version of this article.)

of the square. It is almost invisible since the contrast from the individual speckle peaks is too bright to resolve it. In the ablation image, the square's structure is only fairly visible. The single peaks and dips prevent the area from being ablated properly.

A 1D scan improves the results significantly as the intensity profile shows only few isolated peaks. The ablation profile shows a clear rectangle with slight craters/peaks remaining.

The 2D averaging intensity profile is highly homogeneous and the ablation profile is almost perfectly smooth. It effectively shows no signs of the individually speckled pulses which ablated the structure and the edges are clear and sharp.

To quantify those observations, the uniformity $U$ [25] is calculated within the targeted area, in our case a square:

$$U = \frac{\sigma}{\mu} = \frac{\sqrt{\langle x^2 \rangle - \langle x \rangle^2}}{\langle x \rangle} \quad , \tag{1}$$

where $\sigma$ is the standard deviation and $\mu$ is the arithmetic mean, which is defined as the expectation value of a variable $x$ with $\langle x \rangle = \mu$. The corresponding values are presented in Table 1. Decreasing values of $U$ describe an improving uniformity with 0% being the highest achievable uniformity. We use the definition of the uniformity to have the same measure for the quality of the intensity profiles and the topology of the ablated surfaces instead of e.g. the roughness which can only be applied to the ablated surface. Within this paper, we call the uniformity for the intensity profile *beam uniformity* and the uniformity calculated from the topology of the ablated square *ablation uniformity* to distinguish them from each other.

**Table 1**
Uniformity of the results in Fig. 6.

| averaging | intensity image | ablation profile |
|---|---|---|
| single pos. | $U = 71\%$ | - |
| 1D scan | $U = 30\%$ | $U = 24\%$ |
| 2D scan | $U = 16\%$ | $U = 11\%$ |

Note that all structures are on-axis and nonetheless no $0^{\text{th}}$ order of non-diffracted light is visible or impairing the ablation results. It should be mentioned that our 1D depth measurements suffer from slight artifacts: Remaining craters only provide poor signal and such areas might be counted as surface area during the depth reconstruction from the laser scanning microscope. We decided not to post-process those images since this also affects the surroundings.

For a precise quantitative evaluation of the ablated topography it is useful to work with a widespread structure like a square. For the further investigation of ablation profiles, we thus work with squares. Nevertheless, Fig. 7 shows that not only widespread homogeneous areas can be shaped but also structures with thin lines and fine details.

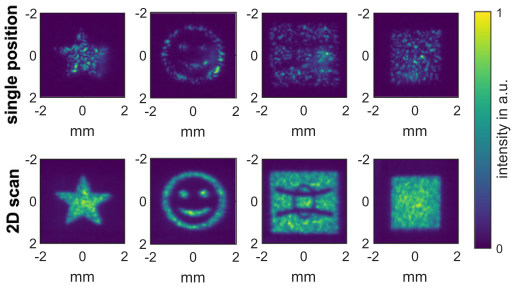


**Fig. 7.** Camera images for a single position on the SLM (corresponding to phase-only beam shaping with speckle overlaying the target structure) in the first row and for a 2D scan over the SLM in the second row. The images are recorded at 1064 nm and the scanner frequencies are $f_x = 813$ Hz and $f_y = 987$ Hz.

### 3.1. ablation rate and ablation uniformity as a function of $F_{th}$

The laser fluence has a strong effect on the quality and efficiency of the ablation results. By defining it in multiples of the threshold fluence $F_{\mathrm{th}}$, which gives the minimum fluence necessary to ablate material, results may be compared between different materials. Since however each single profile exhibits speckle, this value can only provide information about the mean fluence while there still exist peaks high above and below the given threshold. For this reason, material is ablated already below $F_{\mathrm{th}}$. The ablation rate, which is defined as the ablated volume over time per applied laser power, scales nonlinearly with the fluence [4,26]. The fluence, where this value is maximized, is typically called optimum fluence $F_{\mathrm{opt}}$. For a homogeneous beam profile, e.g. a top-hat, this happens at $e \cdot F_{\mathrm{th}}$. However, a more commonly used Gaussian beam profile exhibits local intensity variations such that the peak fluence needs to be $e^2 \cdot F_{\mathrm{th}}$ for maximization of the volume ablation rate [26].

Even though we achieve homogeneous profiles, each single pulse exhibits a strong speckle pattern with high deviations from the mean fluence. Nonetheless, we measure a maximum close to the optimum fluence for a top-hat beam profile. The volume ablation rate for 1D and 2D averaging is plotted in Fig. 8. Thereby, the almost perfectly averaged squares for a 2D scan achieve a higher volume ablation rate than the ablated squares for a 1D scan for the same applied laser fluence. We underline the experimental measurements with a simple logarithmic simulation model [27–29]. Here, the ablation scales logarithmically with the fluence in multiples of $F_{\mathrm{th}}$ times the optical penetration depth $\delta$:

$$d_{\mathrm{abl}} = \delta \cdot \log\left(\frac{F}{F_{\mathrm{th}}}\right) \quad , \tag{2}$$

where $d_{\mathrm{abl}}$ gives the ablated depth. Based on simulated intensity profiles of the used phase mask for the given scanning movement, we simulate averaging and use this formula to estimate the expected volume ablation rate. Thereby, the optical penetration depth $\delta$ is treated as a fit variable since we mainly want to compare the curvature of both results. The simulated optimum fluence is $F_{\mathrm{opt}} = 2.3 \cdot F_{\mathrm{th}}$. While this value is a bit less then the optimum fluence of a top hat beam, the experimental results tend to be closer to $e \cdot F_{\mathrm{th}}$.

In contrast to the volume ablation rate, the ablation uniformity is expected to improve with increasing laser fluence [20]. This trend is followed well in the two graphs in Fig. 8 for a 1D and 2D scan over the SLM. Here, we also add the theoretically expected curve from the logarithmic ablation model. Simulated and measured results fit well for a 1D and 2D scan. For a 2D scan, the ablation uniformity is already almost stagnating in the area of the maximum ablation rate. This brings together the area of highest efficiency with the achievement of highest ablation quality. For a 1D scan, it rather makes sense to work with a higher fluence to achieve better results even though this decreases the overall efficiency of the ablation process.

### 3.2. Dependence of averaging on the scanning frequency

Optical averaging on a camera is invariant to the speed of averaging as long as all the information which is required to improve the quality is collected within the exposure time. It effectively makes no difference if a single line scan is performed in contrast to multiples of this line scan. For averaging during material ablation the pre-ablated structure may affect the incoupling or the ablation process of the thereafter following pulses. A slow scan during ablation will cause dips and peaks which can not be averaged out. For this reason, 1D scans over the SLM with 1000 pulses at a laser repetition frequency of 20 kHz are evaluated for different scanning speeds, starting from a single line scan at 10 Hz up to 200 passes over the SLM at 2 kHz. To this end, we only consider a 1D scan with a sinusoidal beam motion over the SLM since 2D averaging rapidly provides new phase information even at low scanning speeds.

Fig. 9 (a) shows the results: The solid line shows the development of the ablation uniformity with respect to the scanning frequency. There is a strong dependence of the ablation uniformity on the scanning frequency. For ablation the speed of averaging is very important compared to optical averaging and a rapid beam motion is better than a slow motion. A similar effect can be observed for the measured ablation depth in dependence of the scanning frequency in Fig. 9 (b). Here, the amount of ablated material is doubled when the scanning frequency increases from 10 Hz to 100 Hz while the number of 1000 pulses is kept constant and the laser repetition frequency is 20 kHz. A similar behavior can be observed in a higher volume ablation rate for a 2D scan in contrast to a 1D scan in Fig. 8. Thus, to achieve optimum results for a 1D scan, a high scanning frequency should be chosen.

One possible explanation for the strong dependence on the scanning frequency might be a decreased incoupling efficiency into a rough surface. At low scanning speeds, single speckle can be assumed to be near-constant for several pulses. Consequently, craters appear which due to their edges increase the effective surface irradiated by the same fluence and thus raise the ablation threshold. The primarily appearing speckle dominate the ablation process and the incoupling decreases for subsequent pulses. Further research is required for the exact interpretation of those results but we believe that the developed method builds the basis for a profound analysis.

### 3.3. Synchronization

This section illuminates the influence of synchronization between the laser emission and the scanner movement. A single line scan needs to be synchronized such that the laser emission starts with the scanning motion and ends at the end of the line on the SLM to provide optimal averaging. However, after a certain number of scans, respectively at higher scanning speeds, a potentially unfinished line will not affect the result anymore. For this reason, the solid lines in Fig. 9 show the behavior when laser system and scanner were synchronized towards each other, independently of the free running pulse repetition frequency. The delay time between the laser trigger and the scanning movement was measured beforehand. The dashed line shows the same scenario without synchronization. After only 3–4 line scans (30 Hz/40 Hz) both curves are already almost identical. This shows that synchronization is effectively of no relevance for fast scanning speeds which strongly eases the experimental implementation of our proposed method. Even if the laser pulse repetition frequency and the scanning frequency are chosen as multiples of each other, the result seems to not be affected. This is probably due to the fact that both frequencies practically marginally deviate from their theoretically chosen value such that there is no exact overlap in the experiment. To stress this, Fig. 9 shows measurements with close but different scanning frequencies at 960 Hz and 1 kHz, and at 1920 Hz and 2 kHz.

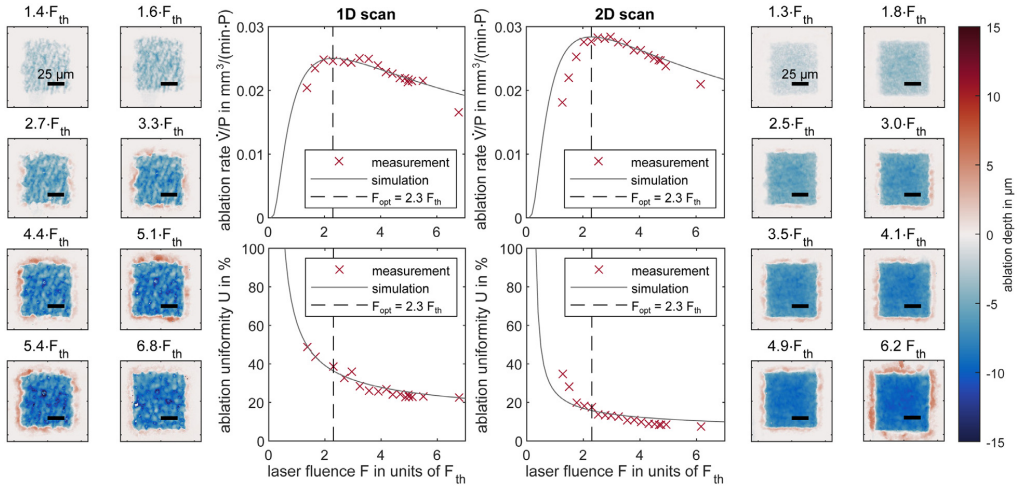


**Fig. 8.** Volume ablation rate and ablation uniformity as function of the laser fluence in units of the threshold fluence $F_{\mathrm{th}}$. The scanning frequency is $f_x = 2\,\mathrm{kHz}$ for a 1D scan and $f_x = 813\,\mathrm{Hz}$ and $f_y = 987\,\mathrm{Hz}$ for a 2D scan. The optimum fluence resulting from the simulation is marked with a dashed line. A selection of the ablated squares is shown besides the figures. The scale bar marks a length of 25 µm in all images.

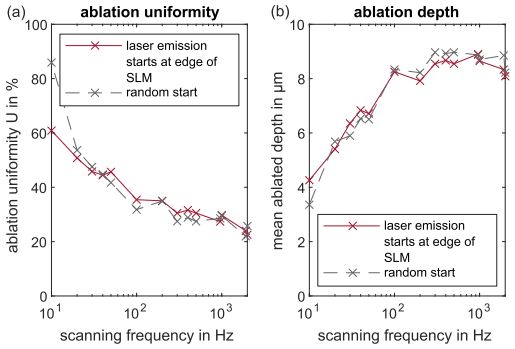


**Fig. 9.** (a) Influence of the scanning frequency on the ablation uniformity for a 1D scan: a fast scanning movement improves the ablation uniformity which suggests that rapid averaging is a relevant factor. The x-axis is scaled logarithmically. Only at low scanning frequencies (i.e. below 30 Hz - 40 Hz), the synchronization of the laser emittance with the galvanometer movement is relevant. (b) Influence of the scanning frequency on the ablation depth: a fast scanning movement increases the amount of ablated material. All those measurements were done at the same laser fluence of $6.2 \cdot F_{\mathrm{th}}$. Due to instabilities of our laser system, we measured a decrease of 10% in laser power during the measurement time. However, this deviation should only marginally influence the results.

For a 2D scan, averaging not only happens fast but due to the second dimension, there is a large range of possible trajectories along the SLM. Almost any configuration of scanning frequencies leads to natural averaging. As a small constraint, the two scanning frequencies should not be multiples of each other since this would soon repeat the scanning path. Apart from that, almost any frequency can be chosen and no synchronization is needed.

Those evaluations show that scanning frequencies can be chosen without the need of synchronizing the exact galvanometer position with the laser trigger to obtain high-quality results. Nonetheless, we would like to mention that synchronization may become necessary if only a small number of pulses can be applied since the area of the SLM needs to be sampled appropriately. Likewise, this scenario may give further constraints to the choice of the applied scanning frequencies. We thus investigate the dependence of the ablation uniformity on the number of applied pulses in Section 3.4.

### 3.4. Dependence of the ablation uniformity on the number of pulses for a 2D scan

This section evaluates the dependence of the number of applied pulses $P$ on the quality of the ablated rectangles measured by the ablation uniformity. Since every single pulse exhibits a speckle pattern, the ablated result gradually smoothes with an increasing number of pulses until it starts stagnating when there is no more gain in information. Given only a small number of applicable pulses, natural averaging may not be given for arbitrary scanning frequencies. The choice of the scanning frequencies may be constrained as well as synchronization between the scanning path and the laser emission may be required to ensure proper sampling of the phase mask. An additional option is to adapt the laser pulse repetition frequency.

We exemplarily evaluate the ablation uniformity in dependence of the number of pulses $P$ for scanning frequencies which were used for the 2D scans within this paper ($f_x = 813\,\mathrm{Hz}$ and $f_y = 987\,\mathrm{Hz}$). Fig. 10 shows the experimentally measured uniformity for ablated rectangles at $F = 5.6 \cdot F_{\mathrm{th}}$. After approximately 200 pulses, there is no significant change in the ablation uniformity until it almost stagnates after 500 or more pulses. This observation is consistent with the scanning trajectory of the laser beam on the SLM: After approximately 200 pulses, the whole area of the phase mask is roughly scanned. Nonetheless, there are strong inequalities in how the pulses are distributed over the area. Even though the illumination does not completely homogenize over time, its distribution saturates after approximately 500 pulses and no strong changes in the ablation uniformity are expected thereafter. While almost any configuration of scanning frequencies for a 2D scan leads to natural averaging, this evaluation suggests that for a small number of applicable pulses the system parameters have to be chosen appropriately: either by increasing the scanning frequency, or by decreasing the pulse repetition frequency. Furthermore, synchronization may help to trigger the laser emission at the proper position.

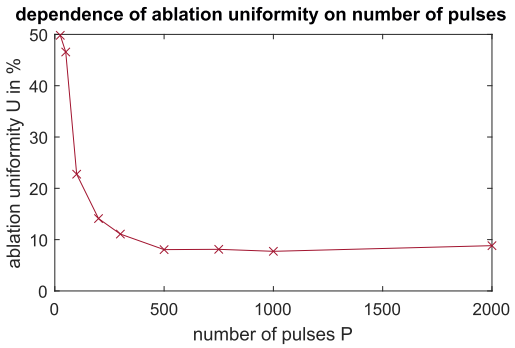


**Fig. 10.** Measured development of the ablation uniformity for $P$ pulses at $F = 5.6 \cdot F_{th}$ and a laser repetition frequency of 20 kHz. For the applied scanning frequencies $f_x = 813$ Hz and $f_y = 987$ Hz, the ablation uniformity rapidly improves and starts stagnating at around 500 pulses.

## 4. Theoretical background

We would like to discuss some relevant questions that should be answered to properly design the setup. First of all, we discuss the choice of the phase mask in Section 4.1. Section 4.2 deals with the proper choice of the beam diameter on the SLM. We also address the scanning movement over the SLM in Section 4.3. While we work with the galvanometer scanner's natural movement, namely a sinusoidal movement, it will be discussed and experimentally verified why no scanning path is necessary, that ensures homogeneous sampling with constant velocity over the phase mask, e.g. skywriting. For the sake of simplicity, those experiments are performed with a continuous wave HeNe laser since no ablation experiments are required. Note that since the speckle size is determined by the diffraction limit, its size changes with the wavelength which slightly affects the beam uniformity.

### 4.1. Choice of the proper phase mask

When designing the phase mask for the scanner setup, two different methods have to be considered: Golan and Shoham propose that cyclic shifting over a single phase mask provides perfect averaging [21]. Provided that all sequentially shifted parts of the hologram are equally weighted, speckle can be completely eliminated. This can be realized with a single phase mask which is padded by itself to provide all kinds of cyclic shifts for different scanning angles. The padding is required to also include the edges of the phase mask.

In contrast, independent phase masks can be used for averaging. Thereby, the beam uniformity $U$ improves with $\frac{1}{\sqrt{N}}$ and the corresponding number of different masks $N$ provides smooth results. The closest realization in our setup would be a single huge mask because this works like several independent masks. Due to the scanning movement, it still has overlapping areas which also follow the idea of cyclic shifting.

To make the best choice for a phase mask, we evaluate first cyclic shifting and then averaging in our setup. All measurements are done at a fixed angle of the galvanometer scanner, i.e. with a stationary beam. For cyclic shifting we load phase masks on the SLM that have been cyclically shifted within the image. The resulting intensity patterns are sequentially recorded with a camera. As a comparison, the same number of independent phase masks is applied to the SLM. Besides the evaluation of the optimum phase mask, this analysis also acts as a reference for our method since it shows the results of averaging without a scanning movement. Images for all three methods are shown in Fig. 11. Even though a 2D scan does not enable perfect angle compensation because there are two individual planes involved from the two galvanometer

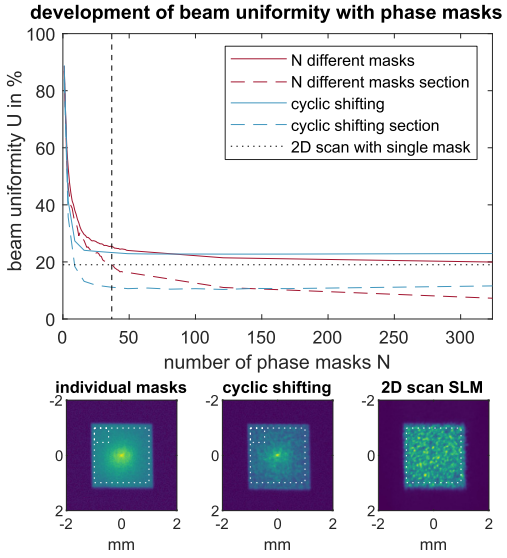


**Fig. 11.** Development of the beam uniformity with the number of newly applied phase masks for averaging of independent phase masks and cyclic shifting. The dashed lines only evaluate the section of the small square to exclude the effect from non-diffracted light. The dotted line shows the resulting beam uniformity from our method with a single phase mask. Recorded images of the resulting squares after 324 phase masks/shifts (corresponding to 18x18 equidistant shifts) and our method ($f_x = 813$ Hz and $f_y = 987$ Hz) are shown below with the evaluated areas marked.

mirrors, the edges are almost as sharp as for the reference of cyclic shifting/individual masks without movement. It should be mentioned that only our proposed method is capable of removing the $0^{th}$ order of non-diffracted light completely. For averaging and cyclic shifting, it appears as a defocussed spot in the center of the two squares.

Above the single squares, Fig. 11 shows the development of the beam uniformity for averaging of $N$ different phase masks and cyclic shifting with $N$ shifts. In both cases, two curves are shown: the solid line evaluates the beam uniformity $U$ over the whole square, while the dashed line indicates the evaluation of a part in the outer area without the presence of the $0^{th}$ order of non-diffracted light (depicted by the small rectangle in the upper left corner of the 2D images). As a reference, we plot the achieved beam uniformity of our method for a 2D scan over a single phase mask as a dotted line. Note that even though a beam diameter of 3 mm provides only 8 non-overlapping areas within the huge phase mask, the averaging result by scanning over the mask is equivalent to applying approximately 40 different masks on the SLM. Furthermore, applying 40 different phase masks takes around 1 s (30 Hz refresh rate of the SLM) while a 2D scan with 1000 pulses lasts 50 ms in our case limited by the laser repetition frequency.

While cyclic shifting shows a significant advance in averaging after a small number of equidistant shifts, it stops improving for a high number of shifts while averaging catches up the backlog and shows better results for a high number of phase masks $N$. The exact phase information for each cyclic shift of the phase mask has to arrive in the target plane to get perfect interference with vanishing speckle. In reality, the SLM cannot provide this requirement: for an LCoS SLM, the cross-talk between adjacent pixels always impairs the final wave front [30,31]. It locally depends on the strength of the phase difference and especially sudden phase jumps result in a strong cross-talk. We assume this to be the major reason for the rather stagnating behavior. Furthermore, aberrations in

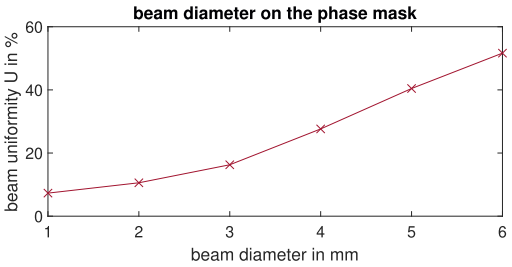


**Fig. 12.** Simulated relation between the beam diameter on the SLM and the resulting beam uniformity of averaged intensity profiles of a square after $P = 1000$ pules with $f_x = 813$ Hz and $f_y = 987$ Hz for a wavelength of $\lambda = 1064$ nm at a repetition frequency of 20 kHz. The individually simulated points are connected with a line.

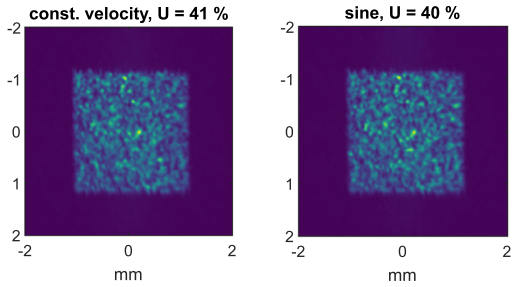


**Fig. 13.** Analysis of the necessity for a scan with constant velocity over the SLM like skywriting: For a 1D scan on a camera a sinusoidal movement gives the same beam uniformity.

the system (e.g. aberrations from the SLM screen) locally affect the wave front. Both effects are equally present during averaging of independent phase masks with the difference that cyclic shifting is physically based on the idea of perfect interference within a single phase mask, while those errors in the setup average out with new masks.

Those results suggest to work with one huge phase mask. Primarily, a shift of the beam over the phase mask has a similar effect in diminishing speckle as for cyclic shifting. With the additionally provided phase information systematic limitations become obsolete and averaging improves. As an additional benefit, this attempt may also be the reason why the overall result is not too sensitive to the exact way of how the beam scans the phase mask on the SLM. Cyclic shifting would need a scan with constant velocity over the SLM, namely equidistant shifts between the evaluated points. This is in general also possible with our method of scanning the SLM but requires a high degree of synchronization.

### 4.2. Choice of the beam size on the SLM

The beam size on the SLM defines the illuminated area of the phase mask. In a first instance, this determines the NA of the optical system and thus the resolution of the target structure as long as no additional magnification/demagnification is conducted thereafter. For cyclic shifting, the beam size specifies the number of required shifts necessary to perform perfect averaging. A smaller beam diameter illuminates less area on the phase mask, corresponding to a smaller number of pixels, and thus fewer shifts are required to conduct all possible shifts within that area. In our implementation, those shifts of the phase mask would be realized by scanning the beam over the mask. For averaging over a single huge phase mask, the illuminated area also defines the remaining free area on the SLM with additional phase information. For our configuration with a beam diameter of 3 mm and an SLM with approximately 12 mm × 7 mm in size this gives 8 independent phase masks. However, as Fig. 11 already indicates, the effect of averaging is a lot stronger since every single position in between counts as well.

There is more free area on the SLM for averaging if the beam diameter is decreased which suggests to work with a small beam. Likewise, it should not be chosen too small since it decreases the NA and the fluence on the SLM has to be kept low enough to avoid damage. Thus, the influence of the beam size on the resulting beam uniformity is evaluated to deduce a proper diameter for experimental applications. We simulate the scan path of the beam over the SLM with $f_x = 813$ Hz and $f_y = 987$ Hz for a wavelength of $\lambda = 1064$ nm and evaluate the beam uniformity of the averaged intensity profiles. With increasing beam diameter the maximum amplitude of the trajectory has to be adapted to not move the beam further to the borders of the SLM than the $1/e^2$ beam radius. The resulting curve in Fig. 12 can be approximated linearly within our region of interest given by the desired beam size of 3 mm. The slope is moderate for small beam diameters and predicts good averaging while it increases for beam diameters which come close to the dimensions of the SLM. Here the scanning movement is strongly limited and averaging decreases significantly. We deduce the near-linear behavior from the theory of averaging for independent phase masks. Here the beam uniformity $U$ is proportional to $\frac{1}{\sqrt{N}}$, while $N$ is proportional to $\frac{1}{d^2}$, with $d$ being the beam diameter. This makes $U$ directly proportional to $d$ and we assume this relation to be a major component when describing the effect of averaging over a single huge phase mask.

For our experimental implementation, we have considered to keep the NA and the laser fluence within a suitable range while optimizing averaging on the SLM. Thus we decided to choose a beam diameter of 3 mm, see Section 2.2.

### 4.3. Movement of the galvanometer scanner

Based on the fact, that each evaluated part of the phase mask gives a contribution to improve the overall result, it would be optimal to illuminate the whole area on the SLM homogeneously by scanning. The natural movement of the galvanometer scanner however is a sinusoidal movement. For a perfectly homogeneous illumination, additional methods like skywriting would be required to ensure a movement with constant velocity while the beam scans over the SLM. This is however much more complicated to achieve, probably reduces the maximum applicable galvanometer frequency, and is less efficient since the laser needs to be switched off during the time of acceleration and deceleration.

The recorded 1D scans in Fig. 13 show that there is no necessity for this additional effort since the resulting beam uniformity is equivalent for a movement over the SLM with constant velocity and with a sinusoidal distribution. For both motions the galvanometer triggers the camera exposure to exactly record a single line scan over the phase mask.

The results show that the averaging effect of a 1D scan over the phase mask is not sensitive to the exact movement. The same holds true for a 2D scan, where the second dimension rather eases the starting conditions since almost every configuration rapidly averages to an almost homogeneous scan field. This suggests to work with the natural sinusoidal movement of a galvanometer scanner and, as high scanning frequencies are beneficial, resonant galvanometer scanners seem to be the best option.

## 5. Conclusion

We present a method for uniform beam shaping with a single phase-only SLM that effectively suppresses speckle noise through averaging by beam scanning. In contrast to other methods which address speckle by averaging, this solution is not limited to the SLM's frame rate and thereby provides a high light efficiency.

Our presented method is simple, easy to implement, and convinces with near-perfect averaging results by applying a single phase mask. The analysis of the experimental parameters shows that neither synchronization, nor a scan with constant velocity over the SLM is necessary. A sinusoidal movement as natural movement of the galvanometer scanner gives equivalent averaging results. Moreover, the required phase mask can be easily calculated with the Gerchberg-Saxton algorithm. We consider this as major benefit of the proposed method since it eases the implementation.

The $0^{th}$ order of non-diffracted light vanishes in the target plane since it is defocussed and averages out without obtaining the proper movement compensation. Likewise, it is defocussed on all optical elements which makes the setup especially capable for the use of high-energy lasers.

The volume ablation rate for a 1D and 2D scan is maximized close to the optimum for a top-hat beam at $e \cdot F_{\mathrm{th}}$ where the ablation uniformity for a 2D scan already tends to stagnate. Our lowest measured ablation uniformity is around 8%. For a 1D scan, the optimum ablation rate has its peak at a similar value but to achieve a better ablation uniformity, a higher fluence should be chosen. Furthermore, the uniformity and the ablated volume show a strong dependence on the scanning frequency.

This novel method makes averaging feasible and we believe that such a setup can be implemented in an industrial application. Furthermore, we think that this method of high-speed averaging provides the chance to have a deeper look into the underlying physical processes of ultrashort pulsed laser material ablation since it paves the way for implementing high-speed changes into the beam profile.

## Funding

The authors gratefully acknowledge funding from the German Research Foundation (DFG) within the project 397,970,984 and funding from the Erlangen Graduate School in Advanced Optical Technologies (SAOT) by the German Research Foundation (DFG) in the framework of the German excellence initiative.

## Declaration of Competing Interest

The authors declare that there are no conflicts of interest related to this article.

## CRediT authorship contribution statement

**Lisa Ackermann:** Conceptualization, Methodology, Formal analysis, Investigation, Writing – original draft, Writing – review & editing. **Clemens Roider:** Conceptualization, Formal analysis, Writing – original draft, Writing – review & editing. **Matthias Gehring:** Writing – original draft. **Kristian Cvecek:** Writing – original draft, Writing – review & editing. **Michael Schmidt:** Writing – original draft, Writing – review & editing, Funding acquisition.

## Data availability

Data will be made available on request.

## Acknowledgments

The authors thank Benjamin Steffan and Konrad Brandmüller for technical support.

## References

[1] Sugioka K, Cheng Y. Ultrafast lasers-reliable tools for advanced materials processing. Light: Sci Appl 2014;3(4). e149–e149
[2] Sugioka K. Progress in ultrafast laser processing and future prospects. Nanophotonics 2017;6(2):393–413. doi:10.1515/nanoph-2016-0004.
[3] Orazi L, Romoli L, Schmidt M, Li L. Ultrafast laser manufacturing: from physics to industrial applications. CIRP Ann 2021;70(2):543–66. doi:10.1016/j.cirp.2021.05.007.
[4] Neuenschwander B, Jaeggi B, Schmid M, Rouffiange V, Martin P-E. Optimization of the volume ablation rate for metals at different laser pulse-durations from ps to fs. In: Hennig G, Xu X, Gu B, Nakata Y, editors. Laser Applications in Microelectronic and Optoelectronic Manufacturing (LAMOM) XVII, vol. 8243. SPIE; 2012. p. 43–55. doi:10.1117/12.908583. International Society for Optics and Photonics
[5] Zhu G, Whitehead D, Perrie W, Allegre OJ, Olle V, Li Q, et al. Investigation of the thermal and optical performance of a spatial light modulator with high average power picosecond laser exposure for materials processing applications. J Phys D: Appl Phys 2018;51(9):095603.
[6] Liu D, Wang Y, Zhai Z, Fang Z, Tao Q, Perrie W, Edwarson SP, Dearden G. Dynamic laser beam shaping for material processing using hybrid holograms. Opt Laser Technol 2018;102:68–73. doi:10.1016/j.optlastec.2017.12.022.
[7] Mikhaylov D, Kiedrowski T, Lasagni AF. Beam shaping using two spatial light modulators for ultrashort pulse laser ablation of metals. In: Laser-based Micro-and Nanoprocessing XIII, vol. 10906. International Society for Optics and Photonics; 2019. p. 1090615.
[8] Allegre OJ, Ouyang J, Perrie W, Jin Y, Edwardson SP, Dearden G. Advanced beam shaping for ultrafast laser micro-processing. In: Hinduja S, da Silva Bartolo PJ, Li L, Jywe W-Y, editors. Proceedings of the 38th International MATADOR Conference. Cham: Springer International Publishing; 2022. p. 105–14. ISBN 978-3-319-64943-6.
[9] Fienup JR. Phase retrieval algorithms: a comparison. Appl Opt 1982;21(15):2758–69.
[10] Gerchberg RW, Saxton WO. A practical algorithm for the determination of phase from image and diffraction plane pictures. Optik (Stuttg) 1972;35:237–46.
[11] Guillon M, Forget BC, Foust AJ, De Sars V, Ritsch-Marte M, Emiliani V. Vortex-free phase profiles for uniform patterning with computer-generated holography. Opt Express 2017;25(11):12640–52.
[12] Bartelt HO. Computer-generated holographic component with optimum light efficiency. Appl Opt 1984;23(10):1499–502. doi:10.1364/AO.23.001499.
[13] Bartelt HO. Applications of the tandem component: an element with optimum light efficiency. Appl Opt 1985;24(22):3811–16. doi:10.1364/AO.24.003811.
[14] Jesacher A, Maurer C, Schwaighofer A, Bernet S, Ritsch-Marte M. Near-perfect hologram reconstruction with a spatial light modulator. Opt Express 2008;16(4):2597–603.
[15] Jesacher A, Maurer C, Schwaighofer A, Bernet S, Ritsch-Marte M. Full phase and amplitude control of holographic optical tweezers with high efficiency. Opt Express 2008;16(7):4479–86.
[16] Ackermann L, Roider C, Schmidt M. Uniform and efficient beam shaping for high--energy lasers. Opt Express 2021;29(12):17997–8009.
[17] Caulfield HJ. Wavefront multiplexing by holography. Appl Opt 1970;9(5):1218–19.
[18] Goodman JW. Some fundamental properties of speckle. J Opt Soc Am 1976;66(11):1145–50.
[19] Häfner T, Heberle J, Holder D, Schmidt M. Speckle reduction techniques in holographic beam shaping for accurate and efficient picosecond laser structuring. J Laser Appl 2017;29(2):022205.
[20] Häfner T, Strauß J, Roider C, Heberle J, Schmidt M. Tailored laser beam shaping for efficient and accurate microstructuring. Appl Phys A 2018;124(2):1–9.
[21] Golan L, Shoham S. Speckle elimination using shift-averaging in high-rate holographic projection. Opt Express 2009;17(3):1330–9.
[22] Bawart M, Jesacher A, Zelger P, Bernet S, Ritsch-Marte M. Modified alvarez lens for high-speed focusing. Opt Express 2017;25(24):29847–55.
[23] Goodman JW. Introduction to fourier optics. Roberts and Company Publishers; 2005.
[24] Liu J-M. Simple technique for measurements of pulsed gaussian-beam spot sizes. Opt Lett 1982;7(5):196–8. doi:10.1364/OL.7.000196.
[25] ISO 13694:2018. Optics and photonics - lasers and laser-related equipment - test methods for laser beam power (energy) density distribution. Standard. Geneva, CH: International Organization for Standardization; 2018.
[26] Neuenschwander B, Jaeggi B, Schmid M, Hennig G. Surface structuring with ultra--short laser pulses: basics, limitations and needs for high throughput. Phys Procedia 2014;56:1047–58.
[27] Preuss S, Demchuk A, Stuke M. Sub-picosecond uv laser ablation of metals. Appl Phys A 1995;61(1):33–7.
[28] Chichkov BN, Momma C, Nolte S, Von Alvensleben F, Tünnermann A. Femtosecond, picosecond and nanosecond laser ablation of solids. Appl Phys A 1996;63(2):109–15.
[29] Nolte S, Momma C, Jacobs H, Tünnermann A, Chichkov BN, Wellegehausen B, Welling H. Ablation of metals by ultrashort laser pulses. J Opt Soc Am B 1997;14(10):2716–22. doi:10.1364/JOSAB.14.002716.
[30] Ronzitti E, Guillon M, de Sars V, Emiliani V. LCoS nematic SLM characterization and modeling for diffraction efficiency optimization, zero and ghost orders suppression. Opt Express 2012;20(16):17843–55. doi:10.1364/OE.20.017843.
[31] Moser S, Ritsch-Marte M, Thalhammer G. Model-based compensation of pixel crosstalk in liquid crystal spatial light modulators. Opt Express 2019;27(18):25046–63. doi:10.1364/OE.27.025046.

### 4.1.2 Spot Arrays for Uniform Material Ablation With Ultrashort Pulsed Lasers

[P2] Published at *Optics & Laser Technology*, 10.1016/j.optlastec.2023.109358.

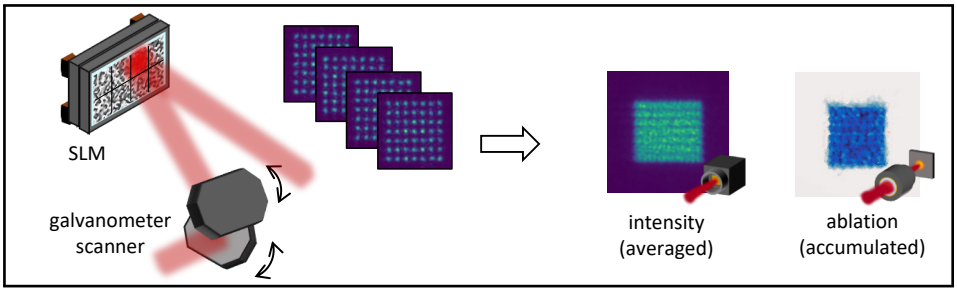


Graphical abstract: Spot Arrays for Uniform Material Ablation With Ultrashort Pulsed Lasers

Averaging by scanning provides near-perfect results. However, if only a small number of pulses should be applied to the material, the corresponding beam positions on the phase mask need to be chosen deliberately and a random scanning movement is no longer possible. In this scenario, it is more beneficial to superimpose the target structure of several spot arrays. Each spot array corresponds to an individual phase mask. Within a single pattern, the spots are separated far enough to not interfere while the subsequent combination of all patterns results in the final image as shown by Wlodarczyk et al. [94], Liu et al. [95], and Wang et al. [96]. This method requires only a small number of masks and thus pulses to achieve the final uniform image. To overcome the slow frame rate of the SLM, the SLM is separated into several sub-masks and the galvanometer scanner is programmed to approach specific positions. An analysis of the connection between the pixel count of a phase mask and the target resolution points out that a fraction of the SLM's area is sufficient for high-quality beam shaping. No spatial resolution is lost as long as the target image does not require the highest possible deflection angles. Furthermore, ablation experiments point out that a pulse-by-pulse change of the sub-mask is crucial to achieve uniform ablation profiles.

#### Highlights

- Phase-only beam shaping for uniform material ablation by superimposing spot patterns
- Pulse-by-pulse averaging of spot arrays is crucial for uniform ablation results
- Superimposing spot arrays combined with averaging gives equivalent ablation results
- Division of the SLM into independent sub-sections for high-speed phase modulation
- Deduction of the optical resolution from the pixel count on the SLM

Optics & Laser Technology 163 (2023) 109358

Contents lists available at ScienceDirect

Optics and Laser Technology

journal homepage: www.elsevier.com/locate/optlastec

Full length article

# Spot arrays for uniform material ablation with ultrashort pulsed lasers

Lisa Ackermann [a,b,*], Matthias Gehring [a,b], Clemens Roider [a], Kristian Cvecek [a,b], Michael Schmidt [a,b]

[a] Institute of Photonic Technologies, Friedrich-Alexander-Universität Erlangen-Nürnberg, Konrad-Zuse-Straße 3/5, Erlangen, 91052, Garmany
[b] School of Advanced Optical Technologies, Friedrich-Alexander-Universität Erlangen-Nürnberg, Paul-Gordan-Straße 6, Erlangen, 91052, Germany

ARTICLE INFO

*Keywords:*
LCoS SLM
Phase-only beam shaping
Spot array
Ultrashort pulsed laser materials processing

ABSTRACT

Phase-only beam shaping with a spatial light modulator (SLM) improves precision and increases efficiency during ultrashort pulsed laser materials processing. Speckle noise appears as not the full complex light field can be controlled by phase-only beam shaping. Adding up several patterns of spot arrays is one method to overcome speckle. Therefore, the targeted pattern is divided into several arrays of spots where adjacent spots within the same pattern are separated far enough to not interfere with each other. We show that a pulse-by-pulse change of the individual spot arrays during material ablation is crucial to achieve a uniform surface of high quality. Furthermore, the amount of ablated material and thus the ablation efficiency increases by a factor of 2 when each laser pulse is shaped with another spot pattern. To realize those rapid changes, we divide the SLM into independent sub-sections and sequentially illuminate the corresponding areas instead of changing phase masks on the SLM. To maintain the resolution while illuminating less area, we investigate the influence of the pixel count on the SLM.

## 1. Introduction

Beam shaping is a valuable tool in optics. Its applications reach from fundamental research on the nano scale to elaborated industrial processes on a large scale, such as laser materials processing for industrial applications [1–5]. The benefits in all those scenarios are similar: improved process quality, higher precision, and an increase in efficiency. In some applications, specific interactions or processes would not be achievable without a tailored light field.

Phase-only beam shaping is the common choice for controlling the wave front or the amplitude of the complex light field, either dynamically with the liquid crystal on silicon (LCoS) spatial light modulator (SLM), or statically with a diffractive optical element (DOE). In both cases the wave front is modulated by applying a phase mask which introduces a spatially varying phase delay typically between 0 and $2\pi$. Demonstrations of beam shaping for ultrashort pulsed laser materials processing date back to works of Momma et al. [6], Kuroiwa et al. [7], Sanner et al. [8,9], and Hayasaki et al. [10]. While Momma et al. and Kuroiwa et al. employ a static DOE, Sanner et al. and Hayasaki et al. use a dynamic device for programmable phase-only beam shaping.

Since phase-only beam shaping does not introduce significant intensity losses, the light efficiency is high and the wave front can be shaped arbitrarily. The shaped profile may improve the precision and ablation efficiency during ultrashort pulsed materials processing [11]. As a drawback, phase-only beam shaping does not allow sufficient control of the full complex light field which is defined by its amplitude and the wave front. Without introducing significant losses, wave front shaping can only be used to achieve a certain amplitude distribution without controlling the wave front in the target plane. Non-continuous phase jumps of the uncontrolled wave front lead to phase vortices which produce an overlaying speckle pattern [12]. Shaping an arbitrary amplitude distribution without speckle is thus only possible with limitations:

For specific geometries, analytical solutions exist and enable uniform beam shaping. Holder et al. demonstrate surface structuring with ultrashort pulsed lasers based on such solutions [13]. Moreover, simple geometries like a top hat profile can be shaped with homogenizers [14] or freeform optics [15]. Beam shaping based on adaptive optics introduces a continuous low-frequency phase modulation [8,9,16]. While this avoids phase discontinuities, the shaped structures exhibit smooth contours without sharp edges. Thus, all those solutions provide poorer freedom in design.

It is also possible to additionally modulate the amplitude on the phase mask during wave front shaping. This is realized by diffracting

* Corresponding author at: Institute of Photonic Technologies, Friedrich-Alexander-Universität Erlangen-Nürnberg, Konrad-Zuse-Straße 3/5, Erlangen, 91052, Garmany.
*E-mail address:* lisa.ackermann@lpt.uni-erlangen.de (L. Ackermann).
*URL:* https://lpt.tf.fau.de (L. Ackermann).

https://doi.org/10.1016/j.optlastec.2023.109358
Received 22 November 2022; Received in revised form 20 February 2023; Accepted 7 March 2023

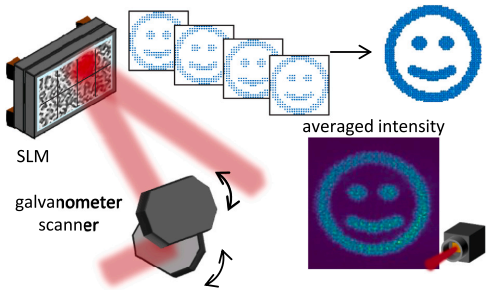


**Fig. 1.** To avoid speckle, the target image is composed of independent patterns of spot arrays. As the SLM's frame rate is low with respect to ultrashort pulsed laser repetition frequencies, the SLM is divided into sub-areas and the exchange of phase masks is transferred to a galvanometer scanner.

certain partitions of the light field away. Such phase holograms with additional amplitude modulation enable exact analytical solutions for perfect hologram reconstruction but exhibit poorer efficiency as the amplitude modulation involves significant losses [17–21]. In contrast, several phase shaping planes can be involved to gain more degrees of freedom during beam shaping. Two modulation planes are sufficient to control the full complex light field by amplitude and wave front shaping without loosing efficiency [22–26] and such methods can be employed for laser materials processing [27]. Moreover, thick holograms with several layers can be designed to generate wavelength- and angular-selective results with a lot more degrees of freedom [28–30]. However, such solutions are more complex to realize in practical implementation.

A simpler solution to implement is averaging of several intensity patterns which altogether result in a uniform ablation profile. One option is calculating different phase masks which result in the same target structure with differing speckle noise [31–33]. As this requires around 40–50 phase masks for a uniform ablation profile [33], another way is composing the target image of individual spot arrays which together form the desired structure [34–37]. The spots within one pattern are separated far enough to prevent them from interfering while superimposing several patterns enables shaping arbitrary and uniform beam profiles. Arranging 2D or 3D focal spot patterns for parallelization is a common method to increase the throughput in laser materials processing [10,38–41]. Such tailored spots also speed up laser machining processes like cutting [42,43]. In contrast to those approaches, we aim for uniform material ablation of arbitrarily shaped structures by superimposing several patterns of spot arrays. Even though we do not envision parallelized structuring such as drilling of several holes or cutting but aim for area ablation, we benefit from the research in that field:

Several algorithms have been developed which are designed to optimize the homogeneity within the individual spots and the efficiency of the used light field. The Gerchberg–Saxton algorithm [44] is only one option for calculating a spot pattern but not the best choice to ensure spots of the same brightness since it has no bias on uniformity within the iterative calculation. Moreover, the precision of the position of the individual spots is limited by the pixel resolution. Di Leonardo et al. developed an algorithm where the individual spots can be positioned precisely on a sub-pixel scale [45]. Furthermore, they work with an additional weighting factor for the individual spots to improve the uniformity of the overall pattern. For this reason, we calculate phase masks based on this algorithm.

Averaging with spot arrays, however, requires a dynamic beam shaping device which is capable of rapidly changing the applied phase mask. Due to dissipation and the inertia of the liquid crystals in an LCoS SLM [46], the frame rate is typically limited to 30 Hz–60 Hz. Thus, instead of changing the phase mask on the SLM, a single phase mask can be divided into individual partitions of sub-masks while a beam deflection device guides the laser beam to the proper position on the SLM [47–49]. The applied deflection angle is compensated within the experimental setup to maintain a static beam with updated phase mask. To make full use of the area on the SLM, we extended those 1D approaches with a galvanometer scanner with two mirrors to perform a 2D scan [50]. Moreover, we do not put the scanner and the SLM in their Fourier plane as this may induce excessive fluence and thus cause damages when working with high energy lasers. In [50], we developed the system to perform high-speed speckle averaging by randomly scanning the beam over the SLM. We propose here an elaborated system for controlling the galvanometer scanner and laser to automatically run specific scan patterns or address a specific area on the display. Our developed setup almost achieves 600 Hz with the perspective of reaching up to 10 kHz with dedicated hardware and proper tuning.

In this paper, we use spot arrays for uniform material ablation. For this we divide the SLM in several sub-masks as Fig. 1 sketches. Therefore, we analyze the role of the beam diameter and the number of illuminated pixels with respect to the resulting resolution in the target plane. We show that typical phase masks can be displayed with less pixels without loosing resolution. This is possible as the pixel count of an SLM or DOE is typically a lot higher than it is required to shape spot arrays or any complex structure as long as they do not exhibit high diffraction angles. The summation of the individual spot arrays results in a smooth profile of arbitrary shape and we evaluate different configurations of spot patterns and distances to optimize the outcome. Moreover, we compare averaging of different spot arrays with additional averaging of the very same spot pattern. Experimental results show that this additional averaging step is equivalent to working with spot arrays of higher order. The individually shaped spot patterns undergo nonlinear interaction during ultrashort pulsed laser material ablation. The resulting topology not only depends on the sum of the shaped intensity profiles but also on their order and the prevailing surface conditions. Our experiments show that a pulse-by-pulse change of the phase mask significantly helps to increase the ablation uniformity and efficiency with respect to the ablated depth. To avoid laser dead times it is thus crucial to rapidly switch between the involved phase masks.

Section 2 of this paper summarizes the experimental setup to perform rapid changes on the phase mask. In Section 3 we analyze the required number of illuminated pixels on the beam shaping device to maintain the initial resolution. Based on this, individual sub-areas can be selected. Finally, we apply this method to generate multiple spot arrays in Section 4. Here, we analyze the ablation uniformity of the ablated structures and the ablation efficiency depending on the speed of varying spot patterns, namely the number of consecutive laser pulses on each sub-mask. Furthermore, we investigate a combination of spot arrays with averaging. In Section 5, we compare our approach with other methods for uniform beam shaping. Technical details about our developed scanner control system for guiding the laser beam to the desired positions on the phase mask are shown in Appendix.

## 2. Materials and methods

This section gives an overview of the experimental setup with the most important aspects. We focus here on the adaptions for composing the target image out of spot arrays and performing high-speed changes between independent sub-masks. The basic principle of the optical setup with more details is presented in [50]. The laser beam diameter is designed to only illuminate a partition of the area on the SLM: The $1/e^2$ beam radius is $\omega = 1.5\,\mathrm{mm}$ and the SLM's dimensions are approximately $12\,\mathrm{mm} \times 7\,\mathrm{mm}$. This enables splitting the SLM into sub-areas and accessing them with the high deflection speed of the galvanometer scanner without being limited to the frame rate of a dynamic beam shaping device or even when working with a static

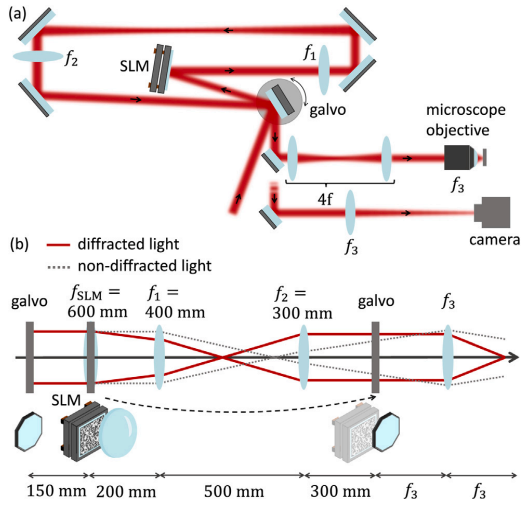


**Fig. 2.** (a) Sketch of the experimental setup. (b) Experimental setup in transmission to indicate the separation of non-diffracted light.
*Source:* Image taken from [50].

element. In our setup we achieve modulation speeds around 600 Hz which is 10 times faster than conventional systems. With proper tuning and dedicated hardware, around 100 times higher modulation speeds up to almost 10 kHz should be possible. A detailed evaluation can be found in Appendix A.

To shape an arbitrary uniform structure, the target image is composed of single spots. By multiplexing these spots into independent sub-patterns, adjacent spots are temporally separated to avoid interference with each other. Therefore, the final phase mask on the SLM consists of several sub-masks which can be accessed with the galvanometer mirror. The resulting spot patterns overlay in the target plane to obtain a continuous target image.

Therefore, the applied scanning angle needs to be compensated with an optical setup to maintain a stationary image while the phase information is changing with the scanner movement. This is realized by guiding the beam back to the galvanometer scanner as Fig. 2 (a) indicates. With a proper lens configuration, the plane of the galvanometer scanner is imaged on itself at the second incidence and thereby the galvanometer scanner not only introduces the scanning movement but also directly compensates for the initially applied angle. The beam leaving the inner part of the scanner setup thus remains stationary while the phase information changes with the position on the phase mask. We designed the SLM as part of a 4-f-imaging system. The first lens of the telescope is split into one physical lens and an additionally applied Fresnel lens term on the phase mask. This separates non-diffracted light: Since light not diffracted by the beam shaping device is not part of the 4-f-imaging system, its movement is neither compensated after reflection on the galvanometer scanner for the second time, nor is it focused in the target plane or on the optical components, cf. Fig. 2 (b). Non-diffracted light disappears in the focal plane and, more importantly, the method is suitable for high-energy lasers as it avoids damaging components. The phase information required to shape the target image is effectively imaged onto the galvanometer scanner. Thus, the galvanometer scanner is broadly illuminated. The target image appears in the focal plane of a lens which can be placed after it.

Besides using a single lens to image the target pattern after the second incidence on the galvanometer scanner, a telescope can also be added. Both options are illustrated in Fig. 2 (a). The telescope not only

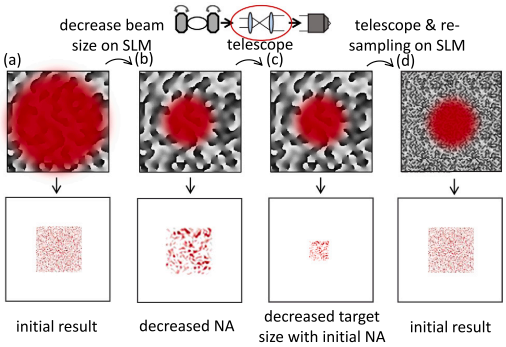


**Fig. 3.** Scheme of the effect of a reduced beam size on the phase mask shown for a targeted square: (a) Initial beam size with the initial result, (b) a decreased beam size reduces the NA, (c) subsequent magnification with a telescope may restore the initial NA while the target size decreases, (d) an additionally adapted phase mask restores the initial results.

images the phase mask into the pupil plane of the focusing lens and thus eases the experimental implementation by providing more space, it also magnifies the beam. As the following Section 3 shows, subsequent magnification is required to maintain the resolution if only a partition of the SLM is illuminated.

The focusing lens for our ablation experiments has a focal length of $f_3 = 18$ mm (LSM02-BB from Thorlabs). The magnification factor of the telescope is $M = 1.7$ with a $f = 300$ mm and $f = 500$ mm lens. The SLM LETO 2 from Holoeye has a 16:9 display with 1920 px × 1080 px and a pixel pitch of 6.4 µm. The laser system Cepheus 1012 (Photon Energy) emits 12 ps pulses at a repetition frequency of 20 kHz and at a wavelength of $\lambda = 1064$ nm. The laser repetition frequency of $f_{rep} = 20$ kHz is chosen as this provides the highest pulse energy for our laser system and it is a typical value for ultrashort pulsed material processing [51]: Heat accumulation is avoided while the repetition frequency is still moderately high. While we use this laser system for material ablation and the experimental analysis, the camera images for arbitrary structures are recorded with a HeNe laser at 633 nm (Melles Griot, 10 mW), cf. Fig. 6. The galvanometer scanner is the model 6210H from Cambridge Technology. We use a monocrystalline Silicon wafer for ablation experiments to have a direct mapping of the beam-shaped profile in the ablation process. The measured ablation threshold for 1000 pulses is $F_{th} = 0.17 \frac{J}{cm^2}$ and is determined according to [52]. This matches well with other values from literature [53,54]. The ablated surface profiles are recorded with the confocal laser scanning microscope Olympus LEXT OLS 4000. This provides an exact measurement of the surface topography to evaluate the ablation quality.

## 3. Deducing the resolution of the target image from the number of illuminated pixels on the SLM

Beam shaping devices offer a certain range of diffraction angles to shape the target structure. As long as the targeted distribution dos not require the highest possible diffraction angles, not the full pixel count of the beam shaping device is required. Therefore, a reduction in beam size (fewer illuminated pixels) does not necessarily mean a reduction in the resolution of the target image. We make use of this fact to divide the device into independent sub-areas. In this section, we quantify how many pixels are required to maintain the initial quality of the image. This analysis of the relation between the illuminated number of pixels and the resolution in the target plane gives the opportunity to find proper sub-divisions.

The applied phase mask lies in the pupil plane of the imaging system. Consequently, there is a Fourier relation between the plane of

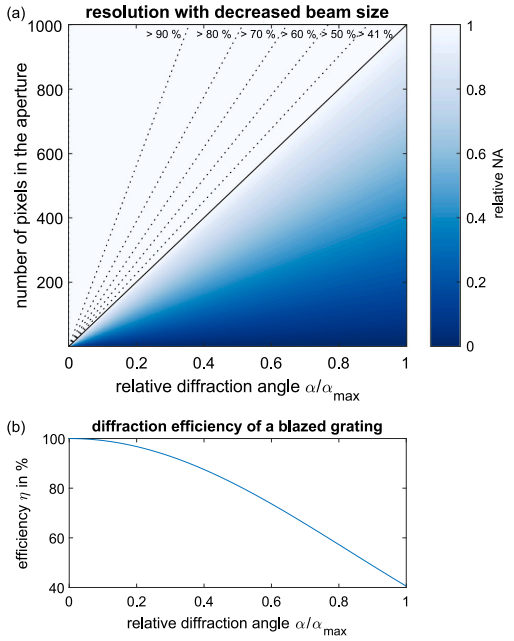


**Fig. 4.** (a) Relation between the number of illuminated pixels and the relative target size to determine parameters without loss of resolution. In this exemplary configuration, 1000 px are plotted along the y-axis, while the diffraction angle on the x-axis corresponds to the target size. Depending on the desired size, there is a degree of flexibility for adjusting the decreased beam size where the NA can be kept constant. (b) The diffraction efficiency for a blazed grating is plotted as reference.

the shaped wave front and the resulting target image. The pixel size of the beam shaping device determines the maximum diffraction angle and thus the field of view:

$$\alpha_{\max} \approx \frac{\lambda}{2u} \quad \text{for } u \gg \lambda \tag{1}$$

Here, $\lambda$ is the wavelength and $u$ is the pixel size of the beam shaping device. The smaller the pixel size $u$ is, the higher the maximum diffraction angle $\alpha_{\max}$ will be. This can be envisioned with a plain slope, such as applying a prism to the beam shaping device in a simple example. Since the phase delay of the beam shaping device typically varies between 0 and $2\pi$, the slope becomes a blazed grating as it is taken $\mod 2\pi$ when it is applied as phase mask. The finer the pixel count is, the higher the introduced slope can be. The maximum diffraction angle is thus given for a period of two pixels as binary grating which leads to the factor of 2 in the denominator in Eq. (1).

The resolution is defined by the numerical aperture (NA) of the optical system, respectively the beam diameter and the focal length $f$. Making the beam smaller automatically reduces the NA of the imaging system. This effect is shown in Fig. 3 (a) for the initial configuration and in Fig. 3 (b) for a decreased beam size. However, this change in the beam diameter does not change the resulting image except for the size of speckles, neither does a change in the position on the phase mask. Returning to the simple example with the blazed grating, the diffraction angle remains the same, independent of the beam size or the position along the slope. This remains the same for more complicated structures like an arbitrary target image that is calculated with the Gerchberg–Saxton algorithm.

To maintain the initial resolution, the NA of the imaging systems needs to be kept constant. This can be easily achieved by magnifying the beam accordingly as Fig. 2 (a) indicates with an additionally added telescope (cf. Fig. 3 (c)). This telescope images a magnified version of the phase mask from the galvanometer mirror into the pupil plane of the imaging system. The initially set beam diameter in our case is 3 mm. The magnification not only restores the initial NA but also affects the size of the target image as the effective pixel size of the phase mask is changed which alters the diffraction angles. Consequently, the required magnification needs to be considered when calculating the phase mask as shown in Fig. 3 (d). In case of a blazed grating, the magnification would reduce the slope and thus decrease the diffraction angle. As a result, the initially applied slope needs to be steeper to compensate for this reduction. This is possible as long as there are enough pixels available to decrease the effective size of the phase mask's pixel by introducing finer sampling on the beam shaping device. As the finest sampling is only required to fill the full field of view, this is possible as long as the target structure is initially not designed to already do so. Typically, the full field of view is not utilized and compensation of the reduced NA is possible. The finer meshing requires applying the initial phase information with less pixels and as a consequence the diffraction efficiency decreases [55]. However, there is no huge loss in efficiency to expect when working with smaller target images while this becomes relevant, when the initially set target size is large with respect to the maximum possible size.

To quantify this analysis, we need to determine the minimum required pixel size in the pupil plane which is required to shape the desired target structure. This pixel size is given by the highest necessary diffraction angle of the target structure. Thus, the required pixel count and sampling in the pupil plane to achieve the required diffraction angles can be determined. Based on this, the minimum possible beam diameter on the SLM is calculated for which the initial resolution can be maintained:

$$u_{\text{eff}} = \frac{\alpha_{\max}}{\alpha_{\text{eff}}} \cdot u \tag{2}$$

Eq. (2) gives the relation between the effective pixel size $u_{\text{eff}}$ in the pupil plane and the initial pixel size $u$ on the beam shaping device. They are connected by the ratio of the maximum possible diffraction angle $\alpha_{\max}$ as given by Eq. (1) and $\alpha_{\text{eff}}$, the desired diffraction angle, respectively the extension/size of the target structure in the image plane. As long as the effective pixel size is smaller than the pixel size on the SLM, the beam size on the SLM can be decreased up to the scaling factor $s$ without impairing the resolution:

$$s = \frac{u}{u_{\text{eff}}} \tag{3}$$

To maintain the initial NA, the beam has to be expanded with a telescope to its initial size while the target image for the phase mask needs to be adapted with the scaling factor within the calculation.

The graph in Fig. 4 (a) shows the possible range within the adaption of the beam diameter for the illuminated number of pixels on the y-axis and the relative diffraction angle, respectively the relative size of the target image, on the x-axis. The line between the origin and the upper right corner splits the two areas. In the upper left part the NA can be kept constant by adapting the phase mask at a reduced diffraction efficiency, while in the lower right the NA needs to be decreased. This solid line is given by

$$N = N_{\text{total}} \cdot \frac{\alpha}{\alpha_{\max}}, \tag{4}$$

where $N_{\text{total}}$ is the total number of available pixels, $N$ is the number of pixels in the aperture to maintain the initial resolution and $\alpha/\alpha_{\max}$ is the relative diffraction angle.

Assuming a blazed grating, the diffraction efficiency for the highest diffraction angle within the structure, respectively the most outer region within the target image, can be calculated [56]. It is shown as line plot in Fig. 4 (b). While the curve decreases slightly for small diffraction angles, it becomes steeper for the highest possible angles. To consider this factor while designing the setup, dotted lines of constant efficiency

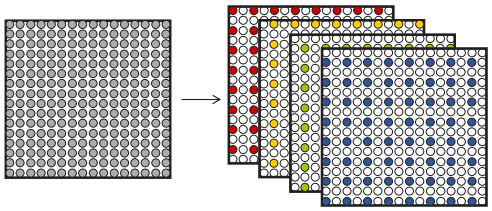

**Fig. 5.** The target structure is divided into single spots which together result in the target image.

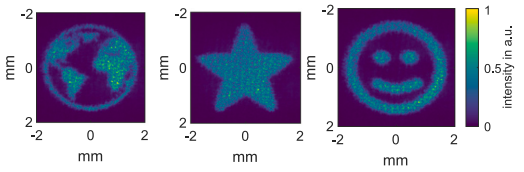


**Fig. 6.** Recorded intensity profiles of exemplary structures shaped with 8 sub-masks.

are added to the evaluation of the NA in Fig. 4 (a). Underneath the solid line, the NA reduces with a decreasing beam diameter/number of illuminated pixels.

Our SLM has a pixel count of $1920 \times 1080$ px and the pixel pitch is 6.4 µm. We split this area into eight sub-areas ($4 \times 2$) of $480 \times 540$ px which results in a beam diameter of 3 mm. Since our targeted square in Section 4 only fills 4.2% of the linear field of view, which means $0.04 \cdot \alpha_{max}$ on the x-axis, the SLM could be split into more sub-areas, i.e. in $8 \times 4$ partitions. Those parameters would be optimal but we set a beam diameter of 3 mm as a threshold to avoid excessive fluences on the SLM which could damage the device. To increase the NA, the beam is magnified by a factor of 1.7. This does not completely restore the initially possible NA but it is sufficient for our application.

## 4. Results and discussion: Uniform material ablation with spot arrays

A common way to overcome speckle during beam shaping is to divide the target structure into several arrays of single spots as Fig. 5 shows. Each of those spot patterns contributes to the final image and summing up all of them gives a smooth and uniform result. Speckle noise is diminished since adjacent spots within the same array are separated far enough to not interfere with each other. Therefore, the minimum peak to peak distance is given by the size of one spot which can be approximated as resolution-limited spot with $\lambda/NA$. For this case, four sub-structures are required where the smallest unit of independent spots is defined by a $2 \times 2$ pattern of four spots and the separation between adjacent spots within the same array is one spot. This scenario is indicated in Fig. 5. Shaping uniform structures with spot arrays has been presented for optical averaging on a camera image [34,35] and for material ablation [36,37]. Only a small number of phase masks is required to shape a uniform target structure as the individual patterns of spot arrays perfectly match in contrast to random averaging. Fig. 6 shows camera images of exemplary structures shaped with 8 sub-masks. While our proposed method enables shaping arbitrary geometries, we work with squares for material ablation as this eases the evaluation of the ablated depth and the achieved surface uniformity.

As this method is based on temporal multiplexing, phase masks have to be exchanged to shape the full target structure and the process is limited by the frame rate of the device. Using a static element, like a DOE, would not even be possible. With our setup it is possible to switch between several phase masks on the SLM. Another advantage of this method is a high tolerance in the experimental alignment. As the phase masks for each sub-area are calculated individually, they can be designed to also correct for slight imperfections in the setup: Perfect movement compensation is not possible as the two galvanometer mirrors do not have a common pivot point. Even though this deviation is small, it can be easily compensated within each phase mask. Moreover, we see the potential for correcting position-dependent aberrations.

We use the algorithm of Di Leonardo [45] to calculate the required phase masks to shape spot arrays. The beam is centered on each sub-mask. After arriving at the desired position, the laser emission is released for a predefined number of pulses until it is send to the next sub-mask, cf. Appendices A and B.

To evaluate the averaged results, we calculate the uniformity $U$ according to [57]:

$$U = \frac{\sigma}{\mu} = \frac{\sqrt{\langle x^2 \rangle - \langle x \rangle^2}}{\langle x \rangle} \quad , \tag{5}$$

Here, $\sigma$ is the standard deviation and $\mu$ is the arithmetic mean, which is defined as the expectation value of a variable $x$ with $\langle x \rangle = \mu$. Decreasing values of $U$ describe an improving uniformity with 0% being the highest achievable uniformity. We call $U$ ablation uniformity if the value is calculated for the surface topography and beam uniformity if the intensity profile is evaluated.

Besides analyzing the uniformity of the ablated results, we take the averaged value of the ablated depth to quantify the ablation efficiency. During all the experiments, the pulse energy was set around 75 µJ while 960 pulses were applied. This number was chosen since it is a multiple of 16. As this value is the same for all experiments, changes in the ablated depth directly indicate the ablation efficiency.

Having eight independent sub-areas on the SLM, we first evaluate different possible configurations of spot patterns. Based on those options, we conduct experiments on the optimum spot distance for material ablation. Having defined proper parameters for the spot arrays, we start evaluating our method: As a first parameter, we analyze the influence of the number of pulses on a single sub-area to ascertain on how often the sub-mask needs to be changed. Moreover, we evaluate the combination of working with spot arrays and additionally averaging them [35].

### 4.1. Configurations of spot array patterns

The concept of working with spot arrays is based on temporally separating adjacent spots and thus preventing them from unwanted interference. Therefore, it needs to be assured that neighboring spots in the summed pattern are close enough to give a smooth result (on the camera or for material ablation) while spots within a single pattern are separated far enough to not interfere with each other. The more substructures are involved, the easier it is for this criterion to be fulfilled but more phase masks are needed. The example in Fig. 5 shows the smallest possible unit: Adjacent spots are separated by a single spot and thus four independent patterns are required to shape the target structure. $2 \times 2$ spots define the unit cell of the temporally separated elements.

Typically, the separation of a single spot is not enough to diminish interference completely as the electric field is declining continuously. A pattern consisting of $3 \times 3$ or $4 \times 4$ spots is thus more advisable. However, having only eight independent sub-areas on our SLM, we are going for solutions which fit well to this number. Possible scenarios are shown in Fig. 7. The resulting uniformity for the intensity image and the ablated surface are noted within the picture.

The first option is to work with a pattern consisting of $2 \times 2$ spots as Fig. 5 shows. As this only requires four independent sub-masks the other four remaining areas are used to repeat this pattern to improve the result by averaging. The same patterns are calculated with different

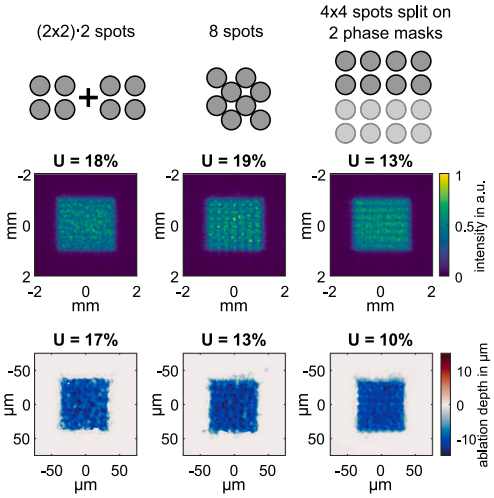


**Fig. 7.** The three evaluated configurations of spot arrays in this paper: The combination of a spot array consisting of 2 ×2 spots and averaging (indicated by $(2\times2)\cdot2$), eight spots with a face-centered core, and 4 × 4 spots where two phase masks are required on the SLM indicated by eight spots either in dark or light gray).

random starting conditions. Thus we abbreviate this method with $(2\times2)\cdot2$ as it is shown in Fig. 7. Based on the averaging method, this results in different interference patterns and improves the result. We also use this option for the exemplary geometries in Fig. 6. This idea is reported in [35], proposing that the combination of spot arrays with averaging may give better results than involving more spots within a unit cell. As these results are only reported for optical averaging, we test this idea for material ablation in Section 4.4.

The next option is similar to a face-centered lattice and requires eight independent masks. The corresponding unit cell is shown in Fig. 7. This option may be beneficial as the diffraction-limited spots exhibit a round geometry and thus better fill intermediate empty spaces. Apart from that, the eight required sub-masks perfectly fit to the amount of sub-areas on the SLM. However, the borders for this configuration cannot be meshed as fine in comparison to the inner area as would be the case for a purely rectangular geometry.

The last option to try is a grid consisting of 4 × 4 spots. In this case, interference is not an issue and we expect a high-quality result. However, there are 16 sub-masks required and the phase mask needs to be exchanged at least once as only half of the required sub-masks can be accommodated on the SLM. For this configuration, we find in Section 4.3 that the two phase masks only need to be exchanged once. As remarked in Section 3, we propose the limit of eight independent sub-areas due to the damage threshold of the SLM rather than the limited number of pixels. Working with an SLM with larger area but the same number of pixels provides more space for independent sub-areas while avoiding excessive fluences.

### 4.2. Determination of the spot distance for material ablation

The spot distance (peak to peak distance) for optical averaging can be deduced from the focal spot size which is defined by the NA. As the diameter of the ablated spot depends on several parameters, we conducted experiments to determine the optimum spot distance based on the ablation quality. Fig. 7 shows camera recordings and ablation profiles for all three spot configurations with the chosen parameters. The required spot distance to achieve a smooth surface for an array of 2 × 2 spots is determined to be 3.75 µm, separating two adjacent

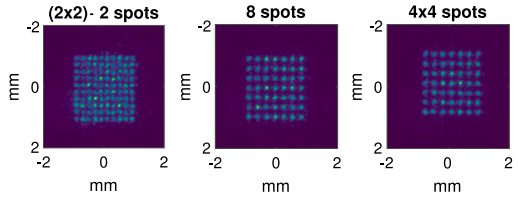


**Fig. 8.** Camera image for the chosen spot distances for the three different configurations.

spots within one pattern only by 7.5 µm. As the spot size is around 7.6 µm ($NA = 0.14$), there is interference within the spot pattern as Fig. 8 shows. This changes for the two other configurations, where the spot distance is set to 3.7 µm for eight spots (separating adjacent spots by 10.5 µm) and 2.6 µm for 4 × 4 spots (separating adjacent spots by 10.5 µm).

### 4.3. Number of consecutive pulses on each sub-area

When working with ultrashort pulsed lasers, the minimum number of pulses to ablate the final target structure is given by the number of sub-masks. Even though this only requires 8–16 pulses for our presented configurations, we work with 960 pulses in total to ablate a deeper structure. Thus, every single pulse can either be shaped with a new sub-mask, or some consecutive pulses can be shaped with the same sub-mask to reduce the number of sub-mask changes. This section investigates the effect of the number of consecutive pulses on the same sub-mask in comparison to a pulse-by-pulse change. For optical averaging, the order of the averaged patterns does not affect the result. Within the exposure time of the sensor, all the recorded intensity information is added up. This changes for material ablation as each pulse interacts nonlinearly with the material. The resulting surface geometry in return influences the subsequent ablation process. Fig. 9 shows that the ablation uniformity and also the amount of ablated material significantly improve when the phase information is exchanged pulse-by-pulse. Thus, the best result is achieved if only one pulse is sent to each sub-area. Here, the ablation uniformity is a single-digit number while it increases to values between 60% and 80% for 120 consecutive pulses on a single sub-mask, which is the maximum possible number for 960 pulses in total (cf. Fig. 9). Moreover, the ablated depth and thus the ablation efficiency decreases by a factor of 2. Taking the same sub-mask for several consecutive pulses is comparable to ultrashort pulsed hole drilling. While the ablation rate is high for a small number of consecutive pulses, it gradually decreases until the ablated depth stagnates completely. The steep edges of the drilled hole cause an increase of the effective area and thus a reduction of the applied laser fluence [58,59]. This effect gets worse with an increasing number of pulses. In contrast, a pulse-by-pulse change of the beam-shaped pattern maintains a rather uniform surface and thus avoids major changes of the ablation conditions within the process. This keeps a stable process with a smoothly ablated surface.

The results unambiguously show the necessity for rapidly changing the phase mask when averaging spot arrays with ultrashort pulsed laser material ablation. Even without optimization, our system can access sub-masks within 1.7 ms which is around 10 times faster than the frame rates of conventional SLMs and almost comparable to a switching time of 1 ms which can be achieved by overdrive with phase change reduction [60]. In our setup the y-axis of the galvanometer is faster by a factor of seven. With the same tuning for the x-axis the system would be faster by at least a factor of 50 compared to a 60 Hz SLM. With dedicated control hardware and tuning we see the potential to further increase this value for our scanner hardware to approximately 10 kHz, cf. Appendices A and C.

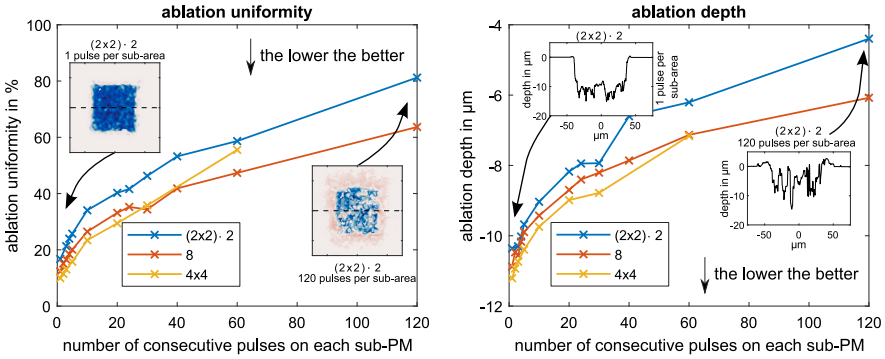


**Fig. 9.** Evaluated ablation uniformity and ablation depth in dependence of the number of consecutive pulses on each sub-phase mask (PM). The ablated profile for the configuration $(2 \times 2) \cdot 2$ is exemplarily shown for 1 and 120 consecutive pulses on the same sub-mask.

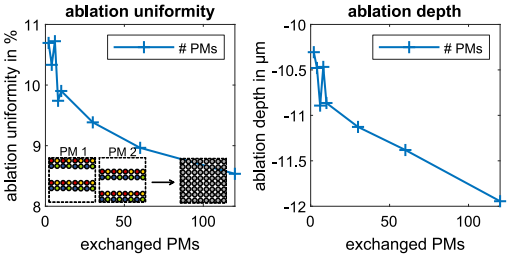


**Fig. 10.** Evaluation of the ablation uniformity and efficiency in dependence of the number of phase mask (PM) exchanges for a $4 \times 4$ pattern while one pulse is sent to each sub-area.

In case of a $4 \times 4$ unit cell, two phase masks are required since only eight sub-masks can be accommodated on the SLM. Thus, a new phase mask needs to be applied at least once during the ablation process. We configure the two phase masks to have adjacent spots on the same phase mask to directly ablate a connected area of lines. Fig. 10 indicates that there is no necessity to switch the phase mask more than once as long as the beam is sent to a new sub-mask after every single pulse (the number of consecutive pulses is $n = 1$ in the figure). The ablation uniformity only improves slightly and the ablation efficiency increases by a factor of 1.2. This increase in the amount of ablated material does not incur the loss in efficiency due to numerous dead times whenever a new phase mask is applied to the SLM. Pulse-by-pulse averaging is of higher-priority even if not all required sub-masks are involved and this can be done with little time effort. For this reason, the following experiments in Section 4.4 are performed with one pulse per sub-area and the phase mask for a $4 \times 4$ pattern is exchanged only once.

### 4.4. Combining spot arrays with averaging

Liu et al. propose a combination of spot arrays and averaging [35]. While they separate the object into individual point groups, they additionally recalculate the same target pattern with different starting conditions and thus additionally average the beam profiles. In their results, they reported combinations of spot arrays and averaging which resulted in a better beam uniformity in contrast to working with the same number of phase masks for spot arrays only. However, this method was never applied to materials processing.

Besides a potential improvement in beam/ablation uniformity for the same number of applied masks, we consider this method to be an interesting approach since it gives more freedom in designing target patterns based on a discrete number of possible sub-areas on a given beam shaping device.

Fig. 11 shows the achieved ablation uniformity for an increasing amount of sub-phase masks for the three proposed configurations. Since both spot arrays and averaging require new sub-phase masks to be applied, this method is evaluated by the required amount of sub-masks. The first plotted point along the x-axis thereby gives the lower limit for each individual configuration where the pattern can be summed up by the required amount of sub-patterns without additional averaging. Going further towards more sub-phase masks shows the development of the ablation uniformity with additional averaging. The results show that both spot arrays and averaging are relatively equal in their effect. Only in the case of a $2 \times 2$ spot pattern the results tend to be marginally worse. This is probably due to the fact that this method is not optimal for configuring spot arrays as two adjacent spots for uniform ablation are too close to each other from the outset.

The achieved ablation uniformity suggests that averaging is a rather equivalent approach with respect to working with spot arrays of higher order. This provides more freedom in designing possible spot patterns since apart from square numbers also multiples of square numbers are an option to properly fill the provided sub-areas on the beam shaping device. Compared to the eight possible sub-masks in our implementation there is some scope of improvement with 16 or even 32 sub-masks until the ablation uniformity tends to stagnate. Based on the analysis in Section 3, we consider the number of pixels on our SLM ($1920 \times 1080$ px) to be sufficient for dividing it into a pattern of $8 \times 4$ sub-areas instead of $4 \times 2$. Here, excessive laser fluence limits the number of sub-areas but there are also SLMs available with a larger area and a similar resolution. For this reason, we consider working with e.g. 32 sub-areas not as an unlikely scenario. Here, a pattern consisting of eight sub-patterns could be averaged four times and a $4 \times 4$ pattern could be averaged twice.

## 5. Comparison of ablation results with other methods

To place the experimental results in an overall context, the achieved surface uniformity is compared with ablation results based on other methods for beam shaping. Phase-only beam shaping without diminishing speckle noise exhibits high intensity contrasts. A camera image of a shaped square whose phase mask is calculated with the Gerchberg–Saxton algorithm [44] is shown in Fig. 12. For comparison, we performed ablation experiments on a Silicon wafer. It should be mentioned that the number of pulses is 1000, while the pulse energy is around 50 µJ. The surface topography shows that almost no material could be ablated. In some regions the intensity profile is below the threshold fluence while only a small amount of material could be ablated at peaks of high intensity. Speckle peaks cause steep edges which increase

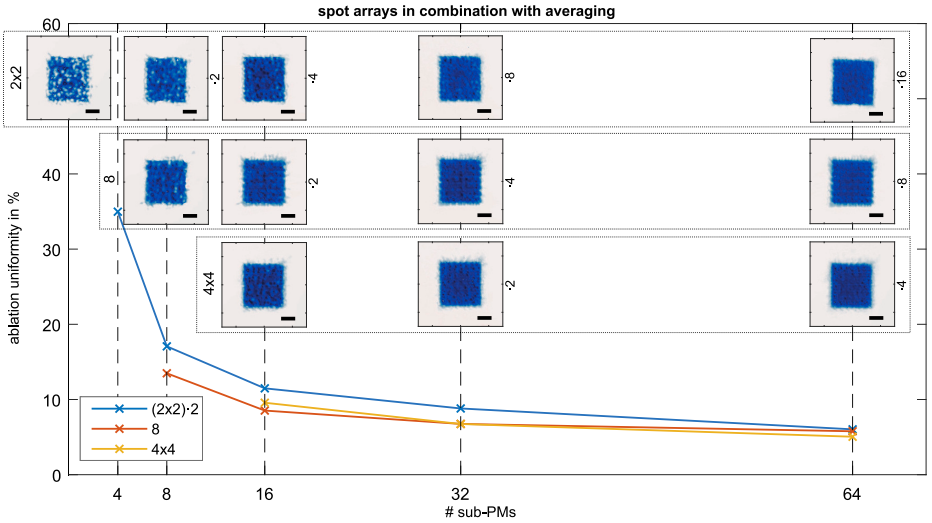


**Fig. 11.** Combination of spot arrays and averaging: After the complete spot pattern is summed up, further phase masks are used to improve the result by averaging. The resulting ablation uniformity is plotted versus the number of required sub-phase masks (sub-PMs). Based on the result in Section 4.3 one pulse is applied to one sub-mask. The scale bar indicates a distance of 25 µm.

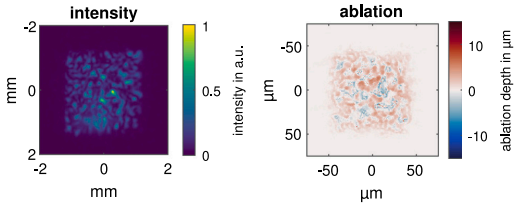


**Fig. 12.** Intensity image and ablation profile for phase-only beam shaping without diminishing speckle noise.
*Source:* Experimental data taken from [50].

the effective area similar to depth-dependent reduction of ablation in drilling [58,59]. This reduces the applied fluence and thus there is almost no material ablation. Those results unambiguously show the necessity for uniform beam shaping as the targeted square is only barely recognizable.

For specific geometries, e.g. a square, analytical solutions exist. Holder et al. perform beam shaping for large-area manufacturing on stainless steel and tungsten carbide with ultrashort pulsed lasers. Ablated squares achieved an ablation uniformity around 8% on stainless steel [13]. Those values are comparable to our results only when working with 64 sub-masks. Thus, this method or approaches by Sanner et al. and others [8,9,14,15] are excellent solutions for specific geometries.

However, if more complicated structures should be shaped, other methods are required which provide full freedom in design. Häfner et al. perform uniform material ablation by speckle averaging with several phase masks [33]. Those phase masks are calculated with the Gerchberg–Saxton algorithm while the varying starting conditions result in differing speckle noise. Ablated squares on a stainless steel alloy AISI304 with 50 different masks resulted in an ablation uniformity between 10% and 20%, depending on the relative fluence with respect to the threshold fluence.

Superimposing spot arrays gives similar results in uniformity and maintains the freedom of shaping arbitrary geometries. In contrast to averaging, only a small number of different phase masks is required. 8 to 16 sub-masks result in a comparable ablation uniformity. All those required sub-masks can be accommodated on a single liquid crystal display or even a static DOE. Thus, high-speed changes in the phase mask can be realized with the proposed control system (scanner system) to avoid laser dead times. Furthermore, only a small number of laser pulses is required to obtain a smooth result by averaging. While our setup is more complex in implementation when compared to standard configurations that e.g. use a single SLM with focusing optics, we see for our case the following benefits: (1) Arbitrary geometries can be shaped with a small number of masks while avoiding laser dead times. (2) Apart from designing spot arrays, our method offers to perform e.g. high-speed changes between different beam shapes and positions on the sample. This avoids heat accumulation within a single ablated structure and facilitates process parallelization. (3) Our method enables quasi-dynamic beam shaping with static beam shaping elements such as DOEs. This is of high interest for high-power (continuous wave) applications far above the damage threshold of liquid crystal displays where DOEs can be used. Different sub-masks on a single DOE could be approached in variable order to enable dynamic high-speed beam shaping.

## 6. Conclusion

A method to overcome speckles during phase-only beam shaping is temporally multiplexing the target structure in multiple arrays of single spots. While adjacent spots within a single pattern are separated far enough to avoid interfering with each other, the sum of all patterns provides a uniform result.

By applying this method for ultrashort pulsed laser ablation, we show how crucial rapidly changing the individual spot patterns is to maintain a smooth ablation profile and maximize the amount of ablated material. In the ideal case every single pulse should be shaped with a different spot pattern. However, the SLM frame rate is typically limited to values between 30 Hz and 60 Hz. We present a solution to overcome the slow frame rate by dividing the SLM into sub-areas. Since the pixel count of commercially available SLMs is high, there is not necessarily a reduction in optical resolution when working with a partition of the full display. We use a galvanometer scanner to deflect the laser

beam to defined positions on the SLM and directly compensate for the applied deflection angle with our developed optical setup. This allows for around 10 times higher switching times then commercial SLMs at a frequency of almost 600 Hz. However, with dedicated hardware and further tuning we see the potential for increasing this value to approximately 10 kHz.

With our developed setup, we further investigate a combination of spot arrays and averaging, a method which was so far only proposed for intensity profiles. The ablation experiments show that with an increasing amount of sub-masks the quality improves. More finely sampled spot arrays consisting of more spots within a single unit give the same result as additionally averaged spot arrays with less sub-patterns for the same number of involved sub-masks. We consider those results as beneficial since the equality of both options gives more freedom in the design of spot arrays when splitting the SLM into independent sub-areas.

The results suggest that averaging with spot arrays is an adequate method for achieving high-quality and high-efficiency results for ultrashort pulsed laser material ablation if spot patterns are rapidly exchanged. This is achieved with the developed scanner setup and the corresponding control system while only a small number of sub-masks is required.

**Funding**

The authors gratefully acknowledge funding from the German Research Foundation (DFG) within the project 397970984 and funding from the Erlangen Graduate School in Advanced Optical Technologies (SAOT), Germany by the German Research Foundation (DFG) in the framework of the German Excellence Initiative.

**CRediT authorship contribution statement**

**Lisa Ackermann:** Conceptualization, Methodology, Formal analysis, Investigation, Writing – original draft, Writing – review & editing. **Matthias Gehring:** Conceptualization, Software, Writing – original draft, Writing – review & editing. **Clemens Roider:** Conceptualization, Writing – original draft, Writing – review & editing. **Kristian Cvecek:** Writing – original draft, Writing – review & editing. **Michael Schmidt:** Writing – original draft, Writing – review & editing, Funding acquisition.

**Declaration of competing interest**

The authors declare that they have no known competing financial interests or personal relationships that could have appeared to influence the work reported in this paper.

**Data availability**

Data will be made available on request.

**Acknowledgments**

The authors thank Benjamin Steffan and Konrad Brandmüller for technical support.

## Appendix A. Computer-based control of the phase-only beam shaping process

The phase-only beam shaping setup in [50] requires the laser to be moved across the SLM for speckle averaging. In previous work, a signal generator with matched frequencies for the x- and y-axis was used to evenly weight the phase mask on the SLM either in 1D or 2D. While this is an easy and efficient way for speckle averaging, we see further potential in using this setup for high-speed switching between individual phase masks. For this reason, we designed a computer-based control system to increase the flexibility of the beam shaping setup and automate the process.

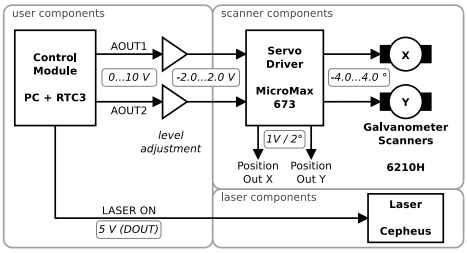


**Fig. A.1.** Overview of signals and components of the control system. While evaluating the phase-only beam shaping process, the SLM is not integrated into the control loop.

### A.1. System overview and software design

Within the optical setup there are three active components: the laser, the SLM and the galvanometer scanners (cf. Fig. A.1). Required parameters for the laser operation (e.g. pulse repetition frequency) are configured with the software provided by the manufacturer. As the laser `Cepheus 1012` does not provide a feedback channel for emitted pulses, only a digital output of the control system is connected to the laser, which acts as gate for the laser output (`HIGH`: laser emits, `LOW`: laser output is blocked).

The galvanometer scanners are equipped with a dedicated driver board. The drive electronics take analog voltages as input for both axes and set the positions based on an integrated closed-loop control. As the position control is tuned by the manufacturer to the individual hardware, it is utilized in this setup. Moreover this allows the computer-based control to be designed in a lightweight open-loop configuration. In the current setup, a standard PC with a `RTC3` plug-in card provides two analog (10 Bit DAC) and one digital output. The DAC outputs drive only positive voltages, but the controller board of the galvanometers takes positive and negative voltages as input. To address positive as well as negative deflections of the galvanometers, a level adjustment stage is implemented. This also allows to map the range of the DACs ($U_{\mathrm{RTC3}} = 0 \ldots 10\,\mathrm{V}$) to the cross section of the SLM ($U_{\mathrm{in}} \approx -2 \ldots 2\,\mathrm{V}$). Currently, the phase mask is applied manually, but this step can be added to the control system in a later stage.

To automate the beam shaping process, the pinpoint mode as shown in Fig. A.2 allows to precisely point the laser at the SLM and "place" a fixed number of pulses at that position. With this mode of operation, subsequent patterns of sub-phase masks can be tailored and applied to the beam shaping process. The control system also implements a scanning mode (cf. Appendix B) that allows the setup to be operated similar to [50].

### A.2. Modulation speed of the control system

The main goal of the computer-based control system is the implementation and automation of a fast positioning system for the laser on the SLM. The galvanometer scanner, being the major component of the control system, has a small angle step response of 100 µs, according to the data sheet. By only accounting for this value, a modulation frequency in the range of 10 kHz could be expected. In the practical implementation, there are more limitations which are determined by the involved control hardware and the tuning of the galvanometer mirrors. Here $\Delta t_{\mathrm{control}}$ is the additional latency added to the overall runtime by "overhead" in the control software. The contribution of the control loop in the current setup with the `RTC3` is $\Delta t_{\mathrm{control}} \approx 35\,\mu\mathrm{s} < \Delta t_{\mathrm{rep}} = 1/f_{\mathrm{rep}}$ (timing analysis in Appendix C). However, the electromechanical galvanometer scanners introduce a noticeable latency: While the factory calibration of the drive electronics is designed to run the x-axis in resonant mode, we design our control system to access

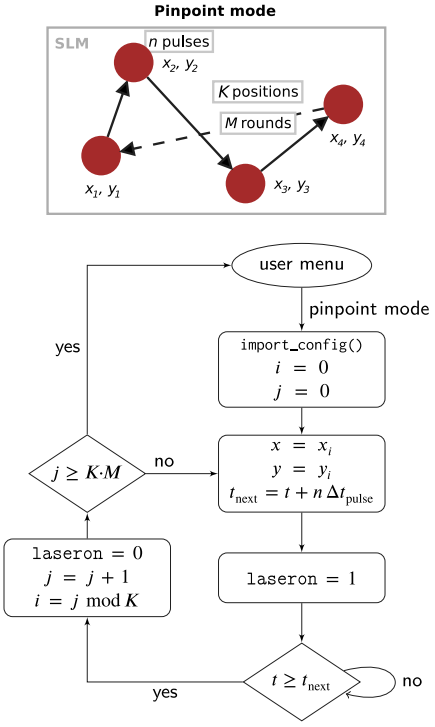


**Fig. A.2.** The configuration file for the pinpoint mode lists the two variables `pulses_per_position` $n$ and `rounds` $M$ as well as a list of $K$ vectors $(x_i, y_i)$. In operation, the laser is precisely pointed at these positions and `LASER ON` is set to high for $n$ laser pulses ($\Delta t_{on} = n \cdot \Delta t_{pulse} = n/f_{rep}$) after reaching the specified position $(x_i, y_i)$. The whole vector list is repeated for $M$ times in total.

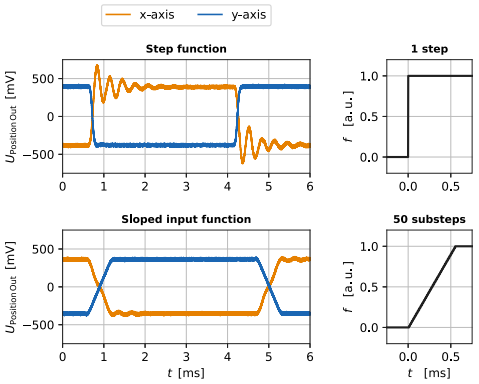


**Fig. A.3.** Step response (`Position Out`) of the scanner components recorded with a `LeCroy WS454` oscilloscope. Measurements were done separately for both axes and combined in this plot.

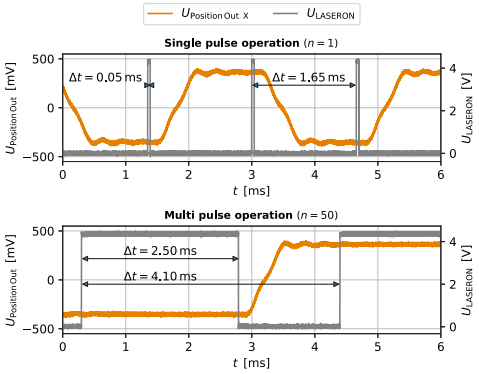


**Fig. A.4.** `Position Out` of the x-axis galvanometer and `LASER ON` signal for single pulse and multi pulse operation recorded with a `LeCroy WS454` oscilloscope.

specific positions instead of a continuous movement. Nonetheless, we consider a continuous operation similar to [61] as potential option to make use of the high scanning speeds during resonant operation. The interval $\Delta t_{scanner}$ is the time between setting a new position and the galvanometer scanners settling there.

Looking at the measured rise times in Fig. A.3 shows, that the tuning of the servo driver results in deviations from the optimum step response. While the step response of the y-axis still is approximately 250 µs, the resonant tuning of the x-axis causes significant oscillations before settling at a specific position. Sloping the input signal, for example by dividing the level change into a number of sub-steps, allows to dampen these oscillations, as can be seen in Fig. A.3. Although a large number of sub-steps allows to completely suppress oscillations on the x-axis, measurements of the rise time show, that using 30 sub-steps results in the shortest time interval between setting a new position and the galvanometer scanner settling there. With a rise time of ∼1.65 ms for the sloped input, one pulse at a different position can be emitted every 1.7 ms.

Fig. A.4 shows measurements of the x-axis and `LASER ON` signal of the system in single and multi pulse operation. While using multiple pulses per position ($n > 1$) reduces laser-off times, it sacrifices rapid changes of sub-masks.

In the current setup with a pulse repetition frequency of $f_{rep} = 20\,\text{kHz}$, being limited by the x-axis we achieve a modulation speed of almost 600 Hz. By retuning the x-axis to run comparable to the y-axis, this can be improved to 3.3 kHz. With further adjustments to the control module and software, the latency $\Delta t_{control}$ introduced by the control module gets negligible. In that case, the rise time of the scanners becomes the sole limit to the modulation speed and it can be pushed towards that limit depending on $f_{rep}$. To summarize, the current setup with galvanometer scanners allows to push the modulation speed in single pulse operation from currently around 600 Hz into the kilohertz range. Compared to conventional SLMs ($f_{mod} = 30...60\,\text{Hz}$), the presented setup has a 10 faster switching rate with prospect of pushing this factor to 100 and higher.

## Appendix B. Scanning mode

Scanning the laser beam across the SLM provides an easy and efficient way for averaging phase information. Therefore the scanning mode shown in Fig. B.5 provides the user with the ability to sweep the SLM with sinusoidal motion. This mode also allows to scan a sequence of subsections on the SLM, each for a predefined time interval. While results in [50] were based on a signal generator, similar experiments can now be designed and performed using the implemented control software.

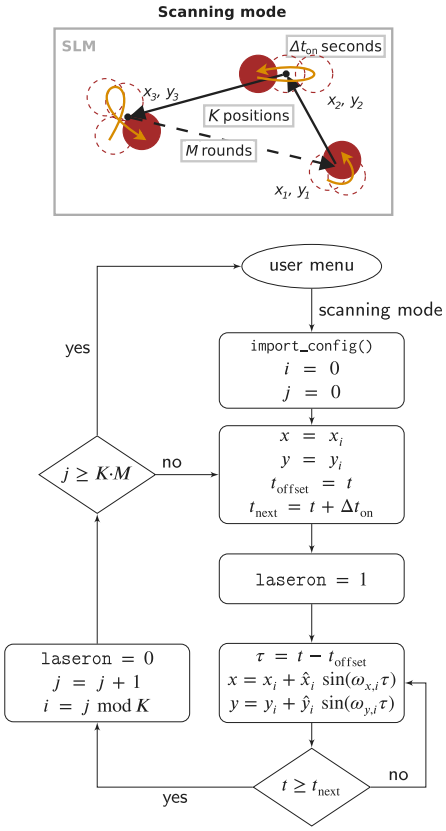


**Fig. B.5.** This mode mimics a signal generator. The configuration file for the scanning mode lists two variables `time_per_position` $\Delta t_{on}$ and `rounds` $M$ as well as a list of $K$ vectors $(x_i, y_i, \hat{x}_i, \hat{y}_i, f_{x,i}, f_{y,i})$. In operation, the laser is moved in sinusoidal patterns $x = x_i + \hat{x}_i \sin(\omega_{x,i}\tau)$, $y = y_i + \hat{y}_i \sin(\omega_{y,i}\tau)$ around the center positions $(x_i, y_i)$, where $\omega = 2\pi f$. After starting the motion pattern, `LASER ON` is set to high for a time interval of $\Delta t_{on}$ seconds, before continuing with the next scan position. The list of scan vectors is repeated for $M$ times in total. Depending on the intended sampling rate of the motion pattern, the wall-clock time of the DAC operation defines an upper limit for the highest usable scan frequencies.

## Appendix C. Timing analysis and possible adjustments to the control system

Appendix A.2 evaluated the galvanometer scanners and how their system dynamics limit the modulation speed. There we implicitly assumed, that the delay introduced by the control software is covered by the time between laser pulses, respectively negligible compared to the rise time of the scanners. This appendix provides further information to show that this assumption is justified.

**Timing analysis**

With the pulse repetition frequency $f_{rep}$ of the laser system in the kilohertz range, the first thing to consider is the time it takes the control module to set output signals. Measuring the wall-clock time in the control software shows, that setting the DACs takes the most time of the individual operations:

`RTC3 write_da_#()` : $\Delta t_{DAC} \sim 11\,\mu s$

As mentioned in the system overview, currently the control software is implemented in open-loop configuration with no feedback signals on the scanner positions or occurrence of laser pulses being connected to the control module. Therefore the control software needs to perform different timing-based sub-tasks:

(1) finished (3) → set analog outputs for next position
(2) finished (1) → wait $\Delta t_{scanner}$, then set `LASER ON = HIGH`
(3) finished (2) → wait $n \cdot \Delta t_{rep}$, then set `LASER ON = LOW` (emit defined number of pulses)

The runtime of sub-tasks (2) and (3) is concurrent with the time it takes the hardware to perform its operations. Isolating the corresponding operations in the control software and measuring the wall-clock time, the additional latency of the open-loop cycle can be evaluated:

Latency open-loop cycle : $\Delta t_{control} \sim 35\,\mu s$

Most of this latency is introduced by the DAC operation. During the design and evaluation phase, low-level commands of the RTC3 card were used to have direct control of the analog outputs and the `LASER ON` port. However the card also provides high-level functionality, that utilizes a DSP chip to generate smooth motion patterns with scanner setups. While this might help to cut the latency of the open-loop cycle, this has not been tested so far.

As the setup already contains a voltage adjustment stage, the control module itself can easily be swapped for other hardware. With plans in mind to design a dedicated controller box for the beam shaping setup, the control software was ported to an available `Raspberry Pi 2` (`RPi 2`). While the `Raspberry Pi 2` provides two independent PWM channels ($\Delta t_{bcm2835\_pwm\_set\_data()} \approx 0.2\,\mu s$) that are often used as DAC, the required RC-filter stage introduces significant latency (~1 ms). To evaluate the capabilities of the `Raspberry Pi 2`, simple 10-bit R2R networks were implemented instead:

`RPi 2 set_10bit_R2R()` : $\Delta t_{DAC} \sim 0.7\,\mu s$
Latency open-loop cycle : $\Delta t_{control} \sim 2.3\,\mu s$

The measured wall-clock times however should also be reproducible with dedicated DAC chips. This means, that the wall-clock time of the DAC operation and therefore the additional latency of the control software can be improved significantly by using a dedicated SoC as control module.

With this information on $\Delta t_{control}$ and $\Delta t_{scanner}$, the achievable modulation speed can be evaluated and the following conclusion can be drawn: If the rise time $\Delta t_{scanner}$ decreases, the additional latency $\Delta t_{control}$ becomes more important.

**Future proofing the control system**

State of the art laser systems provide a feedback signal, whether a pulse has been emitted already. Also the driver board of the galvanometer scanners provides feedback on the current position of the scanners. Integrating this information into a closed-loop control would eliminate the necessity to run timing-based sub-tasks in the control software. Although some additional computation would be required, the closed-loop approach increases the flexibility of the control software (e.g. optimized input signals for driver board) and should also be capable of reducing the latency $\Delta t_{control}$.

Another adjustment for production use-cases, is adding a parent loop to the control software, that displays precomputed phase masks to the SLM. This can be implemented both for a standard PC with RTC3 card as well as the `Raspberry Pi` in a dedicated controller box. The latter solution would also allow to integrate the control module, the level adjustment stage, the driver board and the required power supplies as well as a user interface (e.g. touch screen) into a standalone "device" to run the beam shaping setup.

## References

[1] Halina Rubinsztein-Dunlop, Andrew Forbes, M.V. Berry, M.R. Dennis, David L. Andrews, Masud Mansuripur, Cornelia Denz, Christina Alpmann, Peter Banzer, Thomas Bauer, Ebrahim Karimi, Lorenzo Marrucci, Miles Padgett, Monika Ritsch-Marte, Natalia M. Litchinitser, Nicholas P. Bigelow, C. Rosales-Guzmán, A.

Belmonte, J.P. Torres, Tyler W. Neely, Mark Baker, Reuven Gordon, Alexander B. Stilgoe, Jacquiline Romero, Andrew G. White, Robert Fickler, Alan E. Willner, Guodong Xie, Benjamin McMorran, Andrew M. Weiner, Roadmap on structured light, J. Opt. 19 (1) (2016) 013001.

[2] Koji Sugioka, Ya Cheng, Ultrafast lasers-reliable tools for advanced materials processing, Light: Sci. Appl. 3 (4) (2014) e149.

[3] Leonardo Orazi, Luca Romoli, Michael Schmidt, Lin Li, Ultrafast laser manufacturing: from physics to industrial applications, CIRP Ann. 70 (2) (2021) 543–566.

[4] Mangirdas Malinauskas, Albertas Žukauskas, Satoshi Hasegawa, Yoshio Hayasaki, Vygantas Mizeikis, Ričardas Buividas, Saulius Juodkazis, Ultrafast laser processing of materials: from science to industry, Light: Sci. Appl. 5 (8) (2016) e16133.

[5] Olivier J. Allegre, Jinglei Ouyang, Walter Perrie, Yang Jin, Stuart P. Edwardson, Geoff Dearden, Advanced beam shaping for ultrafast laser micro-processing, in: Proceedings of the 38th International MATADOR Conference, Springer International Publishing, Cham, 2022, pp. 105–114.

[6] Carsten Momma, Stefan Nolte, Günter Kamlage, Ferdinand von Alvensleben, Andreas Tünnermann, Beam delivery of femtosecond laser radiation by diffractive optical elements, Appl. Phys. A 67 (5) (1998) 517–520.

[7] Yutaka Kuroiwa, Nobuhito Takeshima, Yoshihiro Narita, Shuhei Tanaka, Kazuyuki Hirao, Arbitrary micropatterning method in femtosecond laser microprocessing using diffractive optical elements, Opt. Express 12 (9) (2004) 1908.

[8] Nicolas Sanner, Nicolas Huot, Eric Audouard, Christian Larat, Jean-Pierre Huignard, Brigitte Loiseaux, Programmable focal spot shaping of amplified femtosecond laser pulses, Opt. Lett. 30 (12) (2005) 1479.

[9] Nicolas Sanner, Nicolas Huot, Eric Audouard, Christian Larat, Jean-Pierre Huignard, Direct ultrafast laser micro-structuring of materials using programmable beam shaping, Opt. Lasers Eng. 45 (6) (2007) 737–741.

[10] Yoshio Hayasaki, Takashi Sugimoto, Akihiro Takita, Nobuo Nishida, Variable holographic femtosecond laser processing by use of a spatial light modulator, Appl. Phys. Lett. 87 (3) (2005) 031101.

[11] Beat Neuenschwander, Beat Jaeggi, Marc Schmid, Vincent Rouffiange, Paul-E. Martin, Optimization of the volume ablation rate for metals at different laser pulse-durations from ps to fs, in: Laser Applications in Microelectronic and Optoelectronic Manufacturing (LAMOM) XVII, 8243, International Society for Optics and Photonics, SPIE, 2012, pp. 43–55.

[12] Marc Guillon, Benoît C. Forget, Amanda J. Foust, Vincent De Sars, Monika Ritsch-Marte, Valentina Emiliani, Vortex-free phase profiles for uniform patterning with computer-generated holography, Opt. Express 25 (11) (2017) 12640–12652.

[13] Daniel Holder, Alexander Peter Simon Hensel, Rudolf Weber, Thomas Graf, Beam shaping for uniform and energy-efficient surface structuring of metals with ultrashort laser pulses in the mJ range, J. Laser Micro/Nanoengineering 17 (1) (2022).

[14] Maik Zimmermann, Norbert Lindlein, Reinhard Voelkel, Kenneth J Weible, Microlens laser beam homogenizer: from theory to application, in: Laser Beam Shaping VIII, 6663, SPIE, 2007, pp. 9–21.

[15] Oliver Homburg, Thomas Mitra, Gaussian-to-top-hat beam shaping: an overview of parameters, methods, and applications, in: SPIE Proceedings, SPIE, 2012.

[16] Patrick S. Salter, Martin J. Booth, Adaptive optics in laser processing, Light: Sci. Appl. 8 (1) (2019).

[17] Frank Wyrowski, Diffractive optical elements: iterative calculation of quantized, blazed phase structures, J. Opt. Soc. Amer. A 7 (6) (1990) 961–969.

[18] Adriaan Hendriks, Darryl Naidoo, Filippus S. Roux, Carlos López-Mariscal, Andrew Forbes, The generation of flat-top beams by complex amplitude modulation with a phase-only spatial light modulator, in: SPIE Proceedings, SPIE, 2012.

[19] Eliot Bolduc, Nicolas Bent, Enrico Santamato, Ebrahim Karimi, Robert W. Boyd, Exact solution to simultaneous intensity and phase encryption with a single phase-only hologram, Opt. Lett. 38 (18) (2013) 3546.

[20] Thomas W. Clark, Rachel F. Offer, Sonja Franke-Arnold, Aidan S. Arnold, Neal Radwell, Comparison of beam generation techniques using a phase only spatial light modulator, Opt. Express 24 (6) (2016) 6249.

[21] Dun Liu, Yutao Wang, Zhongsheng Zhai, Zheng Fang, Qing Tao, Walter Perrie, Stuart P. Edwarson, Geoff Dearden, Dynamic laser beam shaping for material processing using hybrid holograms, Opt. Laser Technol. 102 (2018) 68–73.

[22] Hartmut O. Bartelt, Computer-generated holographic component with optimum light efficiency, Appl. Opt. 23 (10) (1984) 1499–1502.

[23] Hartmut O. Bartelt, Applications of the tandem component: an element with optimum light efficiency, Appl. Opt. 24 (22) (1985) 3811–3816.

[24] Alexander Jesacher, Christian Maurer, Andreas Schwaighofer, Stefan Bernet, Monika Ritsch-Marte, Full phase and amplitude control of holographic optical tweezers with high efficiency, Opt. Express 16 (7) (2008) 4479–4486.

[25] Alexander Jesacher, Christian Maurer, Andreas Schwaighofer, Stefan Bernet, Monika Ritsch-Marte, Near-perfect hologram reconstruction with a spatial light modulator, Opt. Express 16 (4) (2008) 2597–2603.

[26] Lisa Ackermann, Clemens Roider, Michael Schmidt, Uniform and efficient beam shaping for high-energy lasers, Opt. Express 29 (12) (2021) 17997–18009.

[27] Lisa Ackermann, Clemens Roider, Kristian Cvecek, Michael Schmidt, Methods for uniform beam shaping and their effect on material ablation, Appl. Phys. A 128 (10) (2022).

[28] Haiyan Wang, Rafael Piestun, Dynamic 2D implementation of 3D diffractive optics, Optica 5 (10) (2018) 1220.

[29] Nicolas Barré, Ravi Shivaraman, Simon Moser, Patrick Salter, Michael Schmidt, Martin J Booth, Alexander Jesacher, Design and manufacturing of efficient computer-generated volume holograms in glass, 2022, arXiv preprint arXiv: 2209.13988.

[30] Paul Buske, Annika Völl, Moritz Eisebitt, Jochen Stollenwerk, Carlo Holly, Advanced beam shaping for laser materials processing based on diffractive neural networks, Opt. Express 30 (13) (2022) 22798.

[31] Jun Amako, Hirotsuna Miura, Tomio Sonehara, Speckle-noise reduction on kinoform reconstruction using a phase-only spatial light modulator, Appl. Opt. 34 (17) (1995) 3165–3171.

[32] Tom Häfner, Johannes Heberle, Daniel Holder, Michael Schmidt, Speckle reduction techniques in holographic beam shaping for accurate and efficient picosecond laser structuring, J. Laser Appl. 29 (2) (2017) 022205.

[33] Tom Häfner, Johannes Strauß, Clemens Roider, Johannes Heberle, Michael Schmidt, Tailored laser beam shaping for efficient and accurate microstructuring, Appl. Phys. A 124 (2) (2018) 1–9.

[34] Su-Juan Liu, Di Wang, Song-Jie Li, Qiong-Hua Wang, Speckle noise suppression method in holographic display using time multiplexing, Opt. Eng. 56 (6) (2017) 063107.

[35] Su-Juan Liu, Di Wang, Qiong-Hua Wang, Speckle noise suppression method in holographic display using time multiplexing technique, Opt. Commun. 436 (2019) 253–257.

[36] Dmitriy Mikhaylov, Thomas Kiedrowski, Andrés F. Lasagni, Beam shaping using two spatial light modulators for ultrashort pulse laser ablation of metals, in: Laser-Based Micro-and Nanoprocessing XIII, 10906, International Society for Optics and Photonics, 2019, 1090615.

[37] Zhipeng Wang, Xiaowei Li, Lan Jiang, Bohong Li, Qunshuo Wei, Lingling Huang, Zhi Wang, Jiangang Yin, Jiangang Lu, High-quality micropattern printing by interlacing-pattern holographic femtosecond pulses, Nanophotonics 9 (9) (2020) 2895–2904.

[38] Zheng Kuang, Walter Perrie, Jonathan Leach, Martin Sharp, Stuart P. Edwardson, Miles Padgett, Geoff Dearden, Ken G. Watkins, High throughput diffractive multi-beam femtosecond laser processing using a spatial light modulator, Appl. Surf. Sci. 255 (5) (2008) 2284–2289.

[39] Satoshi Hasegawa, Yoshio Hayasaki, Parallel femtosecond laser processing with a computer-generated hologram, in: SPIE Proceedings, SPIE, 2009.

[40] Zheng Kuang, Dun Liu, Walter Perrie, Stuart Edwardson, Martin Sharp, Eamonn Fearon, Geoff Dearden, Ken Watkins, Fast parallel diffractive multi-beam femtosecond laser surface micro-structuring, Appl. Surf. Sci. 255 (13–14) (2009) 6582–6588.

[41] Yoshio Hayasaki, Satoshi Hasegawa, Honghao Zhang, Ryo Onodera, Takefumi Kosugi, Nami Kuroo, Fumiya Ishita, Holographic beam-shaping optimized in a laser processing system, in: Holography, Diffractive Optics, and Applications XII, SPIE, 2022.

[42] Cyril Mauclair, Ultrafast laser machining of micro grooves on stainless steel with spatially optimized intensity distribution, J. Laser Micro/Nanoengineering 8 (1) (2013) 11–14.

[43] Cyril Mauclair, David Pietroy, Yoan Di Maïo, Emmanuel Baubeau, Jean-Philippe Colombier, Razvan Stoian, Florent Pigeon, Ultrafast laser micro-cutting of stainless steel and PZT using a modulated line of multiple foci formed by spatial beam shaping, Opt. Lasers Eng. 67 (2015) 212–217.

[44] Ralph W. Gerchberg, W. Owen Saxton, A practical algorithm for the determination of phase from image and diffraction plane pictures, Optik 35 (1972) 237–246.

[45] Roberto Di Leonardo, Francesca Ianni, Giancarlo Ruocco, Computer generation of optimal holograms for optical trap arrays, Opt. Express 15 (4) (2007) 1913–1922.

[46] Peder Aursand, Johanna Ridder, The role of inertia and dissipation in the dynamics of the director for a nematic liquid crystal coupled with an electric field, Commun. Comput. Phys. 18 (1) (2015) 147–166.

[47] Neal Radwell, Dominykas Brickus, Thomas W. Clark, Sonja Franke-Arnold, High speed switching between arbitrary spatial light profiles, Opt. Express 22 (11) (2014) 12845.

[48] Martin Bawart, Alexander Jesacher, Philipp Zelger, Stefan Bernet, Monika Ritsch-Marte, Modified Alvarez lens for high-speed focusing, Opt. Express 25 (24) (2017) 29847–29855.

[49] Boris Braverman, Alexander Skerjanc, Nicholas Sullivan, Robert W. Boyd, Fast generation and detection of spatial modes of light using an acousto-optic modulator, Opt. Express 28 (20) (2020) 29112.

[50] Lisa Ackermann, Clemens Roider, Matthias Gehring, Kristian Cvecek, Michael Schmidt, High-speed speckle averaging for phase-only beam shaping in laser materials processing, Opt. Lasers Eng. 165 (2023) 107537.

[51] Rudolf Weber, Thomas Graf, Peter Berger, Volkher Onuseit, Margit Wiedenmann, Christian Freitag, Anne Feuer, Heat accumulation during pulsed laser materials processing, Opt. Express 22 (9) (2014) 11312.

[52] Jia-Ming Liu, Simple technique for measurements of pulsed Gaussian-beam spot sizes, Opt. Lett. 7 (5) (1982) 196–198.

[53] Christian Fornaroli, Jens Holtkamp, Arnold Gillner, Dicing of thin Si wafers with a picosecond laser ablation process, Physics Procedia 41 (2013) 603–609.

[54] Hewei Liu, Feng Chen, Xianhua Wang, Qing Yang, Hao Bian, Jinhai Si, Xun Hou, Influence of liquid environments on femtosecond laser ablation of silicon, Thin Solid Films 518 (18) (2010) 5188–5194.

[55] Christian Lingel, Tobias Haist, Wolfgang Osten, Optimizing the diffraction efficiency of SLM-based holography with respect to the fringing field effect, Appl. Opt. 52 (28) (2013) 6877.

[56] Joseph W. Goodman, Introduction To Fourier Optics, Roberts and Company Publishers, 2005.

[57] I.S.O. 13694:2018, Optics and photonics - Lasers and laser-related equipment - Test methods for laser beam power (energy) density distribution, Standard, International Organization for Standardization, Geneva, CH, 2018.

[58] Sven Döring, Sören Richter, Stefan Nolte, Andreas Tünnermann, In situ imaging of hole shape evolution in ultrashort pulse laser drilling, Opt. Express 18 (19) (2010) 20395–20400.

[59] Sven Döring, Sören Richter, Andreas Tünnermann, Stefan Nolte, Evolution of hole depth and shape in ultrashort pulse deep drilling in silicon, Appl. Phys. A 105 (1) (2011) 69–74.

[60] Gregor Thalhammer, Richard W. Bowman, Gordon D. Love, Miles J. Padgett, Monika Ritsch-Marte, Speeding up liquid crystal SLMs using overdrive with phase change reduction, Opt. Express 21 (2) (2013) 1779–1797.

[61] Ashwathama Dilipkumar, Alaa Al-Shemmary, Lucas Kreiß, Kristian Cvecek, Birgitta Carlé, Ferdinand Knieling, Jean Gonzales Menezes, Oana-Maria Thoma, Michael Schmidt, Markus F Neurath, et al., Label-free multiphoton endomicroscopy for minimally invasive in vivo imaging, Adv. Sci. 6 (8) (2019) 1801735.

## 4.2 Uniform and Efficient Beam Shaping for High-Energy Lasers

[P3] Published at *Optics Express*, 10.1364/oe.426953.


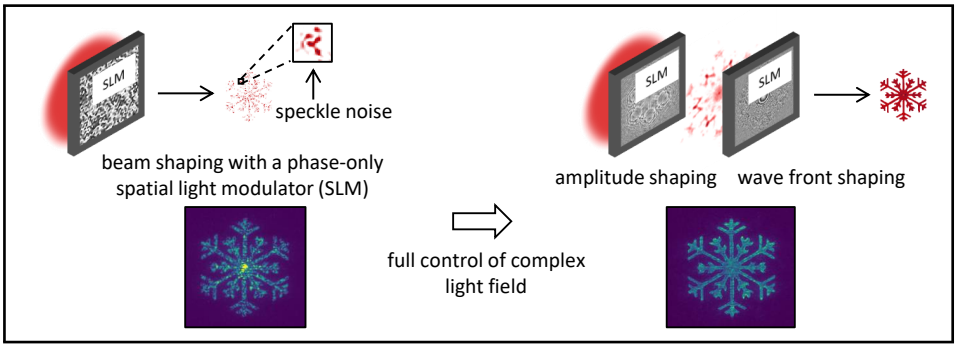


Graphical abstract: Uniform and Efficient Beam Shaping for High-Energy Lasers

In some scenarios, averaging is no option as already the single laser pulse needs to exhibit a certain intensity distribution and probably even the wave front needs to be confined. Some applications require single-shot laser processing and full control of the light field might be required when utilizing light as optical tweezers [102] or when triggering neurons in optogenetics [202]. To gain full control of the light field while avoiding losses, two phase-only beam shaping planes are required. Although there exist several publications and concepts [100–103, 203–206], a method is required which avoids excessive fluences on the involved beam shaping planes when working with ultrashort pulse lasers. This also involves taking into account non-diffracted light which may induce excessive fluences when being focused. These requirements are provided by the following method. While the publication [P3] only evaluates the achieved intensity profiles, ablation experiments will be discussed in Section 5.1. This analysis provides a direct comparison between ablation results for "single pulse" uniform beam shaping and averaging.

### Highlights

- Full control of amplitude and wave front to realize "single-shot" uniform beam shaping
- Applicability for high-energy lasers: no excessive fluences on the beam shaping planes
- High efficiency and feasibility

Research Article | Vol. 29, No. 12 / 7 June 2021 / Optics Express 17997
Optics EXPRESS

# Uniform and efficient beam shaping for high-energy lasers

LISA ACKERMANN,[1,2,*] CLEMENS ROIDER,[1] AND MICHAEL SCHMIDT[1,2]

[1] Institute of Photonic Technologies, Friedrich-Alexander-Universität Erlangen-Nürnberg, Konrad-Zuse-Str. 3/5, 91052 Erlangen, Germany
[2] Erlangen Graduate School in Advanced Optical Technologies (SAOT), Friedrich-Alexander-Universität Erlangen-Nürnberg, Paul-Gordan-Str. 6, 90152 Erlangen, Germany
[*] lisa.ackermann@lpt.uni-erlangen.de

**Abstract:** Phase-only beam shaping with liquid crystal on silicon spatial light modulators (SLM) allows modulating the wavefront dynamically and generating arbitrary intensity patterns with high efficiency. Since this method cannot take control of all degrees of freedom, a speckle pattern appears and drastically impairs the outcome. There are several methods to overcome this issue including algorithms which directly control phase and amplitude, but they suffer from low efficiency. Methods using two SLMs yield excellent results but they are usually limited in the applicable energy due to damage to the SLM's backplane. We present a method which makes use of two SLMs and simultaneously gives way for high-energy laser applications. The algorithm and setup are designed to keep the fluence on the SLMs low by distributing the light over a large area. This provides stability against misalignment and facilitates experimental feasibility while keeping high efficiency.



## 1. Introduction

Various research topics and optical applications are based on the use of structured light. Tailoring the spatial or temporal appearance of light allows for controlling its interaction, encoding information or refining existing methods in fields of optical metrology, biomedicine, laser material processing, and many other applications [1]. The term structured light addresses different ways of tailoring light. As one particular application, dynamic beam shaping is intended to manipulate the intensity profile. This not only requires the control of the beam's amplitude but also of its wave front in a joint plane. Several devices enable dynamic light shaping but they are usually limited to a single characteristic which they may control. One option is to directly shape the amplitude. However, this method implies high losses since a considerable portion of the light field cannot be used. Beam shaping is thus often performed with a phase-only liquid crystal on silicon (LCoS) spatial light modulator (SLM) [2]. It dynamically shapes the wave front of the beam and thereby enables a highly efficient intensity modulation as the wave front determines the propagation of the light field and is inherently connected with the formation of the intensity pattern. It is not possible to shape both target intensity pattern and phase simultaneously, since at each pixel only one degree of freedom can be controlled with the SLM. Conventionally, the phase on the SLM is adjusted to control the intensity pattern in the target plane under the admission of an uncontrolled phase. This manifests itself in random phase jumps which cause phase vortices [3]. Those singularities lead to destructive interference whereas other locations exhibit constructive interference. The resulting speckle pattern overlays the target distribution with full contrast between completely extinguished and in other places enhanced signal.

To avoid these speckle, also the phase in the target plane has to be controlled, ideally chosen planar. As an analytical correspondence exists between the two planes, the needed amplitude and phase in the SLM plane can be unambiguously calculated. Usually they are set in a Fourier

#426953 https://doi.org/10.1364/OE.426953
Journal © 2021 Received 6 Apr 2021; revised 18 May 2021; accepted 18 May 2021; published 25 May 2021

Research Article Vol. 29, No. 12 / 7 June 2021 / Optics Express 17998
Optics EXPRESS

relation with a lens in-between and the mathematical description is the Fourier transform (FT). In this case the plane of the SLM corresponds to the Fourier space of the target signal. We can assign the low spatial frequencies to the central area and higher frequencies correspond to the outer parts and the amplitude acts as a weighting of the spatial frequencies. Usually, the lower spatial frequencies have a substantially higher contribution to the target distribution but nonetheless a Gaussian illumination does not improve the weighting over a homogenous illumination. If, regardless of the non-corresponding frequency partitions, all light should contribute to the target distribution, those not correctly weighted spatial frequencies disturb the wave front, causing the aforementioned phase vortices and speckle.

By using an additional phase grating on a single phase-only SLM, corresponding to an off-axis configuration, it is possible to control the amplitude and phase in the target plane. The additional grating shifts the whole field laterally and the local modulation depth of the grating influences the diffraction efficiency and therefore the weighting of the amplitude of the spatial frequencies. The shifted partition consists of the required amplitude and appropriate phase yielding a speckle-free intensity profile [4–9]. A significant drawback of this method is that the efficiency decreases as the correct amplitude weighting can only be achieved by sending light into the non-diffracted zero order. The basis for the calculation of phase masks, which make full use of the available light, is the Gerchberg-Saxton (GS) algorithm [10] or modified adaptations. The algorithm itself is a special case of the hybrid input-output (HIO) algorithm [11] which retrieves the 'unknown' phase from intensity information by error reduction. This method can be used to find a proper phase distribution for the desired intensity profile. The algorithm is constructed to confine the intensity pattern in the target plane and to make full use of the available illumination by using a diffuser-based phase mask. The appropriate phase mask will, as mentioned, result in the target image with overlaid speckle noise. To reduce speckle it is possible to combine the analytically calculated wave front with an additional diffraction mask, similar to a grating with adapted modulation depth. The additional diffraction mask can be adjusted to diffract the surplus partition of the amplitude to an area outside the target signal. In this way, the SLM only uses the analytically corresponding part of the light field and diffracts the rest away. The intensity profile is speckle-free but only a small percentage of the light can be used. Many groups proposed this method with error reduction algorithms on basis of the GS algorithm [12–17].

Another approach is to add a quadratic phase term [18–21]. This phase term acts like a lens and changes the initial relation between the two planes. In the following, we will abbreviate this method as $GS_\Phi$. The focal length of the lens can be adjusted such that the resulting beam size resembles the dimensions of the beam-shaped target distribution. This reduces speckle noise since less light has to be redirected. In the case of a diffuser-based GS algorithm, the phase mask works like a scattering pattern where each spatial frequency contributes equally to each point in the target distribution. With the additionally applied quadratic phase, a main part of the amplitude corresponds to the analytical solution. Only the remaining partition of the amplitude needs to be scattered over the target area. The calculated phase mask is sensitive to changing experimental conditions like the initial beam shape or a lateral shift. A similar result can be achieved by setting the target distribution out of focus which additionally defocuses non-diffracted light residuals due to imperfect devices. Since the quadratic phase condition only facilitates the reduction of phase vortices, some methods completely restrict the phase and diffract the non-corresponding light partition away, which again reduces the efficiency.

Another way is to compose the target distribution out of small single spots [22]. The SLM works as a multiplexer but the method starts to suffer from speckle as soon as the individual spots come too close and interfere with each other. The pulse front tilt of an ultra-short pulse can be used to overcome the unwanted interference in one direction [23]. Two differently polarized beams which are individually multiplexed by one SLM each also reduce speckle noise [24].

Research Article | Vol. 29, No. 12 / 7 June 2021 / Optics Express 17999
Optics EXPRESS

Bartelt proposed in 1984 the use of two phase shaping elements for simultaneously taking full control of the wave front and the intensity distribution while keeping the efficiency high [25,26]. Some subsequent publications are based on this idea, nowadays dynamically applying the phase masks on two SLMs [27–32]. The most popular method is to use the first SLM as an amplitude shaper on the plane of the second SLM. The second SLM's task is to readjust the proper wave front [29,30].

This is done via compensating for the current phase distribution given by the iterative algorithm and adding the analytically calculated phase. This attempt is usually based on a Fourier relation between the two SLMs. The first SLM thus shapes the FT as intensity pattern on the second SLM. At that plane, only the phase needs to be corrected such that a speckle-free distribution is derived in the target plane. This method works well as long as the beam's energy is low as the FT is usually tightly centered such that the beam is close to being focused on the SLM. The larger the image is in the target plane, the smaller will be its FT. This decreases the covered area on the SLM and thus increases the fluence which can easily exceed the damage threshold.

In this work, we present an algorithm which controls phase and amplitude with two SLMs. This enables high-quality hologram reconstruction while keeping the efficiency high. The emphasis lies on avoiding high fluences on the SLM. The proposed algorithm enables speckle-free beam shaping for high-energy laser systems by intentionally displacing the SLM planes from the Fourier planes. This constraint additionally gives the chance to work in a relation that resembles the conditions of the quadratic phase approach. The algorithm adapts for changing target sizes to ensure full illumination of both SLMs for all kinds of target structures and thereby reduces the peak fluence. This is especially relevant since high-energy lasers are usually single mode and thus have a high degree of spatial coherence which would cause a strong speckle pattern.

In Section 2, we present the calculation of the required phase masks. Experimental and simulated results are shown thereafter in Section 3. We evaluate the results, show the maximum fluence on the second SLM and compare the reconstructed holograms with results derived from conventional methods. Besides that, we address experimental feasibility and the general stability of the proposed method. Finally, we evaluate lateral and axial shifts of the target distribution.

## 2. Methods

The full control of amplitude and phase is made possible by the use of two phase-only SLMs. The first SLM acts as an amplitude shaper on the plane of the second SLM where the second SLM can apply the proper phase to shape the target distribution. The distance between the two SLMs is chosen in such a way that both SLMs are fully illuminated by the laser beam when no beam modulation is performed. Figure 1 shows a scheme of the relative distances. The configuration resembles a 4-f setup with the first SLM as starting point and a lens in its focal distance. The second lens is replaced by the second SLM which can act as a lens with focal length $f_2$ by adding the proper wave front. This configuration also defocuses the $0^{\text{th}}$ order of diffraction of the first SLM thereby avoiding possible damage by non-diffracted light on the second SLM. Another lens is placed after the second SLM and forms the final image.

For the calculation of the phase masks first the target distribution $E^{\text{target}}$ needs to be set. The amplitude is given by the desired target amplitude $\mathcal{E}^{\text{target}} = |E^{\text{target}}|$. The phase $\Phi^{\text{target}} = \arg(E^{\text{target}})$ is assumed as a spherical wave front since the target plane is set out of focus. In principle, the fluence on the second SLM varies with the dimensions of the final target size. To keep the illuminated area almost independent of the final output, the focal length of the second SLM's lens term is adapted to control the magnification. The matrix method [33] gives a relation between the size of the target object $2s_{\text{target}}$ and its size on the plane of the second SLM $2s_{\text{SLM}_2}$. This relation is a function of the focal length $f_2$ which gives the opportunity to adapt $f_2$ to keep $s_{\text{SLM}_2}$

Research Article | Vol. 29, No. 12 / 7 June 2021 / Optics Express 18000
Optics EXPRESS

constant independently of the size of the target image (see Supplement 1, Section 1):

$$f_2 = \frac{d_1^2 d_2 - d_1 f_3^2}{2 d_1 d_2 - f_3^2 + d_1 f_3 \frac{s_{\text{target}}}{s_{\text{SLM}_2}}}. \tag{1}$$

$d_1$ and $d_2$ are the distances from the focal planes to $\text{SLM}_2$ and the target plane, respectively (see Fig. 1), and $f_3$ is the focal length of the used focusing lens. The calculated focal length $f_2$ is encoded in the target wave front $\Phi^{\text{target}}$ and the target distribution can be defined as

$$E^{\text{target}} = \mathcal{E}^{\text{target}} \cdot e^{\imath \Phi^{\text{target}}}. \tag{2}$$

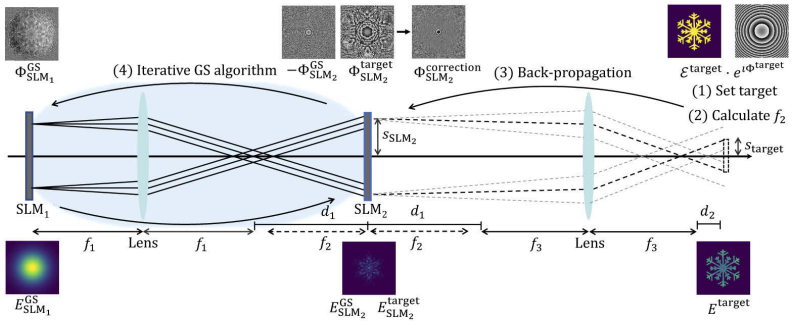


**Fig. 1.** Illustration of the setup, algorithm, and the corresponding complex light field: To achieve a certain image, the target pattern (1) needs to be set. The calculated focal length $f_2$ (2) determines the corresponding spherical phase and the signal can be back-propagated (3) to the plane of the second SLM. The required phase mask on $\text{SLM}_1$ is iteratively calculated with the GS algorithm (4).

Depending on the application, the target plane can be chosen in front of or behind the focus position of the focusing lens. The physical implications of the choice are discussed in detail in Section 3.4.

Then, the analytically correct phase and amplitude distribution on the plane of the second SLM needs to be determined. An analytical distribution $E^{\text{target}}_{\text{SLM}_2}$ is calculated by propagating the field backwards. The beam propagation calculations were performed with the method of angular spectrum of plane waves [34]. The Fourier Transform $\mathcal{F}$ decodes the target signal $E$ into a spectrum of its individual spatial frequencies $\tilde{E}$ and backwards with the inverse operation $\mathcal{F}^{-1}$. A propagation in free space adds an additional phase term $\Phi$ in Fourier space which can be written as

$$e^{\imath \Phi^{\text{prop.}}_{\Delta z}} = e^{\imath \Delta z \cdot \Delta k_z} = e^{\imath \Delta z \cdot \sqrt{k^2 - k_\perp^2}}, \tag{3}$$

where $\Delta z$ is the relative propagation distance in z-direction, $k = \frac{2\pi}{\lambda}$ is the wave vector, $k_\perp$ its perpendicular projection and $\lambda$ the wavelength. A lens introduces a spherical wave front according to

$$e^{\imath \Phi^{\text{lens}}_f} = e^{\imath \frac{k}{2f}(x^2 + y^2)}, \tag{4}$$

where $f$ is the focal length of the corresponding lens and $x$ and $y$ are the coordinates in position space. With these equations, the desired field on $\text{SLM}_2$ can be written as:

$$E^{\text{target}}_{\text{SLM}_2} = \mathcal{F}^{-1}\left\{\mathcal{F}\left[\mathcal{F}^{-1}\left(\tilde{E}^{\text{target}} \cdot e^{-\imath \Phi^{\text{prop.}}_{\Delta z = f_3 + d_2}}\right) \cdot e^{\imath \Phi^{\text{lens}}_{f = f_3}}\right] \cdot e^{-\imath \Phi^{\text{prop.}}_{\Delta z = d_1 + f_3}}\right\}, \tag{5}$$

Research Article | Vol. 29, No. 12 / 7 June 2021 / Optics Express 18001
Optics EXPRESS

where $\tilde{E}^{\text{target}}$ is the FT of the target distribution. The resulting amplitude $\mathcal{E}^{\text{target}}_{\text{SLM}_2} = |E^{\text{target}}_{\text{SLM}_2}|$ needs to be achieved with beam shaping since this amplitude and the corresponding phase will then give the desired target image.

The GS algorithm gives the opportunity to shape the amplitude on the plane of the second SLM. The iterative algorithm propagates between the planes of the two SLMs. The forward propagation from the first SLM plane to the second one is

$$E^{\text{GS}}_{\text{SLM}_2} = \mathcal{F}^{-1}\left\{\mathcal{F}\left[\mathcal{F}^{-1}\left(\tilde{E}^{\text{GS}}_{\text{SLM}_1} \cdot e^{\imath\Phi^{\text{prop.}}_{\Delta z=f_1}}\right) \cdot e^{-\imath\Phi^{\text{lens}}_{f=f_1}}\right] \cdot e^{\imath\Phi^{\text{prop.}}_{\Delta z=f_1+d_1}}\right\} \tag{6}$$

and the corresponding back-propagation reads

$$E^{\text{GS}}_{\text{SLM}_1} = \mathcal{F}^{-1}\left\{\mathcal{F}\left[\mathcal{F}^{-1}\left(\tilde{E}^{\text{GS}}_{\text{SLM}_2} \cdot e^{-\imath\Phi^{\text{prop.}}_{\Delta z=f_1+d_1}}\right) \cdot e^{\imath\Phi^{\text{lens}}_{f=f_1}}\right] \cdot e^{-\imath\Phi^{\text{prop.}}_{\Delta z=f_1}}\right\}, \tag{7}$$

where $f_1$ is the focal length of the lens as it is depicted in Fig. 1. The result of the iterative propagation algorithm is the required phase front $\Phi^{\text{GS}}_{\text{SLM}_1}$ on the plane of the first SLM to obtain the calculated intensity pattern on the plane of the second SLM.

$$\Phi^{\text{GS}}_{\text{SLM}_1} = \arg\left(E^{\text{GS}}_{\text{SLM}_1}\right) \tag{8}$$

The initial amplitude on the first SLM can be any beam profile, e.g., Gaussian or top-hat, but it needs to be properly defined in the calculation since the algorithm is sensitive to it. The resulting phase mask does not work as a typical diffraction mask. There are broad areas with smooth phase transitions which, as an additional benefit, reduce the effects of cross-talk in the LCoS SLM [35,36]. An exemplary mask is shown in the upper left corner of Fig. 1. Note that the intended large illumination area on the second SLM intrinsically leads to something resembling a lens term on the first SLM. Since the beam-shaped profile fills the area on the second SLM, the fluence on the second SLM is of a comparable strength to the initial beam on the first SLM (compare Section 3).

The phase of the beam-shaped distribution on the second SLM's plane is indeed uncontrolled. This can be compensated with the second SLM. The phase for the target distribution is well known from the back-propagation in Eqs. (5) and (6) gives the resulting phase after beam shaping. The SLM thus needs to compensate for the uncontrolled phase and reset it with the analytical solution which already contains the corresponding lens term. The correction phase mask is thus given by:

$$\Phi^{\text{correction}}_{\text{SLM}_2} = \arg\left(e^{\imath\Phi^{\text{target}}_{\text{SLM}_2}} \cdot e^{-\imath\Phi^{\text{GS}}_{\text{SLM}_2}}\right) = \text{mod}2\pi\left[\Phi^{\text{target}}_{\text{SLM}_2} - \Phi^{\text{GS}}_{\text{SLM}_2}\right]. \tag{9}$$

Therefore, by displaying $\Phi^{\text{GS}}_{\text{SLM}_1}$ on $\text{SLM}_1$ and $\Phi^{\text{correction}}_{\text{SLM}_2}$ on $\text{SLM}_2$ the target image with reduced speckle is formed.

## 3. Results

We used a 5 mW cw laser with a wavelength of 1064 nm to experimentally verify our method. The LCoS SLM is the model P1920-1064 from Meadowlark Optics with an aspect ratio of 16:9 such that it can easily be separated in two virtual halves with $960 \times 960$ px each and only one SLM is required. This reduces costs and calibration effort as the same system characteristics are present. The look-up table for 1064 nm is evaluated according to [37]. The experimental setup is shown in Fig. 2. A disadvantage of using just a single SLM twice is an increased angle of incidence on the SLM due to the size of the optics. The angles of incidence (measured to the normal) are 12 ° on the first half and 1.75 ° on the second half. It is preferable to choose a small angle of incidence on the second plane since the tilt on the applied lens term disturbs the

Research Article | Vol. 29, No. 12 / 7 June 2021 / Optics Express 18002
Optics EXPRESS

result. Two well-corrected lenses with a focal length of $f_{1/3} = 200\,\text{mm}$ (Nikon 200 mm tube lens) are used to minimize errors on the wave front. The resulting intensity distribution is directly recorded with a 12 bit monochrome CMOS camera (IDS UI-3080).

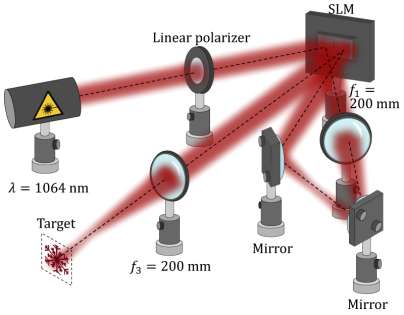


**Fig. 2.** Experimental setup (dimensions not to scale): The light is sent through a linear polarizer before it impinges on the first half of the SLM. Here, a phase term is applied to shape the intensity pattern on the second plane. Two mirrors give the opportunity to direct the light precisely to the second half and adapt for occurring rotations. Finally, the target image is recorded with a camera.

### 3.1. Experiment and simulation

Figure 3 shows experimental and simulated results of our proposed method. Starting with a Gaussian beam as input (lower left corner), the algorithm calculates phase masks to approach the ideal output shown in the upper left corner. In contrast to the usually confined target signal, the theoretically back-propagated distribution on the plane of the second SLM consists of a broad range of frequencies and is not band-limited [38]. The SLM is of finite size and cannot resolve the full analytical solution. Even an ideally reconstructed amplitude distribution (see Fig. 3 bottom) on the area of the second SLM cannot reproduce perfectly sharp edges and a homogeneous surface. The theoretical outcome right next to the ideal structure in Fig. 3 is not purely homogeneous but possesses values above and below its mean value, known as the Gibb's phenomenon [39]. In practice, the amplitude distribution on the second SLM is only approximated by the GS algorithm. The simulated and experimentally measured intensity profiles can be compared in the bottom row of Fig. 3. A slight speckle pattern overlays the distribution. The appropriate phase correction forms the desired target signal (top row). Wave front distortion and imperfect alignment mostly contribute to differences between experiment and simulation. This distorts the mapping between the shaped amplitude and the applied phase correction. The consequences are slight inhomogeneities as well as a reduction in efficiency. How the individual facets of experimental deviations affect the target profile will be discussed in depth in Section 3.3.

The efficiency is defined as the ratio of the signal within the target area $I_{\text{target}}$ divided by the total signal $I_{\text{total}}$ times the ratio between output $P_{\text{output}}$ and input $P_{\text{input}}$ power corresponding to losses in the setup: $\eta_{\text{total}} = \frac{\sum I_{\text{signal}}}{\sum I_{\text{total}}} \cdot \frac{P_{\text{output}}}{P_{\text{input}}}$. In our case, the SLM only reflects around 85% of the light and the two lenses show similar losses. These losses can be avoided with proper IR coating and are not intrinsic to our method. We thus additionally define the relative efficiency $\eta$:

$$\eta = \frac{\sum I_{\text{signal}}}{\sum I_{\text{total}}} \cdot \frac{P_{\text{output}}}{P_{\text{reference}}}, \tag{10}$$

Research Article Vol. 29, No. 12 / 7 June 2021 / Optics Express 18003
Optics EXPRESS

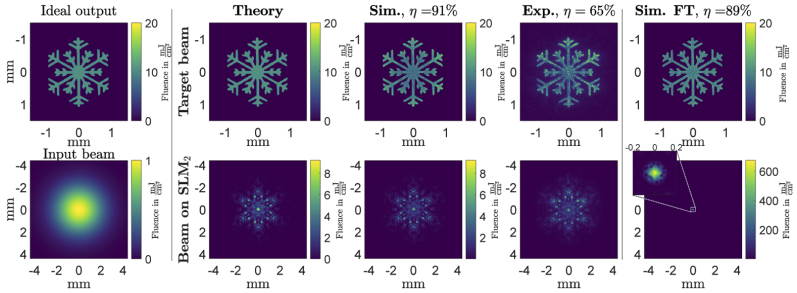


**Fig. 3.** From left to right: Ideal output and Gaussian input beam ($\omega_0 = 3.1$ mm). Target distribution which results from the ideal but bandwidth-limited amplitude distribution. Simulated outcome and experimentally measured data. The right side shows simulated data for distances in direct Fourier relation. In the simulation, the input beam's maximum fluence is assumed to be 1 $\frac{\text{mJ}}{\text{cm}^2}$. Our used SLM has a destruction threshold of 15 $\frac{\text{GW}}{\text{cm}^2}$ which would restrict the pulse energy to 259 µJ in case of our proposed method in contrast to a maximum of 3.5 µJ for a direct Fourier relation (assuming a pulse duration of 1 ps).

where $P_{\text{reference}}$ is the total measured power in case that the SLM is used as a mirror with no applied phase mask. This reflects the efficiency of the algorithm without the losses of the optical components. The power measurement is performed with the power meter PM160 (Thorlabs). The snowflake in Fig. 3 yields $\eta = 65\%$ efficiency (26% total efficiency) in the experiment and $\eta = 91\%$ in the simulation. The simulation does neither consider losses of optical components nor limitations of the SLM (e.g., cross-talk) but it measures the ratio of the diffracted light in the target area versus the total amount of light. The alignment was performed without an external correction loop. The results show that the method is stable and gives good results for normal experimental conditions. For comparison, simulated results for a configuration in direct Fourier relation are shown on the right side of Fig. 3. For the chosen system parameters, the snowflake occupies around 10% of the linear field of view, corresponding to 1% of the total area. The outcome is of the same quality and roughly same efficiency as our proposed method. The major difference lies in the shaped amplitude which impinges on the SLM. In case of the snowflake, the maximum fluence is around two orders of magnitude higher for a configuration in direct Fourier relation even though the snowflake is relatively small with respect to the shapeable field of view. Figure 4 shows the maximum fluence on the second SLM divided by the maximum fluence on the first SLM for both methods together with the experimental results of the corresponding target distributions. In case of our proposed method, individual structures give a variable peak fluence but they usually do not exceed the input beam's peak fluence by more than an order of magnitude. Due to the variable lens term, a change in the structure size does not change the maximum fluence as it is exemplarily demonstrated for different rectangles. This changes in a direct Fourier relation, where the fluence on both SLMs differs by several magnitudes. The factor drastically increases if the target structure is enlarged.

Ideally, the peak fluence on the second SLM is in the same order of magnitude as on the first one. Our method gives solutions which lie in a range within the next higher magnitude. The outcome is still bound to an analytical solution within the beam propagation and may exhibit local peaks. Even with that limitation, the method still enables using significantly higher pulse energies for ultra-short-pulsed laser applications.

Research Article Vol. 29, No. 12 / 7 June 2021 / Optics Express 18004
Optics EXPRESS

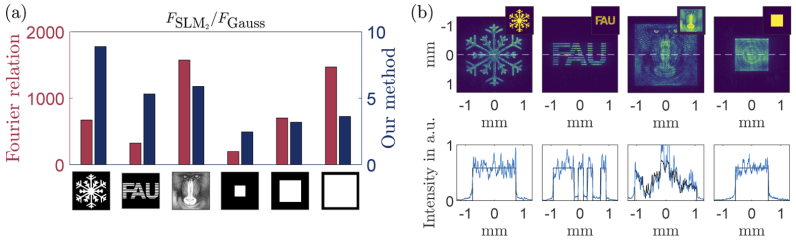


**Fig. 4.** (a) The calculated fluence on the second SLM is set in relation to the input Gaussian beam as it is defined in Fig. 3. Left axis: ratio resulting from a direct Fourier relation; right axis: ratio for our proposed method. Note that the exemplary structures maximally occupy 1% of the shapeable area for a direct Fourier relation. (b) Experimental results for exemplary images with target distribution. A cross section underneath compares the ideal (black) and experimental result (blue).

### 3.2. Evaluation of beam uniformity and flatness factor

Figure 5 shows typical results of beam shaping where only the amplitude is constrained in the target plane. While our method works on-axis as the 0$^{th}$ order is defocused, in a single SLM implementation an off-axis geometry is needed to avoid the 0$^{th}$ order. The quality of the measured structures can be evaluated with the beam uniformity $U$ and the flatness factor $FF$ [40]:

$$U = \frac{\sigma}{\mu} = \frac{\sqrt{\langle I^2 \rangle - \langle I \rangle^2}}{\langle I \rangle}, \tag{11}$$

$$FF = \frac{\mu}{I_{max}} = \frac{\langle I \rangle}{\max(I)}, \tag{12}$$

where $\sigma$ is the standard deviation and $\mu$ is the arithmetic mean, which is defined as the expectation value of a variable $x$ with $\langle x \rangle = \mu$. We applied the two formulas on recorded rectangles which can be found in Fig. S3 (Supplement 1) and in Fig. 4 for our proposed method ($d_2 = 50$ mm). In case of an on-axis configuration, we intentionally left out the central area for the calculation of the beam uniformity and flatness factor. Nevertheless, the 0$^{th}$ order of diffraction is a part of the light field and cannot be neglected for the calculation of the efficiency. Since it is much brighter than the rest of the light, it is saturated in the recordings. For both, an on- and off-axis configuration, the value of efficiency is a bit overestimated even though the impact is low due to the saturation. In case of our proposed method the 0$^{th}$ order of diffraction is strongly defocussed since it does either not see the applied lens term $f_2$ or relatively homogeneously illuminates the second SLM. Since it does not strongly affect the outcome and can not be separated easily, this efficiency value is also slightly overestimated.

However, we measured those profiles in the same setup with an unnecessarily shallow angle of incidence (12 ° which is required in case of a second incidence). Under optimal conditions, the efficiency could be slightly higher. Even though those efficiency values are not perfectly exact, we show them together with the beam uniformity and flatness factor in Table 1.

It shows that the efficiency of our proposed method is not too far from conventionally derived values. Note that the stronger reduction in total efficiency of our method is due to the second pass on the SLM and the additional lens. Besides that, the beam uniformity and flatness factor can be improved significantly.

Research Article | Vol. 29, No. 12 / 7 June 2021 / Optics Express 18005
Optics EXPRESS

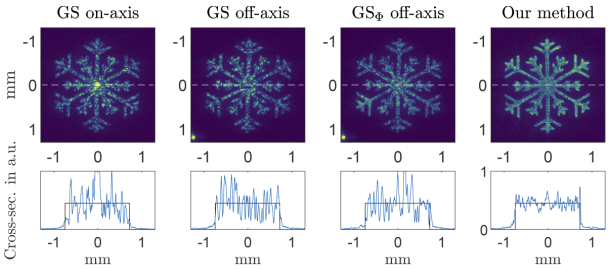


**Fig. 5.** From left to right: Experimental target distribution and cross section for our method, GS algorithm, GS algorithm off-axis, and GS algorithm off-axis with quadratic phase condition. Note the saturated spot at the center (off-axis: in the lower left corner) due to the $0^{\text{th}}$ order.

**Table 1. Experimental Evaluation of different Methods**

| Method | $\eta$ ($\eta_{\text{total}}$) | $U$ | $FF$ |
|---|---|---|---|
| Our method | 73% (29%) | 25% | 54% |
| GS on-axis | 81% (52%) | 46% | 30% |
| GS off-axis | 69% (44%) | 47% | 37% |
| GS$_\Phi$ off-axis | 70% (45%) | 42% | 39% |

### 3.3. Evaluation of stability

Our method works well for all kinds of conditions like sharp contours, thin lines, plain areas or different levels of brightness as it is exemplary shown in Fig. 4. Slight concentric waves overlay the structure. On plain surfaces, like the rectangle, they become visible. We attribute those structures to cross-talk (especially from the concentric rings of the lens term on the second phase mask) and interference with the $0^{\text{th}}$ order of diffraction. LCoS SLMs exhibit cross-talk between adjacent pixels and thus slight variations in diffraction efficiency occur. The cross-talk becomes more dominant in the outer areas of both phase masks since rapid phase jumps occur more likely in those regions. We found that it is helpful to reduce the diameter of the Gaussian input beam in the calculation to directly compensate for a reduction in diffraction efficiency. In that way, the algorithm directly designs the phase masks for less light in the regions with reduced diffraction efficiency. In general, the focal length $f_2$ on the second SLM has to be chosen large enough to avoid degrading effects by the cross-talk. For an ideal SLM the Nyquist theorem describes the limits on the maximal phase change above which unwanted artefacts will appear in the final image caused by undersampling (aliasing) on the SLM [41]. For a given pixel size this especially limits the shortest applicable focal length of the lens term on the second SLM [42]. In the experimental implementation it is however the cross-talk which drastically impairs the result before those limits are reached. Besides those effects, various misalignment can be addressed in the simulation which helps to model the stability of the experimental setup. The beam-shaped amplitude has to match the correction phase mask over its whole extension. Lateral misalignment shifts both patterns against each other. The simulation in Fig. 6 shows the impact on our method and in comparison on a setup in direct Fourier relation. Since the amplitude in case of a direct Fourier relation is rather centered around a few pixels, a shift reduces the efficiency more significantly. Another kind of misalignment is an axial mismatch between the calculated propagation path and the real distance to the plane of the SLM where the shaped amplitude combines with the correction phase front. For both configurations the impact on efficiency is moderate. A mismatch

Research Article | Vol. 29, No. 12 / 7 June 2021 / Optics Express 18006
Optics EXPRESS

in propagation distance slightly changes the size of the generated amplitude pattern on the SLM and distorts the beam profile. Especially inhomogeneities occur because the strength of the amplitude does not correspond to the calculation.

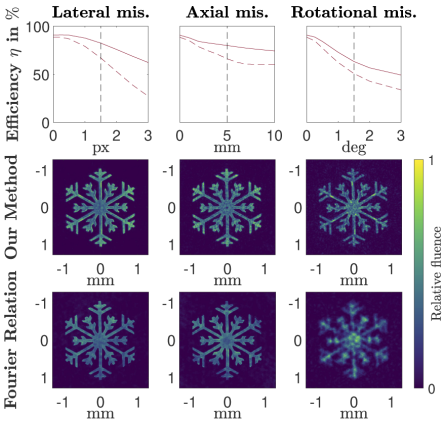


**Fig. 6.** Various misalignment and its impact on efficiency for our proposed method (solid line) and direct Fourier relation (dashed line). From left to right: lateral misalignment, exemplarily shown for $\Delta x = 1.5\,\mathrm{px}$. Axial misalignment for a mismatch of 5 mm, and rotational misalignment at 1.5 °. The fluence is normalized to the perfect and undistorted solution for both configurations.

Rotational misalignment around the $z$-axis (axis of propagation) also distorts the mapping. It may occur as a side effect during beam shaping or because of a lateral shift between two mirrors in the setup. Rotational misalignment can be corrected in the setup by adapting the tilt of two mirrors against each other. In all cases of simulated misalignment, one can observe that our method starts to suffer from speckle whereas the method in direct Fourier relation rather decreases in efficiency (see Supplement 1, Section 4 for simulation results on plain rectangles with an additional evaluation of beam uniformity $U$ and flatness factor $FF$). The major drawback is that there has to be an almost perfect mapping over the whole area of the SLM and unexpected deviations on the wave front such as aberrations may distort this process. We obtained good results by using well-corrected lenses (Nikon tube lens) without having the need to include information about aberrations in the algorithm. The two different angles of incidence inherently cause a slight compression or extension of the shaped field in one direction. We compensated this in the calculation by modelling a target distribution which is stretched/compressed by this factor. With those adaptations, we acquired quite good results without too much alignment effort. The exact alignment procedure is explained in Section 2 of Supplement 1.

### 3.4. Evaluation of lateral and axial shifts

The generated pattern can be shifted laterally by applying an additional grating on the second SLM. The maximum angle of deflection is thereby determined by the pixel size of the SLM. Experimental results for a laterally shifted pattern with different grating periods are shown in Fig. 7. For small shifts corresponding to a large period of the grating the homogeneity and diffraction efficiency are preserved. As expected, the efficiency decreases for very short periods due to worse sampling. For a period of 3 px we attribute the decrease in image quality to additional cross-talk effects. If different target patters shall be multiplexed simultaneously, the shift has to

Research Article | Vol. 29, No. 12 / 7 June 2021 / Optics Express 18007
Optics EXPRESS

be implemented beforehand in the target distribution. This automatically decreases the maximum sampling size, illumination area and increases the cross-talk since the patterns are shifted to the borders at the second SLM where rapid phase jumps appear more likely. We observed a reduction in homogeneity which is exemplarily shown on the right side in Fig. 7. Besides a lateral shift, our methods allows shifting the target plane continuously along the axial direction by adapting the defocus $d_2$. This has two consequences on the setup parameters. The focal length of the lens term on the second SLM changes to maintain the same illumination conditions, optionally generating an intermediate focus. Simultaneously, this changes the effective numerical aperture (NA) of the system. Three recorded resolution patterns in Fig. 8 with a defocus of +50 mm, 0 mm and −50 mm show this effect. The target distribution shows sharper edges at $d_2 = 50$ mm. Even the contour of the smallest structure can be approximated in the line plot whereas it is completely unresolvable for the lower NA-configuration at $d_2 = -50$ mm. Slightly higher efficiencies can be achieved if the focal length $f_2$ increases since this reduces the number of phase jumps and thus cross-talk (78% instead of 73% for the rectangle which is evaluated in Table 1). The available volume in which the pattern can be positioned is limited by the sampling on the second SLM [43,44]. Note that our method does not change the axial confinement and provides the same conditions as achieved with conventional methods.

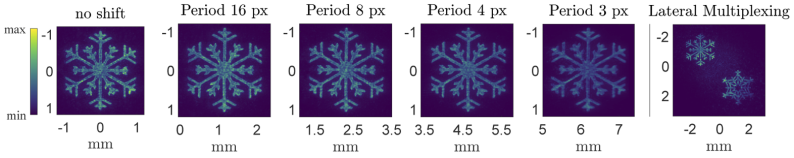


**Fig. 7.** A lateral shift of the image can be performed with an additional grating on the second SLM. All images are recorded with the same integration time. The quality and signal strength decrease visually with increasing cross-talk and worse sampling for the lowest period of 3 px which is almost at the lower limit of a binary grating (2 pixels). The right image shows an exemplary result for two different laterally shifted structures.

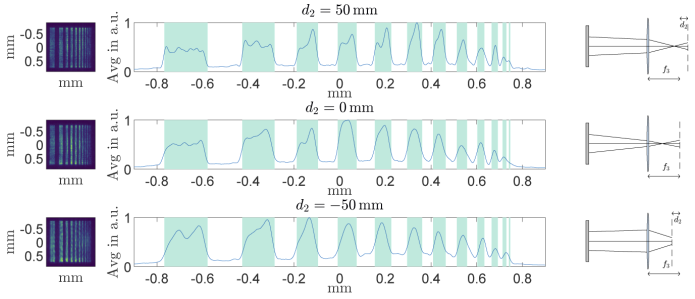


**Fig. 8.** The defocus $d_2$ can be chosen to shift the target distribution along the axis of propagation.The three images show possible configurations. The line plots underneath give a hint of resolvable scales since the applied lens term affects the NA. It is derived as the average value within the resolution pattern and the intended signal area is marked within the plot. Note that even in the initial focus of the lens $f_3$ the $0^{\text{th}}$ order of diffraction is completely defocussed.

Research Article | Vol. 29, No. 12 / 7 June 2021 / Optics Express 18008
Optics EXPRESS

Nonetheless, we see the main factor of choosing a positive or negative defocus $d_2$ in whether an intermediate focus is allowable. When using high-energy ultra-short-pulsed lasers, non-linear interaction in the focus might lead to distortions in the wave front or in the worst case also to additional energy loss if a plasma is ignited. When transparent media are illuminated, the defocus should be chosen in order for the focus to be outside the material to mitigate risk of undesired damage.

## 4. Conclusion

There are many ways to tailor light fields. Usually they offer a compromise between good quality, high efficiency, experimental feasibility and laser power restrictions. The use of two SLMs enables simultaneous phase and amplitude shaping to acquire high quality results. Our method is based on that idea and is thus capable of diminishing speckle noise while keeping high efficiency. By bringing the two SLMs intentionally out of a direct Fourier relation, the method is not restricted to low-energy laser systems. By adapting the phase correction hologram, we make sure that the illuminated area on the SLM stays large independent of the target distributions. The shaped amplitude on the SLM is in a comparable order of magnitude to the initial distribution. Additionally, the $0^{\text{th}}$ order of diffraction is set out of focus on the SLM to negate a local peak of high power and equally in the final target plane to keep high signal quality. Therefore, our method is suited for high-energy ultra-short-pulsed lasers. The experimental setup can be aligned without requiring a subsequent error reduction loop and is less sensitive in terms of efficiency compared to a direct Fourier relation. The experimentally derived results are not completely free from speckle ($U = 25\%$) but the quality is quite good while keeping high efficiency ($\eta = 73\%$) along with experimental feasibility.

**Funding.** Erlangen Graduate School of Advanced Optical Technologies; Deutsche Forschungsgemeinschaft (SCHM2115/67-1).

**Acknowledgments.** The authors gratefully acknowledge funding of the Erlangen Graduate School in Advanced Optical Technologies (SAOT) by the Bavarian State Ministry for Science and Art.

**Disclosures.** The authors declare that there are no conflicts of interest related to this article.

**Data availability.** Data underlying the results presented in this paper may be obtained from the authors upon reasonable request.

**Supplemental document.** See Supplement 1 for supporting content.

### References

1. H. Rubinsztein-Dunlop, A. Forbes, M. V. Berry, M. R. Dennis, D. L. Andrews, M. Mansuripur, C. Denz, C. Alpmann, P. Banzer, T. Bauer, E. Karimi, L. Marrucci, M. Padgett, M. Ritsch-Marte, N. M. Litchinitser, N. P. Bigelow, C. Rosales-Guzmán, A. Belmonte, J. P. Torres, T. W. Neely, M. Baker, R. Gordon, A. B. Stilgoe, J. Romero, A. G. White, R. Fickler, A. E. Willner, G. Xie, B. McMorran, and A. M. Weiner, "Roadmap on structured light," J. Opt. **19**(1), 013001 (2017).
2. P. Yeh and C. Gu, *Optics of Liquid Crystal Displays*, vol. 67 (John Wiley & Sons, 2009).
3. M. Guillon, B. C. Forget, A. J. Foust, V. De Sars, M. Ritsch-Marte, and V. Emiliani, "Vortex-free phase profiles for uniform patterning with computer-generated holography," Opt. Express **25**(11), 12640–12652 (2017).
4. J. P. Kirk and A. L. Jones, "Phase-only complex-valued spatial filter," J. Opt. Soc. Am. **61**(8), 1023–1028 (1971).
5. J. A. Davis, D. M. Cottrell, J. Campos, M. J. Yzuel, and I. Moreno, "Encoding amplitude information onto phase-only filters," Appl. Opt. **38**(23), 5004–5013 (1999).
6. J. Leach, M. R. Dennis, J. Courtial, and M. J. Padgett, "Vortex knots in light," New J. Phys. **7**, 55 (2005).
7. C. Maurer, A. Jesacher, S. Fürhapter, S. Bernet, and M. Ritsch-Marte, "Tailoring of arbitrary optical vector beams," New J. Phys. **9**(3), 78 (2007).
8. A. Hendriks, D. Naidoo, F. S. Roux, C. López-Mariscal, and A. Forbes, "The generation of flat-top beams by complex amplitude modulation with a phase-only spatial light modulator," in *Laser Beam Shaping XIII*, vol. 8490 A. Forbes and T. E. Lizotte, eds., International Society for Optics and Photonics (SPIE, 2012), pp. 55–62.
9. E. Bolduc, N. Bent, E. Santamato, E. Karimi, and R. W. Boyd, "Exact solution to simultaneous intensity and phase encryption with a single phase-only hologram," Opt. Lett. **38**(18), 3546–3549 (2013).
10. R. W. Gerchberg and W. O. Saxton, "A practical algorithm for the determination of phase from image and diffraction plane pictures," Optik **35**, 237–246 (1972).

Research Article | Vol. 29, No. 12 / 7 June 2021 / Optics Express 18009

Optics EXPRESS

11. J. R. Fienup, "Phase retrieval algorithms: a comparison," Appl. Opt. **21**(15), 2758–2769 (1982).
12. H. Akahori, "Spectrum leveling by an iterative algorithm with a dummy area for synthesizing the kinoform," Appl. Opt. **25**(5), 802–811 (1986).
13. F. Wyrowski, "Diffractive optical elements: iterative calculation of quantized, blazed phase structures," J. Opt. Soc. Am. A **7**(6), 961–969 (1990).
14. M. Pasienski and B. DeMarco, "A high-accuracy algorithm for designing arbitrary holographic atom traps," Opt. Express **16**(3), 2176–2190 (2008).
15. A. L. Gaunt and Z. Hadzibabic, "Robust digital holography for ultracold atom trapping," Sci. Rep. **2**(1), 721 (2012).
16. C. Chang, J. Xia, L. Yang, W. Lei, Z. Yang, and J. Chen, "Speckle-suppressed phase-only holographic three-dimensional display based on double-constraint Gerchberg-Saxton algorithm," Appl. Opt. **54**(23), 6994–7001 (2015).
17. L. Chen, H. Zhang, Z. He, X. Wang, L. Cao, and G. Jin, "Weighted constraint iterative algorithm for phase hologram generation," Appl. Sci. **10**(10), 3652 (2020).
18. T. Shimobaba and T. Ito, "Random phase-free computer-generated hologram," Opt. Express **23**(7), 9549–9554 (2015).
19. T. Shimobaba, T. Kakue, Y. Endo, R. Hirayama, D. Hiyama, S. Hasegawa, Y. Nagahama, M. Sano, M. Oikawa, T. Sugie, and T. Ito, "Random phase-free kinoform for large objects," Opt. Express **23**(13), 17269–17274 (2015).
20. H. Pang, J. Wang, M. Zhang, A. Cao, L. Shi, and Q. Deng, "Non-iterative phase-only fourier hologram generation with high image quality," Opt. Express **25**(13), 14323–14333 (2017).
21. D. Fischer and S. Sinzinger, "Evaluation of quadratic phase hologram calculation algorithms in the fourier regime," Appl. Opt. **59**(6), 1501–1506 (2020).
22. H. Caulfield, "Wavefront multiplexing by holography," Appl. Opt. **9**(5), 1218–1219 (1970).
23. B. Sun, P. S. Salter, C. Roider, A. Jesacher, J. Strauss, J. Heberle, M. Schmidt, and M. J. Booth, "Four-dimensional light shaping: manipulating ultrafast spatiotemporal foci in space and time," Light: Sci. Appl. **7**(1), 17117 (2018).
24. D. Mikhaylov, T. Kiedrowski, and A. F. Lasagni, "Beam shaping using two spatial light modulators for ultrashort pulse laser ablation of metals," in *Laser-based Micro-and Nanoprocessing XIII*, vol. 10906 (International Society for Optics and Photonics, 2019), p. 1090615.
25. H. Bartelt, "Computer-generated holographic component with optimum light efficiency," Appl. Opt. **23**(10), 1499–1502 (1984).
26. H. O. Bartelt, "Applications of the tandem component: an element with optimum light efficiency," Appl. Opt. **24**(22), 3811–3816 (1985).
27. D. A. Gregory, J. C. Kirsch, and E. C. Tam, "Full complex modulation using liquid-crystal televisions," Appl. Opt. **31**(2), 163–165 (1992).
28. M.-L. Hsieh, M.-L. Chen, and C.-J. Cheng, "Improvement of the complex modulated characteristic of cascaded liquid crystal spatial light modulators by using a novel amplitude compensated technique," Opt. Eng. **46**(7), 070501 (2007).
29. A. Jesacher, C. Maurer, A. Schwaighofer, S. Bernet, and M. Ritsch-Marte, "Near-perfect hologram reconstruction with a spatial light modulator," Opt. Express **16**(4), 2597–2603 (2008).
30. A. Jesacher, C. Maurer, A. Schwaighofer, S. Bernet, and M. Ritsch-Marte, "Full phase and amplitude control of holographic optical tweezers with high efficiency," Opt. Express **16**(7), 4479–4486 (2008).
31. A. Siemion, M. Sypek, J. Suszek, M. Makowski, A. Siemion, A. Kolodziejczyk, and Z. Jaroszewicz, "Diffuserless holographic projection working on twin spatial light modulators," Opt. Lett. **37**(24), 5064–5066 (2012).
32. L. Zhu and J. Wang, "Arbitrary manipulation of spatial amplitude and phase using phase-only spatial light modulators," Sci. Rep. **4**(1), 7441 (2015).
33. A. Gerrard and J. M. Burch, *Introduction to Matrix Methods in Optics* (Courier Corporation, 1994).
34. J. W. Goodman, *Introduction to Fourier Optics* (Roberts and Company Publishers, 2005).
35. E. Ronzitti, M. Guillon, V. de Sars, and V. Emiliani, "LCoS nematic SLM characterization and modeling for diffraction efficiency optimization, zero and ghost orders suppression," Opt. Express **20**(16), 17843–17855 (2012).
36. S. Moser, M. Ritsch-Marte, and G. Thalhammer, "Model-based compensation of pixel crosstalk in liquid crystal spatial light modulators," Opt. Express **27**(18), 25046–25063 (2019).
37. D. Engström, M. Persson, J. Bengtsson, and M. Goksör, "Calibration of spatial light modulators suffering from spatially varying phase response," Opt. Express **21**(13), 16086–16103 (2013).
38. F. Wyrowski and O. Bryngdahl, "Iterative fourier-transform algorithm applied to computer holography," J. Opt. Soc. Am. A **5**(7), 1058–1065 (1988).
39. K. Khare, *Fourier optics and computational imaging* (John Wiley & Sons, 2015).
40. ISO 13694:2018, "Optics and photonics – lasers and laser-related equipment – test methods for laser beam power (energy) density distribution," Standard, International Organization for Standardization, Geneva, CH (2018).
41. D. M. Cottrell, J. A. Davis, T. R. Hedman, and R. A. Lilly, "Multiple imaging phase-encoded optical elements written as programmable spatial light modulators," Appl. Opt. **29**(17), 2505–2509 (1990).
42. I. Moreno, D. M. Cottrell, J. A. Davis, M. M. Sánchez-López, and B. K. Gutierrez, "In-phase sub-nyquist lenslet arrays encoded onto spatial light modulators," J. Opt. Soc. Am. A **37**(9), 1417–1422 (2020).
43. P. Salter, Z. Iqbal, and M. Booth, "Analysis of the three-dimensional focal positioning capability of adaptive optic elements," Int. J. Optomechatronics **7**(1), 1–14 (2013).
44. A. Jesacher, C. Roider, and M. Ritsch-Marte, "Enhancing diffractive multi-plane microscopy using colored illumination," Opt. Express **21**(9), 11150–11161 (2013).

# 5 Ultrashort Pulse Laser Processing

Ultrashort pulse laser material ablation with shaped intensity profiles is a complex process that depends on many parameters. Both the beam profile and the chosen material exhibit distinctive properties whose interplay make process characterization a multidimensional problem.
The laser fluence determines the ablation regime and thus the process dynamics. Depending on the beam profile, local variations in fluence appear. Methods for uniform beam shaping provide a homogeneous intensity profile but this is not necessarily the case for the individual pulses. In case of averaging-based methods, every pulse exhibits a strong speckle pattern and only their accumulation will smooth the result. Contrarily, wave front and amplitude shaping instantly generates a uniform beam profile.
Besides the influence of the beam shaping method, a full investigation needs to include material-specific properties such as melting temperature, thermal conductivity, and enthalpy of vaporization as they also affect the process dynamics. Moreover, grain boundaries in the micro structure induce locally varying characteristics. As the material's grain structure strongly depends on its fabrication process, not only can local variations be present, but the whole grain structure may vary between batches.
To analyze this complex interplay and gain insights and process understanding, the multidimensional problem needs to be simplified. This is possible by starting with a specifically chosen material which is well-polished and exists in an either mono crystalline or amorphous crystal structure. This makes experimental results position-independent, predictable and thus reproducible. Based on these conditions, a direct comparison of different beam shaping methods is possible. Section 5.1 is based on publication [P4] and gives an overview on effects which originate from the differing methodology of beam shaping and the beam profile itself while material-specific influences are minimized. After having characterized the influences of beam shaping, material-specific characteristics are considered in Section 5.2. This is especially relevant for industrial applications as beam shaping needs to be applicable to materials which are of industrial interest. For this reason, shaped beam profiles will be tested on various metals, including standardized and industrially used materials. The same laser wavelength at 1064 nm is used for all ablation experiments. This provides high comparability, although material-specific wavelength tuning could further optimize processing results. Further, this experimental design provides a statistical basis to deduce material-dependent influences.

## 5.1 Methods for Uniform Beam Shaping and Their Effect on Material Ablation

[P4] Published at *Applied Physics A*, 10.1007/s00339-022-06004-y.
Reproduced with permission from Springer Nature.

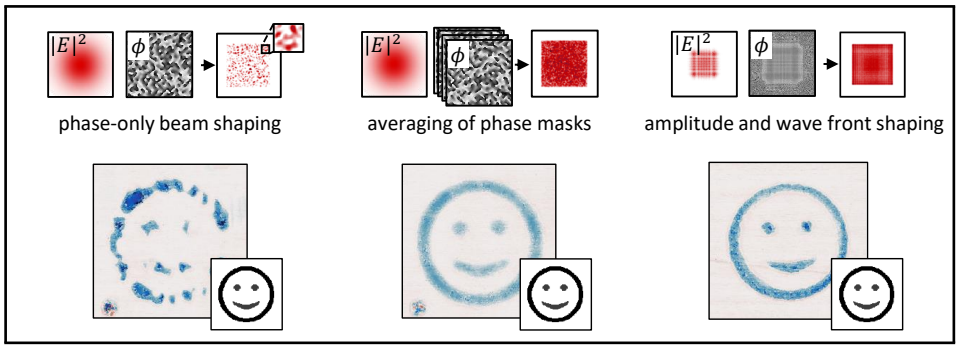


Graphical abstract: Methods for Uniform Beam Shaping and Their Effect on Material Ablation

Averaging-based beam shaping and direct uniform beam shaping are compared with each other to deduce methodology-specific characteristics. Experiments are conducted using an identical setup to maintain experimental conditions. While all presented methods within this thesis require dedicated setups, averaging of individual phase masks can be realized within most configurations. Thus, experiments are performed within the setup for uniform beam shaping and averaging is realized by exchanging phase masks as no scanning loop can be realized simultaneously. Averaging by scanning already proved to achieve near-perfect ablation results on mono crystalline silicon (Section 4.1.1 and Section 4.1.2) and it is thus sufficient to revert to the well-established method of exchanging individual phase masks to evaluate both methods in the very same setup. An amorphous metal is chosen to avoid effects originating from the micro structure. Based on the direct comparison of the ablation results, the methods for uniform beam shaping are characterized and this analysis builds the basis for further investigations on the material's influence.
Ablation results show that both methods are comparable in the amount of ablated material when working with the same (average) laser power. While wave front and amplitude shaping is favourable for achieving sharp edges, averaging is especially beneficial for ablating homogeneous areas as Gerchberg-Saxton-based phase masks are not sensitive to the exact shape of the input beam profile. This changes for wave front and amplitude shaping, where the input beam profile and the exact propagation path are critical parameters for the achievable quality. Small experimental deviations are practically unavoidable, see Section 4.2, and these deviations are rather

enhanced during material ablation as they reappear from pulse to pulse.

**Highlights**

- Comparison of averaging and direct uniform beam shaping for material ablation
- Experiments with an amorphous metal (VIT 105 from Heraeus) to avoid effects from the material's micro structure
- "Single pulse" uniform beam shaping provides sharper edges and averaging is beneficial for ablating homogeneous areas
- Analysis of the duty cycle for speckle averaging by displaying different phase masks on the SLM

Applied Physics A (2022) 128:877
https://doi.org/10.1007/s00339-022-06004-y

Applied Physics A
Materials Science & Processing

S.I. : COLA 2021/2022

# Methods for uniform beam shaping and their effect on material ablation

Lisa Ackermann[1,2] · Clemens Roider[1] · Kristian Cvecek[1,2] · Michael Schmidt[1,2]

Received: 28 April 2022 / Accepted: 25 August 2022 / Published online: 12 September 2022


**Abstract**
Phase-only beam shaping with a spatial light modulator (SLM) is a powerful tool in laser materials processing. It enables adapting the shaped profile to the ablation geometry and thereby tailoring the energy deposition. To mitigate speckle noise in tailored beam profiles, methods for uniform beam shaping were proposed. The two main approaches either implement averaging of speckled profiles or directly yield a uniform profile, i.e. by amplitude and wave front shaping. Even though both approaches provide comparable results in optical homogeneity, the ablation process differs. Even though it is important to know which method should be used for practical applications, a direct comparison of those two methods has not been studied before to the best of our knowledge. By employing both techniques in one setup, we perform ablation experiments on amorphous metal and investigate the results with respect to quality, efficiency, and feasibility. Averaging is especially suitable for ablating large areas with focus on homogeneity and simplicity. Amplitude and wave front shaping enables finer contours and sharper edges besides the obvious advantage of a uniform profile for single shot applications. Additionally, it exhibits no 0th order of non-diffracted light. These features arise from the inherently more sophisticated and complex experimental setup.

**Keywords** Ultrashort-pulsed laser materials processing · Beam shaping · Spatial light modulator · Speckle

## 1 Introduction

Ultrashort-pulsed laser (USP) sources nowadays provide pulse energies up to several mJ and they find application in many fields of laser materials processing [1–3]. However, their potential often remains unused since the processing quality and efficiency may be reduced due to a too high fluence. Ultrashort-pulsed laser material ablation is a nonlinear process as it scales nonlinearly with the fluence. The optimum fluence indicates the position, where the volume ablation rate per energy is maximized [4]. However, the provided peak fluence is typically orders of magnitude higher than the optimum fluence.

To make full use of the provided pulse energy, beam shaping with a phase-only spatial light modulator (SLM) enables tailoring the intensity profile to optimize the amount of deposited energy, inter alia, by distributing the light field over a large area. The process is highly efficient, since almost no losses occur. Furthermore, new phase masks can be dynamically applied to adapt for new processing geometries. Beam shaping with the SLM finds application in laser materials processing [5] and there are reports employing a liquid crystal SLM for high average power lasers [6].

Besides a direct modulation of the wave front, phase-only beam shaping enables arbitrary intensity distributions in the target plane. Iterative algorithms like the Gerchberg–Saxton algorithm are often used to calculate the required phase masks [7]. Those phase masks are calculated as a diffuser that redirects the light. Thus, each region of the phase mask equally contributes to the target

✉ Lisa Ackermann
lisa.ackermann@lpt.uni-erlangen.de

Clemens Roider
clemens.roider@lpt.uni-erlangen.de

Kristian Cvecek
kristian.cvecek@lpt.uni-erlangen.de

Michael Schmidt
michael.schmidt@lpt.uni-erlangen.de

[1] Institute of Photonic Technologies, Friedrich-Alexander-Universität Erlangen-Nürnberg, Konrad-Zuse-Str. 3/5, Erlangen 91052, Germany

[2] Erlangen Graduate School in Advanced Optical Technologies (SAOT), Friedrich-Alexander-Universität Erlangen-Nürnberg, Paul-Gordan-Str. 6, Erlangen 91052, Germany

image. It is, however, not possible to control the full complex light field with a single phase-only element. While the amplitude can be constrained in the target plane, the wave front remains uncontrolled and phase vortices occur, which result in a speckle pattern overlaying the tailored target structure [8].

Since speckle strongly impair the shaped intensity pattern and thereby the processing result, methods for uniform beam shaping in laser materials processing are required. Several methods have been proposed, all of which have their advantages and disadvantages. In this paper we study two main approaches: averaging of independent phase masks, and amplitude and wave front shaping by employing two SLM planes.

In the case of averaging, several phase masks designed for the same target structure but with different speckle patterns can be sequentially applied on the SLM to obtain a uniform result [9–11]. Thereby, the optical homogeneity scales with $\frac{1}{\sqrt{N_{\mathrm{PM}}}}$, where $N_{\mathrm{PM}}$ is the number of independent phase masks [12]. Furthermore, shift averaging of a single hologram completely averages out speckle [13].

If, however, each individual pulse needs to be speckle-free, averaging is not an option. A single phase mask may be used to get uniform results if only a small fraction of the light field is used to shape the target distribution [14, 15]. Since this method is highly inefficient, it is inappropriate for laser material ablation. Another option to achieve uniform beam profiles is adaptive beam shaping with an encoded phase grating [16, 17]. The target pattern is effectively cut from the remaining light by imaging the SLM plane with a 4f configuration and applying a phase grating to spatially separate the target image from the remaining light in the Fourier plane. While this method provides excellent results, only the separated portion can be used.

To this end, two consecutive SLMs can be used to control the full complex light field [18–22], namely amplitude and wave front, and by this make full use of the available light. To apply this method to high energy lasers, the fluence has to remain below the damage threshold of the device and therefore the energy has to be distributed over a large area on the SLM. In prior work, we developed a setup that meets those requirements [22].

Even though averaging and amplitude and wave front shaping give similar results in optical homogeneity, the ablation process on the material is different. For a fully controlled light field, an already homogeneous intensity profile interacts with the material whereas in the other case each single profile is overlaid with a speckle pattern and the homogeneity is only created by averaging.

For practical applications in laser materials processing it is important to know which method should be used. We analyze and evaluate both methods with respect to the resulting quality and efficiency of the ablated profiles. Both methods are implemented in the same setup to maintain the same experimental conditions. To obtain a direct mapping of the tailored beam in the ablation process, we work with the amorphous metal Heraeus AMLOY VIT105 which provides homogeneous and isotropic material characteristics since it exhibits no grain structure. Based on the analysis of two fundamentally different methods for achieving a uniform profile, we give suggestions which method should be applied depending on the requirements.

The paper is structured in the following way: in Sect. 2, we outline the method of amplitude and wave front shaping for high-energy lasers. Thereby, we present the experimental setup which can be adapted to accommodate both methods. Information about the used laser source and the amorphous metal sample with the ablation threshold follow thereafter. Sect. 3 shows the ablation profiles resulting from both methods. Here, we gradually analyze the results on different criteria, categorized within quality, efficiency, and feasibility, to finally conclude the paper based on this analysis.

## 2 Methods

To achieve a certain amplitude distribution, phase-only beam shaping with the SLM typically applies a phase mask which is calculated with the Gerchberg–Saxton algorithm. Figure 1 exemplarily shows this for a rectangular target structure. Figure 1a indicates that this results in a speckle pattern which can be averaged out with several independent phase masks as Fig. 1b shows. While averaging still works with this basic

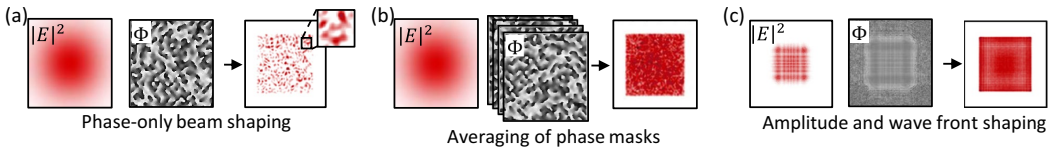


**Fig. 1** Methods for beam shaping: **a** phase-only beam shaping exhibits speckle, **b** averaging of independent phase masks can be used to get a uniform beam profile, **c** amplitude and wave front need to be controlled to fully shape the target structure

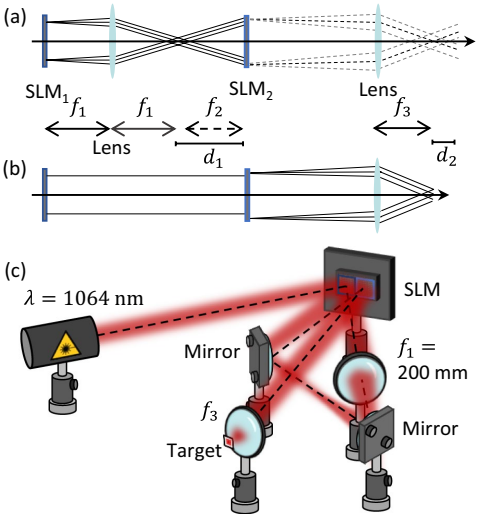


**Fig. 2** Experimental setup plotted in transmission for **a** amplitude and wave front shaping, and **b** for averaging. **c** Shows a 3D image of the setup in case of amplitude and wave front shaping. It can be adapted to averaging by removing the lens $f_1$ and applying a plane wave front on the first SLM plane

configuration, amplitude and wave front shaping (Fig. 1c) requires a more sophisticated setup. For this reason, our experimental setup is designed for amplitude and wave front shaping but it can easily be adapted to perform averaging. We will thus first outline the concept of amplitude and wave front shaping and present the experimental setup for this method before we continue with the adaptions for averaging.

## 2.1 Experimental setup

**Amplitude and wave front shaping**

Two SLM planes are employed to create a uniform beam profile. Based on the desired intensity pattern in the target plane, the complex light field is backpropagated to the second plane of the SLM. Shaping this amplitude and wave front distribution will result in the target pattern. Thereby, the first plane of the SLM is used to shape the amplitude on the second plane of the SLM. The corresponding phase mask is calculated with the Gerchberg–Saxton algorithm. The resulting intensity pattern exhibits speckle but with that method the amplitude itself can be controlled on the second plane of the SLM. The target wave front is well-known from the backpropagated light field and the second plane of the SLM is now capable of applying the proper wave front. A phase mask is applied that compensates for the arriving wave front and likewise applies the proper wave front to shape the full complex light field [18–22]. Figure 2a shows the setup in transmission. To avoid high peak fluences on the plane of the second SLM, the setup is designed in a 4-f-like configuration with a tube lens $f_1$ between the two planes. Furthermore, an additional variable lens term $f_2$ is part of the second SLM's phase mask and controls the magnification of the target structure. This enables target structures of arbitrary scale while the illuminated area on the second SLM stays constant.

The target structure is finally imaged with a lens $f_3$ into the target plane. An additional benefit of the 4-f-like setup is the vanishing 0th order of non-diffracted light since it is inherently defocussed on the second SLM and in the target plane. We additionally introduce an adaptable defocus in the target plane since this enables some modifications of the numerical aperture (NA).

In our experimental implementation, we work with one liquid crystal SLM (Meadowlark P1920-1064) that is split in two individual areas as Fig. 2c shows. While a relatively long focal length can be chosen for $f_3$ to image the target structure on a camera (IDS UI-1240LE-M-GL), it can be exchanged with a short focal length lens ($f_3 = 50$ mm (Thorlabs LA1255-B) or $f_3 = 18$ mm (Thorlabs LSM02-BB)) to focus on the surface of the sample and ablate material. The distance between the second SLM's plane and the imaging lens can be chosen freely as long as the target structure is calculated on-axis. Since the NA changes with the applied lens term on the second SLM as a consequence of magnification control, we add a positive defocus of a quarter of the used focal length to keep the NA high.

**Averaging**

To maintain the same experimental conditions for averaging of individual phase masks, the same setup is used. A plane wave front is applied to the first plane of the SLM to use it as a mirror. Additionally, the lens between the two SLM planes has to be removed. The remaining elements build the typical setup for phase-only beam shaping as can be seen in Fig. 2b. By providing different starting conditions for the Gerchberg–Saxton algorithm, independent phase masks are calculated. The target structure thereby appears in the focus of the lens $f_3$. It is shifted slightly off-axis to separate it from the 0th order of non-diffracted light. Based on the results in [11], we use 40 different phase masks to get a smooth averaged profile.

## 2.2 Laser parameter

The laser system Cepheus (Photon Energy) emits 12 ps pulses at a wavelength of $\lambda = 1064$ nm. The repetition frequency is set to its minimum at 20 kHz where the laser system provides the highest pulse energy (150 µJ). Inappropriate coating of the tube lens and high losses at the backplane of our SLM strongly reduce the laser power such that we measured 55 µJ on the surface of the material. Those

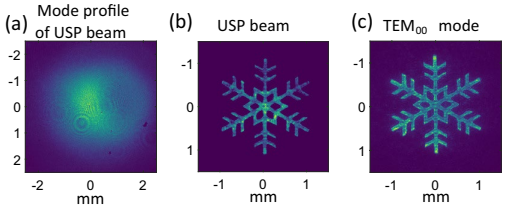


**Fig. 3** **a** Recorded intensity profile of the used ultrashort pulsed (USP) laser source in front of the SLM ($w_0 = 2.5$ mm). The asymmetric mode profile affects the homogeneity of the beam shaped output. For comparison an intensity image of a snowflake shaped with this laser mode (**b**) and a snowflake shaped with a mode-filtered $TEM_{00}$ mode ($w_0 = 3.1$ mm) **c** are shown for amplitude and wave front shaping

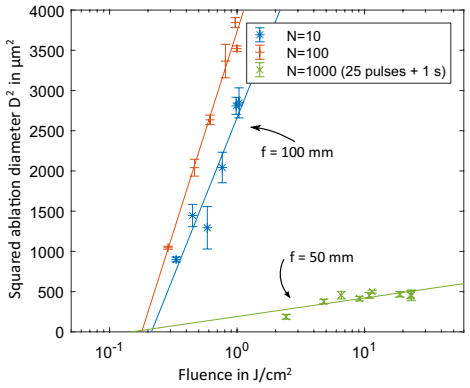


**Fig. 4** Determination of the ablation threshold according to Liu [23]. Each measurement was performed three times ($n = 3$)

are technical limitations of our used system and no general constraints. The reflectivity of our SLM's aluminium mirror is 85 % whereas dielectric mirrors are available which achieve a reflectivity > 95 %. The same applies for the anti-reflection coating of the tube lens. Based on measurements of shaped rectangles in [22], the total efficiency is 73 % for amplitude and wave front shaping, whereas phase-only beam shaping results in 81 % on-axis and 69 % off-axis if those two losses are excluded. This shows that both methods are almost comparable in their optical efficiency. To work with comparable laser fluences for both methods, we reduced the laser power in the case of averaging slightly since the tube lens was removed from the setup.

We made ablation experiments with 500 and 1000 pulses. In both cases, we apply 40 different phase masks for averaging. For 1000 pulses, a new phase mask is applied after 25 pulses. In the case of 500 pulses, either 12 or 13 pulses are applied until a new phase mask is loaded to end up with 500 pulses in total. To provide similar conditions for amplitude and wave front shaping, we added regular pauses even though no new phase masks needed to be loaded on the SLM. Similar to averaging, a pause of 1 s was added after 25 pulses for 1000 pulses. In case of 500 pulses, a pause of 1 s was added after 50 pulses.

It is worth mentioning that the mode profile of our laser source is relatively bad. A recorded image can be seen in Fig. 3a. Based on this recording, we fitted a beam width of $w_0 = 2.5$ mm. While phase-only beam shaping with phase masks based on a diffuser mask should not exhibit any dependence on the mode profile, our method is more sensitive to deviations from an ideal Gaussian input. Comparing camera images recorded with a high-quality mode-filtered Gaussian beam reveals a reduction in homogeneity as can be seen in Fig. 3b, c.

### 2.3 Material parameter

To achieve a direct mapping of the shaped beam profile within the ablation process, we use the Zirconium-based amorphous alloy Heraeus AMLOY VIT105. We specifically chose this material because it does not exhibit a grain structure which otherwise would locally affect the ablation result and probably limit the achieved quality from a material's perspective.

The ablated samples are cleaned in an ultrasound bath to remove residuals around the ablation area. We use the confocal laser scanning microscope Olympus LEXT OLS 4000 to perform depth and size measurements.

In preceding experiments, we determined the ablation threshold of the amorphous metal VIT105 according to Liu [23]. Therefore, we conducted two different measurement series: one within our setup with the lens for ablation experiments ($f_3 = 50$ mm and $w_0 = 2.5$ mm) and another series with a lower NA ($f = 100$ mm f-$\theta$-lens, Rodenstock F-Theta-Ronar, $w_0 = 1.5$ mm) outside the setup (compare Fig. 4). The latter experiments serve as a reference since the relatively high NA in the first case makes it difficult to get precise results due to the low slope resulting from the small hole diameters. The ablation threshold is around 0.15 $\frac{\mathrm{J}}{\mathrm{cm}^2}$ for 1000 pulses with a pause of 1 s after 25 pulses. The reference measurements gave $F_{\mathrm{th}} = 0.18\ \frac{\mathrm{J}}{\mathrm{cm}^2}$ and $F_{\mathrm{th}} = 0.22\ \frac{\mathrm{J}}{\mathrm{cm}^2}$ for 100, and respectively 10 pulses. Those values match well with the determined ablation threshold for 1000 pulses.

## 3 Results and discussion

In the following section, we present ablation results and evaluate them with respect to quality (roughness and homogeneity, shape accuracy, 0th order of non-diffracted

light, influence of the laser fluence), efficiency, and feasibility.

Figure 5 shows ablation profiles and the corresponding intensity images. In the upper left corner the target structure can be seen. The laser fluence is $F = 3 \cdot F_{\text{th}}$ ($F_{\text{th}} = 0.15 \frac{\text{J}}{\text{cm}^2}$ and calculation with a pulse energy of 55 µJ, where 80 % of the light shapes the target structure). For speckled profiles in the case of averaging, this value accounts for the mean fluence even though individual speckle peaks may be far above that value. The first row shows phase-only beam shaping results with a single phase mask. The overlaying speckle pattern mirrors in the ablated profile which makes it difficult to recognize the initial target structure. The 0th order of non-diffracted light appears in the lower left corner beside the target structure. The second row shows the averaging results for 40 different phase masks. The smooth ablated profiles show that speckle can be averaged out well even though each single pulse exhibits a strong speckle pattern. A simulated intensity profile and the corresponding camera recording can be seen in the left column. The images for the camera recordings are generated with a 300 mm lens and are thereafter projected to the target structure's size where the ratio between the two focal lengths gives the scaling. The ablated profiles for amplitude and wave front shaping can be seen in the third row. Similar to averaging, this method gives smooth results. Again, the simulated intensity profile and a camera recording of the beam are shown in the left columns.

## 3.1 Quality

### Roughness and homogeneity

To compare the homogeneity of the ablated structures, we evaluated the roughness $R_a$ along the outer circle's line as average of the profile height deviations from the mean line [24]. In case of averaging, we measured $R_a^{\text{avg}}(500 \text{ pulses}) = 0.7\,\mu\text{m}$ and $R_a^{\text{avg}}(1000 \text{ pulses}) = 1.8\,\mu\text{m}$. In comparison, amplitude and wave front shaping results in $R_a^{\text{A\&WF}}(500 \text{ pulses}) = 1.2\,\mu\text{m}$ and $R_a^{\text{A\&WF}}(1000 \text{ pulses}) = 1.8\,\mu\text{m}$. While the line roughness for both methods is relatively comparable, it more than doubles after averaging with 1000 instead of 500 pulses. In both cases 40 different phase masks are applied but averaging happens faster for a lower number of pulses and this provides a smoother surface. We also expect the roughness for a uniformly shaped beam profile to marginally increase with a higher number of pulses since the prevalent roughness from 500 pulses tends to strengthen with further pulses being applied.

The ablation profile in case of amplitude and wave front shaping is very sensitive to small inhomogeneities in the profile. A slight deviation from the targeted structure not

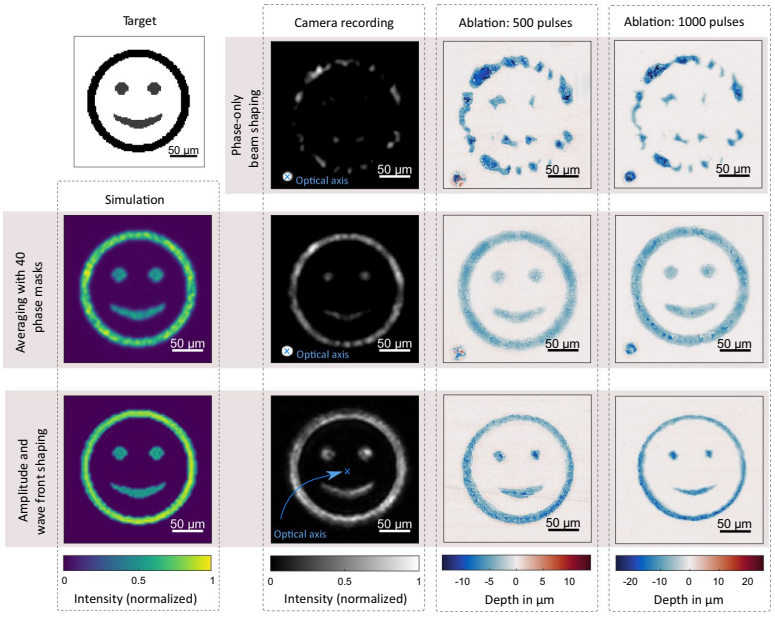


**Fig. 5** Comparison of ablation results with 500 and 1000 pulses for phase-only beam shaping, averaging, and amplitude and wave front shaping ($f_3 = 50\,\text{mm}$). Camera images and simulated intensity distributions are added on the left side for comparison. In case of phase-only beam shaping and averaging, the 0th order of non-diffracted light can be seen on the bottom on the left side

only reproduces with every single pulse but also affects the incoupling of new pulses due to an increased roughness/inhomogeneity in the surface structure. This may cause strengthened deviations in the final ablation profile. Comparing the intensity image of the camera measurement with the ablated profiles shows that slightly weaker illuminated areas result in less ablation or a thinner width of the ablated circle. Furthermore, the outer ring of the smiley shape was intentionally set slightly brighter than the inner part. This still can be recognized in the case of averaging whereas this nuance disappears for amplitude and wave front shaping.

**Shape accuracy**

Besides homogeneity, there is a clear difference in the sharpness resulting from both methods. The contours for amplitude and wave front shaping are sharper and show clear edges even though both experiments were performed in the same setup with the identical beam diameter and optical elements. 20 averaged line profile along the outer circle in Fig. 6 stress this observation. Radial slices of the outer ring are shown as mean edge contour: averaging results in a less steep and deep but broader profile. Here, the resolution is limited to the diffraction limit of the optical system, namely the beam diameter and the focal length of the imaging lens. If however, the amplitude is shaped beforehand, this step already selects only the relevant frequencies which are required to shape the target structure. This affects the resolution and provides sharper edges and thus finer details. This is an inherent effect of the pre-shaped amplitude whereas phase-only beam shaping is restricted to the initial light distribution on the SLM plane.

**0$^{th}$ Order of non-diffracted light**

Due to the 4-f-like configuration for amplitude and wave front shaping, the 0th order of non-diffracted light is defocussed on the plane of the second SLM. Since here only the wave front is adjusted to obtain the proper analytical solution, there appears no focused 0th order of non-diffracted light, neither while working in the focus, nor while working in the defocus. Phase-only beam shaping only enables shifting the target structure off-axis to separate the 0th order of non-diffracted light away from the shaped profile or applying an additional lens term to work in the defocus.

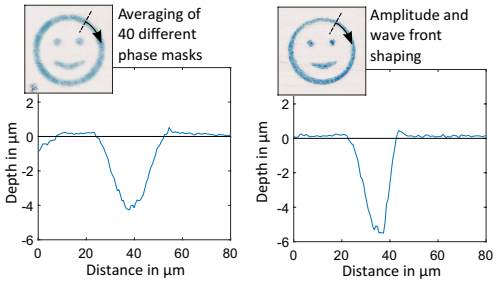


**Fig. 6** Mean edge contour of the outer circle. The profile shows a sharper slope and a clear edge for amplitude and wave front shaping. Apart from that, the amount of ablated material is equal for both methods

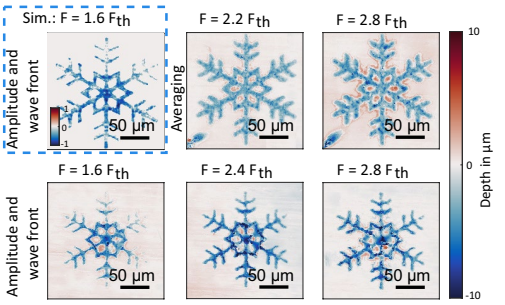


**Fig. 7** Dependence of the ablation result on the laser fluence: the first image in the upper row shows the simulated ablation profile for amplitude and wave front shaping on basis of the recorded intensity image in Fig. 3b with the fluence set to $F = 1.6 \cdot F_{\mathrm{th}}$. The color map here is normalized to the maximum ablation depth. The two images on the right show averaged profiles with differing laser fluence. The lower row illustrates the results for amplitude and wave front shaping in dependence of the chosen laser fluence. To shape the complex structure of a snowflake with the limited laser power, we used a micro scanner objective $f_3 = 18\,\mathrm{mm}$. All measurements are done with 500 pulses (50 pulses with 1 s in between). A median filter with a kernel size of $3 \times 3$ px was applied to the recorded depth shapes to suppress outliers from low-signal areas. The threshold fluence is $F_{\mathrm{th}} = 0.15\,\frac{\mathrm{J}}{\mathrm{cm}^2}$ and we assume that 80 % of the measured laser power shape the target structure

The marked optical axis in Fig. 5 denotes the position of the 0th order of non-diffracted light. It is focussed for phase-only beam shaping and averaging whereas it is vanished for amplitude and wave front shaping.

**Influence of laser fluence**

The nonlinear ablation process in ultrashort-pulsed laser material interaction can be approximated logarithmically [25]. This indicates that the chosen laser fluence is a relevant parameter to tune the homogeneity and flatness of the ablation profiles. As Häfner et al. [11], the quality of averaging improves with higher fluences since intensity fluctuations from the speckle profile have less impact on the ablation profile. Besides this difference in homogeneity and apart from the ablation depth itself, there appear no local deviations in flatness as the upper row in Fig. 7 indicates. Inhomogeneities in the intensity profile for amplitude and wave front shaping however strongly reduce the flatness of the ablated results especially close to the threshold fluence. While the ablated snowflake in Fig. 7 for $F = 2.8 \cdot F_{\mathrm{th}}$ gives a uniform ablation profile, the weaker illuminated outer parts (compare the camera recording in Fig. 3) start to disappear for $F = 1.6 \cdot F_{\mathrm{th}}$. The same effect can be observed in the

simulated ablation profile for $F = 1.6 \cdot F_{\mathrm{th}}$. Deviations in the resulting intensity profile are rather enhanced for low fluences but they tend to disappear for higher fluences with respect to the threshold fluence.

### 3.2 Efficiency

Judging efficiency with respect to the amount of ablated material gives comparable results for both methods. Even though the ablated volume per applied energy is similar, averaging requires regular pauses for switching with the result that only a fraction of the emitted pulses can be used, leading to a reduced duty cycle. Here, two different systems have to be synchronized: the ultrashort pulsed laser typically emits pulses with a repetition frequency $f_{\mathrm{rep}}$ of several tens of kHz for materials processing, whereas typical frame rates $f_{\mathrm{s}}$ of a liquid crystal SLM are around several Hz. $\tau$ gives a measure for the non-instantaneous response of the liquid crystals until a new phase mask is loaded.

The duty cycle is given by:

$$\mathrm{DutyCycle} = \frac{N_{\mathrm{t}}}{f_{\mathrm{rep}}/f_{\mathrm{s}} \cdot N_{\mathrm{PM}} \cdot \left\lceil \frac{N_{\mathrm{t}}/N_{\mathrm{PM}} + f_{\mathrm{rep}} \cdot \tau}{f_{\mathrm{rep}}/f_{\mathrm{s}}} \right\rceil} \quad \text{for } N_{\mathrm{t}} \geq N_{\mathrm{PM}} > 1, \tag{1}$$

where $N_{\mathrm{t}}$ is the total number of pulses needed for the desired depth, and $N_{\mathrm{PM}}$ is the number of applied phase masks. The brackets $\lceil\ \rceil$ in the equation indicate the ceil-operation. Figure 8 sketches the relative distances for the corresponding number of pulses. The denominator in Eq. 1 counts the total number of pulses provided by the laser during the machine time. This involves the number of passing pulses within the SLM's response time $f_{\mathrm{rep}} \cdot \tau$ plus the number of pulses which shall be applied to a single phase mask $N_{\mathrm{t}}/N_{\mathrm{PM}}$. Due to the fixed frame rate of the SLM, we can not directly take this sum but we have to find the next greater multiple of the number of pulses within the SLM's time frame $f_{\mathrm{rep}}/f_{\mathrm{s}}$. This gives the total number of pulses for a single phase mask. Multiplied with the number of phase masks $N_{\mathrm{PM}}$ we can calculate the duty cycle.

This duty cycle multiplied with the optical efficiency gives the total efficiency of the setup.

Contrary to a naive guess, the total efficiency does not monotonically decrease with an increasing number of applied phase masks (compare Fig. 9) nor monotonically increase with an increasing number of applied pulses (compare Fig. 10). This is a result of the fixed frame rate of the SLM leading to a large dead-time if the time where a single phase mask is displayed can only be used partially for processing. Therefore, the number of used phase masks should be chosen such that the argument of the ceil-operation is close but still below an integer value.

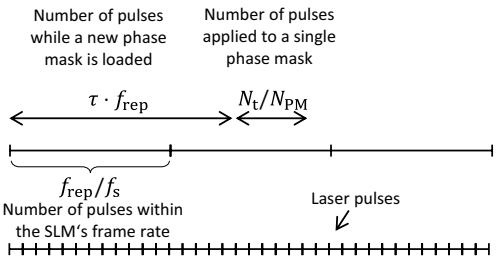


**Fig. 8** Sketch of the relative distances for the corresponding number of pulses

As typical frame rates of commercially available liquid crystal SLMs are about 60 Hz, the total efficiency is significantly reduced for a high number of phase masks. Typical response times, i.e. rise/fall times, -defined as the time a change from 10 % to 90 % takes and vice versa - for liquid crystal SLMs in the near infrared range from a few milliseconds to a few tens of milliseconds. Note that after the response time has elapsed the SLM will not have reached its full diffraction efficiency yet but only after the settling time, which is on the order of tens of milliseconds. Settling times can be reduced to about 3 ms by applying overdrive and phase change reduction [26]. Depending on the application, either the response time or the settling time can be chosen for $\tau$ in Eq. 1.

A higher frame rate increases the efficiency especially for a low number of phase masks but still the efficiency is low if few pulses and a large number of masks is needed.

If the SLM does not have a fixed frame rate but switching can be performed on demand, the duty cycle is only influenced by the response time $\tau$. A corresponding equation for the duty cycle can be derived by taking the limit of the frame rate towards infinity in Eq. 1:

$$\lim_{f_{\mathrm{s}} \to \infty} \mathrm{DutyCycle} = \frac{N_{\mathrm{t}}}{N_{\mathrm{t}} + \tau \cdot N_{\mathrm{PM}} \cdot f_{\mathrm{rep}}} = \frac{t_0}{t_0 + \tau \cdot N_{\mathrm{PM}}}, \tag{2}$$

with $t_0 = N_{\mathrm{t}}/f_{\mathrm{rep}}$ being the optimal processing time. This equation can be either interpreted in terms of pulses, where the denominator corresponds to the sum of used and unused pulses, or in terms of time, where the denominator corresponds to the prolonged processing time due to switching. In this case, the duty cycle will be close to unity if $N_{\mathrm{t}} \gg \tau \cdot N_{\mathrm{PM}} \cdot f_{\mathrm{rep}}$. Therefore, for a large number of used pulses and a low laser repetition frequency, averaging could be a viable option from an efficiency point of view.

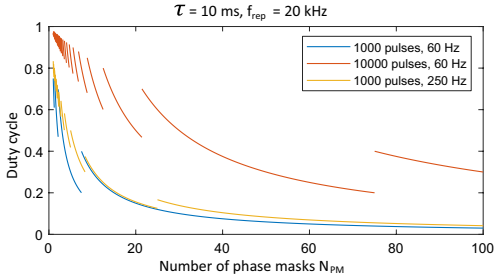


**Fig. 9** Duty cycle as a function of the number of phase masks: appropriate system parameters and a carefully chosen number of applied phase masks enable a high duty cycles even for low frame rates

### 3.3 Feasibility

Apart from the required synchronization in the case of averaging, a setup for phase-only beam shaping can be built with little effort especially since not a lot of optical components are required and alignment is easy. For amplitude and wave front shaping, there has to be a near perfect mapping between the preshaped amplitude profile and the applied phase mask on the plane of the second SLM. Besides more optical components, this requires fine alignment and readjustment from time to time.

## 4 Conclusion

Both, averaging and amplitude and wave front shaping give convincing results. Depending on the chosen criteria, the one or the other way of achieving a uniform ablation profile seems to be more advantageous. Averaging is more reliable when the focus lies on the ablation depth, whereas amplitude and wave front shaping enables sharper and more precise contours in the lateral plane. The introduced roughness does not significantly differ between the methods. In both cases approximately the same amount of material is ablated, however, the system parameters have to be chosen appropriately that averaging can compete in efficiency. While averaging requires almost no expense in alignment, the 0th order of non-diffracted light completely vanishes for amplitude and wave front shaping and only this method can be chosen if a single pulse already needs to exhibit a uniform profile.

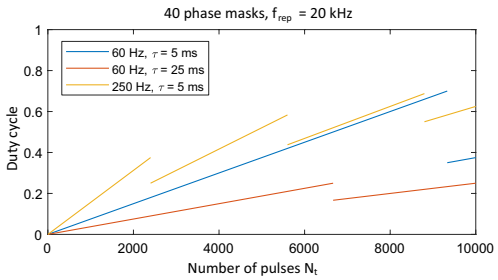


**Fig. 10** Duty cycle as a function of the number of pulses: a high pulse number, in general, increases the duty cycle but an unfavorable number might lead to a strong drop of the duty cycle due an increased dead time

**Acknowledgements** The authors gratefully acknowledge funding from the German Research Foundation (DFG) within the Project 397970984 and funding from the Erlangen Graduate School in Advanced Optical Technologies (SAOT) by the German Research Foundation (DFG) in the framework of the German excellence initiative.

**Funding** Open Access funding enabled and organized by Projekt DEAL.

**Data Availability** The datasets generated during and/or analyzed during the current study are available from the corresponding author on reasonable request.

## Declarations

**Conflict of interest** The authors declare that there are no conflicts of interest related to this article.



## References

1. K. Sugioka, Y. Cheng, Ultrafast laser-reliable tools for advanced materials processing. Light Sci. Appl. **3**(4), e149–e149 (2014)
2. K. Sugioka, Progress in ultrafast laser processing and future prospects. Nanophotonics **6**(2), 393–413 (2017)
3. L. Orazi, L. Romoli, M. Schmidt, L. Li, Ultrafast laser manufacturing: from physics to industrial applications. CIRP Ann. **70**(2), 543–566 (2021)
4. B. Neuenschwander, B. Jaeggi, M. Schmid, V. Rouffiange, P.-E. Martin. Optimization of the volume ablation rate for metals at different laser pulse-durations from ps to fs. In: Laser Applications in Microelectronic and Optoelectronic Manufacturing (LAMOM) XVII, volume 8243, pp 824307. International Society for Optics and Photonics (2012)
5. D. Liu, Y. Wang, Z. Zhai, Z. Fang, Q. Tao, Walter Perrie, Stuart P. Edwarson, Geoff Dearden, Dynamic laser beam shaping for

material processing using hybrid holograms. Opt. Laser Technol. **102**, 68–73 (2018)
6. G. Zhu, D. Whitehead, W. Perrie, O.J. Allegre, V. Olle, Q. Li, Y. Tang, K. Dawson, Y. Jin, S.P. Edwardson, G. Dearden, Investigation of the thermal and optical performance of a spatial light modulator with high average power picosecond laser exposure for materials processing applications. J. Phys. D Appl. Phys. **51**(9), 095603 (2018)
7. R.W. Gerchberg, W. Owen Saxton, A practical algorithm for the determination of phase from image and diffraction plane pictures. Optik **35**, 237–246 (1972)
8. M. Guillon, B.C. Forget, A.J. Foust, V. De Sars, M. Ritsch-Marte, V. Emiliani, Vortex-free phase profiles for uniform patterning with computer-generated holography. Opt. Express **25**(11), 12640–12652 (2017)
9. J. Amako, H. Miura, T. Sonehara, Speckle-noise reduction on kinoform reconstruction using a phase-only spatial light modulator. Appl. Opt. **34**(17), 3165–3171 (1995)
10. T. Häfner, J. Heberle, D. Holder, M. Schmidt, Speckle reduction techniques in holographic beam shaping for accurate and efficient picosecond laser structuring. J. Laser Appl. **29**(2), 022205 (2017)
11. T. Häfner, J. Strauß, C. Roider, J. Heberle, M. Schmidt, Tailored laser beam shaping for efficient and accurate microstructuring. Appl. Phys. A **124**(2), 1–9 (2018)
12. J.W. Goodman, Some fundamental properties of speckle. J. Opt. Soc. Am. **66**(11), 1145–1150 (1976)
13. L. Golan, S. Shoham, Speckle elimination using shift-averaging in high-rate holographic projection. Opt. Express **17**(3), 1330–1339 (2009)
14. H. Akahori, Spectrum leveling by an iterative algorithm with a dummy area for synthesizing the kinoform. Appl. Opt. **25**(5), 802–811 (1986)
15. F. Wyrowski, Diffractive optical elements: iterative calculation of quantized, blazed phase structures. J. Opt. Soc. Am. A **7**(6), 961–969 (1990)
16. V. Bagnoud, J.D. Zuegel, Independent phase and amplitude control of a laser beam by use of a single-phase-only spatial light modulator. Opt. Lett. **29**(3), 295–297 (2004)
17. Y. Nakata, K. Osawa, N. Miyanaga, Utilization of the high spatial-frequency component in adaptive beam shaping by using a virtual diagonal phase grating. Sci. Rep. **9**(1), 1–7 (2019)
18. H.O. Bartelt, Computer-generated holographic component with optimum light efficiency. Appl. Opt. **23**(10), 1499–1502 (1984)
19. H.O. Bartelt, Applications of the tandem component: an element with optimum light efficiency. Appl. Opt. **24**(22), 3811–3816 (1985)
20. A. Jesacher, C. Maurer, A. Schwaighofer, S. Bernet, M. Ritsch-Marte, Full phase and amplitude control of holographic optical tweezers with high efficiency. Opt. Express **16**(7), 4479–4486 (2008)
21. A. Jesacher, C. Maurer, A. Schwaighofer, S. Bernet, M. Ritsch-Marte, Near-perfect hologram reconstruction with a spatial light modulator. Opt. Express **16**(4), 2597–2603 (2008)
22. L. Ackermann, C. Roider, M. Schmidt, Uniform and efficient beam shaping for high-energy lasers. Opt. Express **29**(12), 17997–18009 (2021)
23. J.-M. Liu, Simple technique for measurements of pulsed gaussian-beam spot sizes. Opt. Lett. **7**(5), 196–198 (1982)
24. ISO 4287:2010-07. Geometrical product specifications (gps)—surface texture: Profile method—terms, definitions and surface texture parameters. Standard (1998)
25. S. Nolte, C. Momma, H. Jacobs, A. Tünnermann, B.N. Chichkov, Bernd Wellegehausen, Herbert Welling, Ablation of metals by ultrashort laser pulses. J. Opt. Soc. Am. B **14**(10), 2716–2722 (1997)
26. G. Thalhammer, R.W. Bowman, G.D. Love, M.J. Padgett, M. Ritsch-Marte, Speeding up liquid crystal slms using overdrive with phase change reduction. Opt. Express **21**(2), 1779–1797 (2013)

## 5.2 Influence of the Material

Within the scope of this thesis, methods for uniform beam shaping were designed and the ablation behaviour on mono crystalline Silicon (compare Section 4.1.1 and Section 4.1.2) and amorphous metal (compare Section 5.1) is well-characterized. Based on these well-characterized methods, the influence of the material can be investigated. This section presents provisional results on the influence of the material which show clear trends but further research is required to formulate a complete and well-founded theory.
This thesis focuses on structuring metal samples. They are polished to provide a flat surface and squares with a dimension of 75 µm × 75 µm are ablated with $N = 1000$ pulses at the same relative fluence with respect to the threshold fluence for each metal. Working with different materials provides a wide range of potential material-specific influence factors. This includes macroscopic material characteristics such as thermal properties. In addition, the micro structure of the material results in different grain orientations and grain boundaries. Even though all these factors have an impact on the final result, there are some expectations on the outcome:

- The shape of the intensity profile is expected to determine the shape of the ablated profile on the metal samples. Thus, a shaped square should result in an ablated square on each individual sample. Process dynamics due to material-specific effects are not expected to severely degrade and alter the predicted outcome to an unrecognizable condition.
- Ablation results for each individual material are expected to be reproducible and position-independent. Effects caused by the material's micro structure are not expected to dominate process dynamics. Furthermore, slight deviations in surface finish are not expected to cause severe distortions. It should thus be possible to reproduce the ablation results.
- Even though the shaped beam profile and the relative fluence remains the same for all experiments, the resulting uniformity of the ablated squares and also the visual impression is expected to vary between different materials as the process dynamics depend on material-specific properties.

While these assumptions need to be proven, shape fidelity, reproducibility, and position independence are relevant requirements for an application in industry. Further, potential reasons for deviations in uniformity between different metals need to be investigated. Based on that, counteractive measures can be taken. This includes refining beam shaping methods and adapting laser parameters.
After presenting the selected materials and the experimental setup, ablation experiments are conducted to analyze shape fidelity, reproducibility, position

independence, and the effect of surface finish. Based on these findings, a statistical analysis of material-specific influence factors can be conducted.

### 5.2.1 Experimental Design

As a homogeneously ablated area is beneficial for statistical evaluations of the material's influence, an averaging-based method will be used for the following investigations. The developed scanner setup, which is presented in Section 4.1.1, provides the basic tools for uniform material ablation by averaging. The method is based on scanning the beam over the phase mask which changes the speckle pattern while the target image gradually smooths. This provides near-perfect speckle averaging so that the averaged intensity profile is smooth with only minor imperfections. To calculate the ablation uniformity, the topography of the ablated profiles is analyzed with a laser scanning microscope (Olympus LEXT OLS 4000). Similar to the analysis in the preceding publications, the uniformity is evaluated according to [207]:

$$U = \frac{\sigma}{\mu} = \frac{\sqrt{\langle u^2 \rangle - \langle u \rangle^2}}{\langle u \rangle} \tag{15}$$

Here, $\sigma$ denotes the standard deviation and $\mu$ is the arithmetic mean of the ablated depth. $\mu$ is defined as the expectation value of a variable $u$ with $\langle u \rangle = \mu$. It should be noted that decreasing values of $U$ describe an improving uniformity with 0 % being the optimum value. While the resulting uniformity of the ablation profile is referred as *»ablation uniformity«*, the uniformity of the measured intensity profile is called *»beam uniformity«*.
The choice of metal samples for ablation experiments follows several criteria. The selection should contain common industrially used metals, e.g. the unalloyed deep-drawn steel DC04 and the aluminium alloys AA6014 (AlMg0.6Si0.6V) and AW5754 (AlMg3). Additionally, metals with a broad range of thermal characteristics should be tested. It makes sense to choose pairs of similar materials as similar behaviour indicates effects occurring from the elementary distribution and common material characteristics. Besides the two aluminium alloys, pure copper and CuSn6 (bronze) are investigated. Further, vanadium shows similar thermal properties as DC04 while TZM (titanium-zirconium-molybdenum) resembles Silicon in this regard. Overall, mono crystalline silicon serves as the main reference material while the amorphous alloy VIT 105 from Heraeus is excluded from the analysis as provisional experiments evinced strong thermal effects and almost immediate melting for pulse repetition frequencies at 20 kHz if no pauses are included as it was the case in Section 5.1. As this analysis focuses on typical application

scenarios, low repetition frequencies should be avoided.
The laser system Cepheus from Photon Energy emits 12 ps pulses at a wavelength of $\lambda = 1064\,\text{nm}$ with a pulse repetition frequency of 20 kHz. To provide the same ablation conditions, all materials are polished and ablated with $N = 1000$ pulses with the same relative fluence of $F = 4.8F_{\text{th}}$. This value is above the optimum fluence of a top hat profile which improves the ablation uniformity as the logarithmic scaling reduces slight deviations in uniformity with an increasing fluence. To scale the fluence for all selected samples with this value, the threshold fluence for $N = 1000$ pulses is experimentally determined according to Liu [114] as shown in Table 1. The corresponding measurements are attached to Appendix I.

Table 1: Measured threshold fluence for $N = 1000$ pulses according to Liu [114].

| **material** | DC04 | AW5754 | AA6014 | TZM | Si | V | Cu | CuSn6 |
|---|---|---|---|---|---|---|---|---|
| $F_{\text{th}}$ **in** J/cm² | 0.11 | 0.13 | 0.14 | 0.14 | 0.17 | 0.20 | 0.21 | 0.23 |

According to the logarithmic ablation model, compare Equation 6, the ablated depth depends on the optical penetration depth which is material-dependent. As the optical penetration depth scales the ablated depth linearly, the ablation profiles for the same relative fluence should only differ in the achieved depth while the resulting uniformity should be equal. Thus, structuring all experimental samples with the same relative fluence makes the results comparable and occurring differences can be deduced to material-specific characteristics which are not included in the simple ablation model.

### 5.2.2 Ablation Results and Discussion

Shape fidelity, position independence and reproducibility is shown by performing ablation experiments on several different positions on two individually prepared samples for mono crystalline silicon, DC04, and copper. Additional samples were prepared with coarse polishing paper to test material ablation with imperfect starting conditions. The detailed analysis is attached to the Appendix II and Appendix III. In all cases, the ablated profile geometry complies with the expected squares. An analysis of the standard deviation for the measurement series of each material suggests that ablation experiments are reproducible and position-independent. Further, an imperfect surface finish does not affect the outcome severely. Preexisting roughness is conserved during material ablation but does not affect the surroundings.
Even though no metallurgical analysis of the grain structure was conducted, experimental results by Sedao et al. indicate only a weak impact of the

material's micro structure [208]. Sedao et al. performed ultrashort pulse laser ablation experiments on metallic surfaces with similar laser parameters and analyzed the grain structure after cutting the ablated sample. When comparing the grain boundaries in the bulk material with their distribution in the skin region, it becomes apparent that ultrashort pulse laser ablation affects the grain structure as the grain sizes are smaller in the skin region. However, the ablated surface is more even than the original grain boundaries in deeper layers of the bulk material. Thus, neither unexpected processing results during the ablation experiments on shape fidelity, reproducibility, and position independence, nor the flat surface finish in [208] indicate strong effects due to the material's micro structure. Based on these observations, the grain structure is not expected to dominate process dynamics.
Visual differences in the resulting ablation profile can thus rather be assigned to material-specific characteristics. The exclusion of the impact factors of sample preparation, surface finish, and grain structure makes it possible to do a statistical analysis of ablation profiles for various materials and deduce material-specific influences.

## Ablation Results for the Selected Metal Samples

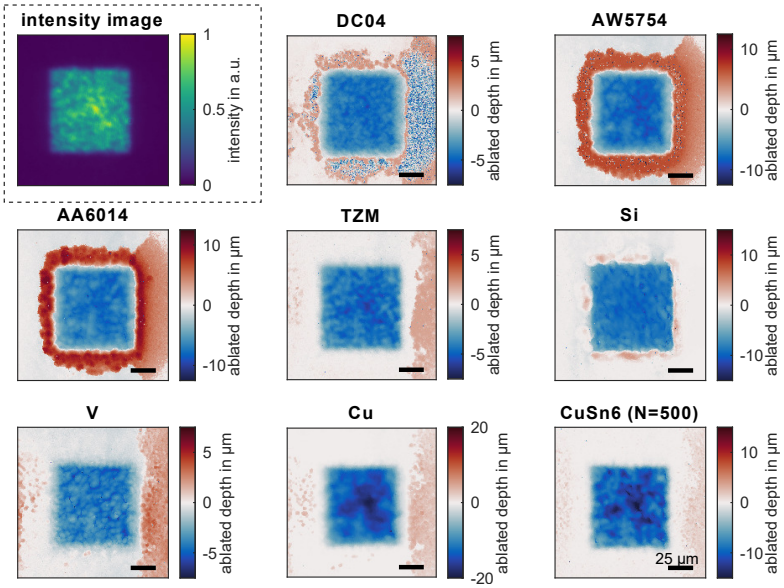


Figure 14: Ablation profiles for $N = 1000$ pulses (apart from CuSn6 which is ablated with $N = 500$ pulses) and a laser repetition frequency of 20 kHz. The ablated squares measure 75 µm × 75 µm and the mean laser fluence is $F = 4.8F_{\mathrm{th}}$ for all materials. The averaged laser intensity profile is shown in the upper left corner as reference. The scale bar denotes 25 µm.

Figure 14 shows recorded surface topographies of ablated squares for the selected metal samples. While bluish hues denote the ablated depth, expelled material in the surroundings appears in reddish hues. Although all evaluated metals demonstrate adequate results, the individual squares exhibit significant differences which suggests an underlying influence of the material, as the same fluence was used throughout on well-polished samples. For comparison, an image of the corresponding averaged laser intensity profile is shown in the upper left corner of Figure 14.
From the visual comparison, it is noticeable that the ablation uniformity differs. While these observations need further quantification, the logarithmic ablation model in Equation 6 covers variations of the ablated depth with the material-specific optical penetration depth. Moreover, some ablated surfaces, e.g. Cu and CuSn6, correlate better with the fluctuations of the averaged intensity profile than others. Besides the differences in ablation uniformity, these correlations will be further evaluated in this section (compare Figure 17).

**Effectiveness of Speckle Averaging by Scanning**

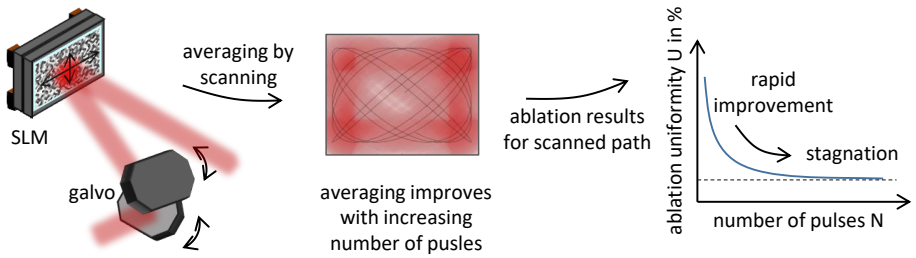


Figure 15: Uniform ablation by averaging provides a characteristic curve for the progression of the beam uniformity with respect to the number of applied pulses.

Figure 15 shows that uniform ablation by scanning provides a characteristic curve when plotting the ablation uniformity against the number of applied pulses $N$. While the ablation profile suffers from a strong speckle pattern for small numbers of pulses, it rapidly improves and then starts stagnating. This happens when the beam has scanned the whole area of the phase mask. Further scanning only leads to small improvements or slight fluctuations until the achieved uniformity fully stagnates. As averaging by scanning only provides near-perfect results with little speckle remaining, stagnation happens on a plateau above the optimum uniformity of 0 %. Thus, a characteristic curve describing the improvement of uniformity with increasing pulse numbers is formed for a set of scanning frequencies $f_x$ and $f_y$. It should be noted that within the developed setup, the scanner movement is not

synchronized with the laser emission. This causes a random starting position. However, any initial differences in starting condition have negligible impact as they equalize after a small number of pulses.

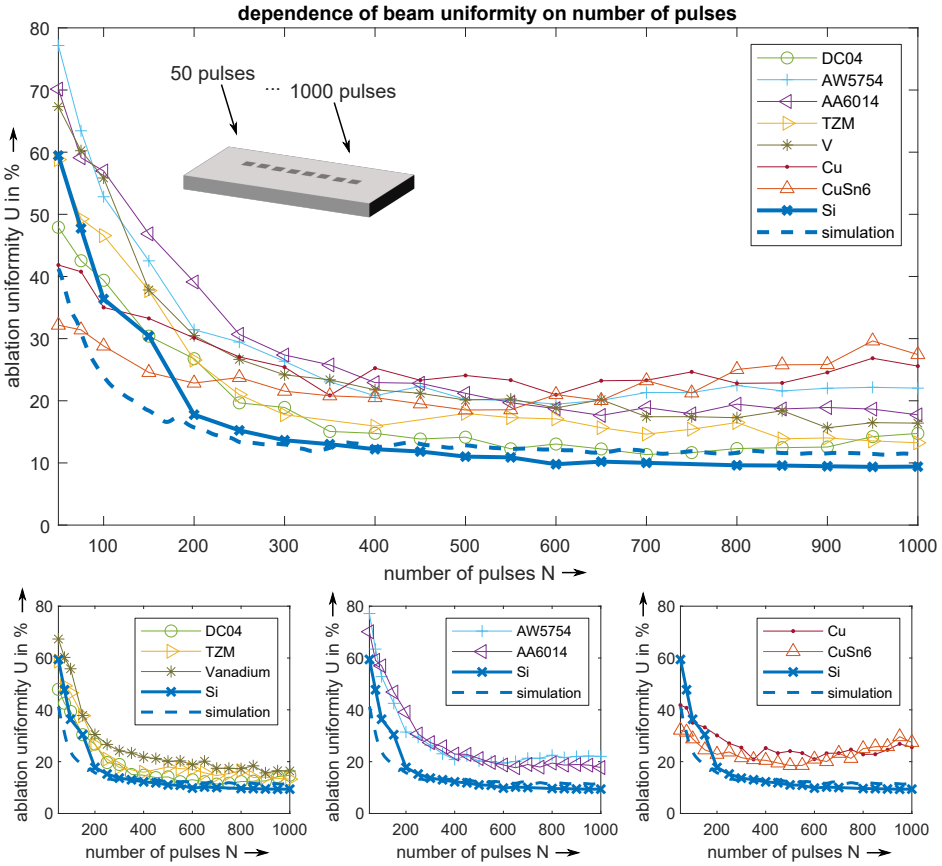


Figure 16: Characteristic averaging curve of the chosen materials with individual subplots for materials with similar characteristics and/or elementary composition.

The characteristic curve for a set of scanning frequencies makes it possible to compare the ablation behaviour of different materials with respect to the averaging curve of an ideal material. Therefore, a series of squares with an increasing number of pulses is ablated on the polished metal samples. Figure 16 shows the resulting curves. The corresponding squares are ablated individually and each data point corresponds to a different position on the sample. This is possible as the analysis in Appendix II did not indicate position-dependent effects. This matches well with the continuously connected data points in Figure 16. Besides the experimental measurements,

an ideal averaging curve is simulated on basis of the logarithmic ablation law in Equation 6 and the beam's scanning curve across the phase mask ($f_x = 813$ Hz and $f_y = 987$ Hz). These values are consistent with the analysis in Section 4.1.1. All materials share the shape of the predicted curve. The characteristic curve of silicon is close to the simulated curve of an ideal material. While those two curves seem to set a limit for the achievable uniformity, many other curves appear shifted along the y-axis with the same shape. It is particularly striking that materials with similar composition also follow a similar curve, compare e.g. copper and CuSn6 or the two aluminium alloys. Therefore, Figure 16 also provides the corresponding subplots with only those materials.
In contrast to the other curves, the uniformity of the copper alloy CuSn6 becomes worse after approximately $N = 500$ pulses. This might be explained by the particularly high ablated depth. The aspect ratio increases and the edges taper with increasing depth. Thus, they start to influence the ablation process with additional reflections and this smooths the corners to a bath-tub-like structure. As the ablation uniformity rather tends to stagnate after $N = 500$ pulses for all materials, further evaluations with CuSn6 are done on basis of the ablation result at $N = 500$ pulses. The significance of such effects might also depend on the reflectivity of the corresponding material.

**Deduction of Material-Specific Characteristics**
The analysis of the characteristic curve in Figure 16 indicates a deterministic ablation behaviour. Materials with similar elementary composition exhibit a similar development of ablation uniformity. Thereby, the predicted trend of saturation occurs for almost all materials after approximately 500 pulses, while the value of saturation depends on the material. This matches well with the visually perceived differences in uniformity for the selected metals in Figure 14. To further investigate the achievable ablation uniformity, the topography of the ablated squares needs to be investigated. Some of the ablated squares in Figure 14 exhibit strong similarities with the averaged intensity profile, compare e.g. copper. This observation can be mathematically measured by calculating the correlation of the ablated squares with the averaged intensity profile. To exclude effects from the varying depth, the ablation profiles were normalized before they were correlated with the recorded intensity profile. Figure 17 shows the resulting relation of the correlation with the ablation uniformity for the chosen samples.
This analysis exposes a linear relationship between the achievable uniformity and the calculated correlation. A stronger variability in surface, i.e. worse uniformity, coincides with an increasing correlation between the ablation profile and the averaged intensity image. This corresponds to a

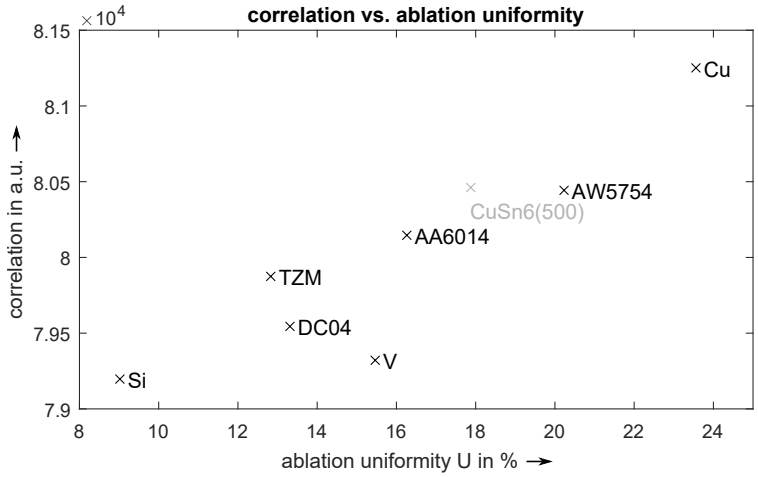


Figure 17: Correlation between the recorded intensity profile and the ablated surface versus the evaluated ablation uniformity. CuSn6 is greyed out as it was ablated with only $N = 500$ pulses.

linear mapping of the averaged intensity profile and the ablated structure. However, the relation between the ablated surface and the shaped intensity profile is more complex: the ablated depth can be estimated logarithmically from the intensity pattern of each single pulse. The accumulation of the results for each single pulse provides an estimate of the ablated square. The ideal curve in Figure 16 is simulated based on that model and it coincides well with the measured curve for mono crystalline silicon. The underlying explanation for the linear relationship between the achievable uniformity and the correlation requires further investigation and might be more complex. However, the evaluated results show a clear trend. If it was possible to find a material-specific parameter that shows a common relationship with the calculated correlation, the ablation uniformity could be predicted from that value. It is thus reasonable to consider the thermal properties of the chosen metal samples.

To further analyze this assumption, Table 2 shows the thermal conductivity $\kappa$ of the selected materials. This value is chosen as it provides a measure of heat transport for the remaining heat within the material.

An evaluation of both thermal conductivity and correlation in Figure 18 shows a near-linear relationship. This relation suggests that the differences in the ablation profiles can be related to thermal effects which are caused by the varying thermal conductivity of the individual materials. This value might directly affect material ablation or influence other material-specific properties, e.g. the refractive index, which in return affects energy incoupling and process dynamics.

Table 2: Thermal conductivity of the selected metals (at room temperature). The correspondings references are noted below the individual values of the thermal conductivity $\kappa$.

| **material** | DC04 | AW5754 | AA6014 | TZM | Si | V | Cu | CuSn6 |
|---|---|---|---|---|---|---|---|---|
| $\kappa$ **in** $\frac{\mathbf{W}}{\mathbf{mK}}$ | 58 [209] | 130 [210] | 211 [211] | 130 [212] | 100 [213] | 35 [214] | 385 [215] | 75 [216] |

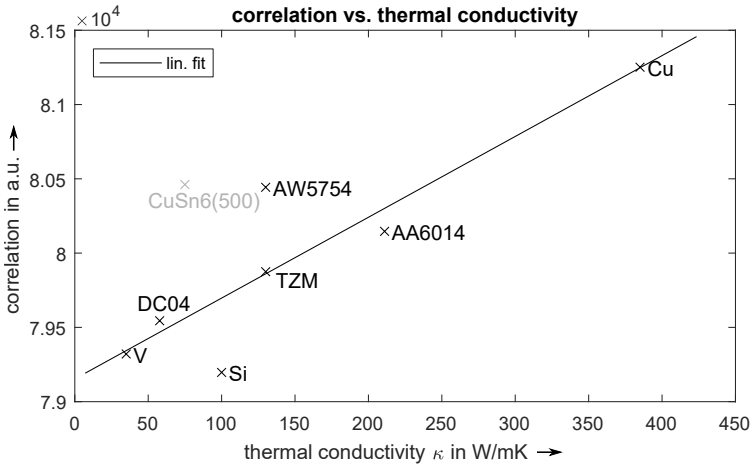


Figure 18: Correlation between the averaged intensity profile and the ablated surface versus the thermal conductivity. CuSn6 is greyed out as it was ablated with only $N = 500$ pulses.

This finding not only shows material-specific limitations which cause worse ablation uniformity, but also possible influence factors. It should be possible to roughly estimate the ablation uniformity from the thermal conductivity of a chosen material as the relation in Figure 19 shows. Having an estimation and depending on the requirements, additional measures can be taken to refine beam shaping: averaging by scanning and averaging by exchanging phase masks can be combined to further improve the ablation uniformity. The beam is scanned over the phase mask but instead of working with a single phase mask, the phase mask can be exchanged during the scanning movement. This provides improved speckle averaging at the cost of laser dead times. In addition, the thermal behaviour of the ablation process can be controlled to a certain extent by the appropriate choice of the laser parameters. This involves the applied laser fluence, the chosen wavelength, the pulse duration, and the repetition frequency of the applied pulses. By adjusting these laser parameters, it should be possible to enhance or suppress thermal effects to some extent. And since the dependence of the heat capacity suggests that thermal effects have a significant impact on the quality, an

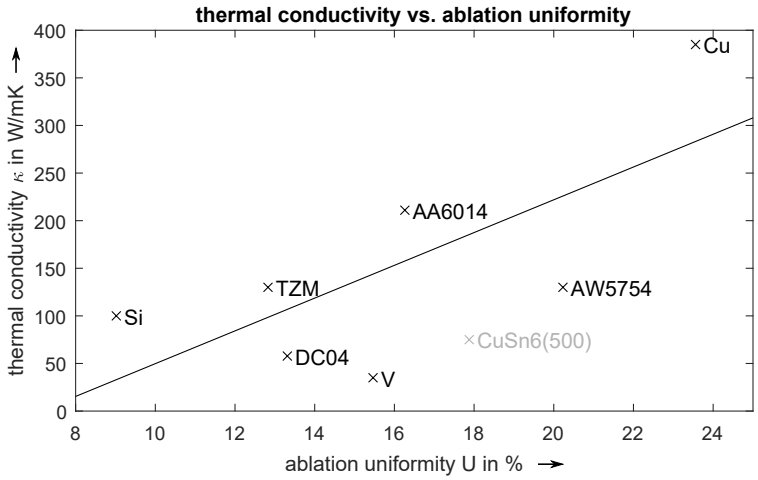


Figure 19: Thermal conductivity versus the evaluated ablation uniformity. CuSn6 is greyed out as it was ablated with only $N = 500$ pulses.

adjustment of these process parameters should provide further control on the processing results.
Likewise, the presented measurements build the basis for further research of the material's influence. The results not only stress that the material has a significant influence on the ablation process but also show the potential dependence on thermal parameters. To validate these observations, further experiments with well-characterized materials need to be conducted. Furthermore, the grain structure needs to be analyzed before and after material ablation (e.g. with electron backscatter diffraction, EBSD). Tailored beam profiles with sharp edges can be set intentionally on grain boundaries. The evaluated results should point out any influences of the grain boundary.
The developed beam shaping methods are not limited to shaping uniform profiles of constant laser fluence. Deliberate adjustments in local fluence could be used to correct unwanted effects such as reflection at edges. Likewise, complex structures of arbitrary shape and intensity distribution can be directly realized.
Even though the current analysis does not provide an explanation of the process dynamics, the measured results show clear trends, confirming that experiments are reproducible and position-independent. The ablation behaviour tends to be predictable and may primarily be related to the elementary composition and the corresponding material characteristics. This makes the results predictable and it can be assessed whether the process parameters and beam shaping method need to be refined or adapted accordingly.

# 6 Nonlinear Beam Shaping

The spectral properties of LCoS SLMs are determined by the liquid crystals within the display. As liquid crystals typically absorb UV light, LCoS SLMs cannot be used to shape light within this spectral range even though applications in surface functionalization [160], photovoltaics [161], and ophthalmology [162] would benefit from that technology. To this end, nonlinear optics helps to expand the spectral range. The beam can be shaped in the visible or infrared spectral range and the frequency is converted thereafter. This is possible as nonlinear conversion is a coherent process and the imprinted phase information is conserved during frequency conversion. However, as the frequency-converted outcome is given by several mixing fields, there needs to be a control mechanism to tailor the outcome. Therefore, the mixing fields can be distinguished by their optical properties, e.g. polarization. As a second requirement, the shaped angular spectrum of wave vectors has to be within the tolerance range of the crystal to maintain phase matching. Given those requirements, a method for nonlinear beam shaping can be designed.

## 6.1 Polarization-Controlled Nonlinear Computer-Generated Holography

[P5] Published at *Scientific Reports*, 10.1038/s41598-023-37443-z.
Reproduced with permission from Springer Nature.

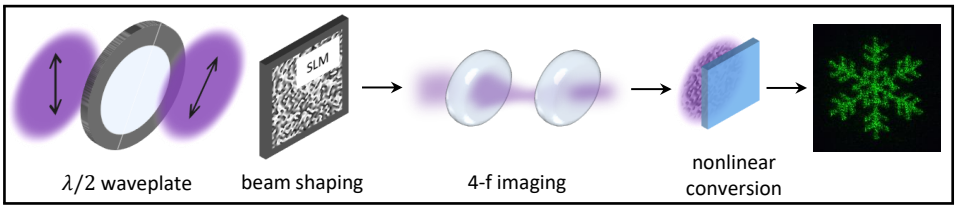


Graphical abstract: Polarization-Controlled Nonlinear Computer-Generated Holography

Second harmonic generation is one of the most popular nonlinear optical processes and it will be used to demonstrate and investigate nonlinear beam shaping. By choosing the type II crystal KTP for the nonlinear conversion, polarization directly acts as the control mechanism. Therefore, only one polarization component is shaped, while the other half of the field remains unshaped. This provides an unambiguous assignment of the mixing fields. The experimental implementation is simple as the SLM is polarization sensitive. It is sufficient to add a half wave plate to the setup which introduces diagonal polarization before the beam impinges on the SLM. The plane of the SLM is thereafter imaged into the nonlinear crystal. Light in the

infrared spectral range is frequency-doubled to the visible spectral range at 532 nm. The method is demonstrated for several exemplary beam shapes. The recorded results at the second harmonic show that nonlinear beam shaping provides results of the same quality as for linear beam shaping and the conversion efficiency is comparable to values without beam shaping. Modeling the nonlinear KTP crystal allows calculating the phase mismatch which occurs due to beam shaping. This builds the basis for simulating the frequency-converted beam-shaped result. As an outlook, proper crystals and the corresponding concepts for UV beam shaping are discussed.

**Highlights**

- Conversion efficiency similar to second harmonic signal without beam shaping
- Analysis of the conversion process by modeling the nonlinear crystal and simulating the relative conversion efficiency
- Quality and spatial intensity distribution same as for linear beam shaping
- Outlook on possible crystals for UV beam shaping

www.nature.com/scientificreports

scientific reports

Check for updates

OPEN

# Polarization-controlled nonlinear computer-generated holography

Lisa Ackermann[1,2]✉, Clemens Roider[1], Kristian Cvecek[1,2], Nicolas Barré[1,2], Christian Aigner[1] & Michael Schmidt[1,2]

**Dynamic phase-only beam shaping with a liquid crystal spatial light modulator is a powerful technique for tailoring the intensity profile or wave front of a beam. While shaping and controlling the light field is a highly researched topic, dynamic nonlinear beam shaping has hardly been explored so far. One potential reason is that generating the second harmonic is a degenerate process as it mixes two fields at the same frequency. To overcome this problem, we propose the use of type II phase matching as a control mechanism to distinguish between the two fields. Our experiments demonstrate that distributions of arbitrary intensity can be shaped in the frequency-converted field at the same quality as for linear beam shaping and with conversion efficiencies similar to without beam shaping. We envision this method as a milestone toward beam shaping beyond the physical limits of liquid crystal displays by facilitating dynamic phase-only beam shaping in the ultraviolet spectral range.**

The first operating laser in the early 1960s[1] was the dawn for many research fields in modern optics although some of their fundamental effects were already demonstrated or proposed in theory decades earlier. Holography and nonlinear optics emerged independently from each other but both fields benefited from the high coherence and high power of new light sources.

Holography is based on the interference of light waves and incorporates phase and amplitude information to go beyond photography. Dynamic phase-only beam shaping with a liquid crystal spatial light modulator (LC-SLM) is a method emerging from holography for arbitrarily controlling the intensity distribution of the beam with many applications in research[2–4] and industry[5–7]. As this method only modulates the wave front, there are no significant losses. As a drawback, liquid crystal displays are technically limited to the visible, near-infrared and mid-infrared spectral ranges. This is not an insurmountable problem, as frequency conversion processes such as second harmonic generation or sum frequency generation are coherent processes that preserve the phase of the impinging fundamental wave. Combining nonlinear optics and holography allows for shaping the light field at the fundamental while achieving the targeted outcome at the frequency-converted field. Even though both research fields can be combined, the concept of nonlinear holography is only currently emerging.

Yariv showed decades ago that four wave mixing can be interpreted as holographic recording and reconstruction and proposed using it for the realization of real time holography[8]. In this process, the interaction between the fields can be interpreted as one field diffracted by the shaped pattern of another field. Meanwhile many investigations followed on the nonlinear conversion of structured light for the conservation of singularities[9,10] and orbital or spin angular momentum and vortex beams[11–24]. Here, the physical principles of the nonlinear conversion of structured light have been well-explored and several works use beam characteristics such as polarization[19,25,26], differing wavelengths[15,17,18] or non-collinear geometries[20] as a control mechanism for the nonlinear conversion of optical vortices. The recent review paper published by Buono and Forbes gives an overview on nonlinear optics with structured light[27].

Currently, there are two major approaches to nonlinear holography: directly structuring the nonlinear crystal or imaging the plane of an LC-SLM into the crystal.

3D structuring of the nonlinear crystal leads to a modulation of the nonlinear susceptibility which shapes the wave front of the emerging light field. Such elements are called nonlinear photonic crystals as the modulation of the nonlinear susceptibility affects the beam generation and propagation[28–34]. There are demonstrations of a binary hologram in a nonlinear crystal[35], a structured element combined with structured light[36,37] or plasmonic metasurfaces[38,39]. Such 3D structured nonlinear crystals act as volume holograms or phased arrays and in theory give more degrees of freedom as a thin hologram. As their implementation is technically challenging, the freedom of design is so far strongly limited and furthermore only static solutions are possible. Such practical limitations motivate the consideration of thin holograms which are easier to realize.

[1]Institute of Photonic Technologies, Friedrich-Alexander-Universität Erlangen-Nürnberg, Konrad-Zuse-Straße 3/5, 91052 Erlangen, Germany. [2]School of Advanced Optical Technologies (SAOT), Friedrich-Alexander-Universität Erlangen-Nürnberg, Paul-Gordan-Straße 6, 91052 Erlangen, Germany. ✉email: lisa.ackermann@lpt.uni-erlangen.de

In a dynamic approach, the plane of a phase-only LC-SLM is directly imaged into the nonlinear crystal[40–43]. It thus acts as a thin hologram and brings the SLM and the nonlinear crystal together in a common plane, where the SLM dynamically shapes the wave front of the fundamental as if the hologram was directly structured into the crystal. The phase mask on the SLM imprints a locally varying phase on the incoming light field which leads to a modification of the resulting wave front where the slope corresponds to wave vectors forming the angular spectrum. During the nonlinear interaction, all light fields which fulfill the phase matching condition interact and create a new, frequency-converted outgoing wave. If the incoming fields are not distinguishable, i.e. the fields are degenerate, all wave vectors will add up, resulting in a new outgoing wave that has an angular spectrum, containing all possible sums of incoming wave vectors. This complicates beam shaping of the outgoing, frequency-converted wave as the initially applied angular spectrum at the SLM is not conserved. Consequently, there needs to be a control mechanism which makes the incoming fields distinguishable.

Current approaches for second harmonic generation[40–43] are based on a degenerate type I phase matching process and thus involve a non-collinear geometry to control the beam-shaped outcome. This imposes severe limitations in the quality and the efficiency of the achievable results. We utilize type II phase matching and demonstrate high-quality and highly-efficient nonlinear beam shaping in the second harmonic with a LC-SLM in a collinear geometry:

Since the nonlinear conversion is only possible with phase matching, this constraint can be exploited for beam shaping. In type II phase matching, only crossed polarization states can mix and through this assignment, the two fields at the fundamental are clearly distinguishable even when working in a collinear geometry. This concept is sketched in Fig. 1. By keeping one field unshaped while the other polarization carries the full phase information, there is an unambiguous assignment of the frequency-doubled wave front for every wave vector. The experimental implementation is simple as the polarization is set diagonally before it impinges on the SLM and as the SLM is polarization-sensitive, only half of the light field is shaped. After imaging this plane into the nonlinear crystal, only crossed polarization components add up for the second harmonic field. The same concept can be transferred to sum frequency generation where the differing frequencies ensure a non-degenerate mixing process.

Based on those physical principles, we present a setup for nonlinear beam shaping with high quality while the conversion efficiency is almost defined by the crystal's conversion efficiency without beam shaping. Besides showing experimental results, we model the chosen KTP crystal to estimate the relative conversion efficiency. Finally, we discuss optimizing the conversion efficiency and give an outlook on the applicability of the method for beam shaping in the ultraviolet spectral range.

## Results

For second harmonic generation, two fields at the fundamental frequency, $\boldsymbol{E_1}^{(\omega)}$ and $\boldsymbol{E_2}^{(\omega)}$, add up to the frequency-doubled field. From the three wave mixing process follows a quadratic relation between the fields $\boldsymbol{E}^{(2\omega)} \propto \boldsymbol{E_1}^{(\omega)} \cdot \boldsymbol{E_2}^{(\omega)}$. The phase matching condition

$$\boldsymbol{k}^{(2\omega)} \stackrel{!}{=} \boldsymbol{k_1}^{(\omega)} + \boldsymbol{k_2}^{(\omega)}, \tag{1}$$

requires the fundamental and the second harmonic to maintain their phase relationship during propagation through the nonlinear material to avoid destructive interference and weak conversion. Here $\boldsymbol{k_{1/2}}^{(\omega)}$ are the wave

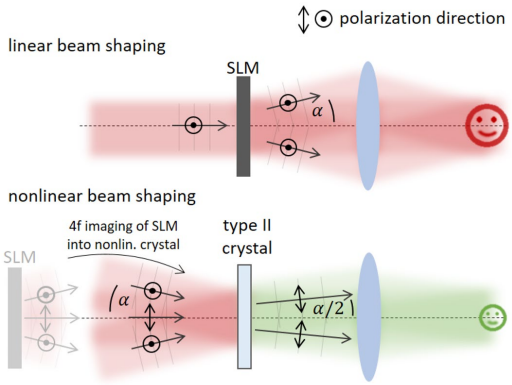


**Figure 1.** Basic concept of nonlinear beam shaping with linear beam shaping as reference: The applied wave front generates an angular spectrum of wave vectors which are centered around the optical axis. Their distribution results in a target image in the far field. The plane of the SLM is imaged into the nonlinear crystal. As for type II phase matching only crossed polarization states mix efficiently, the shaped light field can only mix with the unshaped one. The addition of the wave vectors results in the tailored light field with only half the initial deflection angle $\alpha$.

vectors at the fundamental frequency and $\boldsymbol{k}^{(2\omega)}$ is the resulting wave vector at the second harmonic. We first present the experimental results before we model the nonlinear crystal to evaluate the relative conversion efficiency.

**Nonlinear beam shaping.** With polarization as a control mechanism, nonlinear beam shaping can be performed similar to linear beam shaping. The phase mask for wave front shaping can be calculated with the same algorithms and tools as for linear beam shaping and the setup basically consists of a half wave plate, a LC-SLM, a 4-f imaging telescope and the nonlinear crystal as Fig. 2 shows. However, as wave front shaping generates an angular spectrum of wave vectors which are centered around the optical axis, the nonlinear crystal needs to equally support vectors which slightly deviate from the optimum phase matching angle. This required angular tolerance or acceptance is one characteristic of nonlinear crystals and it is defined for an angular deviation where the conversion efficiency drops to half of its maximum value. We chose KTP as the nonlinear crystal for our application as it exhibits a high angular acceptance.

Figure 3 shows experimentally recorded profiles of the second harmonic at 532 nm and images of the fundamental at 1064 nm (Fig. 3a–d) as reference. The corresponding phase masks are calculated with the Gerchberg Saxton algorithm[44]. When tailoring the target image in the far field, the propagation can be mathematically described by a Fourier transform. Thus, the intensity profile of the target image effectively reflects the generated angular spectrum. Its size directly shows the required angles of the wave vectors which need to be supported during frequency conversion. Consequently, the larger the targeted image size is, the higher the angular acceptance of the nonlinear KTP crystal needs to be, to equally convert the second harmonic signal for all wave vectors.

As a shorter nonlinear crystal exhibits a higher angular acceptance, second harmonic generation is supported for a broad spectrum of wave vectors and arbitrary target structures can be shaped over a large area. We demonstrate this in Fig. 3e–h for four different target distributions with a 2 mm long KTP crystal. All structures are homogeneously converted and the quality is comparable to the results at the fundamental. The read-out at the second harmonic appears slightly degraded with respect to the fundamental. The impression of degradation probably arises from a change in speckle size with respect to the structure size. We calculate the conversion efficiency by dividing the measured power of the shaped target structure at the second harmonic by the power at the fundamental. The conversion efficiency is around 6—8 % for all structures. Conversely, a 9 mm long KTP crystal promises higher conversion efficiency at lower angular acceptance. The results of the two smaller target structures for the 9 mm long crystal (Fig. 3i,j) are of the same quality as for the 2 mm crystal. The conversion efficiency is $>$ 30 % and this is only a little less than the initial conversion efficiency of the nonlinear crystal without beam shaping which is around 40 %. For the 2 mm crystal the values are even closer with 8.5 % without and values around 6—8 % with beam shaping. Those results demonstrate the applicability of nonlinear beam shaping in a regime of high conversion efficiency while maintaining high quality. The homogeneous conversion in the range of the initial conversion efficiency of the nonlinear crystal is due to a plateau in the conversion efficiency for small angular deflections. We further investigate this favorable effect for beam shaping in the next section. Figure 3k,l also shows the limitations of nonlinear beam shaping when working beyond this plateau. The globe and snowflake are almost cut at the borders as the required angles are not supported by phase matching. As parts of the light field are not converted, the conversion efficiency decreases. These results are shown to demonstrate the limitations outside the plateau of high conversion efficiency. It is nonetheless possible to shape a smaller target structure which is magnified with a telescope afterwards.

**Modeling the nonlinear crystal.** The wave vector is a function of the wavelength and the corresponding refractive index, which depends on the wavelength. Consequently, the phase matching condition in Eq. (1) is generally not fulfilled if fields with different wavelengths are propagating through a dispersive medium. Birefringence is one effect which is used for phase matching: For a biaxial crystal the refractive index is determined by three direction-dependent indices $n_x$, $n_y$, and $n_z$ along the principal axes[45]. The effective refractive index at any position in space is given by their projection. This projection results in a refractive index ellipsoid as it is shown in Fig. 4 for a KTP crystal. The direction of the polarization determines the refractive index which is perceived by the corresponding light field.

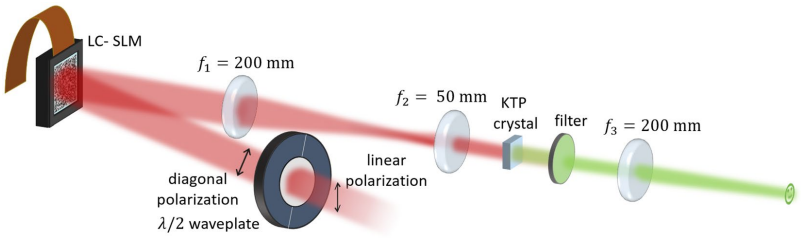


**Figure 2.** Setup for nonlinear beam shaping: the polarization-sensitive LC-SLM shapes only half of the light field. The plane of the SLM is imaged into the nonlinear KTP crystal and the unshaped and shaped field components combine during nonlinear conversion and form the target structure.

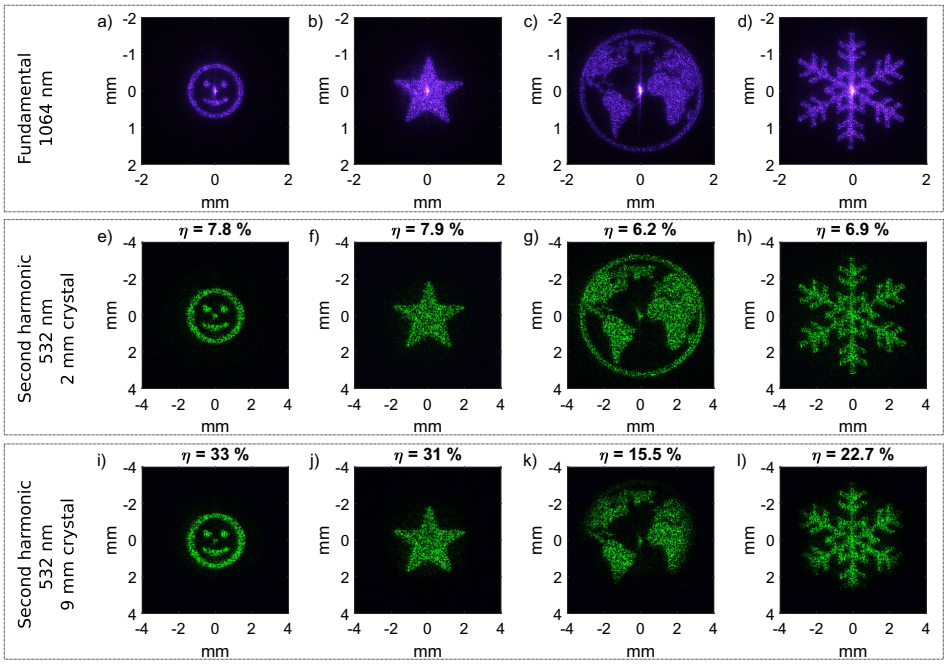


**Figure 3.** Experimentally recorded results for nonlinear beam shaping for two different crystal lengths and the initial result at the fundamental as reference. The measured conversion efficiency $\eta$ is denoted above the individual images.

Thus, phase matching can occur under a specific angle of incidence depending on the phase matching type. Type II phase matching is fulfilled, if two crossed polarization states mix where their average value of the refractive indices corresponds to the refractive index of the second harmonic.

KTP is a biaxial crystal which allows for type I and type II phase matching at different angles of incidence $\theta$ and $\phi$. As KTP exhibits a higher conversion efficiency for type II phase matching, this option is the typical choice. The phase matching angles $\theta_m$ and $\phi_m$ are marked in the refractive index ellipsoid in Fig. 4. The two red curves along the three mutually perpendicular planes of the coordinate system indicate the effective refractive index at the fundamental resulting for a field either polarized within the plane of incidence or perpendicular to that plane. From a perspective of the highest symmetry, the beam oscillating perpendicular to the plane of incidence is called the ordinary beam (dashed lines in Fig. 4) as the refractive index is the same for any angle while a beam with the polarization axis within the plane of incidence is called the extraordinary beam (solid lines in Fig. 4) as the effective refractive index is given by the corresponding ellipse defined by the two refractive indices of the axes spanning that plane. Likewise, the two green curves indicate the refractive index for the frequency-doubled field. As the blue curve marks the mean value of the refractive indices at the fundamental for the two polarization states, its crossing point with the green curve marks the angles for type II phase matching according to $(n_{o/e}^{(\omega)} + n_{e/o}^{(\omega)}) \cdot 0.5 = n_{e/o}^{(2\omega)}$.

Wave front shaping introduces a spectrum of wave vectors centered around the optical axis. Even in a collinear geometry, the generated angular spectrum deviates from the ideal phase matching condition. This deviation causes a refractive index mismatch and affects the conversion efficiency. Due to the high angular acceptance of the chosen KTP crystal, a deflection along $\delta\theta$ and $\delta\phi$ only causes marginal contributions to the phase mismatch. Our application for beam shaping is different from the general definition of the angular acceptance which accounts for a deflection of the total field of the fundamental: The two mixing fields have a slightly different angle as the shaped field is deflected while the other field propagates without any modifications along the phase matching angle. The two incident beams in Fig. 4 refer to this scenario, where the ordinary beam is deflected along $\delta\phi$, while the extraordinary beam follows the phase matching angle. In dependence of the deflection angles $\delta\theta$ and $\delta\phi$, this results in the phase mismatch $\Delta\boldsymbol{k}$:

$$\begin{aligned}\Delta\boldsymbol{k} = \boldsymbol{k}_1^{(\omega)}(\theta_m, \phi_m) + \boldsymbol{k}_2^{(\omega)}(\theta_m + \delta\theta, \phi_m + \delta\phi) \\ - \boldsymbol{k}^{(2\omega)}(\theta_m + \delta\theta/2, \phi_m + \delta\phi/2)\end{aligned} \tag{2}$$

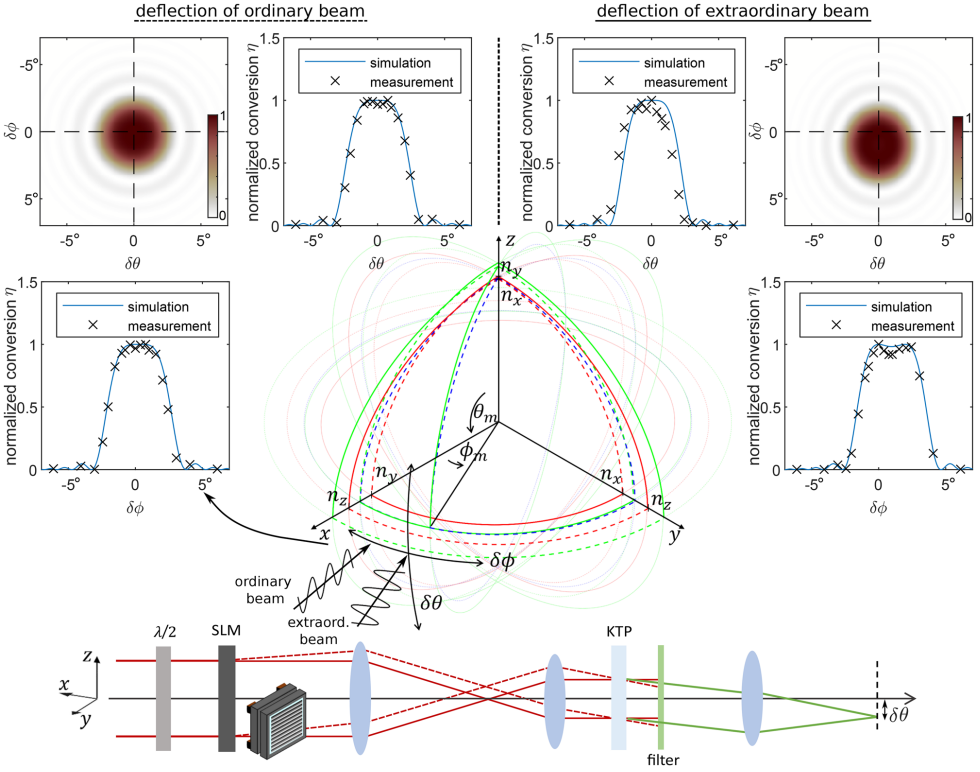


**Figure 4.** Normalized conversion efficiency $\eta$ for a lateral deflection of the ordinary/extraordinary beam and projection along the two axes $\delta\theta$ and $\delta\phi$ for a 2 mm KTP crystal. Experimental measurements along these axes are in good agreement with the simulated curves. The refractive index ellipsoid for the biaxial KTP crystal (dimensions not to scale) shows the phase matching angles $\theta_m = 90\,^\circ$ and $\phi_m = 24.8\,^\circ$ with the axes for beam deflection along $\delta\theta$ and $\delta\phi$. The deflection of the ordinary beam along $\delta\phi$ is indicated with two incoming fields where the extraordinary beam is polarized along the xy plane of the crystal and the deflected ordinary beam is polarized along the z-axis.

We calculate the refractive index mismatch for a deflection along $\delta\theta$ and $\delta\phi$ by calculating the corresponding refractive indices[46] for the wave vectors. In good approximation, the resulting wave vector at the second harmonic is generated at half of the initial deflection angle, as this is the mean value between the deflected and undeflected wave vector at the fundamental. The phase mismatch is thus given by the difference of the wave vectors projected in the direction of the frequency doubled field. The relative conversion efficiency can be deduced from the projected mismatch $\Delta k$ by solving the following equation:

$$I^{(2\omega)} \propto (I^{(\omega)})^2 L^2 \,\mathrm{sinc}^2\left(\frac{\Delta k L}{2}\right) \tag{3}$$

This analytical relation between the second harmonic intensity $I^{(2\omega)}$ and the intensity at the fundamental $I^{(\omega)}$ with respect to the crystal length $L$ and the phase mismatch $\Delta k$ follows when solving the nonlinear wave equation for the assumption of low depletion and the slowly varying amplitude approximation[47]. On this basis, we calculate the relative 2D conversion efficiency for a deviation within the plane of $\delta\theta$ and $\delta\phi$ in Fig. 4. The projection along $\delta\theta$ and $\delta\phi$ is shown in the line plots. An arrow indicates the corresponding curve of conversion for the exemplary deflection in front of the refractive index ellipsoid. According to Snell's law and assuming the small angle approximation, the internal angle corresponds to the external angle connected via the effective refractive index which is perceived by the corresponding wave vector. The graphs in Fig. 4 show the external angle, as this is the relevant value for beam shaping.

Besides calculating the relative conversion efficiency, we perform experiments for an angular deviation introduced by the SLM for beam shaping. To evaluate different angles, we apply a blazed grating either in horizontal

or vertical direction on the SLM and image this plane into the nonlinear crystal which has a length of 2 mm. Similar to beam shaping, only one polarization component is shaped. The corresponding setup is sketched at the bottom of Fig. 4. The coordinate system of the refractive index ellipsoid is rotated with respect to the beam propagation axis as the beam propagates along the matching angle of the KTP crystal.

In the far field we measure the resulting power of the frequency-doubled field and divide it by the measured power of the field at the fundamental. This results in two curves for the relative conversion efficiency, either in the direction of $\delta\theta$ or $\delta\phi$, with respect to no deflection at 0 ° at the optimum phase matching angle. As either the ordinary or extraordinary polarization state can be deflected within the $\delta\theta$ and $\delta\phi$ plane, two different scenarios are possible and both are shown in Fig. 4. Deflecting the ordinary beam causes a highly symmetric profile of the relative conversion efficiency and is thus the favorable option for our application.

Simulation and experiment are in good agreement and show that the conversion efficiency exhibits a broad plateau. Within that range, the light is homogeneously converted, independently of the exact deflection angle. Moreover, the conversion efficiency is not significantly reduced with respect to the actual conversion efficiency without beam shaping. Thus, arbitrary intensity profiles can be shaped within that angular range without reduction in homogeneity or efficiency. The acceptance angle approximately reaches ±2 ° for a 2 mm crystal and ±1 ° for the 9 mm long crystal. It makes sense to compare this value with the maximum deflection angle of the SLM which is determined by $\sin^{-1}(\lambda/(2u)) \cdot 1/M$, where $u$ is the pixel pitch and $M$ is the magnification between the SLM and the crystal. The two smaller images in Fig. 3 approximately acquire 19 % of the SLM's linear field of view, while the two bigger images acquire 32 %. This corresponds to deflection angles of approximately 1.1 ° and 1.9 ° (bearing in mind that the plane of the SLM is imaged with a factor of $M = 0.25$ into the nonlinear crystal and thus the maximum deflection angle is ±6 °).

At the phase matching angle $\theta_m = 90$ °, the crystal is non-critically phase-matched along $\delta\theta$. This means when expanding the mismatch $\Delta k$ in a Taylor series, the first derivative $\partial\Delta k/\partial\theta = 0$ due to the crystal's symmetry and thus only higher order terms with a weaker effect on the phase mismatch contribute[48]. Besides the control mechanism for the wave mixing process it is crucial to choose a nonlinear crystal with a high angular acceptance. We consider temperature-controlled noncritical phase matching or quasi-phase matching as another option but do not discuss this further within the scope of this paper.

## Discussion

Nonlinear beam shaping is a powerful tool as it enables dynamic phase-only beam shaping in new spectral ranges. To optimize this process, two parameters should be considered: While the conversion efficiency should be maximized, the angular acceptance needs to be high enough to ensure homogeneous conversion of the angular spectrum. As both parameters are mutually dependent, we discuss the proper choice of the experimental parameters to optimize the outcome. Moreover, we give an outlook on dynamic phase-only beam shaping in the ultraviolet spectral range.

**Optimizing the conversion efficiency with respect to the angular acceptance.** When approaching a high conversion regime, it is more critical to maintain proper phase matching as the phase mismatch gains an increasing impact on the efficiency of the converted outcome. At high conversion, the angular range of tolerance narrows and this decreases the plateau of homogeneous conversion for the generated angular spectrum. Equation (3) shows the impact of the experimental parameters on the conversion efficiency while keeping the laser power constant. Both increasing the intensity and the crystal length promises higher conversion efficiency. However, both parameters also affect the angular acceptance of the nonlinear crystal.

The effect of the crystal length $L$ is directly stated in Eq. (3). While a longer crystal increases the relative conversion with $L^2$, it also increases the contribution of the phase mismatch as a multiplier of $\Delta k$ in the argument of the sinc function. We use the model of the nonlinear crystal to calculate the relative conversion of the target structures for the 9 mm crystal as they are shown in Fig. 3.

The beam-shaped structures directly reflect the generated angular spectrum and thus the relative conversion can be simulated when multiplying the target image with the calculated angular conversion. Figure 5 shows the simulated results with the corresponding conversion efficiency. This value is calculated as the total measured efficiency without beam shaping multiplied by the integrated relative conversion. Working beyond the limits of phase matching results in weak conversion and the simulated as well as the measured values for the conversion efficiency drop significantly. The experimental parameters should be chosen to work within the pleateau of homogeneous conversion as otherwise not only the quality gets worse but also the efficiency drops significantly. The comparison of the simulated and experimentally measured conversion efficiency explains the strong decrease in efficiency for the two larger structures with their measured conversion efficiency marked as gray crosses in Fig. 6. This decrease can be traced back to insufficient phase matching as the structures are chosen larger than the angular acceptance. As simulation and experiment are in good agreement, proper experimental parameters can be derived on that basis even in a high conversion regime.

Similar to the crystal length $L$, an increase in intensity also improves the conversion efficiency. It can either be increased by increasing the power of the chosen light source or by reducing the illuminated area. As the laser power is typically technically limited, we will focus on the second case. Here the plane of the SLM is imaged with a certain demagnification into the nonlinear crystal to decrease the illuminated area. It is also possible to illuminate the SLM with a smaller beam but this reduces the number of illuminated pixels and unnecessarily increases the intensity on the SLM with respect to potential damage thresholds. It is thus beneficial to design the telescope with the required demagnification. This demagnification increases the intensity in the nonlinear crystal and scales the intensity with $1/M^2$ to gain higher conversion efficiencies. Likewise, the telescope increases the angular spectrum as the deflection angles are proportional to $M$. Similar to the crystal length $L$, this factor

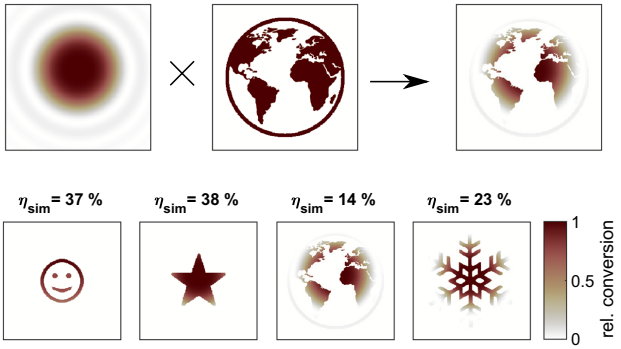


**Figure 5.** Simulated beam conversion for the 9 mm crystal. The simulated efficiency is calculated from the integrated relative conversion multiplied with the efficiency of the 9 mm crystal without beam shaping (compare Fig. 6).

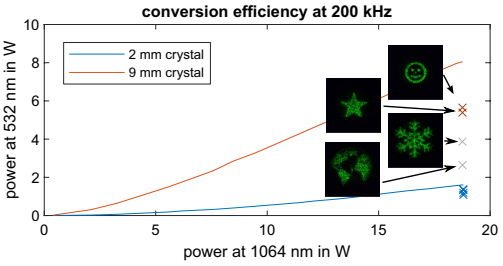


**Figure 6.** Measured output power vs. input power for second harmonic generation with a 2 mm and 9 mm KTP crystal without beam shaping. The crosses indicate the conversion efficiency of the structures in Fig. 3 for beam shaping, with the two intentionally cropped structures in gray.

also affects the phase mismatch $\Delta k$ in the argument of the sinc function as it acts as a multiplier of the initially induced angular spectrum. Consequently, the intensity needs to be considered when modeling the phase mismatch to determine optimum parameters.

In our experimental setup we work with a telescope that decreases the image size by a factor of 0.25 and thus increases the intensity by a factor of 16. This reduction affects the deflection angles and increases them by a factor of 4 as the effective pixel size of the SLM changes. We consider that adjusting the intensity with respect to the required angular spectrum for a given crystal length is reasonable. The resulting plateau should be exactly within the required angular range—neither broader nor narrower—to ensure homogeneous conversion with maximized efficiency.

**Towards dynamic phase-only beam shaping in UV range.** Dynamic beam shaping in the ultraviolet (UV) spectral range is highly limited as many devices absorb the UV light, including liquid crystal displays. This paper demonstrates nonlinear beam shaping from the infrared to visible spectral range. Nonetheless, other conversion processes are possible, reaching from second harmonic generation at different fundamental frequencies up to other nonlinear processes like sum frequency generation. Currently, there is research on new materials with tunable birefringence in the UV spectral range for spatial light modulators with results showing light modulation at 303 nm[49]. We see the potential of our method for approaching even deeper UV spectral ranges.

This section presents a few thoughts on proper nonlinear crystals and conversion processes for dynamic phase-only beam shaping in the UV range.

Ultrashort pulsed laser systems often feature nonlinear crystals for frequency conversion, for example to the second or third harmonic. High-energetic short wavelengths in the UV range of ultrashort pulsed laser systems are thus often generated with nonlinear frequency conversion from the visible or infrared range. Consequently, the initial conditions often enable a direct integration of nonlinear beam shaping into the laser setup and ideally this can be performed with conversion efficiencies close to the initial values.

To achieve high-quality results, the nonlinear crystal should have a broad angular acceptance and the conversion process needs to be non-degenerate. Sum frequency generation with an LBO crystal from 1064 nm and 532 nm to 355 nm is one option. The major benefit of this crystal is the high angular acceptance. Similarly, sum frequency generation with CLBO[50] from 1064 nm and 266 nm to 213 nm should be possible. In both options the process is inherently non-degenerate as two different wavelengths mix. While the SLM can either shape the light field in the infrared or visible spectral range, only the infrared light can be shaped in the latter case as the SLM can not shape light at 266 nm. With one of the options suggested here or other nonlinear processes, we see the potential of using nonlinear beam shaping to approach the UV spectral range. This enables dynamic phase-only beam shaping beyond the physical limits of the liquid crystal display.

## Methods

Nonlinear phase-only beam shaping with a liquid crystal display is possible as the applied phase information is conserved during the frequency conversion. However, as second harmonic generation is a degenerate process, the mixing waves need to be controlled by making the interacting fields distinguishable. We use the requirements of type II phase matching to unambiguously define the outcome of the second harmonic. Under this condition, only fields of crossed polarization can mix efficiently. A half wave plate, abbreviated with $\lambda/2$ in Fig. 7 is placed in front of the SLM to generate diagonal polarization with respect to the SLM's orientation. As the liquid crystals are polarization-sensitive, only half of the field is shaped, while the other part remains unshaped. Consequently, a shaped component can only mix with the unshaped plane wave front. In Fig. 7 the two polarization components are indicated as the ordinary and the extraordinary beam. The polarization configuration in the figure refers to where the ordinary beam is shaped. If the extraordinary beam is shaped, an additional half wave plate after the SLM helps to rotate the polarization states correspondingly. This might be beneficial when working off-axis to separate non-diffracted light as the area of quasi-homogeneous conversion is shifted away from the center of the optical axis.

A telescope images the plane of the SLM into the nonlinear crystal. This ensures a homogeneous intensity distribution within the nonlinear crystal which is required to convert all field components equally within a range of proper phase matching. In good approximation, the resulting wave vectors at the second harmonic reduce to half of the initially set angle of the shaped field component, as this is the sum of the two involved wave vectors.

The SLM is the model LSH0701010 from Hamamatsu (Hamamatsu, Japan) and has a pixel resolution of 800 px × 600 px with a pixel pitch of 20 µm. The beam diameter on the LC-SLM is 14 mm. To increase the intensity to obtain a higher conversion efficiency, we design our telescope to demagnify the beam by $M = 0.25$. The corresponding focal lengths are $f_1 = 200$ mm and $f_2 = 50$ mm. Before the target distribution is imaged to the far field with a $f_3 = 200$ mm lens, the remaining IR light is blocked with the filter FL532-10 from Thorlabs (NJ, USA). The laser system Fuego from Time-Bandwidth Products (CA, USA) emits 10 ps pulses at a repetition frequency of 200 kHz at a wavelength of 1064 nm. The power measurements were done with the power meter PM10 from Coherent (CA, USA) and PM160 from Thorlabs. We record RGB images with the camera model UI-3000SE-C-HQ from IDS (Obersulm, Germany).

## Conclusion

Nonlinear computer-generated holography is gaining increasing attention and there is a lot of research on structuring nonlinear crystals but this process is technically challenging and static. These deficiencies can be overcome by thin holograms generated with dynamic liquid crystal displays. However, research on nonlinear

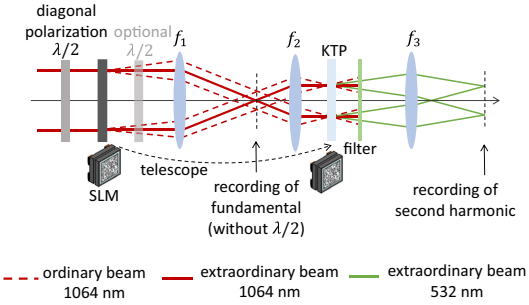


**Figure 7.** Experimental setup for nonlinear beam shaping: A half wave plate introduces diagonal polarization on the beam impinging on the SLM. Thus, only half of the field is shaped while the crossed polarization component remains unshaped. A telescope images the plane of the SLM into the nonlinear KTP crystal. Here, the two polarization components mix and shape the targeted field. After a filter separates the second harmonic from the fundamental, a lens images the target image, where the second harmonic signal is recorded. As the shaped result is sensitive to the deflected polarization component, a half wave plate after the SLM allows for changing the deflected and non-deflected polarization component.

beam shaping is still in its infancy. We present a high-quality and highly efficient method for nonlinear dynamic phase-only beam shaping with a simple concept: The mixing process needs to be non-degenerate by employing a control mechanism and the angular acceptance of the nonlinear crystal needs to support the angular spectrum generated by wave front shaping. Based on this, we demonstrate beam shaping at the second harmonic with conversion efficiencies close to the ones without beam shaping. This is mainly due to the fact that we work at a plateau of constant conversion efficiency for the generated angular spectrum. While working within that range, the conversion efficiency is mainly given by the conversion efficiency without beam shaping and thus this method is highly efficient. Furthermore, the quality of the frequency-converted result is of the same quality as for beam shaping at the fundamental. We see high potential in this approach as it not only enables highly-efficient and high-quality beam shaping with thin holograms but due to its simplicity, it can be easily combined with other elaborated processes. Based on nonlinear beam shaping, the spectral range of dynamic liquid crystal displays can be extended beyond the physical limits as we discuss here for the UV spectral range.

## Data availability

Data underlying the results presented in this paper may be obtained from the corresponding author upon reasonable request.

Received: 5 April 2023; Accepted: 21 June 2023
Published online: 26 June 2023

## References

1. Mainman, T. H. Stimulated optical radiation in ruby. *Nature* **187**, 493–494. https://doi.org/10.1038/187493a0 (1960).
2. Maurer, C., Jesacher, A., Bernet, S. & Ritsch-Marte, M. What spatial light modulators can do for optical microscopy. *Laser Photon. Rev.* **5**, 81–101. https://doi.org/10.1002/lpor.200900047 (2010).
3. Rubinsztein-Dunlop, H. *et al.* Roadmap on structured light. *J. Opt.* **19**, 013001 (2016).
4. Accanto, N. *et al.* Multiplexed temporally focused light shaping for high-resolution multi-cell targeting. *Optica* **5**, 1478–1491. https://doi.org/10.1364/OPTICA.5.001478 (2018).
5. Sugioka, K. & Cheng, Y. Ultrafast lasers–reliable tools for advanced materials processing. *Light Sci. Appl.* **3**, e149. https://doi.org/10.1038/lsa.2014.30 (2014).
6. Sugioka, K. Progress in ultrafast laser processing and future prospects. *Nanophotonics* **6**, 393–413. https://doi.org/10.1515/nanoph-2016-0004 (2017).
7. Orazi, L., Romoli, L., Schmidt, M. & Li, L. Ultrafast laser manufacturing: From physics to industrial applications. *CIRP Ann.* **70**, 543–566. https://doi.org/10.1016/j.cirp.2021.05.007 (2021).
8. Yariv, A. Four wave nonlinear optical mixing as real time holography. *Opt. Commun.* **25**, 23–25. https://doi.org/10.1016/0030-4018(78)90079-2 (1978).
9. Abraham, N. B. & Firth, W. J. Overview of transverse effects in nonlinear-optical systems. *J. Opt. Soc. Am. B* **7**, 951. https://doi.org/10.1364/josab.7.000951 (1990).
10. Basistiy, I., Bazhenov, V., Soskin, M. & Vasnetsov, M. Optics of light beams with screw dislocations. *Opt. Commun.* **103**, 422–428. https://doi.org/10.1016/0030-4018(93)90168-5 (1993).
11. Dholakia, K., Simpson, N. B., Padgett, M. J. & Allen, L. Second-harmonic generation and the orbital angular momentum of light. *Phys. Rev. A* **54**, R3742–R3745. https://doi.org/10.1103/physreva.54.r3742 (1996).
12. Courtial, J., Dholakia, K., Allen, L. & Padgett, M. J. Second-harmonic generation and the conservation of orbital angular momentum with high-order Laguerre-Gaussian modes. *Phys. Rev. A* **56**, 4193–4196. https://doi.org/10.1103/physreva.56.4193 (1997).
13. Mair, A., Vaziri, A., Weihs, G. & Zeilinger, A. Entanglement of the orbital angular momentum states of photons. *Nature* **412**, 313–316. https://doi.org/10.1038/35085529 (2001).
14. Shao, G.-H., Wu, Z.-J., Chen, J.-H., Xu, F. & Lu, Y.-Q. Nonlinear frequency conversion of fields with orbital angular momentum using quasi-phase-matching. *Phys. Rev. A* **88**, 063827. https://doi.org/10.1103/physreva.88.063827 (2013).
15. Zhou, Z.-Y. *et al.* Generation of light with controllable spatial patterns via the sum frequency in quasi-phase matching crystals. *Sci. Rep.* **4**, 1–5. https://doi.org/10.1038/srep05650 (2014).
16. Libster-Hershko, A., Trajtenberg-Mills, S. & Arie, A. Dynamic control of light beams in second harmonic generation. *Opt. Lett.* **40**, 1944. https://doi.org/10.1364/ol.40.001944 (2015).
17. Li, Y., Zhou, Z.-Y., Ding, D.-S. & Shi, B.-S. Sum frequency generation with two orbital angular momentum carrying laser beams. *J. Opt. Soc. Am. B* **32**, 407. https://doi.org/10.1364/josab.32.000407 (2015).
18. Steinlechner, F., Hermosa, N., Pruneri, V. & Torres, J. P. Frequency conversion of structured light. *Sci. Rep.* **6**, 1–8. https://doi.org/10.1038/srep21390 (2016).
19. Buono, W. T. *et al.* Polarization-controlled orbital angular momentum switching in nonlinear wave mixing. *Opt. Lett.* **43**, 1439. https://doi.org/10.1364/ol.43.001439 (2018).
20. Qiu, X., Li, F., Liu, H., Chen, X. & Chen, L. Optical vortex copier and regenerator in the Fourier domain. *Photon. Res.* **6**, 641. https://doi.org/10.1364/prj.6.000641 (2018).
21. Shen, Y. *et al.* Optical vortices 30 years on: OAM manipulation from topological charge to multiple singularities. *Light Sci. Appl.* **8**, 90. https://doi.org/10.1038/s41377-019-0194-2 (2019).
22. Li, J. *et al.* Directly generating vortex beams in the second harmonic by a spirally structured fundamental wave. *Chin. Opt. Lett.* **19**, 060005 (2021).
23. da Silva, B. P. *et al.* Spin to orbital angular momentum transfer in frequency up-conversion. *Nanophotonics* **11**, 771–778. https://doi.org/10.1515/nanoph-2021-0493 (2021).
24. Hancock, S. W., Zahedpour, S. & Milchberg, H. M. Second-harmonic generation of spatiotemporal optical vortices and conservation of orbital angular momentum. *Optica* **8**, 594. https://doi.org/10.1364/optica.422743 (2021).
25. Wu, H.-J. *et al.* Radial modal transitions of Laguerre-Gauss modes during parametric up-conversion: Towards the full-field selection rule of spatial modes. *Phys. Rev. A* **101**, 063805. https://doi.org/10.1103/physreva.101.063805 (2020).
26. Fang, X. *et al.* High-dimensional orbital angular momentum multiplexing nonlinear holography. *Adv. Photon.* **3**, 015001. https://doi.org/10.1117/1.ap.3.1.015001 (2021).
27. Buono, W. T. & Forbes, A. Nonlinear optics with structured light. *Opto-Electron. Adv.* **5**, 210174–1 (2022).
28. Berger, V. Nonlinear photonic crystals. *Phys. Rev. Lett.* **81**, 4136–4139. https://doi.org/10.1103/physrevlett.81.4136 (1998).
29. Hong, X.-H., Yang, B., Zhang, C., Qin, Y.-Q. & Zhu, Y.-Y. Nonlinear volume holography for wave-front engineering. *Phys. Rev. Lett.* **113**, 163902. https://doi.org/10.1103/physrevlett.113.163902 (2014).
30. Shapira, A., Naor, L. & Arie, A. Nonlinear optical holograms for spatial and spectral shaping of light waves. *Sci. Bull.* **60**, 1403–1415. https://doi.org/10.1007/s11434-015-0855-3 (2015).

31. Xu, T. *et al.* Three-dimensional nonlinear photonic crystal in ferroelectric barium calcium titanate. *Nat. Photon.* **12**, 591–595. https://doi.org/10.1038/s41566-018-0225-1 (2018).
32. Wei, D. *et al.* Experimental demonstration of a three-dimensional lithium niobate nonlinear photonic crystal. *Nat. Photon.* **12**, 596–600. https://doi.org/10.1038/s41566-018-0240-2 (2018).
33. Liu, S. *et al.* Nonlinear wavefront shaping with optically induced three-dimensional nonlinear photonic crystals. *Nat. Commun.* **10**, 3208. https://doi.org/10.1038/s41467-019-11114-y (2019).
34. Liu, S., Mazur, L. M., Krolikowski, W. & Sheng, Y. Nonlinear volume holography in 3d nonlinear photonic crystals. *Laser Photon. Rev.* **14**, 2000224. https://doi.org/10.1002/lpor.202000224 (2020).
35. Zhu, B. *et al.* Second-harmonic computer-generated holographic imaging through monolithic lithium niobate crystal by femtosecond laser micromachining. *Opt. Lett.* **45**, 4132. https://doi.org/10.1364/ol.394162 (2020).
36. Trajtenberg-Mills, S. & Arie, A. Shaping light beams in nonlinear processes using structured light and patterned crystals. *Opt. Mater. Express* **7**, 2928. https://doi.org/10.1364/ome.7.002928 (2017).
37. Liu, H. & Chen, X. The manipulation of second-order nonlinear harmonic wave by structured material and structured light. *J. Nonlinear Opt. Phys. Mater.* **27**, 1850047. https://doi.org/10.1142/s0218863518500479 (2018).
38. Keren-Zur, S., Avayu, O., Michaeli, L. & Ellenbogen, T. Nonlinear beam shaping with plasmonic metasurfaces. *ACS Photon.* **3**, 117–123. https://doi.org/10.1021/acsphotonics.5b00528 (2015).
39. Almeida, E., Bitton, O. & Prior, Y. Nonlinear metamaterials for holography. *Nat. Commun.* **7**, 12533. https://doi.org/10.1038/ncomms12533 (2016).
40. Liu, H. *et al.* Dynamic computer-generated nonlinear-optical holograms. *Phys. Rev. A* **96**, 023801. https://doi.org/10.1103/physreva.96.023801 (2017).
41. Liu, H., Zhao, X., Li, H., Zheng, Y. & Chen, X. Dynamic computer-generated nonlinear optical holograms in a non-collinear second-harmonic generation process. *Opt. Lett.* **43**, 3236. https://doi.org/10.1364/ol.43.003236 (2018).
42. Wu, Y., Liu, H. & Chen, X. Three-dimensional nonlinear optical holograms. *Phys. Rev. A* **102**, 063505. https://doi.org/10.1103/physreva.102.063505 (2020).
43. Yao, W. *et al.* Angle-multiplexing nonlinear holography for controllable generations of second-harmonic structured light beams. *Front. Phys.* **9**, 751860. https://doi.org/10.3389/fphy.2021.751860 (2021).
44. Gerchberg, R. W. & Saxton, W. O. A practical algorithm for the determination of phase from image and diffraction plane pictures. *Optik* **35**, 237–246 (1972).
45. Zhang, W., Yu, H., Wu, H. & Halasyamani, P. S. Phase-matching in nonlinear optical compounds: A materials perspective. *Chem. Mater.* **29**, 2655–2668. https://doi.org/10.1021/acs.chemmater.7b00243 (2017).
46. Yao, J. Q. & Fahlen, T. S. Calculations of optimum phase match parameters for the biaxial crystal KTiOPO_4. *J. Appl. Phys.* **55**, 65–68. https://doi.org/10.1063/1.332850 (1984).
47. Boyd, R. W. *Nonlinear Optics* (Academic Press, 2020).
48. Fan, T. Y. *et al.* Second harmonic generation and accurate index of refraction measurements in flux-grown KTiOPO_4. *Appl. Opt.* **26**, 2390. https://doi.org/10.1364/ao.26.002390 (1987).
49. Xu, Y. *et al.* Deep ultraviolet hydrogel based on 2D cobalt-doped titanate. *Light Sci. Appl.* **12**, 1. https://doi.org/10.1038/s41377-022-00991-6 (2023).
50. Mori, Y., Kuroda, I., Nakajima, S., Sasaki, T. & Nakai, S. New nonlinear optical crystal: Cesium lithium borate. *Appl. Phys. Lett.* **67**, 1818–1820. https://doi.org/10.1063/1.115413 (1995).

## Acknowledgements
The authors gratefully acknowledge funding from the Erlangen Graduate School in Advanced Optical Technologies (SAOT) by the German Research Foundation (DFG) in the framework of the German excellence initiative and the authors acknowledge financial support by Deutsche Forschungsgemeinschaft and Friedrich-Alexander-Universität Erlangen-Nürnberg within the funding programme "Open Access Publication Funding".

## Author contributions
L.A. and C.R. conceived the method. L.A. recorded the experimental data and performed simulations. L.A., C.R. and K.C. analyzed the data. C.A. performed provisional experiments. L.A., C.R., K.C., N.B. and M.S. contributed to the manuscript and MS acquired funding.

## Funding
Open Access funding enabled and organized by Projekt DEAL.

## Competing interests
The authors declare no competing interests.

## Additional information
**Correspondence** and requests for materials should be addressed to L.A.

**Reprints and permissions information** is available at www.nature.com/reprints.

**Publisher's note** Springer Nature remains neutral with regard to jurisdictional claims in published maps and institutional affiliations.

## 6.2 Diminishing Speckle Noise during Nonlinear Phase-Only Beam Shaping

[P6] Published at *2023 Conference on Lasers and Electro-Optics Europe & European Quantum Electronics Conference (CLEO/Europe-EQEC)*, 10.1109/CLEO/Europe-EQEC57999.2023.10232165.


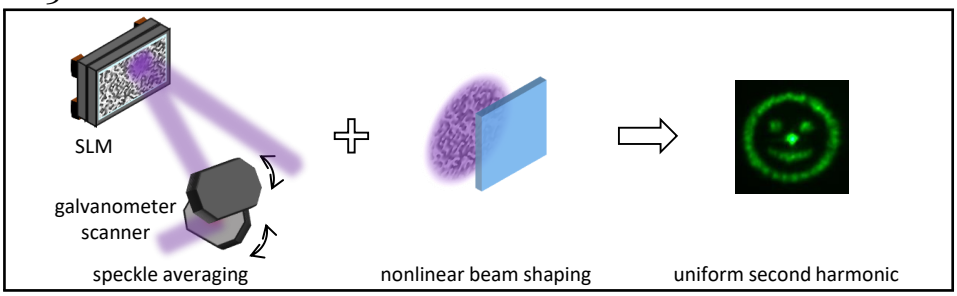


Graphical abstract: Diminishing Speckle Noise during Nonlinear Phase-Only Beam Shaping

To diminish speckle during nonlinear phase-only beam shaping, it requires only little adaptions to transfer the developed method of uniform beam shaping by averaging in Section 4.1.1 to nonlinear beam shaping. As a first step, a half wave plate introduces diagonal polarization before the beam impinges on the LCoS SLM. Originally, the phase mask in the speckle averaging setup (compare Section 4.1.1) is combined with an additional Fresnel lens term. Its intention is to separate non-diffracted light from the target structure. However, this requires shaping the full light field. While separating non-diffracted light is highly beneficial, it intervenes with the basic principle of nonlinear beam shaping where diagonal polarization on the LCoS SLM causes only half of the light field being shaped. This step is required to achieve an unambiguous assignment of the resulting field at the second harmonic. Keeping the Fresnel lens term part of the phase mask in the scanner setup would thus only shape half of the light field and only this part is imaged back on the galvanometer mirror. Consequently, the lens within the phase mask is exchanged with a physical lens. For the sake of simplicity, this lens is directly positioned in front of the LCoS SLM display. Both polarization components interact with this physical lens and only one polarization component is shaped by the phase mask on the LCoS SLM. After the beam leaves the scanner setup, the plane of the SLM is imaged into the nonlinear KTP crystal. The resulting target structure in the focal plane

appears uniform as the speckle pattern averages with the scanner movement. The experimental results demonstrate the possibility of combining speckle averaging with nonlinear beam shaping.

## Highlights

- Uniform beam shaping at the second harmonic by averaging
- Compatibility of nonlinear beam shaping with speckle averaging provides high-quality results at the frequency-converted output
- Perspective of uniform beam shaping beyond the spectral limits of liquid crystal displays

# Diminishing Speckle Noise during Nonlinear Phase-Only Beam Shaping

**Lisa Ackermann**[1,2], **Clemens Roider**[1], **Kristian Cvecek**[1,2], **Nicolas Barré**[1,2], **and Michael Schmidt**[1,2]
*1. Institute of Photonic Technologies, Friedrich-Alexander-Universität Erlangen-Nürnberg, Konrad-Zuse-Str. 3, 91052 Erlangen, Germany*
*2. School of Advanced Optical Technologies (SAOT), Friedrich-Alexander-Universität Erlangen-Nürnberg, Paul-Gordan-Str. 6, 91052 Erlangen, Germany*

The liquid crystal spatial light modulator (LC-SLM) is a powerful device to dynamically shape arbitrary intensity distributions and finds application in research and industry. While wave front shaping is highly efficient and thus favorable, the shaped intensity profile suffers from speckle noise and, moreover, LC-SLMs are technically limited to the visible, near-infrared and mid-infrared spectral ranges. We make use of nonlinear optics to enlarge the spectral range by shaping the light field at the fundamental but achieving the desired outcome at the second harmonic [1]. Moreover, we diminish speckle noise by temporal averaging to achieve results of high uniformity and quality. To this end, usually several different patterns are displayed sequentially on the SLM what results in poor efficiency due to the low frame rate. We overcome this problem by using a single phase mask while the beam is scanned over the SLM with a galvanometer scanner and subsequently de-scanned [2].

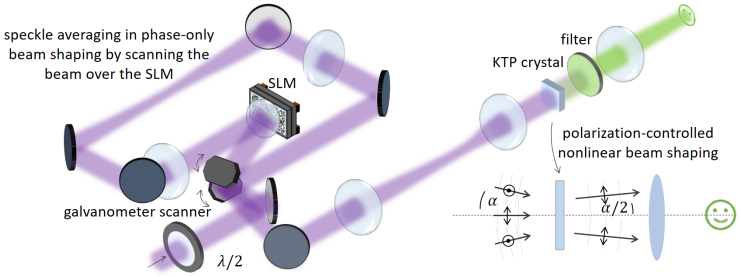


**Fig. 1** Experimental setup to combine speckle averaging with nonlinear beam shaping.

Combining those two methods enables uniform beam shaping at the frequency-converted field. The experimental setup is presented in Fig. 1. Moving the beam over a single phase mask provides excellent speckle averaging and the galvanometer scanner, which introduces the movement, directly compensates for the applied angle as the beam is sent back to it. Thus, the speckle pattern gets averaged, while the beam remains static. For frequency doubling, the plane of the SLM is subsequently imaged into the nonlinear KTP crystal. As second harmonic generation is a coherent process, the applied phase distribution from the SLM is conserved. However, the process is also degenerate as two fields at the same frequency mix and they need to be made distinguishable to keep control on the outcome phase. The crossed polarization states at type II phase matching may act as such a control mechanism: When impinging on the SLM with diagonal polarization, only half of the light field is shaped as the liquid crystals are polarization-sensitive. Consequently, only an unshaped field component mixes with a shaped component and the frequency-converted wave front is determined by the initially applied phase mask on the SLM while to deflection angles are reduced by half. We show experimental results for beam shaping at the second harmonic in Fig. 2 with the results at the fundamental as reference. We envision this technique as step toward beam shaping beyond the physical limits of the LC-SLM.

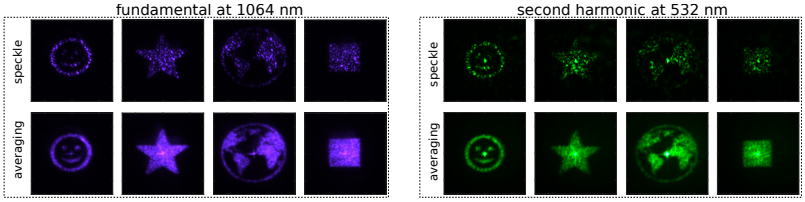


**Fig. 2** Experimentally recorded RGB images at the fundamental and second harmonic with and without averaging.

## References

[1] L. Ackermann, C. Roider, K. Cvecek, N. Barré, C. Aigner, M. Schmidt, "Polarization-Controlled Nonlinear Computer-Generated Holography," ArXiv, `https://doi.org/10.48550/arXiv.2301.10093` (2023)
[2] L. Ackermann, C. Roider, M. Gehring, K. Cvecek, M. Schmidt, "High-speed speckle averaging for phase-only beam shaping in laser materials processing," SSRN, `http://dx.doi.org/10.2139/ssrn.4178974` (2022)

# 7 Summary and Conclusion

Dynamic phase-only beam shaping with liquid crystal displays is a versatile and widely used tool in many research applications. Phase-only beam shaping using LCoS SLMs does not cause significant losses and the outcome can be dynamically adjusted. This provides high flexibility and the option of dynamic process control. However, as phase-only beam shaping does not allow sufficient control of the full light field, amplitude and wave front cannot be shaped in the same image plane without inducing significant losses. When aiming for a specific intensity distribution, the wave front in the beam shaping plane is typically tailored so that the beam emerges into the desired amplitude distribution while the wave front in the target plane remains uncontrolled. This leads to so-called phase vortices. These phase vortices cause destructive interference, which manifests itself as speckle superimposed on the target structure.
Many methods have been developed to overcome this issue. However, typically, they provide a compromise between efficiency and quality. This thesis developed and experimentally validated three methods for uniform beam shaping. All of these maintain the initially high light efficiency and provide beam shaping results of high quality. As the methods are conceived for ultrashort pulse laser materials processing, they avoid excessive fluences on the involved optical elements while featuring high feasibility. All developed methods are application-oriented and thus especially robust in their practical implementation. Two methods are based on averaging intensity patterns without being limited by the frame rate of the liquid crystal display. To achieve uniform beam profiles within each single pulse, the third method employs two phase modulation planes.
Even though averaging-based methods and direct uniform beam shaping provide intensity patterns of similar appearance, the methodologies differ and this thesis investigates the thereby caused influence on material ablation. The evaluation of the ablated profiles shows that both approaches result in a similar amount of ablated material when working with the same laser power and number of pulses. While wave front and amplitude shaping with two phase-only beam shaping planes is especially beneficial for resolving fine contours, averaging is the more robust method and especially powerful when ablating uniform areas. On that basis, an averaging-based method was chosen to further investigate the influence of the material on the processing result. The method was used to ablate uniform areas on different metal samples. While effects of the grain structure are not expected to dominate process dynamics and a series of ablation experiments on each material indicated position independence and good reproducibility, significant differ-

ences in ablation uniformity appeared between the different materials. The results reveal a correlation between the averaged intensity profile and the topography of the ablated squares. This correlation suggests that thermal material properties play an important role. As the resulting uniformity of the ablated surfaces and the material-specific thermal conductivity show a near-linear relationship, the achievable ablation uniformity can be estimated based on the thermal conductivity. Having a prediction of the ablation uniformity allows for assessing the expected outcome with the ability to refine the developed beam shaping methods, e.g. combining averaging by scanning with additional averaging of individual phase masks. To some extent, it is also possible to optimize the outcome by adapting the laser parameters as this influences the process dynamics.

Similar to the shaped intensity profile and the analyzed influence of the processed materials, the laser wavelength is another crucial process parameter to optimize the outcome. The laser wavelength determines the physical mechanisms of light matter interaction and it thus needs to be chosen carefully when aiming for precise and efficient laser materials processing. However, liquid crystal displays are currently technically limited to the visible, near-infrared, and mid-infrared spectral ranges. As some materials have to be processed with UV light, the concept of nonlinear computer-generated holography provides the basis for phase-only beam shaping at spectral ranges beyond the current limits of liquid crystal displays. As nonlinear light conversion is a coherent process, the phase information is conserved and this method can be combined with phase-only beam shaping. It is thus possible to shape the wave front at the fundamental and convert the wavelength thereafter. While this thesis only analyzed the general concept of frequency-converting the shaped light field from the infrared to the visible spectral range, the results give an outlook on phase-only beam shaping at the UV spectral range. This provides a wide range of new opportunities for future research. Further, nonlinear beam shaping was combined with speckle averaging to achieve uniform beam profiles at the second harmonic. Besides improving the quality of the outcome, this experimental implementation shows the applicability and compatibility of the developed methods.

Overall, this thesis contributes methods for creating uniform beam profiles of arbitrary shape while maintaining high precision and efficiency. The identification of potential influence factors of the beam shaping method and the processed material helps to estimate and control the uniformity of the ablated outcome. In combination with nonlinear light conversion, uniform beam shaping is not limited to the spectral range of the liquid crystal display and the wavelength can be adapted specifically to the requirements. This enables precise and efficient ultrashort pulse laser materials processing for a wide range of applications in research and industry.

**Contributions in brief**

- Methods for uniform beam shaping featuring
  - high efficiency and quality,
  - high feasibility and practicality,
  - applicability to high-energy lasers,
  - and laser ablation results of high uniformity.
- Analysis of the influence of the material during laser ablation enables
  - the identification of potential impact factors, e.g. thermal conductivity
  - and the possibility to estimate and potentially adjust the uniformity.
- Nonlinear phase-only beam shaping
  - is a step towards beam shaping beyond the spectral limits of liquid crystal displays
  - and uniform beam profiles can be achieved by speckle averaging.

⇒ Uniform beam shaping at the optimum wavelength while elucidating material-specific properties pertinent to ablation results with high uniformity.

# 8 Zusammenfassung und Ausblick

Die dynamische Wellenfrontformung mit Flüssigkristalldisplays ist eine vielseitige und weit verbreitete Methode in vielen Forschungsanwendungen. Reine Wellenfrontformung mit LCoS SLMs verursacht keine nennenswerten Verluste und die Stahlform kann dynamisch angepasst werden. Das gewährleistet hohe Flexibilität und die Möglichkeit zur dynamischen Prozesssteuerung. Da die reine Wellenfrontformung jedoch keine ausreichende Kontrolle über das gesamte Lichtfeld ermöglicht, können Amplitude und Wellenfront nicht in der gleichen Bildebene geformt werden, ohne dass es zu erheblichen Verlusten kommt. Wenn eine bestimmte Intensitätsverteilung angestrebt wird, wird die Wellenfront in der Strahlformungsebene in der Regel so angepasst, dass der propagierende Strahl in die gewünschte Amplitudenverteilung mündet, während die Wellenfront in der Zielebene unkontrolliert bleibt. Dies führt zu sogenannten Phasenwirbeln. Diese Phasenwirbel verursachen destruktive Interferenzen, die sich als überlagerndes Specklemuster in der Zielstruktur manifestieren.
Es wurden viele Methoden entwickelt, um dieses Problem zu lösen. In der Regel ermöglichen sie jedoch nur einen Kompromiss zwischen Effizienz und Qualität. In dieser Arbeit wurden drei Methoden zur ebenen Strahlformung entwickelt und experimentell validiert. Alle diese Methoden erhalten die ursprünglich hohe Lichteffizienz und liefern Strahlformungsergebnisse von hoher Qualität. Da die Verfahren für die ultrakurzgepulste Lasermaterialbearbeitung konzipiert sind, vermeiden sie übermäßig hohe Fluenzen auf den beteiligten optischen Elementen und zeichnen sich durch eine hohe Nutzerfreundlichkeit aus. Alle entwickelten Methoden sind anwendungsorientiert und daher besonders robust in der praktischen Umsetzung. Zwei Verfahren basieren auf der Mittelung von Intensitätsmustern, ohne durch die Bildrate der Flüssigkristallanzeige begrenzt zu sein. Die dritte Methode verwendet zwei Phasenmodulationsebenen, um ebene Strahlprofile innerhalb jedes einzelnen Pulses zu erreichen.
Obwohl die auf Mittelwertbildung basierenden Methoden und die direkte ebene Strahlformung ähnlich aussehende Intensitätsmuster erzeugen, unterscheiden sich die Methoden und diese Arbeit untersucht den dadurch verursachten Einfluss auf den Materialabtrag. Die Auswertung der abgetragenen Profile zeigt, dass beide Ansätze bei gleicher Laserleistung und Pulszahl zu einer ähnlichen Menge an abgetragenem Material führen. Während Wellenfront- und Amplitudenformung mit zwei phasenmodulierenden Strahlformungsebenen vor allem zur Auflösung feiner Konturen vorteilhaft ist, ist Mittelung die robustere Methode und besonders leistungsfähig, wenn gleichförmige Bereiche abgetragen werden sollen. Aus diesem Grund wurde

eine auf Mittelwertbildung basierende Methode gewählt, um den Einfluss des Materials auf das Bearbeitungsergebnis weiter zu untersuchen. Die Methode wurde genutzt, um ebene Bereiche auf verschiedenen Metallproben abgetragen. Während nicht zu erwarten ist, dass Effekte der Kornstruktur die Prozessdynamik dominieren und eine Reihe von Ablationsexperimenten an den einzelnen Materialien positionsunabhängig und reporduzierbar waren, zeigten sich signifikante Unterschiede in der Gleichförmigkeit der abgetragenen Oberflächen zwischen den verschiedenen Materialien. Die Ergebnisse weisen eine Korrelation zwischen dem gemittelten Intensitätsprofil und der Topographie der abgetragenen Quadrate auf. Diese Korrelation deutet darauf hin, dass die thermischen Materialeigenschaften eine wichtige Rolle spielen. Da die resultierende Gleichförmigkeit der abgetragenen Oberflächen und die materialspezifische Wärmeleitfähigkeit einen nahezu linearen Zusammenhang aufweisen, kann die erreichbare Abtragsgleichförmigkeit anhand der Wärmeleitfähigkeit abgeschätzt werden. Diese Vorhersage ermöglicht die Beurteilung des zu erwartenden Ergebnisses und die Option zur Verfeinerung der entwickelten Strahlformungsmethoden, z. B. die Kombination von Mittelung durch Scannen und zusätzlicher Mittelung einzelner Phasenmasken. Bis zu einem gewissen Grad ist es auch möglich, das Ergebnis durch Anpassung der Laserparameter zu optimieren, da dies die Prozessdynamik beeinflusst.

Ähnlich wie das geformte Intensitätsprofil und der analysierte Einfluss der bearbeiteten Materialien ist die Laserwellenlänge ein weiterer entscheidender Prozessparameter zur Optimierung des Ergebnisses. Die Laserwellenlänge bestimmt die physikalischen Mechanismen der Licht-Materie-Wechselwirkung und muss daher sorgfältig ausgewählt werden, wenn eine präzise und effiziente Lasermaterialbearbeitung angestrebt wird. Flüssigkristalldisplays sind jedoch derzeit technisch auf den sichtbaren, den nah infraroten und den mittleren infraroten Spektralbereich beschränkt. Da einige Materialien mit UV Licht bearbeitet werden müssen, bietet das Konzept der nichtlinearen computergenerierten Holografie die Grundlage für Wellenfrontformung in Spektralbereichen, die über die derzeitigen Grenzen von Flüssigkristalldisplays hinausgehen. Da es sich bei der nichtlinearen Lichtkonversion um einen kohärenten Prozess handelt, bleibt die Phaseninformation erhalten, und diese Methode kann mit der Wellenfrontformung kombiniert werden. Es ist also möglich, die Wellenfront der Fundamentalen zu formen und die Wellenlänge danach umzuwandeln. Während in dieser Arbeit nur das allgemeine Konzept der Frequenzkonversion des geformten Lichtfeldes vom infraroten in den sichtbaren Spektralbereich analysiert wurde, geben die Ergebnisse einen Ausblick auf Wellenfrontformung im UV Spektralbereich. Daraus hinaus ergeben sich zahlreiche neue Möglichkeiten für die zukünftige Forschung. Außerdem wurde nichtlineare Strahlformung

mit der Specklemittelung kombiniert, um ebene Strahlprofile in der zweiten Harmonischen zu erzeugen. Diese experimentelle Umsetzung verbessert nicht nur die Qualität der Ergebnisse, sondern zeigt auch die Anwendbarkeit und Kompatibilität der entwickelten Methoden.
Die vorliegende Arbeit stellt Methoden zur Verfügung, die ebene Strahlprofile beliebiger Form mit hoher Präzision und Effizienz erzeugen. Die Identifizierung potenzieller Einflussfaktoren der Strahlformungsmethoden und des verarbeiteten Materials helfen bei der Abschätzung und Kontrolle der Gleichförmigkeit des Abtragsergebnisses. In Kombination mit nichtlinearer Lichtkonversion ist die ebene Strahlformung nicht auf den Spektralbereich des Flüssigkristalldisplays beschränkt und die Wellenlänge kann gezielt an die Anforderungen angepasst werden. Dies ermöglicht eine präzise und effiziente ultrakurzgepulste Lasermaterialbearbeitung für ein breites Spektrum von Anwendungen in Forschung und Industrie.

**Beiträge in Stichpunkten**

- Methoden zur ebenen Strahlformung mit
  - hoher Effizienz und Qualität,
  - hoher Machbarkeit und Praktikabilität,
  - Anwendbarkeit für Hochenergielaser,
  - und Abtragsergebnissen von hoher Gleichförmigkeit.
- Analyse des Materialeinflusses beim Laserabtrag ermöglicht
  - die Identifizierung potenzieller Einflussfaktoren, z. B. der Wärmeleitfähigkeit
  - und die Möglichkeit, die Gleichförmigkeit abzuschätzen und eventuell anzupassen.
- Nichtlineare Wellenfrontformung
  - ist ein Schritt zur Strahlformung jenseits der spektralen Grenzen von Flüssigkristalldisplays
  - und Specklemittelung ermöglicht ebene Strahlprofile.

⇒ Ebene Strahlformung bei der optimalen Wellenlänge unter Ermittlung von für die Ablation relevanten materialspezifischen Eigenschaften, liefert Ergebnisse hoher Gleichförmigkeit.

# 9 Appendix - Further Results

## I Ablation Threshold for Selected Metals

Figure 20 presents the measured data points for the determination of the ablation threshold for the chosen materials in Section 5.2.1. The ablation threshold is determined for $N = 1000$ and $N = 100$ pulses. The latter one serves as reference. The corresponding measurement for silicon in included in Section 4.1.1.

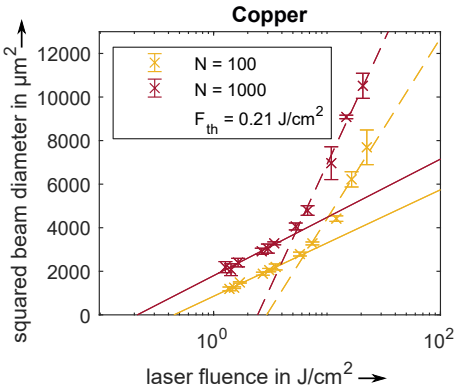


(a) Ablation threshold for pure copper.

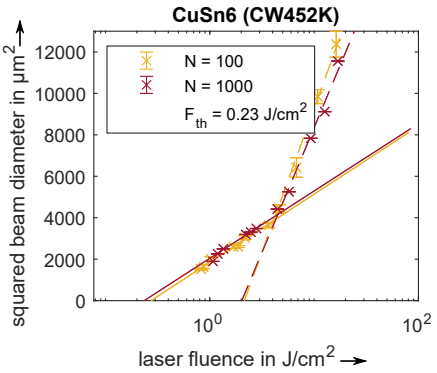


(b) Ablation threshold for bronze.

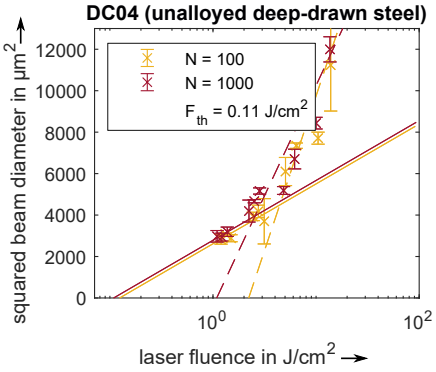


(c) Ablation threshold for DC04.

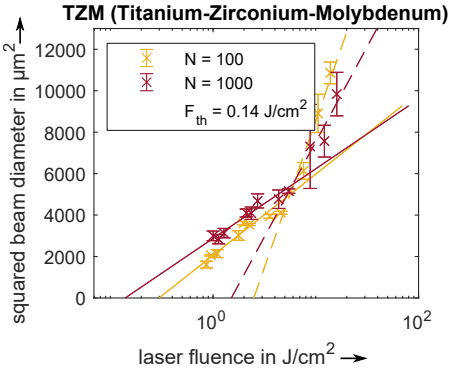


(d) Ablation threshold for TZM.

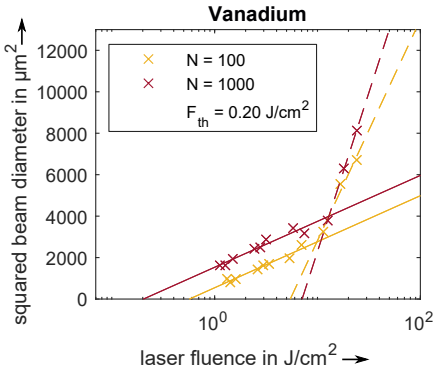


(e) Ablation threshold for Vanadium.

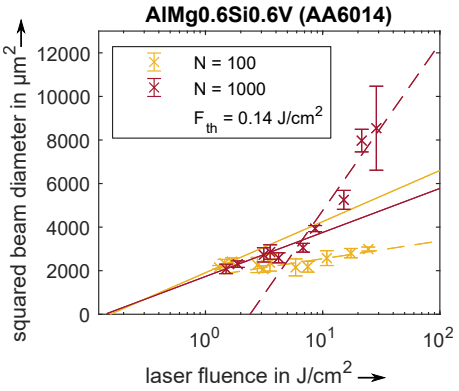


(f) Ablation threshold for pure AA6014.

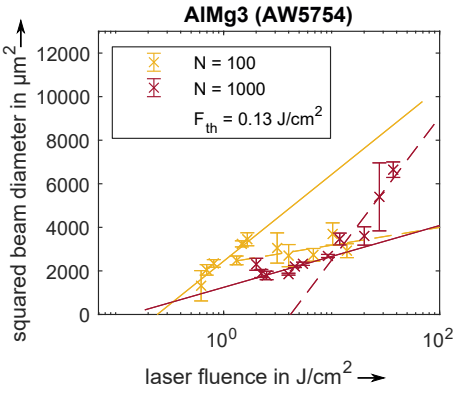


(g) Ablation threshold for AW5754.

Figure 20: Ablation threshold for $N = 100$ and $N = 1000$ pulses for the evaluated metal samples in Section 5.2.

# II Analysis of Reproducibility and Position Independence

Three distinctive materials silicon, DC04, and copper were selected and ablation experiments were each repeated on independently prepared samples. Besides the ablation results in Figure 14, the additionally prepared samples serve as a measure of reproducibility. While the results in Figure 14 are referred as sample № 1, the additionally prepared samples of the appendix are referred as sample № 2. Similar to the metal samples № 1, the surfaces of all samples № 2 were polished and the laser parameters are consistent. However, due to technical issues with the laser, the relative fluence for copper was set to $F = 3.9F_{\text{th}}$. The lower fluence in case of copper is expected to

impair the ablation uniformity slightly as intensity fluctuations are more pronounced.
To additionally evaluate the effect of position, ablation experiments on sample № 2 were conducted and evaluated at three different positions. As Table 3 shows, the results provide good reproducibility, as a similar ablation uniformity was achieved for both samples. Furthermore, the relatively small standard deviation for sample № 2 at different positions on the same sample also indicates position independence. The differences between the three materials are a lot more significant than the deviations between the individual measurements and different samples.

Table 3: Analysis of reproducibility and position-dependence with two individual samples. Sample № 2 was evaluated at three different positions (pos.) and the error is given by the standard deviation.

| **material** | **DC04** | | **Si** | | **Cu** | |
|---|---|---|---|---|---|---|
| | **№1** | **№2** (3 pos.) | **№1** | **№2** (3 pos.) | **№1** | **№2** (3 pos.) |
| $U$ **in** % | 14.8 | $12.0 \pm 0.1$ | 9.4 | $9.3 \pm 0.9$ | 25.6 | $26.5 \pm 1.5$ |

Good reproducibility and position independence is important because only the exclusion of these impact factors makes it possible to do a statistical analysis of the material's influence on basis of ablation results for various distinctive metals.

## III Influence of Preexisting Surface Roughness

To analyze the influence of surface roughness, additional samples with increasing surface roughness were prepared by using coarse grinding paper. The surface roughness was characterized using $S_a$. This value is defined as the arithmetic mean of height deviations with respect to the mean value within a selected area [217]. For better comparability, the achieved surface roughness on the ablated area was plotted versus the measured surface roughness in the surroundings in Figure 21. The results show a trend of degrading surface roughness with increasing preexisting roughness. Conversely, copper and DC04 show a slight trend of improvement. However, the differences between the individual materials are more significant than differences due to roughness.
Moreover, the selected ablation profiles of copper and DC04 in Figure 21 suggest that the preexisting surface roughness is conserved instead of being filtered out. The scratches superimpose on the resulting profiles. The impaired ablation uniformity can probably be attributed to the additionally

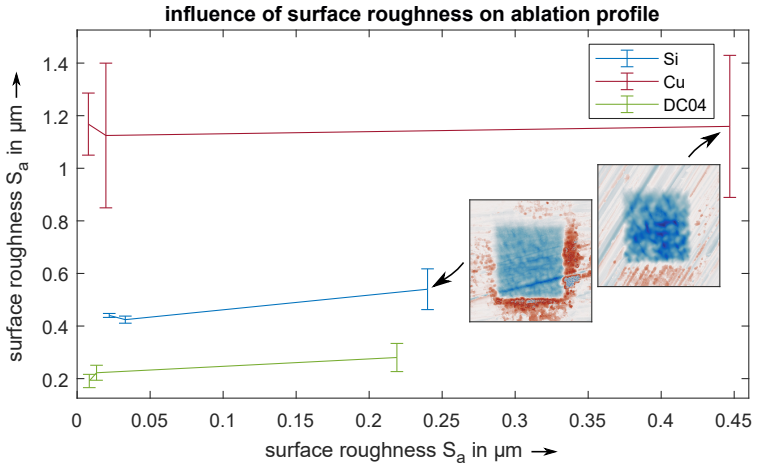


Figure 21: Dependence of the ablation uniformity on the surface roughness $S_a$ for mono crystalline silicon, pure copper and the unalloyed deep-drawn steel DC04. Scratches due to an increasing surface roughness reappear almost unaffected in the ablated profiles.

overlaying roughness. If the surface roughness was a crucial influence factor of the ablation process, it would not reappear unaffected after ablation.
Even though surface roughness does not seem to affect the ablated profiles strongly, the analysis in Section 4.1.1 and Section 4.1.2 shows a significant dependence of the ablation uniformity on the surface conditions. Too slow averaging is attributed to the generation of an uneven surface that strongly affects the process dynamics. This is caused by a quasi-static speckle pattern with speckle dimensions given by the resolution limit of the optical system. Consequently, the ablated structures have similar dimensions while the high fluences within such speckle peaks ablate more material than in the surroundings. This causes steep edges with an increased threshold fluence, potentially above the applied laser fluence. This scenario rather resembles ultrashort pulse hole drilling [218, 219] where material ablation gradually decreases until it stagnates.
The results within this analysis suggest that slight imperfections in surface finish do not have a strong impact on the ablated profile. They are conserved during material ablation but do not further affect the surroundings. Visual differences in the resulting ablation profile can thus rather be assigned to material-specific characteristics. This finding is especially valuable as sample preparation is hard to control whereas material characteristics like thermal properties are well-defined.

# List of Figures

# List of Tables

# Bibliography


[1] Dickey, F. M., ed. *Laser Beam Shaping*. CRC Press, 2018. DOI: 10.1201/b17140.

[2] Dickey, F. M. and Lizotte, T. E. *Laser beam shaping applications*. Vol. 1. CRC Press, 2017.

[3] May, M. A.; Barré, N.; Kummer, K. K.; Kress, M.; Ritsch-Marte, M., and Jesacher, A. "Fast holographic scattering compensation for deep tissue biological imaging". *Nature Communications* 12.1 (2021). DOI: 10.1038/s41467-021-24666-9.

[4] Orazi, L.; Romoli, L.; Schmidt, M., and Li, L. "Ultrafast laser manufacturing: from physics to industrial applications". *CIRP Annals* 70.2 (2021), pp. 543–566. DOI: https://doi.org/10.1016/j.cirp.2021.05.007.

[5] Häfner, T.; Strauß, J.; Roider, C.; Heberle, J., and Schmidt, M. "Tailored laser beam shaping for efficient and accurate microstructuring". *Applied Physics A* 124.2 (2018), pp. 1–9. DOI: https://doi.org/10.1007/s00339-017-1530-0.

[6] Labroille, G.; Barré, N.; Pinel, O.; Denolle, B.; Lenglé, K.; Garcia, L.; Jaffrès, L.; Jian, P., and Morizur, J.-F. "Characterization and applications of spatial mode multiplexers based on Multi-Plane Light Conversion". *Optical Fiber Technology* 35 (2017), pp. 93–99. DOI: 10.1016/j.yofte.2016.09.005.

[7] Mico, V.; Zalevsky, Z.; García-Martínez, P., and García, J. "Synthetic aperture superresolution with multiple off-axis holograms". *Journal of the Optical Society of America A* 23.12 (2006), p. 3162. DOI: 10.1364/josaa.23.003162.

[8] Zalevsky, Z. and Mendlovic, D. *Optical Superresolution*. Springer New York, 2004. DOI: 10.1007/978-0-387-34715-8.

[9] Zupancic, P.; Preiss, P. M.; Ma, R.; Lukin, A.; Tai, M. E.; Rispoli, M.; Islam, R., and Greiner, M. "Ultra-precise holographic beam shaping for microscopic quantum control". *Optics Express* 24.13 (2016), p. 13881. DOI: 10.1364/oe.24.013881.

[10] Maxwell, J. C. "A dynamical theory of electromagnetic field". *Royal society transactions* 155 (1864), pp. 526–597.

[11] Hecht, E. *Optics 4th Edition*. Addison Wesley, 2001.

[12] Goodman, J. W. *Introduction to Fourier optics*. Roberts and Company publishers, 2005.

[13] Novotny, L. and Hecht, B. *Principles of Nano-Optics*. Cambridge University Press, 2012. DOI: 10.1017/cbo9780511794193.

[14] Ackermann, G. K. and Eichler, J. *Holography: A Practical Approach*. Physics textbook. Wiley, 2008.

[15] Johnston, S. *Holograms: A Cultural History*. Oxford University Press, 2016.

[16] Gabor, D. "A New Microscopic Principle". *Nature* 161.4098 (1948), pp. 777–778. DOI: 10.1038/161777a0.

[17] Gabor, D. "Holography, 1948-1971". *Science* 177.4046 (1972), pp. 299–313. DOI: 10.1126/science.177.4046.299.

[18] Hsieh, C.; Momtahan, O.; Karbaschi, A., and Adibi, A. "Compact Fourier-transform volume holographic spectrometer for diffuse source spectroscopy". *Optics Letters* 30.8 (2005), p. 836. DOI: 10.1364/ol.30.000836.

[19] Redding, B.; Liew, S. F.; Sarma, R., and Cao, H. "Compact spectrometer based on a disordered photonic chip". *Nature Photonics* 7.9 (2013), pp. 746–751. DOI: 10.1038/nphoton.2013.190.

[20] Glezer, E. N.; Milosavljevic, M.; Huang, L.; Finlay, R. J.; Her, T.-H.; Callan, J. P., and Mazur, E. "Three-dimensional optical storage inside transparent materials". *Optics Letters* 22.6 (1997), p. 422. DOI: 10.1364/OL.21.002023.

[21] Bruder, F.-K.; Hagen, R.; Rölle, T.; Weiser, M.-S., and Fäcke, T. "From the Surface to Volume: Concepts for the Next Generation of Optical-Holographic Data-Storage Materials". *Angewandte Chemie International Edition* 50.20 (2011), pp. 4552–4573. DOI: 10.1002/anie.201002085.

[22] Ashley, J.; Bernal, M.-P.; Burr, G. W.; Coufal, H.; Guenther, H.; Hoffnagle, J. A.; Jefferson, C. M.; Marcus, B.; Macfarlane, R. M.; Shelby, R. M., and Sincerbox, G. T. "Holographic data storage technology". *IBM Journal of Research and Development* 44.3 (2000), pp. 341–368. DOI: 10.1147/rd.443.0341.

[23] Bishop, C. "The Real AI Revolution". Neural Information Processing Systems, Conference, 2020.

[24] Moughames, J.; Porte, X.; Thiel, M.; Ulliac, G.; Larger, L.; Jacquot, M.; Kadic, M., and Brunner, D. "Three-dimensional waveguide interconnects for scalable integration of photonic neural networks". *Optica* 7.6 (2020), p. 640. DOI: 10.1364/optica.388205.

[25] Liao, K.; Chen, Y.; Yu, Z.; Hu, X.; Wang, X.; Lu, C.; Lin, H.; Du, Q.; Hu, J., and Gong, Q. "All-optical computing based on convolutional neural networks". *Opto-Electronic Advances* 4.11 (2021), pp. 200060–200060. DOI: 10.29026/oea.2021.200060.

[26] Situ, G. "Deep holography". *Light: Advanced Manufacturing* 3 (2022), p. 278. DOI: 10.37188/lam.2022.013.

[27] Wyrowski, F. "Characteristics of diffractive optical elements/digital holograms". *SPIE Proceedings*. Ed. by Cindrich, I. and Lee, S. H. SPIE, 1990. DOI: 10.1117/12.17951.

[28] Browar, A.; Shusteff, M.; Panas, R.; Ellis, J., and Spadaccini, C. *Overview and comparison of spatial light modulator calibration methods*. Tech. rep. Lawrence Livermore National Lab.(LLNL), Livermore, CA (United States), 2016.

[29] Lazarev, G.; Chen, P.-J.; Strauss, J.; Fontaine, N., and Forbes, A. "Beyond the display: phase-only liquid crystal on Silicon devices and their applications in photonics [Invited]". *Optics Express* 27.11 (2019), p. 16206. DOI: 10.1364/oe.27.016206.

[30] Engström, D.; Persson, M.; Bengtsson, J., and Goksör, M. "Calibration of spatial light modulators suffering from spatially varying phase response". *Optics Express* 21.13 (2013), p. 16086. DOI: 10.1364/oe.21.016086.

[31] Deng, X.; Liang, X.; Chen, Z.; Yu, W., and Ma, R. "Uniform illumination of large targets using a lens array". *Applied Optics* 25.3 (1986), p. 377. DOI: 10.1364/ao.25.000377.

[32] Dickey, F. M. and O'Neil, B. D. "Multifaceted Laser Beam Integrators: General Formulation And Design Concepts". *Optical Engineering* 27.11 (1988). DOI: 10.1117/12.7976799.

[33] Voelkel, R. and Weible, K. J. "Laser beam homogenizing: limitations and constraints". *SPIE Proceedings*. Ed. by Duparré, A. and Geyl, R. SPIE, 2008. DOI: 10.1117/12.799400.

[34] Harder, I.; Lano, M.; Lindlein, N., and Schwider, J. "Homogenization and beam shaping with microlens arrays". *SPIE Proceedings*. Ed. by Wyrowski, F. SPIE, 2004. DOI: 10.1117/12.549015.

[35] Zimmermann, M.; Lindlein, N.; Voelkel, R., and Weible, K. J. "Microlens laser beam homogenizer: from theory to application". *SPIE Proceedings*. Ed. by Dickey, F. M. and Shealy, D. L. SPIE, 2007. DOI: 10.1117/12.731391.

[36] Völkel, R. "Microlens array imaging system for photolithography". *Optical Engineering* 35.11 (1996), p. 3323. DOI: 10.1117/1.601080.

[37] Horn, I.; Guillong, M., and Günther, D. "Wavelength dependant ablation rates for metals and silicate glasses using homogenized laser beam profiles — implications for LA-ICP-MS". *Applied Surface Science* 182.1-2 (2001), pp. 91–102. DOI: 10.1016/s0169-4332(01)00465-2.

[38] Guillong, M.; Horn, I., and Günther, D. "Capabilities of a homogenized 266 nm Nd:YAG laser ablation system for LA-ICP-MS". *Journal of Analytical Atomic Spectrometry* 17.1 (2002), pp. 8–14. DOI: 10.1039/b107823m.

[39] Pfadler, S.; Beyrau, F.; Löffler, M., and Leipertz, A. "Application of a beam homogenizer to planar laser diagnostics". *Optics Express* 14.22 (2006), p. 10171. DOI: 10.1364/oe.14.010171.

[40] Hoffnagle, J. A. and Jefferson, C. M. "Design and performance of a refractive optical system that converts a Gaussian to a flattop beam". *Applied Optics* 39.30 (2000), p. 5488. DOI: 10.1364/ao.39.005488.

[41] Nemoto, K.; Kanai, Y.-k.; Fujii, T.; Goto, N., and Nayuki, T. "Transformation of a laser beam intensity profile by a deformable mirror". *Optics Letters* 21.3 (1996), p. 168. DOI: 10.1364/ol.21.000168.

[42] Salter, P. S.; Jesacher, A.; Spring, J. B.; Metcalf, B. J.; Thomas-Peter, N.; Simmonds, R. D.; Langford, N. K.; Walmsley, I. A., and Booth, M. J. "Adaptive slit beam shaping for direct laser written waveguides". *Optics Letters* 37.4 (2012), p. 470. DOI: 10.1364/ol.37.000470.

[43] Cumming, B. P.; Debbarma, S.; Luther-Davis, B., and Gu, M. "Simultaneous compensation for aberration and axial elongation in three-dimensional laser nanofabrication by a high numerical-aperture objective". *Optics Express* 21.16 (2013), p. 19135. DOI: 10.1364/oe.21.019135.

[44] Sanner, N.; Huot, N.; Audouard, E.; Larat, C.; Huignard, J.-P., and Loiseaux, B. "Programmable focal spot shaping of amplified femtosecond laser pulses". *Optics Letters* 30.12 (2005), p. 1479. DOI: 10.1364/ol.30.001479.

[45] Sanner, N.; Huot, N.; Audouard, E.; Larat, C., and Huignard, J.-P. "Direct ultrafast laser micro-structuring of materials using programmable beam shaping". *Optics and Lasers in Engineering* 45.6 (2007), pp. 737–741. DOI: 10.1016/j.optlaseng.2006.10.009.

[46] Henderson, B. G. and Mansell, J. D. "Laser beam shaping with membrane deformable mirrors". *Advanced Wavefront Control: Methods, Devices, and Applications VI*. Ed. by Gonglewski, J. D.; Carreras, R. A., and Rhoadarmer, T. A. Vol. 7093. International Society for Optics and Photonics. SPIE, 2008, p. 70930I. DOI: 10.1117/12.796714.

[47] Salter, P. S. and Booth, M. J. "Adaptive optics in laser processing". *Light: Science & Applications* 8.1 (2019). DOI: 10.1038/s41377-019-0215-1.

[48] Bechtold, P.; Hohenstein, R., and Schmidt, M. "Beam shaping and high-speed, cylinder-lens-free beam guiding using acousto-optical deflectors without additional compensation optics". *Optics Express* 21.12 (2013), pp. 14627–14635. DOI: 10.1364/OE.21.014627.

[49] Strauß, J. *Die akustooptische Strahlformung in der Lasermaterialbearbeitung*. FAU University Press, 2021.

[50] Baum, M.; Bechtold, P.; Strauß, J., and Schmidt, M. "Towards Dynamic Holographic Laser Beam Shaping". *Journal of Laser Micro/Nanoengineering* 10.2 (2015), pp. 216–221. DOI: 10.2961/jlmn.2015.02.0020.

[51] Grünewald, J.; Blickle, V.; Allenberg-Rabe, M.; Wagenblast, P., and Wudy, K. "Flexible and highly dynamic beam shaping for Laser-Based Powder Bed Fusion of metals". *Procedia CIRP* 111 (2022), pp. 65–70. DOI: 10.1016/j.procir.2022.08.124.

[52] Zhu, G.; Whitehead, D.; Perrie, W.; Allegre, O. J.; Olle, V.; Li, Q.; Tang, Y.; Dawson, K.; Jin, Y.; Edwardson, S. P.; Li, L., and Dearden, G. "Investigation of the thermal and optical performance of a spatial light modulator with high average power picosecond laser exposure for materials processing applications". *Journal of Physics D: Applied Physics* 51.9 (2018), p. 095603. DOI: 10.1088/1361-6463/aaa948.

[53] Gerchberg, R. W. and Saxton, W. O. "A practical algorithm for the determination of phase from image and diffraction plane pictures". *Optik* 35 (1972), pp. 237–246.

[54] Fienup, J. R. "Phase retrieval algorithms: a comparison". *Applied Optics* 21.15 (1982), pp. 2758–2769. DOI: 10.1364/AO.21.002758.

[55] Guillon, M.; Forget, B. C.; Foust, A. J.; De Sars, V.; Ritsch-Marte, M., and Emiliani, V. "Vortex-free phase profiles for uniform patterning with computer-generated holography". *Optics Express* 25.11 (2017), pp. 12640–12652. DOI: 10.1364/OE.25.012640.

[56] Fienup, J. R. "Phase-retrieval algorithms for a complicated optical system". *Applied Optics* 32.10 (1993), p. 1737. DOI: 10.1364/ao.32.001737.

[57] Glückstad, J. and Mogensen, P. C. "Optimal phase contrast in common-path interferometry". *Applied Optics* 40.2 (2001), p. 268. DOI: 10.1364/ao.40.000268.

[58] Di Leonardo, R.; Ianni, F., and Ruocco, G. "Computer generation of optimal holograms for optical trap arrays". *Optics Express* 15.4 (2007), pp. 1913–1922. DOI: 10.1364/OE.15.001913.

[59] Sinha, A.; Lee, J.; Li, S., and Barbastathis, G. "Lensless computational imaging through deep learning". *Optica* 4.9 (2017), p. 1117. DOI: 10.1364/optica.4.001117.

[60] Mikhaylov, D.; Zhou, B.; Kiedrowski, T.; Mikut, R., and Lasagni, A. F. "Machine learning aided phase retrieval algorithm for beam splitting with an LCoS-SLM". *Laser Resonators, Microresonators, and Beam Control XXI*. Ed. by Kudryashov, A. V.; Paxton, A. H., and Ilchenko, V. S. SPIE, 2019. DOI: 10.1117/12.2508673.

[61] Buske, P.; Völl, A.; Eisebitt, M.; Stollenwerk, J., and Holly, C. "Advanced beam shaping for laser materials processing based on diffractive neural networks". *Optics Express* 30.13 (2022), p. 22798. DOI: 10.1364/oe.459460.

[62] Mikhaylov, D.; Zhou, B.; Kiedrowski, T.; Mikut, R., and Lasagni, A.-F. "High accuracy beam splitting using spatial light modulator combined with machine learning algorithms". *Optics and Lasers in Engineering* 121 (2019), pp. 227–235. DOI: 10.1016/j.optlaseng.2019.04.010.

[63] Dickey, F. M.; Weichman, L. S., and Shagam, R. N. "Laser beam shaping techniques". *High-Power Laser Ablation III*. Ed. by Phipps, C. R. Vol. 4065. International Society for Optics and Photonics. SPIE, 2000, pp. 338–348. DOI: 10.1117/12.407361.

[64] Bawart, M.; Bernet, S., and Ritsch-Marte, M. "Programmable freeform optical elements". *Optics Express* 25.5 (2017), pp. 4898–4906. DOI: 10.1364/OE.25.004898.

[65] Bagnoud, V. and Zuegel, J. D. "Independent phase and amplitude control of a laser beam by use of a single-phase-only spatial light modulator". *Optics Letters* 29.3 (2004), p. 295. DOI: 10.1364/ol.29.000295.

[66] Hendriks, A.; Naidoo, D.; Roux, F. S.; López-Mariscal, C., and Forbes, A. "The generation of flat-top beams by complex amplitude modulation with a phase-only spatial light modulator". *Laser Beam Shaping XIII*. Ed. by Forbes, A. and Lizotte, T. E. Vol. 8490. International Society for Optics and Photonics. SPIE, 2012, p. 849006. DOI: 10.1117/12.932224.

[67] Liu, D.; Wang, Y.; Zhai, Z.; Fang, Z.; Tao, Q.; Perrie, W.; Edwarson, S. P., and Dearden, G. "Dynamic laser beam shaping for material processing using hybrid holograms". *Optics & Laser Technology* 102 (2018), pp. 68–73. DOI: 10.1016/j.optlastec.2017.12.022.

[68] Nakata, Y.; Osawa, K., and Miyanaga, N. "Utilization of the high spatial-frequency component in adaptive beam shaping by using a virtual diagonal phase grating". *Scientific Reports* 9.1 (2019). DOI: 10.1038/s41598-019-40829-7.

[69] Akahori, H. "Spectrum leveling by an iterative algorithm with a dummy area for synthesizing the kinoform". *Applied Optics* 25.5 (1986), p. 802. DOI: 10.1364/ao.25.000802.

[70] Wyrowski, F. "Diffractive optical elements: iterative calculation of quantized, blazed phase structures". *Journal of the Optical Society of America A* 7.6 (1990), pp. 961–969. DOI: 10.1364/JOSAA.7.000961.

[71] Georgiou, A.; Christmas, J.; Collings, N.; Moore, J., and Crossland, W. A. "Aspects of hologram calculation for video frames". *Journal of Optics A: Pure and Applied Optics* 10.3 (2008), p. 035302. DOI: 10.1088/1464-4258/10/3/035302.

[72] Pasienski, M. and DeMarco, B. "A high-accuracy algorithm for designing arbitrary holographic atom traps". *Optics Express* 16.3 (2008), p. 2176. DOI: 10.1364/oe.16.002176.

[73] Gaunt, A. L. and Hadzibabic, Z. "Robust digital holography for ultracold atom trapping". *Scientific Reports* 2.1 (2012). DOI: 10.1038/srep00721.

[74] Wu, L.; Cheng, S., and Tao, S. "Simultaneous shaping of amplitude and phase of light in the entire output plane with a phase-only hologram". *Scientific Reports* 5.1 (2015). DOI: 10.1038/srep15426.

[75] Chang, C.; Xia, J.; Yang, L.; Lei, W.; Yang, Z., and Chen, J. "Speckle-suppressed phase-only holographic three-dimensional display based on double-constraint Gerchberg–Saxton algorithm". *Applied Optics* 54.23 (2015), p. 6994. DOI: 10.1364/ao.54.006994.

[76] Pang, H.; Wang, J.; Cao, A., and Deng, Q. "High-accuracy method for holographic image projection with suppressed speckle noise". *Optics Express* 24.20 (2016), p. 22766. DOI: 10.1364/oe.24.022766.

[77] Chen, L.; Zhang, H.; He, Z.; Wang, X.; Cao, L., and Jin, G. "Weighted Constraint Iterative Algorithm for Phase Hologram Generation". *Applied Sciences* 10.10 (2020), p. 3652. DOI: 10.3390/app10103652.

[78] Chen, L.; Tian, S.; Zhang, H.; Cao, L., and Jin, G. "Phase hologram optimization with bandwidth constraint strategy for speckle-free optical reconstruction". *Optics Express* 29.8 (2021), p. 11645. DOI: 10.1364/oe.422115.

[79] Liu, K.; He, Z., and Cao, L. "Double amplitude freedom Gerchberg–Saxton algorithm for generation of phase-only hologram with speckle suppression". *Applied Physics Letters* 120.6 (2022), p. 061103. DOI: 10.1063/5.0080797.

[80] Bolduc, E.; Bent, N.; Santamato, E.; Karimi, E., and Boyd, R. W. "Exact solution to simultaneous intensity and phase encryption with a single phase-only hologram". *Optics Letters* 38.18 (2013), p. 3546. DOI: 10.1364/ol.38.003546.

[81] Clark, T. W.; Offer, R. F.; Franke-Arnold, S.; Arnold, A. S., and Radwell, N. "Comparison of beam generation techniques using a phase only spatial light modulator". *Optics Express* 24.6 (2016), p. 6249. DOI: 10.1364/oe.24.006249.

[82] Shimobaba, T. and Ito, T. "Random phase-free computer-generated hologram". *Optics Express* 23.7 (2015), p. 9549. DOI: 10.1364/oe.23.009549.

[83] Shimobaba, T.; Kakue, T.; Endo, Y.; Hirayama, R.; Hiyama, D.; Hasegawa, S.; Nagahama, Y.; Sano, M.; Oikawa, M.; Sugie, T., and Ito, T. "Random phase-free kinoform for large objects". *Optics Express* 23.13 (2015), pp. 17269–17274. DOI: 10.1364/OE.23.017269.

[84] Pang, H.; Wang, J.; Zhang, M.; Cao, A.; Shi, L., and Deng, Q. "Non-iterative phase-only Fourier hologram generation with high image quality". *Optics Express* 25.13 (2017), p. 14323. DOI: 10.1364/oe.25.014323.

[85] Nagahama, Y.; Shimobaba, T.; Kakue, T.; Masuda, N., and Ito, T. "Speeding up image quality improvement in random phase-free holograms using ringing artifact characteristics". *Applied Optics* 56.13 (2017), F61–F66. DOI: 10.1364/ao.56.000f61.

[86] Fischer, D. and Sinzinger, S. "Evaluation of quadratic phase hologram calculation algorithms in the Fourier regime". *Applied Optics* 59.6 (2020), p. 1501. DOI: 10.1364/ao.381547.

[87] Caulfield, H. J. "Wavefront Multiplexing by Holography". *Applied Optics* 9.5 (1970), p. 1218. DOI: 10.1364/ao.9.001218.

[88] Goodman, J. W. "Some fundamental properties of speckle". *Journal of the Optical Society of America* 66.11 (1976), p. 1145. DOI: 10.1364/josa.66.001145.

[89] Amako, J.; Miura, H., and Sonehara, T. "Speckle-noise reduction on kinoform reconstruction using a phase-only spatial light modulator". *Applied optics* 34.17 (1995), pp. 3165–3171. DOI: 10.1364/AO.34.003165.

[90] Häfner, T.; Heberle, J.; Holder, D., and Schmidt, M. "Speckle reduction techniques in holographic beam shaping for accurate and efficient picosecond laser structuring". *Journal of Laser Applications* 29.2 (2017), p. 022205. DOI: 10.2351/1.4983497.

[91] Häfner, T. *Multipulseffekte beim Mikro-Materialabtrag von Stahllegierungen mit Pikosekunden-Laserpulsen*. FAU University Press, 2021.

[92] Goodman, J. W. *Speckle Phenomena in Optics: Theory and Applications*. Roberts & Company, 2007.

[93] Golan, L. and Shoham, S. "Speckle elimination using shift-averaging in high-rate holographic projection". *Optics Express* 17.3 (2009), pp. 1330–1339.

[94] Wlodarczyk, K. L.; Kaakkunen, J. J. J.; Vahimaa, P., and Hand, D. P. "Efficient speckle-free laser marking using a spatial light modulator". *Applied Physics A* 116.1 (2013), pp. 111–118. DOI: 10.1007/s00339-013-8186-1.

[95] Liu, S.-J.; Wang, D., and Wang, Q.-H. "Speckle noise suppression method in holographic display using time multiplexing technique". *Optics Communications* 436 (2019), pp. 253–257. DOI: 10.1016/j.optcom.2018.12.038.

[96] Wang, Z.; Li, X.; Jiang, L.; Li, B.; Wei, Q.; Huang, L.; Wang, Z.; Yin, J., and Lu, J. "High-quality micropattern printing by interlacing-pattern holographic femtosecond pulses". *Nanophotonics* 9.9 (2020), pp. 2895–2904. DOI: 10.1515/nanoph-2020-0138.

[97] Tauro, S.; Bañas, A.; Palima, D., and Glückstad, J. "Experimental demonstration of Generalized Phase Contrast based Gaussian beam-shaper". *Optics Express* 19.8 (2011), p. 7106. DOI: 10.1364/oe.19.007106.

[98] Glückstad, J.; Palima, D.; Rodrigo, P. J., and Alonzo, C. A. "Laser projection using generalized phase contrast". *Optics Letters* 32.22 (2007), p. 3281. DOI: 10.1364/ol.32.003281.

[99] Mikhaylov, D.; Kiedrowski, T., and Lasagni, A. F. "Beam shaping using two spatial light modulators for ultrashort pulse laser ablation of metals". *Laser-based Micro- and Nanoprocessing XIII*. Ed. by Klotzbach, U.; Watanabe, A., and Kling, R. Vol. 10906. International Society for Optics and Photonics. SPIE, 2019, p. 1090615. DOI: 10.1117/12.2508682.

[100] Bartelt, H. O. "Computer-generated holographic component with optimum light efficiency". *Applied Optics* 23.10 (1984), pp. 1499–1502. DOI: 10.1364/AO.23.001499.

[101] Bartelt, H. O. "Applications of the tandem component: an element with optimum light efficiency". *Applied Optics* 24.22 (1985), pp. 3811–3816. DOI: 10.1364/AO.24.003811.

[102] Jesacher, A.; Maurer, C.; Schwaighofer, A.; Bernet, S., and Ritsch-Marte, M. "Full phase and amplitude control of holographic optical tweezers with high efficiency". *Optics Express* 16.7 (2008), pp. 4479–4486. DOI: 10.1364/OE.16.004479.

[103] Jesacher, A.; Maurer, C.; Schwaighofer, A.; Bernet, S., and Ritsch-Marte, M. "Near-perfect hologram reconstruction with a spatial light modulator". *Optics Express* 16.4 (2008), pp. 2597–2603. DOI: 10.1364/OE.16.002597.

[104] Wang, H. and Piestun, R. "Dynamic 2D implementation of 3D diffractive optics". *Optica* 5.10 (2018), p. 1220. DOI: 10.1364/optica.5.001220.

[105] Barré, N.; Shivaraman, R.; Moser, S.; Salter, P.; Schmidt, M.; Booth, M. J., and Jesacher, A. "Direct laser-written aperiodic photonic volume elements for complex light shaping with high efficiency: inverse design and fabrication". *Advanced Photonics Nexus* 2.3 (2023), p. 036006. DOI: 10.1117/1.APN.2.3.036006.

[106] Chichkov, B. N.; Momma, C.; Nolte, S.; Alvensleben, F., and Tünnermann, A. "Femtosecond, picosecond and nanosecond laser ablation of solids". *Applied Physics A* 63.2 (1996), pp. 109–115. DOI: 10.1007/bf01567637.

[107] Bonse, J.; Hohm, S.; Kirner, S. V.; Rosenfeld, A., and Kruger, J. "Laser-Induced Periodic Surface Structures— A Scientific Evergreen". *IEEE Journal of Selected Topics in Quantum Electronics* 23.3 (2017). DOI: 10.1109/jstqe.2016.2614183.

[108] Rethfeld, B.; Ivanov, D. S.; Garcia, M. E., and Anisimov, S. I. "Modelling ultrafast laser ablation". *Journal of Physics D: Applied Physics* 50.19 (2017), p. 193001. DOI: 10.1088/1361-6463/50/19/193001.

[109] Shcheblanov, N. S. and Itina, T. E. "Femtosecond laser interactions with dielectric materials: insights of a detailed modeling of electronic excitation and relaxation processes". *Applied Physics A* 110.3 (2012), pp. 579–583. DOI: 10.1007/s00339-012-7130-0.

[110] Kaganov, M. I.; M., L. I., and V., T. L. "Relaxation between electrons and the crystalline lattice". *Journal of Experimental and Theoretical Physics* 4.2 (1957), p. 173.

[111] Anisimov, S. I.; Kapeliovich, B. L.; Perelman, T. L., et al. "Electron emission from metal surfaces exposed to ultrashort laser pulses". *Soviet Journal of Experimental and Theoretical Physics* 66.2 (1974), pp. 375–377.

[112] Rethfeld, B.; Sokolowski-Tinten, K.; Linde, D. von der, and Anisimov, S. "Timescales in the response of materials to femtosecond laser excitation". *Applied Physics A* 79.4-6 (2004), pp. 767–769. DOI: 10.1007/s00339-004-2805-9.

[113] Byskov-Nielsen, J.; Savolainen, J.-M.; Christensen, M. S., and Balling, P. "Ultra-short pulse laser ablation of metals: threshold fluence, incubation coefficient and ablation rates". *Applied Physics A* 101.1 (2010), pp. 97–101. DOI: 10.1007/s00339-010-5766-1.

[114] Liu, J.-M. "Simple technique for measurements of pulsed Gaussian-beam spot sizes". *Optics Letters* 7.5 (1982), pp. 196–198. DOI: 10.1364/OL.7.000196.

[115] Samad, R. E. and Vieira, N. D. "Geometrical method for determining the surface damage threshold for femtosecond laser pulses". *Laser Physics* 16.2 (2006), pp. 336–339. DOI: 10.1134/s1054660x06020228.

[116] Ashkenasi, D.; Rosenfeld, A., and Stoian, R. "Laser-induced incubation in transparent materials and possible consequences for surface and bulk microstructuring with ultrashort pulses". *SPIE Proceedings*. Ed. by Edwards, G. S.; Neev, J.; Ostendorf, A., and Sutherland, J. C. SPIE, 2002. DOI: 10.1117/12.461367.

[117] Kramer, T.; Remund, S.; Jäggi, B.; Schmid, M., and Neuenschwander, B. "Ablation dynamics – from absorption to heat accumulation/ultra-fast laser matter interaction". *Advanced Optical Technologies* 7.3 (2018), pp. 129–144. DOI: 10.1515/aot-2018-0010.

[118] Paltauf, G. and Dyer, P. E. "Photomechanical Processes and Effects in Ablation". *Chemical Reviews* 103.2 (2003), pp. 487–518. DOI: 10.1021/cr010436c.

[119] Leveugle, E.; Ivanov, D., and Zhigilei, L. "Photomechanical spallation of molecular and metal targets: molecular dynamics study". *Applied Physics A* 79.7 (2004), pp. 1643–1655. DOI: 10.1007/s00339-004-2682-2.

[120] Wellershoff, S.-S.; Hohlfeld, J.; Güdde, J., and Matthias, E. "The role of electron–phonon coupling in femtosecond laser damage of metals". *Applied Physics A* 69.S1 (1999), S99–S107. DOI: 10.1007/s003399900305.

[121] Bulgakova, N. and Bulgakov, A. "Pulsed laser ablation of solids: transition from normal vaporization to phase explosion". *Applied Physics A* 73.2 (2001), pp. 199–208. DOI: 10.1007/s003390000686.

[122] Lorazo, P.; Lewis, L. J., and Meunier, M. "Short-Pulse Laser Ablation of Solids: From Phase Explosion to Fragmentation". *Physical Review Letters* 91.22 (2003). DOI: 10.1103/physrevlett.91.225502.

[123] Ivanov, D. S. and Zhigilei, L. V. "Combined atomistic-continuum modeling of short-pulse laser melting and disintegration of metal films". *Physical Review B* 68.6 (2003). DOI: 10.1103/physrevb.68.064114.

[124] Neuenschwander, B.; Jaeggi, B.; Schmid, M.; Rouffiange, V., and Martin, P.-E. "Optimization of the volume ablation rate for metals at different laser pulse-durations from ps to fs". *Laser Applications in Microelectronic and Optoelectronic Manufacturing (LAMOM) XVII*. Ed. by Hennig, G.; Xu, X.; Gu, B., and Nakata, Y. Vol. 8243. International Society for Optics and Photonics. SPIE, 2012, pp. 43–55. DOI: 10.1117/12.908583.

[125] Wu, C. and Zhigilei, L. V. "Microscopic mechanisms of laser spallation and ablation of metal targets from large-scale molecular dynamics simulations". *Applied Physics A* 114.1 (2013), pp. 11–32. DOI: 10.1007/s00339-013-8086-4.

[126] Sokolowski-Tinten, K.; Bialkowski, J.; Cavalleri, A.; von der Linde, D.; Oparin, A.; Meyer-ter-Vehn, J., and Anisimov, S. I. "Transient States of Matter during Short Pulse Laser Ablation". *Physical Review Letters* 81.1 (1998), pp. 224–227. DOI: 10.1103/physrevlett.81.224.

[127] Du, K. "Thin layer ablation with lasers of different beam profiles: energy efficiency and over filling factor". *SPIE Proceedings*. Ed. by Pfleging, W.; Lu, Y.; Washio, K.; Hoving, W., and Amako, J. SPIE, 2009. DOI: 10.1117/12.810158.

[128] Neuenschwander, B.; Bucher, G. F.; Nussbaum, C.; Joss, B.; Muralt, M.; Hunziker, U. W., and Schuetz, P. "Processing of metals and dielectric materials with ps-laserpulses: results, strategies, limitations and needs". *Laser Applications in Microelectronic and Optoelectronic Manufacturing XV*. Ed. by Niino, H.; Meunier, M.; Gu, B.; Hennig, G., and Dubowski, J. J. Vol. 7584. International Society for Optics and Photonics. SPIE, 2010, 75840R. DOI: 10.1117/12.846521.

[129] Bechtold, P.; Hohenstein, R., and Schmidt, M. "Evaluation of disparate laser beam deflection technologies by means of number and rate of resolvable spots". *Optics Letters* 38.16 (2013), p. 2934. DOI: 10.1364/ol.38.002934.

[130] Spence, D. E.; Kean, P. N., and Sibbett, W. "60-fsec pulse generation from a self-mode-locked Ti: sapphire laser". *Optics letters* 16.1 (1991), pp. 42–44. DOI: 10.1364/OL.16.000042.

[131] Squier, J.; Salin, F.; Mourou, G., and Harter, D. "100-fs pulse generation and amplification in Ti:Al2O3". *Optics Letters* 16.5 (1991), pp. 324–326. DOI: 10.1364/OL.16.000324.

[132] Momma, C.; Nolte, S.; Kamlage, G.; Alvensleben, F. von, and Tünnermann, A. "Beam delivery of femtosecond laser radiation by diffractive optical elements". *Applied Physics A* 67.5 (1998), pp. 517–520. DOI: 10.1007/s003390050814.

[133] Kuroiwa, Y.; Takeshima, N.; Narita, Y.; Tanaka, S., and Hirao, K. "Arbitrary micropatterning method in femtosecond laser microprocessing using diffractive optical elements". *Optics Express* 12.9 (2004), p. 1908. DOI: 10.1364/opex.12.001908.

[134] Hayasaki, Y.; Sugimoto, T.; Takita, A., and Nishida, N. "Variable holographic femtosecond laser processing by use of a spatial light modulator". *Applied Physics Letters* 87.3 (2005), p. 031101. DOI: 10.1063/1.1992668.

[135] Kuang, Z.; Perrie, W.; Leach, J.; Sharp, M.; Edwardson, S. P.; Padgett, M.; Dearden, G., and Watkins, K. G. "High throughput diffractive multi-beam femtosecond laser processing using a spatial light modulator". *Applied Surface Science* 255.5 (2008), pp. 2284–2289. DOI: 10.1016/j.apsusc.2008.07.091.

[136] Hasegawa, S. and Hayasaki, Y. "Parallel femtosecond laser processing with a computer-generated hologram". *SPIE Proceedings*. SPIE, 2009. DOI: 10.1117/12.810234.

[137] Kuang, Z.; Liu, D.; Perrie, W.; Edwardson, S.; Sharp, M.; Fearon, E.; Dearden, G., and Watkins, K. "Fast parallel diffractive multi-beam femtosecond laser surface micro-structuring". *Applied Surface Science* 255.13-14 (2009), pp. 6582–6588. DOI: 10.1016/j.apsusc.2009.02.043.

[138] Mauclair, C. "Ultrafast Laser Machining of Micro Grooves on Stainless Steel with Spatially Optimized Intensity Distribution". *Journal of Laser Micro/Nanoengineering* 8.1 (2013), pp. 11–14. DOI: 10.2961/jlmn.2013.01.0003.

[139] Mauclair, C.; Pietroy, D.; Maïo, Y. D.; Baubeau, E.; Colombier, J.-P.; Stoian, R., and Pigeon, F. "Ultrafast laser micro-cutting of stainless steel and PZT using a modulated line of multiple foci formed by spatial beam shaping". *Optics and Lasers in Engineering* 67 (2015), pp. 212–217. DOI: 10.1016/j.optlaseng.2014.11.018.

[140] Wang, J.; Sun, S.; Zhang, H.; Hasegawa, S.; Wang, P., and Hayasaki, Y. "Holographic Femtosecond Laser Parallel Processing Method Based on the Fractional Fourier Transform". *Optics and Lasers in Engineering* 146 (2021), p. 106704. DOI: 10.1016/j.optlaseng.2021.106704.

[141] Hayasaki, Y.; Hasegawa, S.; Zhang, H.; Onodera, R.; Kosugi, T.; Kuroo, N., and Ishita, F. "Holographic beam-shaping optimized in a laser processing system". *Holography, Diffractive Optics, and Applications XII*. SPIE, 2022. DOI: 10.1117/12.2641880.

[142] Kuang, Z.; Li, J.; Edwardson, S.; Perrie, W.; Liu, D., and Dearden, G. "Ultrafast laser beam shaping for material processing at imaging plane by geometric masks using a spatial light modulator". *Optics and Lasers in Engineering* 70 (2015), pp. 1–5. DOI: 10.1016/j.optlaseng.2015.02.004.

[143] Li, J.; Tang, Y.; Kuang, Z.; Schille, J.; Loeschner, U.; Perrie, W.; Liu, D.; Dearden, G., and Edwardson, S. "Multi imaging-based beam shaping for ultrafast laser-material processing using spatial light modulators". *Optics and Lasers in Engineering* 112 (2019), pp. 59–67. DOI: 10.1016/j.optlaseng.2018.09.002.

[144] Flamm, D.; Grossmann, D. G.; Sailer, M.; Kaiser, M.; Zimmermann, F.; Chen, K.; Jenne, M.; Kleiner, J.; Hellstern, J.; Tillkorn, C.; Sutter, D. H., and Kumkar, M. "Structured light for ultrafast laser micro- and nanoprocessing". *Optical Engineering* 60.02 (2021). DOI: 10.1117/1.oe.60.2.025105.

[145] Holder, D.; Hensel, S.; Peter, A.; Weber, R., and Graf, T. "Beam Shaping for Uniform and Energy-efficient Surface Structuring of Metals with Ultrashort Laser Pulses in the mJ Range". *Journal of Laser Micro/Nanoengineering* 17.1 (2022). DOI: 10.2961/jlmn.2022.01.2006.

[146] Rasch, M.; Roider, C.; Kohl, S.; Strauß, J.; Maurer, N.; Nagulin, K. Y., and Schmidt, M. "Shaped laser beam profiles for heat conduction welding of aluminium-copper alloys". *Optics and Lasers in Engineering* 115 (2019), pp. 179–189. DOI: 10.1016/j.optlaseng.2018.11.025.

[147] Shi, R.; Khairallah, S. A.; Roehling, T. T.; Heo, T. W.; McKeown, J. T., and Matthews, M. J. "Microstructural control in metal laser powder bed fusion additive manufacturing using laser beam shaping strategy". *Acta Materialia* 184 (2020), pp. 284–305. DOI: 10.1016/j.actamat.2019.11.053.

[148] Wischeropp, T. M.; Tarhini, H., and Emmelmann, C. "Influence of laser beam profile on the selective laser melting process of AlSi10Mg". *Journal of Laser Applications* 32.2 (2020), p. 022059. DOI: 10.2351/7.0000100.

[149] Grünewald, J.; Gehringer, F.; Schmöller, M., and Wudy, K. "Influence of Ring-Shaped Beam Profiles on Process Stability and Productivity in Laser-Based Powder Bed Fusion of AISI 316L". *Metals* 11.12 (2021), p. 1989. DOI: 10.3390/met11121989.

[150] Belay, G. Y.; Kinds, Y.; Goossens, L.; Gurung, K.; Bosmans, N.; Diltoer, R.; Eraly, J.; Vervaeke, M.; Thienpont, H.; Hooreweder, B. V., and Erps, J. V. "Dynamic optical beam shaping system to generate Gaussian and top-hat laser beams of various sizes with circular and square footprint for Additive Manufacturing applications". *Procedia CIRP* 111 (2022), pp. 75–80. DOI: 10.1016/j.procir.2022.08.134.

[151] Galbusera, F.; Caprio, L.; Previtali, B., and Demir, A. G. "The influence of novel beam shapes on melt pool shape and mechanical properties of LPBF produced Al-alloy". *Journal of Manufacturing Processes* 85 (2023), pp. 1024–1036. DOI: 10.1016/j.jmapro.2022.12.007.

[152] Gafner, M.; Remund, S.; Chaja, M. V.; Mähne, T., and Neuenschwander, B. "Ultrafast stamping by combination of synchronized galvanometer scanning with DOE's or SLM". *Procedia CIRP* 94 (2020), pp. 802–806. DOI: 10.1016/j.procir.2020.09.126.

[153] Lutz, C.; Roth, G.-L.; Rung, S.; Esen, C., and Hellmann, R. "Efficient Ultrashort Pulsed Laser Processing by Dynamic Spatial Light Modulator Beam Shaping for Industrial Use". *Journal of Laser Micro/Nanoengineering* (2021). DOI: 10.2961/jlmn.2021.01.2011.

[154] Fontaine, N. K.; Ryf, R.; Chen, H.; Neilson, D. T.; Kim, K., and Carpenter, J. "Multi-plane light conversion of high spatial mode count". *Laser Beam Shaping XVIII*. SPIE, 2018. DOI: 10.1117/12.2323200.

[155] Pallier, G. and Poisson, J.-F. "Beam shaping to scale up microprocessing". *PhotonicsViews* 20.1 (2023), pp. 32–35. DOI: 10.1002/phvs.202300003.

[156] Lee, K.-S.; Yang, D.-Y.; Park, S. H., and Kim, R. H. "Recent developments in the use of two-photon polymerization in precise 2D and 3D microfabrications". *Polymers for Advanced Technologies* 17.2 (2006), pp. 72–82. DOI: 10.1002/pat.664.

[157] Zorba, V.; Tzanetakis, P.; Fotakis, C.; Spanakis, E.; Stratakis, E.; Papazoglou, D. G., and Zergioti, I. "Silicon electron emitters fabricated by ultraviolet laser pulses". *Applied Physics Letters* 88.8 (2006). DOI: 10.1063/1.2177653.

[158] Hermann, J.; Benfarah, M.; Coustillier, G.; Bruneau, S.; Axente, E.; Guillemoles, J.-F.; Sentis, M.; Alloncle, P., and Itina, T. "Selective ablation of thin films with short and ultrashort laser pulses". *Applied Surface Science* 252.13 (2006), pp. 4814–4818. DOI: 10.1016/j.apsusc.2005.06.057.

[159] Hammer, C. M.; Petsch, C.; Klenke, J.; Skerl, K.; Paulsen, F.; Kruse, F. E.; Seiler, T., and Menzel-Severing, J. "Corneal tissue interactions of a new 345 nm ultraviolet femtosecond laser". *Journal of Cataract and Refractive Surgery* 41.6 (2015), pp. 1279–1288. DOI: 10.1016/j.jcrs.2014.11.046.

[160] Häfner, T. "Effect of Picosecond Laser Based Modifications of Amorphous Carbon Coatings on Lubricant-free Tribological Systems". *Journal of Laser Micro/Nanoengineering* 12.2 (2017), pp. 132–140. DOI: 10.2961/jlmn.2017.02.0015.

[161] Engelhart, P.; Hermann, S.; Neubert, T.; Plagwitz, H.; Grischke, R.; Meyer, R.; Klug, U.; Schoonderbeek, A.; Stute, U., and Brendel, R. "Laser ablation of SiO2 for locally contacted Si solar cells with ultrashort pulses". *Progress in Photovoltaics: Research and Applications* 15.6 (2007), pp. 521–527. DOI: 10.1002/pip.758.

[162] Hu, L.; Huang, Y., and Lin, M. "Excimer Laser and Femtosecond Laser in Ophthalmology". *High Energy and Short Pulse Lasers*. InTech, 2016. DOI: 10.5772/64238.

[163] Li, S.; Alverson, S.; Bohler, D.; Egger, A.; Fry, A.; Gilevich, S.; Huang, Z.; Miahnahri, A.; Ratner, D.; Robinson, J., and Zhou, F. "Ultraviolet laser transverse profile shaping for improving x-ray free electron laser performance". *Physical Review Accelerators and Beams* 20.8 (2017). DOI: 10.1103/physrevaccelbeams.20.080704.

[164] Alcock, S. G.; Nistea, I.-T.; Signorato, R.; Owen, R. L.; Axford, D.; Sutter, J. P.; Foster, A., and Sawhney, K. "Dynamic adaptive X-ray optics. Part II. High-speed piezoelectric bimorph deformable Kirkpatrick–Baez mirrors for rapid variation of the 2D size and shape of X-ray beams". *Journal of Synchrotron Radiation* 26.1 (2019), pp. 45–51. DOI: 10.1107/s1600577518015965.

[165] Xu, Y.; Ding, B.; Huang, Z.; Dai, L.; Liu, P.; Li, B.; Cai, W.; Cheng, H.-M., and Liu, B. "Deep ultraviolet hydrogel based on 2D cobalt-doped titanate". *Light: Science & Applications* 12.1 (2023). DOI: 10.1038/s41377-022-00991-6.

[166] Boyd, R. W. *Nonlinear optics 4th edition*. Academic press, 2020.

[167] Franken, P.; Hill, A. E.; Peters, C. e., and Weinreich, G. "Generation of optical harmonics". *Physical Review Letters* 7.4 (1961), p. 118.

[168] Pedrotti, F. L.; Pedrotti, L. S.; Bausch, W., and Schmidt, H. *Optik für Ingenieure*. Springer-Verlag, 2005. DOI: 10.1007/b139018.

[169] Fan, T. Y.; Huang, C. E.; Hu, B. Q.; Eckardt, R. C.; Fan, Y. X.; Byer, R. L., and Feigelson, R. S. "Second harmonic generation and accurate index of refraction measurements in flux-grown KTiOPO_4". *Applied Optics* 26.12 (1987), p. 2390. DOI: 10.1364/ao.26.002390.

[170] Zhang, W.; Yu, H.; Wu, H., and Halasyamani, P. S. "Phase-matching in nonlinear optical compounds: a materials perspective". *Chemistry of Materials* 29.7 (2017), pp. 2655–2668. DOI: 10.1021/acs.chemmater.7b00243.

[171] Yao, J.; Shi, W., and Sheng, W. "Accurate calculation of the optimum phase-matching parameters in three-wave interactions with biaxial nonlinear-optical crystals". *Journal of the Optical Society of America B* 9.6 (June 1992), p. 891. DOI: 10.1364/josab.9.000891.

[172] Boyd, R. W.; Gaeta, A. L., and Giese, E. "Nonlinear optics". *Springer Handbook of Atomic, Molecular, and Optical Physics*. Springer, 2008, pp. 1097–1110.

[173] Baltuška, A.; Fuji, T., and Kobayashi, T. "Controlling the Carrier-Envelope Phase of Ultrashort Light Pulses with Optical Parametric Amplifiers". *Physical Review Letters* 88.13 (2002). DOI: 10.1103/physrevlett.88.133901.

[174] Sellmeier. "Zur Erklärung der abnormen Farbenfolge im Spectrum einiger Substanzen". *Annalen der Physik und Chemie* 219.6 (1871), pp. 272–282. DOI: 10.1002/andp.18712190612.

[175] Yao, J. Q. and Fahlen, T. S. "Calculations of optimum phase match parameters for the biaxial crystal KTiOPO_4". *Journal of Applied Physics* 55.1 (1984), pp. 65–68. DOI: 10.1063/1.332850.

[176] Buono, W. T. and Forbes, A. "Nonlinear optics with structured light". *Opto-Electronic Advances* 5.6 (2022), pp. 210174–1. DOI: 10.29026/oea.2022.210174.

[177] Dholakia, K.; Simpson, N. B.; Padgett, M. J., and Allen, L. "Second-harmonic generation and the orbital angular momentum of light". *Physical Review A* 54.5 (1996), R3742–R3745. DOI: 10.1103/physreva.54.r3742.

[178] Courtial, J.; Dholakia, K.; Allen, L., and Padgett, M. J. "Second-harmonic generation and the conservation of orbital angular momentum with high-order Laguerre-Gaussian modes". *Physical Review A* 56.5 (1997), pp. 4193–4196. DOI: 10.1103/physreva.56.4193.

[179] Mair, A.; Vaziri, A.; Weihs, G., and Zeilinger, A. "Entanglement of the orbital angular momentum states of photons". *Nature* 412.6844 (2001), pp. 313–316. DOI: 10.1038/35085529.

[180] Shao, G.-H.; Wu, Z.-J.; Chen, J.-H.; Xu, F., and Lu, Y.-Q. "Nonlinear frequency conversion of fields with orbital angular momentum using quasi-phase-matching". *Physical Review A* 88.6 (2013). DOI: 10.1103/physreva.88.063827.

[181] Zhou, Z.-Y.; Li, Y.; Ding, D.-S.; Jiang, Y.-K.; Zhang, W.; Shi, S.; Shi, B.-S., and Guo, G.-C. "Generation of light with controllable spatial patterns via the sum frequency in quasi-phase matching crystals". *Scientific Reports* 4.1 (2014), pp. 1–5. DOI: 10.1038/srep05650.

[182] Li, Y.; Zhou, Z.-Y.; Ding, D.-S., and Shi, B.-S. "Sum frequency generation with two orbital angular momentum carrying laser beams". *Journal of the Optical Society of America B* 32.3 (2015), p. 407. DOI: 10.1364/josab.32.000407.

[183] Steinlechner, F.; Hermosa, N.; Pruneri, V., and Torres, J. P. "Frequency conversion of structured light". *Scientific Reports* 6.1 (2016). DOI: 10.1038/srep21390.

[184] Shen, Y.; Wang, X.; Xie, Z.; Min, C.; Fu, X.; Liu, Q.; Gong, M., and Yuan, X. "Optical vortices 30 years on: OAM manipulation from topological charge to multiple singularities". *Light: Science & Applications* 8.1 (2019). DOI: 10.1038/s41377-019-0194-2.

[185] Silva, B. P. da; Buono, W. T.; Pereira, L. J.; Tasca, D. S.; Dechoum, K., and Khoury, A. Z. "Spin to orbital angular momentum transfer in frequency up-conversion". *Nanophotonics* 11.4 (2021), pp. 771–778. DOI: 10.1515/nanoph-2021-0493.

[186] Hancock, S. W.; Zahedpour, S., and Milchberg, H. M. "Second-harmonic generation of spatiotemporal optical vortices and conservation of orbital angular momentum". *Optica* 8.5 (2021), p. 594. DOI: 10.1364/optica.422743.

[187] Hong, X.-H.; Yang, B.; Zhang, C.; Qin, Y.-Q., and Zhu, Y.-Y. "Nonlinear Volume Holography for Wave-Front Engineering". *Physical Review Letters* 113.16 (2014). DOI: 10.1103/physrevlett.113.163902.

[188] Shapira, A.; Naor, L., and Arie, A. "Nonlinear optical holograms for spatial and spectral shaping of light waves". *Science Bulletin* 60.16 (2015), pp. 1403–1415. DOI: 10.1007/s11434-015-0855-3.

[189] Xu, T.; Switkowski, K.; Chen, X.; Liu, S.; Koynov, K.; Yu, H.; Zhang, H.; Wang, J.; Sheng, Y., and Krolikowski, W. "Three-dimensional nonlinear photonic crystal in ferroelectric barium calcium titanate". *Nature Photonics* 12.10 (2018), pp. 591–595. DOI: 10.1038/s41566-018-0225-1.

[190] Wei, D.; Wang, C.; Wang, H.; Hu, X.; Wei, D.; Fang, X.; Zhang, Y.; Wu, D.; Hu, Y.; Li, J.; Zhu, S., and Xiao, M. "Experimental demonstration of a three-dimensional lithium niobate nonlinear photonic crystal". *Nature Photonics* 12.10 (2018), pp. 596–600. DOI: 10.1038/s41566-018-0240-2.

[191] Liu, S.; Switkowski, K.; Xu, C.; Tian, J.; Wang, B.; Lu, P.; Krolikowski, W., and Sheng, Y. "Nonlinear wavefront shaping with optically induced three-dimensional nonlinear photonic crystals". *Nature Communications* 10.1 (2019). DOI: 10.1038/s41467-019-11114-y.

[192] Liu, S.; Mazur, L. M.; Krolikowski, W., and Sheng, Y. "Nonlinear Volume Holography in 3D Nonlinear Photonic Crystals". *Laser & Photonics Reviews* 14.11 (2020), p. 2000224. DOI: 10.1002/lpor.202000224.

[193] Berger, V. "Nonlinear Photonic Crystals". *Physical Review Letters* 81.19 (1998), pp. 4136–4139. DOI: 10.1103/physrevlett.81.4136.

[194] Liu, H.; Li, J.; Fang, X.; Zhao, X.; Zheng, Y., and Chen, X. "Dynamic computer-generated nonlinear-optical holograms". *Physical Review A* 96.2 (2017). DOI: 10.1103/physreva.96.023801.

[195] Liu, H.; Zhao, X.; Li, H.; Zheng, Y., and Chen, X. "Dynamic computer-generated nonlinear optical holograms in a non-collinear second-harmonic generation process". *Optics Letters* 43.14 (2018), p. 3236. DOI: 10.1364/ol.43.003236.

[196] Wu, Y.; Liu, H., and Chen, X. "Three-dimensional nonlinear optical holograms". *Physical Review A* 102.6 (2020). DOI: 10.1103/physreva.102.063505.

[197] Yao, W.; Zhou, C.; Wang, T.; Chen, P.; Xiao, M., and Zhang, Y. "Angle-Multiplexing Nonlinear Holography for Controllable Generations of Second-Harmonic Structured Light Beams". *Frontiers in Physics* 9 (2021). DOI: 10.3389/fphy.2021.751860.

[198] Buono, W. T.; Santiago, J.; Pereira, L. J.; Tasca, D. S.; Dechoum, K., and Khoury, A. Z. "Polarization-controlled orbital angular momentum switching in nonlinear wave mixing". *Optics Letters* 43.7 (2018), p. 1439. DOI: 10.1364/ol.43.001439.

[199] Radwell, N.; Brickus, D.; Clark, T. W., and Franke-Arnold, S. "High speed switching between arbitrary spatial light profiles". *Optics Express* 22.11 (2014), p. 12845. DOI: 10.1364/oe.22.012845.

[200] Bawart, M.; Jesacher, A.; Zelger, P.; Bernet, S., and Ritsch-Marte, M. "Modified Alvarez lens for high-speed focusing". *Optics Express* 25.24 (2017), pp. 29847–29855. DOI: 10.1364/OE.25.029847.

[201] Braverman, B.; Skerjanc, A.; Sullivan, N., and Boyd, R. W. "Fast generation and detection of spatial modes of light using an acousto-optic modulator". *Optics Express* 28.20 (2020), p. 29112. DOI: 10.1364/oe.404309.

[202] Accanto, N.; Molinier, C.; Tanese, D.; Ronzitti, E.; Newman, Z. L.; Wyart, C.; Isacoff, E.; Papagiakoumou, E., and Emiliani, V. "Multiplexed temporally focused light shaping for high-resolution multi-cell targeting". *Optica* 5.11 (2018), p. 1478. DOI: 10.1364/optica.5.001478.

[203] Gregory, D. A.; Kirsch, J. C., and Tam, E. C. "Full complex modulation using liquid-crystal televisions". *Applied Optics* 31.2 (1992), p. 163. DOI: 10.1364/ao.31.000163.

[204] Hsieh, M.-L.; Chen, M.-L., and Cheng, C.-J. "Improvement of the complex modulated characteristic of cascaded liquid crystal spatial light modulators by using a novel amplitude compensated technique". *Optical Engineering* 46.7 (2007), p. 070501. DOI: 10.1117/1.2750658.

[205] Siemion, A.; Sypek, M.; Suszek, J.; Makowski, M.; Siemion, A.; Kolodziejczyk, A., and Jaroszewicz, Z. "Diffuserless holographic projection working on twin spatial light modulators". *Optics Letters* 37.24 (2012), p. 5064. DOI: 10.1364/ol.37.005064.

[206] Zhu, L. and Wang, J. "Arbitrary manipulation of spatial amplitude and phase using phase-only spatial light modulators". *Scientific Reports* 4.1 (2014). DOI: 10.1038/srep07441.

[207] ISO 13694:2018. *Optics and photonics - Lasers and laser-related equipment - Test methods for laser beam power (energy) density distribution*. Standard. Geneva, CH: International Organization for Standardization, 2018.

[208] Sedao, X.; Lenci, M.; Rudenko, A.; Faure, N.; Pascale-Hamri, A.; Colombier, J., and Mauclair, C. "Influence of pulse repetition rate on morphology and material removal rate of ultrafast laser ablated metallic surfaces". *Optics and Lasers in Engineering* 116 (2019), pp. 68–74. DOI: 10.1016/j.optlaseng.2018.12.009.

[209] Assunção, E.; Quintino, L., and Miranda, R. "Comparative study of laser welding in tailor blanks for the automotive industry". *The International Journal of Advanced Manufacturing Technology* 49.1-4 (2009), pp. 123–131. DOI: 10.1007/s00170-009-2385-0.

[210] Iron Boar Labs Ltd. *5754-F Aluminum*. 2020. https://www.makeitfrom.com/material-properties/5754-F-Aluminum (visited on 04/13/2023).

[211] Hagenlocher, C.; Wagner, J.; Michel, J.; Weber, R.; Bachmann, M.; Karadogan, C.; Liewald, M., and Graf, T. "The influence of residual stresses on laser beam welding processes of aluminium sheets". *Procedia CIRP* 94 (2020), pp. 713–717. DOI: 10.1016/j.procir.2020.09.124.

[212] Wieland Duro GmbH. *TZM Technical Datasheet*. https://www.wieland.com/en/content/download/12678/file/TZM_EX_EN.pdf (visited on 04/14/2023).

[213] Henini, M. and Razeghi, M., eds. *Handbook of Infra-red Detection Technologies*. Elsevier, 2002. DOI: 10.1016/b978-1-85617-388-9.x5000-x.

[214] Jung, W. D. and Danielson, G. C. "The Thermal Conductivity of High Purity Vanadium". *Thermal Conductivity 14*. Springer US, 1976, pp. 96–96. DOI: 10.1007/978-1-4899-3751-3_16.

[215] HyperPhysics Georgia State University. *Thermal Conductivity*. http://hyperphysics.phy-astr.gsu.edu/hbase/Tables/thrcn.html (visited on 04/13/2023).

[216] Heider, A.; Stritt, P.; Hess, A.; Weber, R., and Graf, T. "Process Stabilization at welding Copper by Laser Power Modulation". *Physics Procedia* 12 (2011), pp. 81–87. DOI: 10.1016/j.phpro.2011.03.011.

[217] ISO 4287:2010-07. *Geometrical Product Specifications (GPS) - Surface texture: Profile method - Terms, definitions and surface texture parameters*. Standard. 1998.

[218] Döring, S.; Richter, S.; Nolte, S., and Tünnermann, A. "In situ imaging of hole shape evolution in ultrashort pulse laser drilling". *Optics express* 18.19 (2010), pp. 20395–20400. DOI: 10.1364/OE.18.020395.

[219] Döring, S.; Richter, S.; Tünnermann, A., and Nolte, S. "Evolution of hole depth and shape in ultrashort pulse deep drilling in silicon". *Applied Physics A* 105.1 (2011), pp. 69–74. DOI: 10.1007/s00339-011-6526-6.

## Own publications referring to this work

[P1] Ackermann, L.; Roider, C.; Gehring, M.; Cvecek, K., and Schmidt, M. "High-speed speckle averaging for phase-only beam shaping in laser materials processing". *Optics and Lasers in Engineering* 165 (2023), p. 107537. DOI: 10.1016/j.optlaseng.2023.107537.

[P2] Ackermann, L.; Gehring, M.; Roider, C.; Cvecek, K., and Schmidt, M. "Spot arrays for uniform material ablation with ultrashort pulsed lasers". *Optics & Laser Technology* 163 (2023), p. 109358. DOI: 10.1016/j.optlastec.2023.109358.

[P3] Ackermann, L.; Roider, C., and Schmidt, M. "Uniform and efficient beam shaping for high-energy lasers". *Optics Express* 29.12 (2021), p. 17997. DOI: 10.1364/oe.426953.

[P4] Ackermann, L.; Roider, C.; Cvecek, K., and Schmidt, M. "Methods for uniform beam shaping and their effect on material ablation". *Applied Physics A* 128.10 (2022). DOI: 10.1007/s00339-022-06004-y.

[P5] Ackermann, L.; Roider, C.; Cvecek, K.; Barré, N.; Aigner, C., and Schmidt, M. "Polarization-controlled nonlinear computer-generated holography". *Scientific Reports* 13.1 (2023). DOI: 10.1038/s41598-023-37443-z.

[P6] Ackermann, L.; Roider, C.; Cvecek, K.; Barré, N., and Schmidt, M. "Diminishing Speckle Noise During Nonlinear Phase-Only Beam Shaping". *2023 Conference on Lasers and Electro-Optics Europe & European Quantum Electronics Conference (CLEO/Europe-EQEC)*. 2023, pp. 1–1. DOI: 10.1109/CLEO/Europe-EQEC57999.2023.10232165.

## Students' theses referring to this work

[S1] Ackermann, S. "Charakterisierung des Übersprechens benachbarter Pixel am Spatial Light Modulator". Master's thesis. Institute of Photonic Technologies, 2019.

[S2] Aigner, C. "Analyse von Strahlformung innerhalb der Frequenzverdopplung und Evaluierung von Prozessgrenzen". Master's thesis. Institute of Photonic Technologies, 2021.

# Kurzfassung

Bei der Lasermaterialbearbeitung ist die reine Phasenformung ein leistungsfähiges Instrument zur Gestaltung des räumlichen Intensitätsprofils und zur Anpassung des Energieeintrags. Dies verbessert die Fertigungspräzision und Effizienz, was wiederum den Durchsatz und die Qualität erhöht. Das typische Gerät der Wahl ist der räumliche Lichtmodulator basierend auf einer Flüssigkristallschicht auf Silizium. Da er nur die Wellenfront des einfallenden Lichtfeldes formt, werden kaum Verluste induziert, und der sich ausbreitende Strahl geht in die gewünschte Intensitätsverteilung über. Da diese Methode jedoch keine ausreichende Kontrolle über das gesamte Lichtfeld ermöglicht, überlagern Speckle die Zielstruktur. In dieser Arbeit werden Methoden zur Strahlformung entwickelt, die Speckle unter Beibehaltung hoher Präzision und Effizienz reduzieren. Die entwickelten Methoden sind anwendungsorientiert und für ultrakurzgepulste Lasersysteme ausgelegt. Abtragsexperimente dienen der experimentellen Validierung und ermöglichen die Charakterisierung der entwickelten Methoden und des Einflusses des bearbeiteten Materials. Da der formbare Spektralbereich von Flüssigkristalldisplays technisch beschränkt ist, ist nichtlineare Strahlformung von besonderem Interesse, da sie genutzt werden kann, um diese Limitierung zu überwinden. In dieser Arbeit wird eine Technik zur nichtlinearen Strahlformung untersucht, die mit schneller Specklemittelung kombiniert wird. Das bereitet den Weg zur ebenen Strahlformung im ultravioletten Spektralbereich bei gleichzeitiger Ermittlung materialspezifischer Eigenschaften, die für einen Materialabtrag mit hoher Gleichmäßigkeit relevant sind.

# Abstract

In laser materials processing, phase-only beam shaping is a powerful tool to form the spatial intensity profile and tailor the energy input. This improves production precision and efficiency which in turn increases throughput and quality. A common device of choice is the liquid crystal on silicon spatial light modulator. As it only shapes the wave front of the incoming light field, it induces almost no losses and the propagating beam emerges into the targeted intensity distribution. However, as this method does not allow sufficient control of the full light field, speckle overlays the target structure. This thesis develops methods for beam shaping counteracting speckle while maintaining high precision and efficiency. The developed methods are application-oriented and designed for ultrashort pulse lasers. Ablation experiments serve as experimental validation and allow for characterizing the developed methods and the influence of the processed material. Since the shapeable spectral range of liquid crystal displays is technically limited, non-linear beam shaping is of particular interest, which can be used to overcome this limitation. This thesis investigates a technique for nonlinear beam shaping which is further combined with rapid speckle averaging. This paves the way towards uniform beam shaping in the ultraviolet spectral range while elucidating material-specific properties pertinent to ablation results with high uniformity.